The Development of the ATLAS SCT as a Luminometer and the Search for SUSY Decays with Compressed Mass Spectra

Claire Malone
of Churchill College
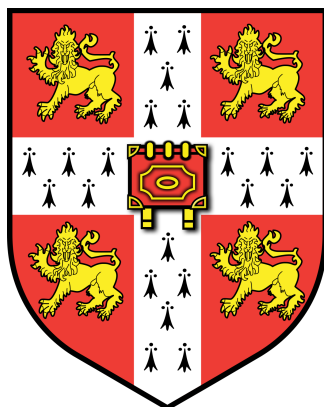
In loving memory of Thierry March

Abstract

The formulation of the Standard Model of particle physics (SM) is one of the greatest scientific achievements of the 20th century. It is, however, incomplete (for example, it lacks a dark matter candidate) as well as the fact that the hierarchy problem violates naturalness arguments. This has motivated the construction of particle accelerators to probe fundamental particles at increasingly high center-of-mass energies and luminosities, the LHC at CERN being the latest to continue this legacy. This thesis covers both the enhancement of luminosity measurements of *pp* collisions at ATLAS, underpinning the accuracy of all measurements made by the detector, and a search for one of the most theoretically viable extensions to the SM: supersymmetry.

ATLAS uses mainly event-counting algorithms to measure luminosity, which break down at higher luminosities. If the ATLAS SemiConductor Tracker (SCT) can be employed as a luminometer using hit-counting algorithms, this issue may be mitigated. It is established here that the SCT can feasibly operate as a luminometer when recording two-or-more strip clusters with the standard binary readout mode (01X). Thus, the SCT can measure the luminosity with an accuracy within 10% of two of ATLAS's existing luminometers: LUCID and TileCal.

The discovery of the supersymmetric *top* (*stop*) would be fundamental for solving the hierarchy problem. An analysis of an experimentally challenging region of phase space, where stop decays have a compressed mass spectrum, complements the ATLAS one-lepton stop search using 13 TeV *pp* collisions at 139 fb^{-1} is presented. The aM_{T2} kinematic variable, designed to give a lower limit on pair-produced particle masses, is found to be effective at differentiating SUSY decays from the SM background, when used as an upper bound. No significant excess was observed above the Standard Model background and limits at 95% confidence level are set. Stop quarks are found to be excluded up to 500 GeV and mass splittings between the stop and the neutralino are found to be excluded up to 130 GeV, complimenting the exclusion limits found by other ATLAS searches for stop decays with one-lepton final states.

Declaration

This dissertation is the result of my own work, except where explicit reference is made to the work of others, and has not been submitted for another qualification to this or any other university. This dissertation does not exceed the word limit for the respective Degree Committee.

Claire Malone

Acknowledgements

Contents

"So before you go out searching,
Don't decide what you will find"
— Frank Turner

Chapter 1.

Introduction

"Imagination is more important than knowledge"
  — Albert Einstein

Throughout history humans have sought to understand the nature of the fundamental constituents of the universe, which are now known as particles. The area of science that is called particle physics represents our most systematic and ambitious attempt to understand the nature of these particles [1]. Although it is difficult to ascribe the birth of a field to one event, it is commonly accepted that modern particle physics began in 1897, when J. J. Thomson discovered the electron. This was followed by E. Rutherford's demonstration that the majority of the mass of an atom is concentrated in the nucleus in 1911 and by E. Chadwick's discovery of the neutron in 1932 [2]. The development of quantum theory in the 1920s and 1930s led to the conception of the Standard Model of particle physics (SM) [3–11], the theoretical basis of our understanding of particle interactions, the salient features of which are described in Chapter 2. With advances in accelerator technology, energy scales of the order of GeV and TeV have become accessible to exploration [12]. This has led to the SM being moulded into a collection of theories that describe the interactions of all *known*[1] particles to a remarkably high level of accuracy.

The process of moulding the SM into a coherent description of the particle content of the universe has driven the construction of successive generations of particle accelerators which seek to extend the exploration of the parameter space with increasingly high centre-of-mass energies and luminosities. At the time of writing, this quest has culminated

---

[1] Even though the SM predicts massless neutrinos, the neutrino mass can be produced by the addition of gauge invariant mass term to the SM Lagrangin.

in the installation of the Large Hadron Collider (LHC) at Conseil Européen pour la Recherche Nucléaire (CERN), which was designed to provide proton-proton (*pp*) collisions at 14 TeV. In 2012, the LHC's two multi-purpose detectors, A Toroidal LHC ApparatuS (ATLAS) [13] and Compact Muon Solenoid (CMS) [14], jointly discovered the Higgs boson [15, 16], the last SM particle to avoid detection, thus completing the experimental picture of the SM. Figure 1.1 summarises the fiducial and cross section measurements made by ATLAS compared to the theoretically expected values predicted by the SM to Next-to-Leading-Order (NLO) or higher. This plot demonstrates the ability of the SM to match cross section measurements made by ATLAS over several orders of magnitude, which can be seen as a testament to the success of the theory. An overview of the ATLAS detector shall be given in Chapter 3.
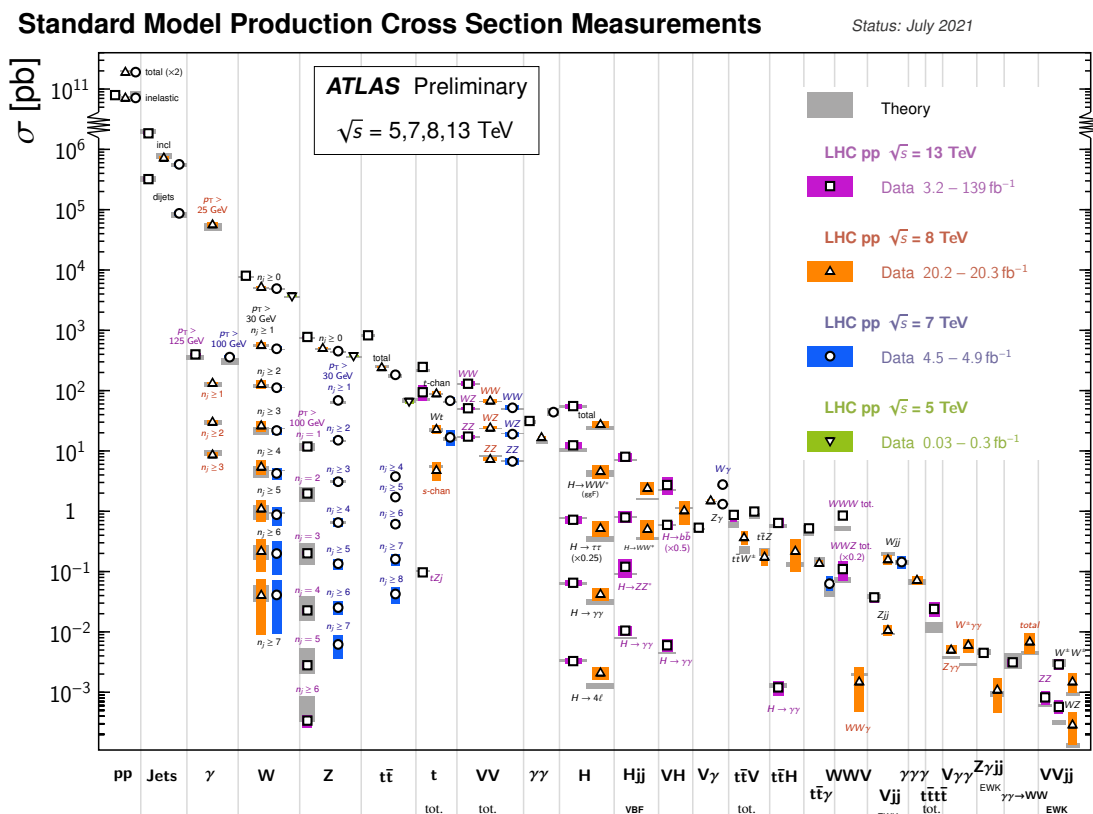
Figure 1.1.: Summary of SM fiducial and total cross section measurements made by ATLAS compared to theoretically expected values predicted by the SM. All theoretically expected values were calculated to NLO or higher. Figure taken from Ref. [17].

Nevertheless, there are some phenomena that the SM cannot explain in its current form. Examples of features of the SM that highlight its incompleteness include: no mechanism to explain the imbalance between matter and antimatter, the sources of Charge-Parity (CP)

violations in the SM being insufficient to explain the matter dominance. Moreover, cosmology tells us that the known particles only account for approximately 4% of the known universe, the remaining proportion being attributed to dark matter and dark energy. These shortcomings are in addition to the hierarchy problem [18–21] which draws attention to the fact that two of the fundamental scales of the SM, the reduced Planck scale and the electroweak scale, have 32 orders of magnitude between them [22]. For this to be true would require either a Higgs mass that was very much larger than the Electroweak (EW) scale of 10^2 GeV or a disturbing fine-tuning in the cancellation between the bare Higgs mass and the radiative corrections [22, 23]. The shortcomings of the SM are discussed in more detail in Section 2.3.

One of the main goals of particle physics at the time of writing is to determine the nature of the physical processes that lie beyond the current formulation of the SM: Beyond Standard Model physics (BSM). The phenomenological landscape of BSM is rich, and so it falls to the experimental particle physicists to determine which of these theories (if any) is realised by nature. Among the theories currently envisaged as one of the strongest BSM candidates is supersymmetry (SUSY), a theory which was first developed in the 1970s. As shall also be explained in Chapter 2, SUSY has gained its enduring popularity through its elegant solution to the hierarchy problem and the ease at which it provides a description of the fundamental particles that dark matter could be comprised of.

The luminosity and the centre of mass energy of it's beams are two of a particle collider's main distinguishing features. The accuracy of all the measurements made by the ATLAS detector rely on precise knowledge of the luminosity[2] of the LHC's beam. To control the systematic uncertainties on this vital measurement, ATLAS compares luminosity measurements from several luminometers, most of which utilise more than one algorithm to make their luminosity measurement. For ATLAS to continue to search for SUSY in unexplored regions of parameter space more data collected as a result of collisions occurring at higher luminosities are needed in order to increase the probability of observing particle interactions that are not described by the SM. This is in additional to extending the scope of the parameter space that a collider can reach by increasing it's centre of mass energy. However, with the increase of the luminosity of the beam, one of the commonly used category of luminosity algorithms[3] that ATLAS relied upon at

---

[2]In Chapter 4, the luminosity of a particle collider is the ratio of the event rate of the collider to the inelastic cross-section of the colliding particles.

[3]Event-counting algorithms, which are defined in Chapter 4

the beginning of its operation begin to break down. Hence alternative techniques were found to continue to control the systematic uncertainties associated with the luminosity measurement. Based on the preliminary results found in [24], relating to the use of the PIXEL detector (PIXEL) of the ATLAS' Inner Detector (ID), a feasibility study of the use of the ID's SemiConductor Tracker (SCT) was conducted. This feasibility study, which is presented in Chapter 4 (see also the author's ATLAS internal note [25]), shows the promising result that the SCT could be used to provide a reliable luminosity measurement through comparison with readings from two of ATLAS' existing luminometers, the LUminosity measurement using Cherenkov Integrating Detector (LUCID) and the Tile Calorimeter (TileCal), to within a 10% uncertainty.

In order for SUSY to provide answers for the open questions within the SM, the theory predicts a plethora of as-yet undiscovered particles, therefore approximately doubling the particle content of the SM. If a theory that so enthusiastically predicts a multitude of new particles is to provide a much-needed extension to the SM, it is clear that one of the main occupations of particle physicists should be to discover these particles. When a new particle is discovered, a question that begs to be answered is 'What is its mass?'. A common method of mass determination is to extract the value of the mass directly on an event-by-event basis from observation. A major advantage of this method is that it does not depend on the configuration of the momenta of the observed particles and hence is independent of the process that was responsible for the production of the detected particles. However, when searching for particles that are not included in the SM, it may not be surprising that such particles are not readily detected by the apparatus at hand. Thus, as is explained in Chapter 5, their existence can only be deduced by an observation of 'missing momentum' in our detectors. As a consequence, it is not possible to employ such methods of direct mass measurement. Hence, it falls to the physicists to be inventive in finding new approaches. One technique that has proved fruitful has been the development of new variables[4] (such as the aM_{T2} variable introduced in Ref. [26]) that can be used to parameterise the masses of the particles in the decay under consideration. In addition, some SUSY scenarios predict decay products in their final states which the ATLAS detector cannot precisely reconstruct e.g. because their transverse momentum (p_{T}) is too low[5]. In such cases, the experimenter is challenged to develop novel techniques to overcome these limitations. The analysis presented in this thesis focuses on such decays where the decay products are liable not to be precisely

---

[4]A mathematical expression built from quantities that can be measured by the detector e.g. momenta, mass, charge e.t.c.

[5]See Chapter 5

reconstructed. Additionally it employs the aM_{T2} variable in an unconventional way to distinguish signal from background events, as explained in Chapter 5.

As the most massive of the fermions predicted by the SM, the *top*-quark has a unique role within SUSY in providing a solution to the hierarchy problem. Its supersymmetric partner, the *stop*-quark, possesses a rich phenomenology predicting a variety of mechanisms for the particle to decay. The parameter space that these decays occupy is far from being fully experimentally explored, providing additional motivation for the development of that ATLAS search for the *stops* that decay into final states involving one isolated lepton [27]. The analysis presented in Chapter 6 is designed to be an extension of this search, focusing specifically on decays that have a very compressed mass spectra[6], where the difference in mass between the *stop* and the Lightest Supersymmetric Particle (LSP) ranges from 7 GeV up to approximately 100 GeV, with particular focus on the experimentally inaccessible lower end of that range. This region of parameter space can easily be unexplored by *stop* searches due to the experimental challenges caused by the decay products having very low transverse momenta. The conclusions of this thesis are put into context with the broader landscape of high energy physics in Chapter 7.

---

[6]Meaning that the mass difference of the *stop* and the Lightest Supersymmetric Particle is relatively small compared to other *stop* decays searched for by ATLAS

Chapter 2.

The Standard Model of Particle Physics and Beyond

"I'm breaking through
I'm bending spoons
I'm keeping flowers in full bloom
I'm looking for answers from the great beyond"
 — Michael Stipe

The SM is undoubtedly one of the triumphs of human scientific endeavour, being able to predict the nature of fundamental particles with an unprecedented degree of accuracy [1]. However, as briefly discussed in Chapter 1, the SM cannot provide a complete description of the particle content of the universe. One of the foci of this thesis is the search for BSM in the form of SUSY. This search is put into context by a brief overview of the SM in the chapter that follows, as well as an introduction to the phenomenological landscape of SUSY.

2.1. Overview of the Standard Model of particle physics

The SM describes fermions, which are half-integer-spin fundamental particles, and bosons, which are integer-spin fundamental particles that mediate the interactions of the fermions. The fermions are described by excitations of a quantum field that satisfied the appropriate

quantum mechanical field equations dictated by Quantum Field Theory (QFT) [28]. Fermions are divided into quarks and leptons and are arranged in three generations with the particles in each successive generation having higher masses than those in the previous one[1]. Details of the masses and charges of the leptons and quarks can be found in Ref. [29].

There are a number of key differences between leptons and quarks. Quarks interact with all three of the fundamental forces that are described by the SM whereas electrons, muons and taus only interact with the Electromagnetic (EM) and weak forces. Neutrinos only interact with the weak force. In addition, the electric charge of a lepton is always either 0 or $\pm e$ where e is the absolute value of the electric charge on an electron. As a consequence of the Dirac equation, the wave equation of relativistic particles, each massive fundamental fermion in the SM is accompanied by an antiparticle that has exactly the same properties as its "particle twin", but with the opposite charge, or the same charge in the case of neutral particles. The electron, muon and tau[2] all have a negative electric charge with positively charged anti-particles whereas in the case of the quarks, one particle per generation has an electric charge of $-e/3$ with the other particle possessing an electric charge of $+2e/3$. Research is ongoing to determine whether neutrinos are their own anti-particle (termed Majorana neutrinos) or not (Dirac neutrinos), discussion of which is beyond the scope of this thesis.

Within each generation, there are two types or 'flavours' of particles: for example in the first generation of leptons, the electron is recognised as one flavour, while the electron neutrinos are recognised as a separate flavour. Quantum Chromodynamics (QCD) also predicts that quarks possess a type of charge, as well as the one predicted by Quantum Electrodynamics (QED), called 'colour'. There are three colour charges, labelled red, green and blue, but, due to the finite range of the strong force, bound states of quarks are always 'colourless' i.e. with no overall colour charge[3]. The SM does not provide any motivation for the number of generations that are required to describe the particle content of the universe (further examples of the shortcomings of the SM shall be discussed in Section 2.3).

The area of particle physics concerned with the determination of the properties of the *top*-quark is still very active at the time of writing - it even has its own name, "top

---

[1]Although the mass spectrum of neutrinos is yet to be experimentally determined.

[2]Muon and tau are leptons in the second and third generations respectively along with muon-neutrinos and tau-neutrinos.

[3]Leptons are also colourless.

physics". As shall be explained Section 2.4, of particular relevance to the search for BSM physics presented in this thesis is the fact that the *top*-quark is significantly more massive than the other quarks - a mass of 173 GeV which gives it around 40 times the mass of the second most massive quark, the *bottom*-quark[4]. The *top*-quark's phenomenology is driven by its notably large mass which grants it the title of the most massive fundamental particle. As it is more massive than the W-boson, it is the only quark that can decay giving an on-shell W-boson as well as a b-quark. It has a very short lifetime and therefore decays prior to hadronisation. Finally, as it has a Yukawa coupling close to unity[5], it has a unique role to play in the solution to one of the greatest pitfalls of the SM, the hierarchy problem discussed in Section 2.3 and Section 2.4 [28, 30].

The spin 1 bosons of the SM mediate the fundamental forces that act on the fermions: photons for the EM force, $W^{\pm}$ and Z for the weak force and gluons for the strong force. The EM force governs the interactions between electrically charged particles via photon exchange, while the weak force can transform one lepton or quark into another. The strong force is responsible for transformations between different colour states in quarks and is described by QCD. Gluons mediate the strong interaction between quark states of different colour, so must carry colour charge for it to be a conserved quantity. The photon and the gluons are massless bosons unlike the W and Z bosons with masses of approximately 80 GeV and 91 GeV respectively. Turning to the forth fundamental force, there is currently no mechanism for including gravity in the SM.

Massless fermions are eigenstates of the helicity[6] operator. For the spin-half particles the component of spin measured along any axis can be quantised to either $+1/2$, corresponding to "left-handed" particles, or $-1/2$, corresponding to "right-handed" particles. The weak force only couples to particles that are described by left handed chiral states [28]. It is known from the decay rates of muons and taus that the weak interaction is the same for all generations of lepton, a principle known as lepton universality[7].

---

[4]Sometimes called the beauty quark or b-quark

[5]The Yukawa coupling is the coupling of a particle to the Higgs field, the field that decorates all particles with their masses.

[6]The physical interpretation of helicity is a projection of a particle's spin along the direction of its momentum [31]

[7]Although, results that were published at the time of writing Ref. [32] suggest that violations of lepton universality could exist in nature, providing evidence of physics not described by the SM, as discussed in Section 2.3.

2.2. The Principle of Symmetry and the Higgs boson

A desirable feature for a model of particle physics is that it can provide a unified description of the fundamental forces of nature. The principle of symmetry, which is expressed in the language of group theory, has guided much of the construction of the SM [33]. The EM interaction can be described by the unitary group of degree one $U(1)$, the strong interaction by the special unitary group of degree three $SU(3)$ and the weak interaction by the special unitary group of degree two $SU(2)_L$, where the subscript L signifies that only left handed fermions couple to the weak force. The SM includes a theoretical framework to combine the EM and the weak forces, provided by the Glashow-Salam-Weiberg (GSW) model, so that the resulting EW interaction has the symmetry group $SU(2)_L \times U(1)_Y$, where the subscript Y denotes the replacement of the electric charge with weak hypercharge Y, which is a combination of electric charge and weak isospin [28]. However, the SM in its current formulation does not have a mechanism to unify the strong force with the EW force[8]. In summary, the SM can be described by the non-abelian group[9] $SU(2)_L \times U(1)_Y \times SU(3)$.

In 1983 the W and Z bosons were discovered at CERN [34–38]. However, unlike the massless photon used to mediate the infinity-ranged EM force, the bosons of the weak interaction were found to be anything but massless [34–38]. Here a stumbling block is encountered: gauge theories do not allow mass terms for gauge bosons, as they break gauge invariance [33]. A mechanism by which these massive gauge fields can be accommodated must exist. This is the so-called Higgs mechanism, which exploits EW symmetry breaking. Manifest in the theory of EW symmetry breaking is the existence of a Higgs boson to mediate the acquisition of particle masses. This particle gained its illustrious reputation by being the particle predicted by the SM which escaped detection for the longest, until its discovery was jointly announced by the ATLAS and CMS collaborations in 2012 [15, 16] – possibly one of the most monumental discoveries in fundamental physics in recent decades along with the detection of gravitational waves, neutrino oscillations and the hints of the violation of lepton universality.

---

[8]Attempts to unify all of the fundamental forces (even gravity) are the motivation behind the development of "Theories of everything". Discussion of such theories is beyond the scope of this thesis.

[9]The group is non-abelian because the generators do not commute.

2.3. Shortcomings of the Standard Model of particle physics

No matter how successful the SM is at describing the properties of fundamental particles, it cannot claim to be a complete theory of matter and forces in this universe. This is not least because it does not incorporate one of the four fundamental forces, gravity, as explained in Section 2.1. In fact, experimental evidence of BSM physics in the form of neutrinos with non-zero masses has already been found. The SM also contains 19 free parameters[10], none of which have values that are predicted by the model itself, but have been determined empirically [31]. The existence of three generations of fermions is also stated without any motivation. In addition, the year of submission of this thesis saw two experiments produce results that were in tension with the SM. The first of these was the measurement of R_K, the ratio of the branching fractions of the decays $B^+ \to K^+ \mu^+ \mu^-$ and $B^+ \to K^+ e^+ e^-$, where K^+ is a positively charged kaon. This was measured by the Large Hadron Collider beauty (LHCb) collaboration with a 3.1 σ tension with the SM prediction (see Ref. [32] for details). This was shortly followed by a publication of the measurement of the positive muon magnetic moment by the Fermilab g–2 experiment with a 4.2 σ tension to the SM prediction [39]. Both of these landmark results bolster the argument mentioned above that the SM is an incomplete theory of nature and could be said to provide hope that a more fundamental understanding of our universe may be within reach.

A fundamental theory of the particle content of the universe should provide an explanation of the nature of the content of the entire universe. In fact, compelling astronomical evidence would suggest that the SM actually only describes just 5% of the energy density of the universe [33]. The observed rotational velocities of galaxies alone suggest that, in some cases, the total mass of a galaxy is far greater than can be accounted for by the luminous matter. This 'missing mass' has been termed dark matter and is predicted to account for 23% of the energy-matter density of the universe [28]. The SM can offer no suitable explanation as to the character of this dark matter[11]. The unexpected discovery that the expansion of the universe is accelerating, rather

---

[10]These are: the three gauge coupling constants, the three Cabibbo-Kobayashi-Maskawa (CKM) matrix angles and the CP-violating phase that describe the CKM matrix, the strong CP parameter, the two parameters in the scalar potential, the masses of the three charged leptons and the six masses of the quarks.

[11]At the risk of spoilers, it shall be seen that the extension to the SM that is the subject of the majority of the research presented here and is discussed in Section 2.4, provides a whole host of plausible dark matter candidates.

than decelerating due to gravitational attraction, points to the existence of a previously undiscovered force acting against gravity on a universal scale. This force, which accounts for the remaining 72% of the energy density of the universe and is now known as dark energy, also has no explanation within the SM [2]. The mere fact that the observed universe is dominated by matter points to a further inconsistency in the SM - there is neither sufficient Charge-Parity (CP) violation nor a non-equilibrium[12] condition is built into the SM to account for this huge asymmetry in matter and antimatter [33]. It is known that CP violation in weak interactions can be attributed to the complex phase δ' in the CKM matrix[13], but the resulting CP violation is vastly insufficient to account for the dominance of matter in the universe [2].

Since the discovery of a Higgs boson, which is consistent with the SM, the hierarchy problem [18–21] has been thrown into the spotlight. This problem draws attention to the fact that there are thirty two orders of magnitude between the reduced Planck scale and the EW scale. If this were the case, it would require either a Higgs mass that was very much larger than the EW scale of 10^2 GeV or a troubling fine-tuning in the cancellation between the bare Higgs mass and the radiative corrections [22, 23]. As the *top*-quark is the most massive of the quarks, it contributes the largest radiative correction to the Higgs mass, which results in quadratic and logarithmic divergences.

2.4. The SUSY Solution

A possible solution to some of the ailments of the SM is offered by supersymmetry (SUSY). The theory is now one of the strongest candidates for an explanation of physics which is not accounted for by the SM. SUSY extends the SM by postulating a symmetry between fermions and bosons - resulting in a supersymmetric particle (sparticle) for every SM particle. These sparticles possess identical quantum numbers to their SM counterparts except for a half unit difference in spin. Single partner states are arranged in supermultiplets, which pair up one SM fermion (boson) with a SUSY boson (fermion). These two particles are known as superpartners of each other [40]. The supersymmetric partners of the quarks and leptons are spin 0 particles and are denoted by prefixing the fermion names with an 's' for scalar. Meanwhile, the standard nomenclature for

---

[12]Without a non-equilibrium condition, any reaction that instigated a preference for baryons over anti-baryons would be counteracted by the reverse reaction [2].

[13]CP violations also occurs in the lepton sector from a complex phase in the Pontecorvo-Maki-Nakagawa-Sakata (PMNS) matrix.

the supersymmetric partners to the SM spin 1 bosons is to suffix the boson names with 'ino'. SUSY requires the presence of an extended Higgs sector consisting of two Higgs supermultiplets in order to avoid a Witten anomaly, which states that an $SU(2)$ gauge theory is inconsistent with itself if it has an odd number of left-handed fermion doublets [41, 42]. It is convenient to write them as conjugate doublets $H_u = (H_u^+, H_u^0)$ and $H_d = (H_d^0, H_d^-)$, and after EW symmetry breaking has been invoked, this implies a Higgs sector with five physical particles: two neutral CP-even scalars, one neutral CP-odd pseudoscalar, and two charged scalars [43] [33]. The components of these doublets correspond to the two components of the Higgs complex scalar field that was discussed in Section 2.2. The two Higgs doublets have spin $1/2$ supersymmetric partners called higgsino denoted $\widetilde{H}_u = (\widetilde{H}_u^+, \widetilde{H}_u^0)$ and $\widetilde{H}_d = (\widetilde{H}_d^0, \widetilde{H}_d^-)$. As SUSY is invoked before EW symmetry breaking, the fields representing the W/Z-bosons form supermultiplets with the wino and bino. Finally the higgsinos can mix with the binos and the winos to produce two mass eigenstates called charginos ($\widetilde{\chi}_r^\pm$, $r = 1, 2$) as well as four mass eigenstates termed neutralinos $\widetilde{\chi}_r^0$, $r = 1, 2, 3, 4$, numbered in order of increasing mass [33].

Table 2.1 and Table 2.2 show some of the properties of the SM particles compared to their SUSY partners. The SUSY particles presented in Table 2.1 and Table 2.2 form the particle content of the Minimal Supersymmetric Standard Model (MSSM), which is the simplest extension of the SM that incorporates SUSY [40]. The title 'minimal' is a slight misnomer, as the model includes a measly 124 parameters: the 19 of the SM plus 105 new parameters[14] [44].

The existence of these sparticles would provide an elegant solution to the hierarchy problem as the quadratically divergent corrections to the square of the Higgs mass would be cancelled between the particles and the sparticles[15] [22]. This is accomplished by the contributions to the Higgs mass term from spin 0 bosons through the quartic and trilinear couplings.

The preservation of lepton and baryon number conservation is implied by the lack of experimental evidence for proton decay, which would violate both quantum numbers [22]. Hence, a discrete, multiplicative symmetry called R-parity is imposed, defined by

---

[14]This exacerbates the problem discussed in Section 2.3 that ideally a fundamental theory should have as few parameters as possible!

[15]Logarithmic divergences are still present in perturbative calculations involving energies of the order of the grand unification scale (approximately 2×10^{16}) GeV but fortunately these divergences can be summed using renormalisation group methods [22] [45].

Names	spin 0		spin 1/2	
squarks/quarks	$(\widetilde{u}_L$	$\widetilde{d}_L)_i$	$(u_L$	$d_L)_i$
	$(\widetilde{u}_R$	$\widetilde{d}_R)_i$	$(u_R$	$d_R)_i$
sleptons/leptons	$(\widetilde{\nu}$	$\widetilde{l}_L)_i$	$(\nu$	$l_L)_i$
	$(\widetilde{\nu}$	$\widetilde{l}_R)_i$	$(\nu$	$l_R)_i$

Table 2.1.: The SM fermions and their supersymmetric partners in the MSSM in their supermultiplets. The generations of particles are denoted by the index $i = 1, 2, 3$. The SM (spin 1/2) fermions are arranged in their chiral supermultiplet while the SUSY (spin 0) fermions are in their vector supermultiplet. For the spin 0 particles, the subscripts 'L' and 'R' refer to the chirality of their SM superpartners.

Names	spin 0		spin 1/2		spin 1	
gluino/gluon	–		$\widetilde{g}$		g	
winos/W-bosons	–		$\widetilde{W}^{\pm}$	$\widetilde{W}^0$	$W^{\pm}$	W^0
bino/B-boson	–		$\widetilde{B}^0$		B^0	
Higgs/higgsinos	$(H_u^+$	$H_u^0)$	$(\widetilde{H}_u^+$	$\widetilde{H}_u^0)$	–	
	$(H_d^0$	$H_d^-)$	$(\widetilde{H}_d^0$	$\widetilde{H}_d^-)$	–	

Table 2.2.: The SM bosons and their supersymmetric partners in the MSSM.

$R = (-1)^{2s+3B+L}$. Here, L and B are the lepton and baryon numbers respectively, with s representing the spin quantum number. Particles are therefore allocated the R-parity quantum number of $R = +1$ whereas $R = -1$ corresponds to sparticles. The physical consequences of R-parity conservation are that sparticles are always produced in pairs (at colliders) and their decay chains involve an even number of sparticles, culminating in a stable LSP [46]. For the analysis presented in this thesis, a simplified, R-parity conserving MSSM is assumed, involving only the *stop* and a stable LSP as the other sparticles are taken to be too massive to be detected. Simplified models are widely used in SUSY searches and are defined by an effective Lagrangian describing the interactions of a small number of particles. Alternatively they can be parametrised by a small number of particle masses and cross-sections because all the masses of the particles that are not involved in the decay chain under consideration are fixed at high values and therefore decouple. The branching fractions for the SUSY decays is also set to 100%, as is a common feature with simplified models [47].

2.4.1. The *Stop*-Quark

The *stop*-quark has a special role to play amongst the squarks. As discussed previously, the *top*-quark is the heaviest fermion so it makes the largest contribution to the correction to the Higgs mass. If SUSY were unbroken (each sparticle having an equal mass to its SM partner) the sparticles would contribute an equal correction to its corresponding particle proportional to its mass, but with an opposite sign. Hence, the *stop*-quark would have the greatest effect in this cancellation. SUSY postulates that the *top* superpartners need to be light enough to cancel the contribution from the *top* mass [48–50]. As a consequence of the logarithmic divergences, the greater the difference in mass between the *top* and the *stop*, the larger the correction to the Higgs mass that remains unaccounted for.

The effects of the renormalisation group equations and naturalness arguments[16] would suggest the existence of light *stops*, capable of being produced at the LHC [52]. Naturalness arguments appeal to the notion that the parameters of a model should not have to be fine-tuned. Such adjustment is seen to be a very undesirable feature of a model that attempts to describe reality [53].

The superpartners of the left- and right-handed *top*-quark, $\tilde{t}_L$ and $\tilde{t}_R$, mix to form the two mass eigenstates, $\tilde{t}_1$ and $\tilde{t}_2$, where $m_{\tilde{t}_1} < m_{\tilde{t}_2}$ [54]. The decay of the *stop*-quark can lead to a variety of final states, which is influenced greatly by the mass spectrum predicted by the SUSY model under consideration as well as the mixing of $\tilde{t}_L$ and $\tilde{t}_R$ [54,55]. The mixing can be strong [56], due to the large mass of the *top* quark entering the non-diagonal terms of the mass matrix which determines the mixing of these two eigenstates given in Ref. [57]. This can result in the mass eigenstate $\tilde{t}_1$ being lighter than the other squarks [57]. The mass of the *top* squark in turn dictates which of its decay modes are dominant. The three main regions of the $m_{\tilde{t}_1} - m_{\tilde{\chi}_1^0}$ plane are shown in Figure 2.1 where $\Delta m(\tilde{t}_1, \tilde{\chi}_1^0) = m_{\tilde{t}_1} - m_{\tilde{\chi}_1^0}$ identifies the distinct regions of phase space where different decay modes of the *stop* are dominant. Each region of Figure 2.1 is discussed below.

If $\Delta m(\tilde{t}_1, \tilde{\chi}_1^0) > m_t$, the decay of the *stop* proceeds via $\tilde{t}_1 \rightarrow t\tilde{\chi}_1^0$. Meanwhile, the three-body decay $\tilde{t}_1 \rightarrow bW\tilde{\chi}_1^0$, which proceeds via an off-shell *top*-quark, is favoured if $m_W + m_b < \Delta m(\tilde{t}_1, \tilde{\chi}_1^0) < m_t$. The decays $\tilde{t}_1 \rightarrow c\tilde{\chi}_1^0$ and $\tilde{t}_1 \rightarrow bff'\tilde{\chi}_1^0$ (where c represents the *charm*-quark and f and f' indicate any fermions originating from the decay of an

---

[16]The renormalisation group equations provide a mathematical way to view a physical system at different scales whilst naturalness arguments dictate that all parameters in a theory should be dimensionless ratios between free parameters or physical constants and of order unity [51] [44].

off-shell W boson) are favoured in the region $\Delta m(\tilde{t}_1, \tilde{\chi}_1^0) < m_W + m_b$. The dominance of the $\tilde{t}_1 \to b f f' \tilde{\chi}_1^0$ decay is determined by the mixing between squark generation allowed by the mostly diagonal super-CKM matrix, details of which can be found in [29, 58]. Decays of the form $\tilde{t}_1 \to b f f' \tilde{\chi}_1^0$ are searched for in this analysis. The region $\Delta m(\tilde{t}_1, \tilde{\chi}_1^0) < 0$ (i.e. $m_{\tilde{t}_1} < m_{\tilde{\chi}_1^0}$) is not kinematically allowed due to conservation of energy. [59].
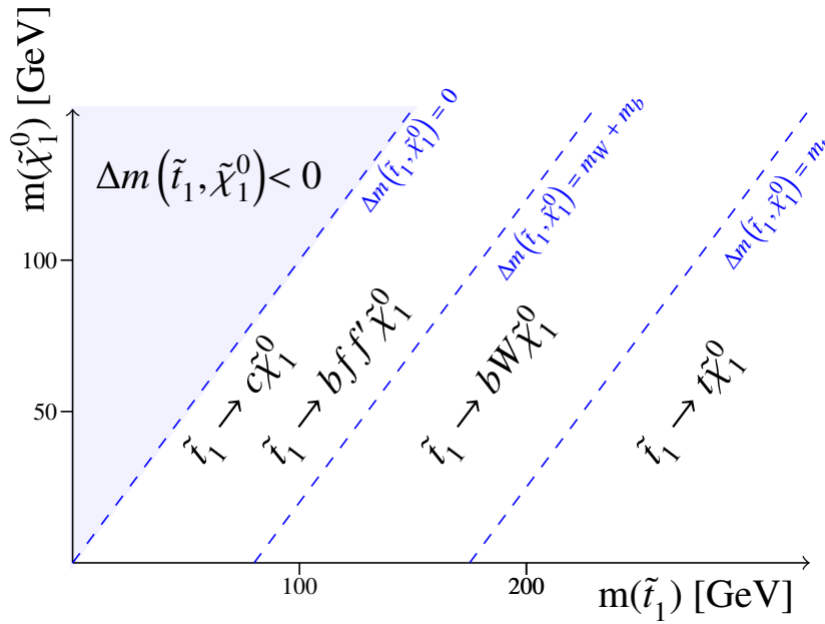
Figure 2.1.: Illustration of the *stop*-decay modes in the $m_{\tilde{t}_1}$–$m_{\tilde{\chi}_1^0}$ plane where $\tilde{\chi}_1^0$ is the lightest neutralino and assumed to be the LSP. The three dashed lines indicate thresholds separating regions where the different decay modes dominate. Figure taken from Ref. [59].

2.4.2. SUSY Breaking

The ability of sparticles to persistently elude discovery is strong evidence of the fact that they do not have equal masses to their SM counterparts, i.e. the supersymmetry between particles and sparticles is a broken symmetry. Broken SUSY can still guarantee the mitigation of quadratically divergent corrections to the square of the Higgs mass. In order to protect the sparticles from quadratic mass divergences, SUSY must be broken 'softly' [60]. Soft supersymmetry breaking implies that the effective Lagrangian for the MSSM can be written as

$$\mathcal{L} = \mathcal{L}_{\text{SUSY}} + \mathcal{L}_{\text{soft}}. \tag{2.1}$$

$\mathcal{L}_{\text{SUSY}}$ includes all the Yukawa and gauge interactions and preserves SUSY invariance, while $\mathcal{L}_{\text{soft}}$ violates SUSY but only comprises the mass terms and coupling parameters that have a positive mass dimension [22]. One consequence of soft SUSY breaking is that the sparticles can obtain masses below the unification mass scale (approximately 10^{18} GeV) without violating naturalness arguments.

As the precise nature of supersymmetry breaking is as yet unknown, the number of free parameters can be reduced by specifying the exact method of supersymmetry breaking under consideration. In the case of EW symmetry breaking, explicit symmetry breaking requires the introduction of non-invariant mass terms, which would make the theory non-renormalizable[17]. Hence, spontaneous symmetry breaking of SUSY (preserving renormalizability) is preferred theoretically and is indicated experimentally through the precision measurement of radiative corrections [62].

A number of SUSY models exist with a predetermined mechanism for SUSY breaking included within them, but there is no consensus on how spontaneous SUSY breaking could be theoretically realised. Most of these models postulate the existence of a visible sector of particles (those predicted by the MSSM) and a hidden sector where SUSY breaking is generated. An example of a group of such models would be models of super-gravity where a particle that is responsible for mediating gravitational interactions is responsible for the breaking of SUSY [29]. The use of simplified models is aiding the search for evidence of such SUSY scenarios within ATLAS.

2.5. Conclusions

In this chapter, an outline of the current theoretical understanding of particle physics, that takes the form of the SM, was given. It was explained, however, that this model cannot provide a complete picture of reality and experimental evidence of BSM physics was highlighted. It was also explained that a very attractive solution to some of these shortcomings can be offered by an extension to the SM – SUSY. Particular attention was paid to the decays of the *stop*-quark, as searching for a evidence of this particle is the aim of the main analysis presented in this thesis. It is therefore paramount for experimental physicists in this field to design experiments that are capable of discovering

---

[17]Symmetries can either be broken explicitly (meaning that they are described by a Lagrangian that contains terms that break the symmetry) or spontaneously (the equations of motion derived from the system's Lagrangian have solutions that are not invariant under the symmetry under consideration) [61].

the particles that are predicted by BSM theories such as SUSY, in order to complete our understanding of particle physics. In the next chapter, one such experiment, the ATLAS detector, shall be described.

Chapter 3.

The ATLAS Detector - Our Subatomic Microscope

"We are, I think, in the right Road of Improvement, for we are making Experiments."

— Benjamin Franklin

There has been a long history of ground-breaking discoveries in the field of high energy physics at CERN, including those of direct CP violation [63, 64], W/Z-bosons [34–38], and the Higgs boson to name but a few [65]. The Large Hadron Collider (LHC), a two-ring superconducting-hadron accelerator and collider, is the most recent of a prestigious line of accelerators built on this site, hosting four main experiments: the A Toroidal LHC ApparatuS (ATLAS) detector [13], the Compact Muon Solenoid (CMS) [14], the Large Hadron Collider beauty (LHCb) [66] and A Large Ion Collider Experiment (ALICE) [67]. ATLAS and CMS are both multi-purpose detectors, designed to measure particles produced in pp and lead ion collisions. All of the results presented in this thesis were deduced by analysing data collected by the ATLAS detector.

ATLAS is designed to study a wide range of physics processes. As well as offering a unique opportunity to test the SM at unprecedented energies of 7-13 TeV, the properties of strongly interacting matter at extreme energy densities are also being explored to an unparalleled degree through lead ion collisions. One of the primary goals of the ATLAS experiment, to determine the existence of the SM Higgs boson, was already achieved during Run 1[1] of the experiment [15, 16]. In addition to this, the main aims

---

[1]Which lasted from the autumn 2009 to February 2013

of the ATLAS physics program include the investigation of extensions to the SM, such as SUSY, undiscovered heavy gauge bosons like W' and Z' and even the existence of extra dimensions leading to a characteristic energy scale of quantum gravity in the TeV region [13, 68]. In Run 1, ATLAS's performance was recorded to have exceeded expectations across the whole range of operations, from collisions to data taking and continued to perform extremely well throughout Run 2[2] [69–71].

44m

5m

Tile calorimeters

LAr hadronic end-cap an
forward calorimeters

Pixel detector

LAr electromagnetic calorimeters

Toroid magnets

Muon chambers

Solenoid magnet

Transition radiation tracker

Semiconductor tracker
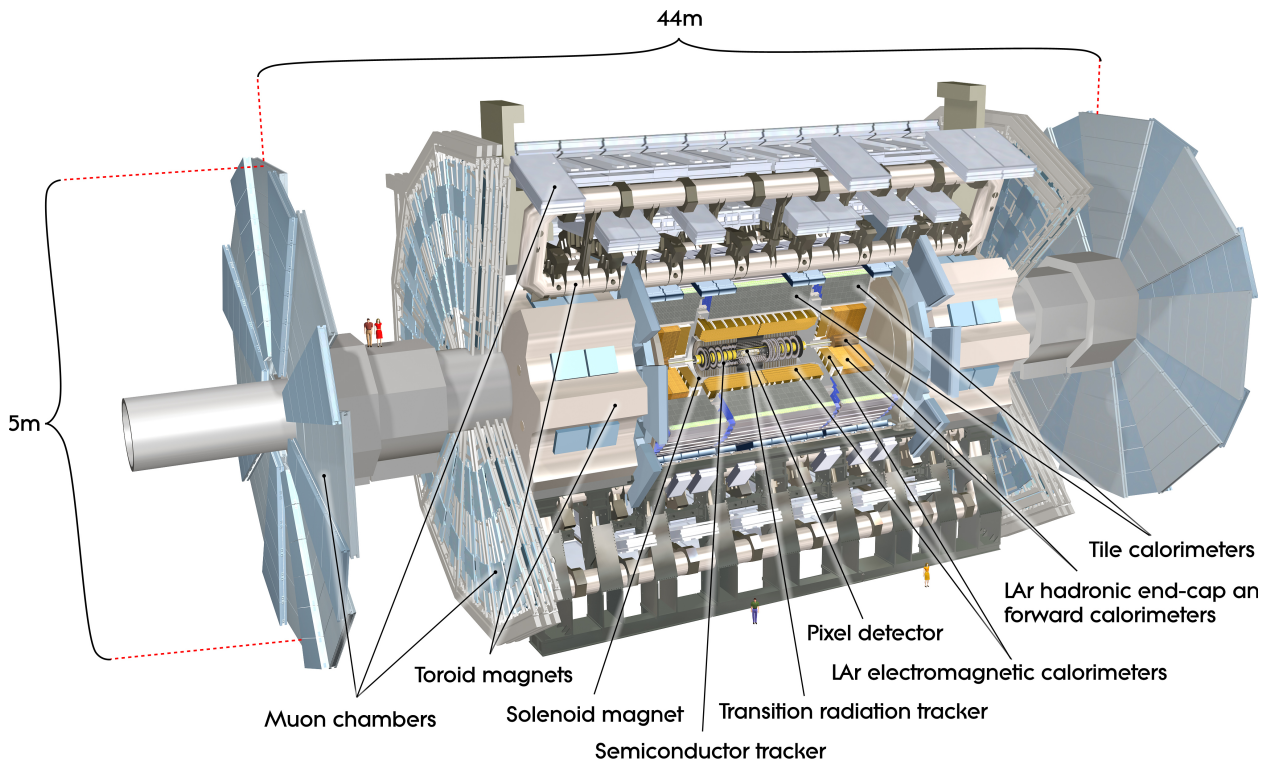
Figure 3.1.: A diagram of the ATLAS detector. Figure taken from Ref. [13].

In order for the results from ATLAS (or any experiment, for that matter) to have even the slightest credibility, a thorough understanding of the behaviour of the detector under all foreseeable conditions (within reason) is essential. This chapter does not even attempt to give a full description of the ATLAS detector (as this would take several books) but it does give a brief description of the main components of the detector and their functions to provide a context in which the experimental results presented here have been obtained. Hence, in the spirit of giving an overview of the detector, a brief description of the entirety of ATLAS is given below and a diagram of its general structure is shown in Figure 3.1.

---

[2]From June 2015 to December 2018

Of course, even the most complete description of the apparatus is useless to an experimenter if they do not understand how to interpret the measurements that it records. To do this, the electronic signals that are generated within ATLAS in response to the particles created in the collisions within the LHC must be *reconstructed* into "physics objects" which are analogous to the particles that prompted the electrical signals to be generated.

In order to provide a logical description of such a complex machine, a coordinate system with which the components of the detector are described with reference to must be established. The origin of this coordinate system is defined to be a nominal interaction point along the beam line running through the centre of ATLAS, which the z-axis is defined to be parallel to. The positive x-axis points towards the centre of the LHC ring while the positive y-axis points upwards. The azimuthal angle ϕ is measured around the beam axis, while the polar angle θ is measured from the beam axis. The pseudo-rapidity is defined as $\eta = -\ln(\tan(\theta/2))$ and the distance ΔR in pseudo-rapidity-azimuthal angle space is $\Delta R = \sqrt{\Delta\eta^2 + \Delta\phi^2}$, where R is the radius parameter. For any given sub-detector, side-A is defined to be the side with a positive z-coordinate, and side-C is defined with a negative z-coordinate [13].

Starting from the Interaction Point (IP) and heading outwards in the radial direction, the Inner Detector (ID) surrounds the beam pipe and consists of the PIXEL Detector, SCT and Transition Radiation Tracker (TRT). The ID, described in Section 3.2, provides tracking and vertex information about charged particles which have a pseudo-rapidity range $|\eta| < 2.5$ [72,73]. This is surrounded by the calorimeter system labelled in Figure 3.1 by the LAr Electromagnetic Calorimeter (ECAL), LAr Hadronic Calorimeter (HCAL) and Forward Calorimeter (FCal) and TileCal. The ECAL and HCAL cover $|\eta| \leq 4.9$, and are discussed in Section 3.3. The calorimeter system is flanked by the Muon Spectrometer (MS) which consists of three layers of gas-filled precision tracking chambers and is immersed in a toroidal magnetic field, which is provided by the magnet systems described in Section 3.4. The MS is responsible for the identification of muons and contributes to the muon momentum measurement, described further in Section 3.4. It covers the range $|\eta| < 2.7$ with $|\eta| < 2.4$ being covered by separate trigger chambers, which are used for the hardware-based Level-1 trigger (L1). Event selection is performed by the trigger system which has a three-level structure: Level-1 trigger (L1), Level-2 trigger (L2) and the Event Filter (EF). Each level of the trigger refines the decisions made at the previous level, and if necessary, applies additional selection criteria. Information from the calorimeter and MS is used by the hardware-based L1. Meanwhile, information

provided by all sub-detectors can be accessed by L2 and EF (together called the High Level Trigger (HLT)) that are both software-based systems [74, 75]. The Trigger and Data AcQuisition (TDAQ) is described in Section 3.5.

Monte Carlo (MC) generators and simulations of the detector are indispensable tools for predicting the behaviour of both the particles created in the LHC and the detectors themselves [76]. The use of these simulations are essential for designing the analyses presented in Chapter 5 and Chapter 6. In Section 3.6 a brief description of how the response of the detector is included in simulations is given. This is followed by an introduction to how the physics objects used in this analysis[3] are reconstructed in Section 3.7.

For a particle collider such as the LHC, two of the main distinguishing quantities are the centre of mass energy of the accelerating particles and the beam luminosity that it can attain. Accurate and precise measurements of the beam luminosity underpin the credibility of virtually all measurements made with the ATLAS detector. ATLAS employs a number of luminometers to provide complementary measurements of the luminosity, which are briefly described in Section 3.1 along with a description of the structure of the colliding beams. Chapter 4 is dedicated to a feasibility study of using the SCT to complement the measurements of these luminometers, which was of particular importance during Run 2 of the LHC, when some of the algorithms used at the start of the run to make this measurement were predicted to break down.

3.1. ATLAS Luminometers

Within the LHC, the proton beams are comprised of bunches of protons, where each bunch is separated by 25 ns (or a multiple thereof) [77]. If a group of bunches is separated in time by more than a few multiples of 25 ns, the group is referred to as a train [78]. For collecting data to be used in physics analysis, the two rings of the LHC are typically filled with more than 2000 bunches; each bunch contains approximately 10^{11} protons. In order to avoid unwanted collisions close to the IP, the beams are not collided head on but with a small crossing angle of 150-200 μrad [77, 79].

ATLAS compares measurements from several luminosity detectors in order to control systematic uncertainties [80]. LUCID is ATLAS's only dedicated luminometer [81].

---

[3]Electrons, muons, taus, photons, jets, Secondary Vertexs (SVs) as well as Missing Transverse Energy (MET). The concept of MET is discussed in detail in Section 3.7.5.

The LUCID detector[4] is composed of two separate modules, which each comprise 16 PhotoMultiplier Tubes (PMTs) close to the beam-line as well as four quartz fibre bundles read by PMTs. The modules are placed around the beam-line on the two forward ends of ATLAS and uses their PMTs to detect charged particles that produce Cherenkov radiation in their quartz windows. The luminosity measurements of LUCID are complemented by the Beam Conditions Monitor (BCM) [83,84], the main function of which is to surveil the LHC beam to protect ATLAS from spikes in its instantaneous luminosity (see Chapter 4). Methods of measuring the luminosity have also been developed using two components of the calorimeter system, the TileCal and the FCal. Details of each of these methods can be found in Refs. [13,80,83,85–87]. The TileCal and the FCal are described in the context of the ATLAS calorimeter in Section 3.3. All of these luminosity detectors consist of two symmetric detector elements, one placed on the A side of the interaction point and the other place on the C side.

3.2. Inner Detector

Out of all the sub-detectors, the ID is found closest to the beam pipe providing ATLAS with tracking and vertex information about charged particles which have a pseudo-rapidity range $|\eta| < 2.5$ within a 2 Tesla magnetic field parallel to the beam direction [72,73]. All tracking detectors rely on the fundamental principle that when a charged particle traverses a medium, it can leave a trail of ionized atoms and displaced electrons from which its path can be reconstructed. Large scale, modern particle physics experiments commonly use two tracking technologies: semiconductor and gaseous based trackers [28], and examples of both can be found in the ATLAS ID. The ID consists of three complementary but independent sub-detectors: the PIXEL Detector, which is surrounded by the SCT, which in turn is enveloped by the gaseous/polypropylene-fibre TRT. At the end of Run 1 an additional fourth layer of silicon semiconductor pixels was added to the existing three layers of the PIXEL Detector: the Insertable B-Layer (IBL) [88]. The two technologies of semiconductor trackers and gaseous/polypropylene-fibre TRT compliment each other to give very robust and high precision pattern recognition both in the ϕ and z-coordinates [72]. The necessity for the PIXEL Detector and SCT to provide highly accurate tracking and be extremely radiation resistant dictates that these two sub-detectors are expensive both in material and monetary terms. In addition, their operations require cooling to -10 to -5 °C. The TRT, by contrast, is designed to operate at room temperature and

---

[4]Which was upgraded to the LUCID2 detector for the start of Run 2 [82].
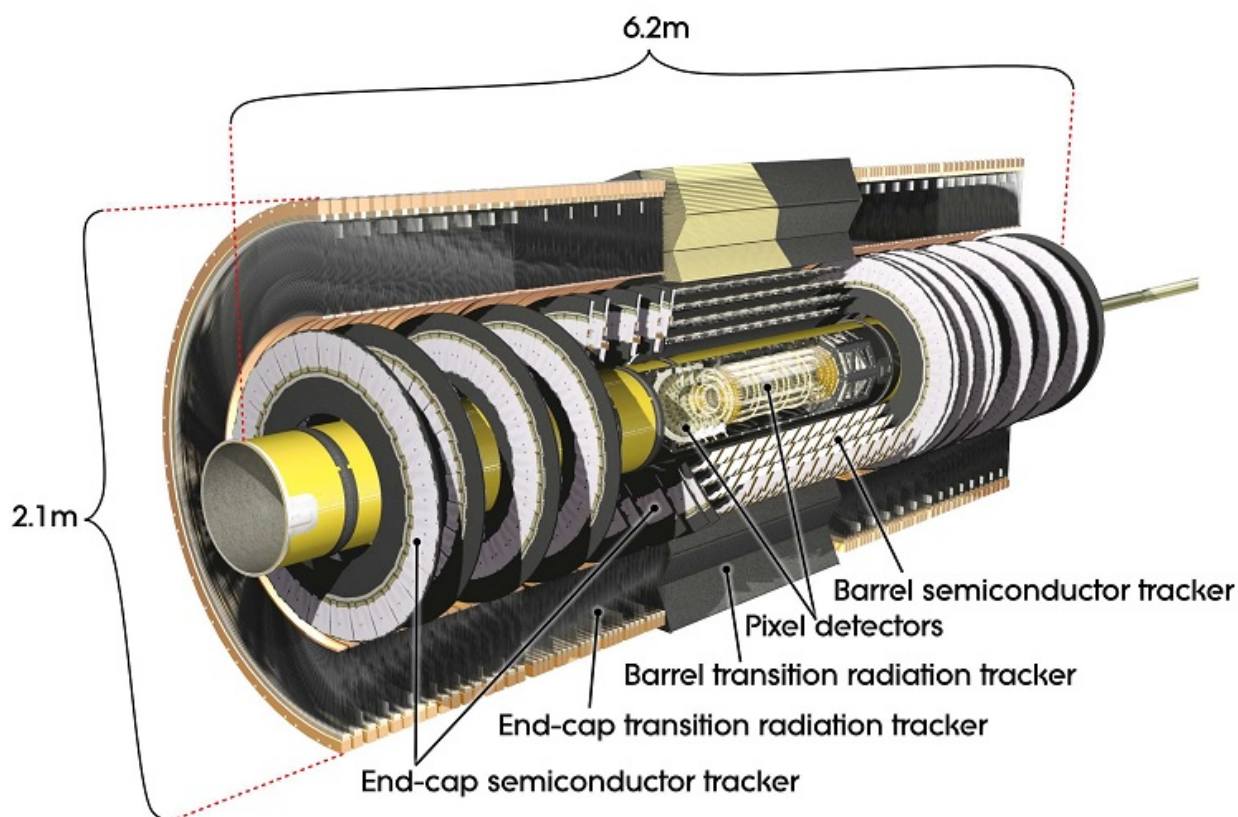
Figure 3.2.: A cut-away view of the ID. Figure taken from Ref. [68]

its construction from polypropylene fibre make it a high volume detector with little material cost. The high multiplicity environment around the interaction point dictates the requirements for the ID to supply hermetic and robust pattern recognition, excellent transverse impact parameter resolution as well as a high standard of *b*-tagging and SV identification (see Section 3.7), the latter two of which are particularly relevant to the results presented in this thesis [89].

A cut-away view of the ID is shown in Figure 3.2, which shows that it is divided into barrel and end-cap regions, in addition to Figure 3.3 which shows the relative positions of the three subdetectors of the ID in the z – y plane. It is constructed in this way in order to minimize the material that particles from the IP need to traverse before they reach other sub-detectors of ATLAS [73]. The operation of the ID, and especially the SCT, is of particular importance to the research presented here. However, to maintain a logical order for the discussion, the PIXEL Detector shall be described first as it is closest to the IP.

The PIXEL Detector is one of the ID's two precision tracking sub-detectors (the SCT being the other one) and is designed to provide a set of measurements with very high granularity, as close to the interaction point as possible [13, 72]. Silicon pixels are a fundamental component of this sub-detector and are connected to the front end electronics [13]. Its constituent modules are divided between three barrel layers and two layers in each of the end-caps. The IBL was added as the fourth barrel layer to maintain robust tracking as well as to provide improved precision for vertexing tagging in the face of the increased luminosity of the beams during Run 2. Its inclusion has had a positive effect on the *b*-tagging performance and efficiency [90].
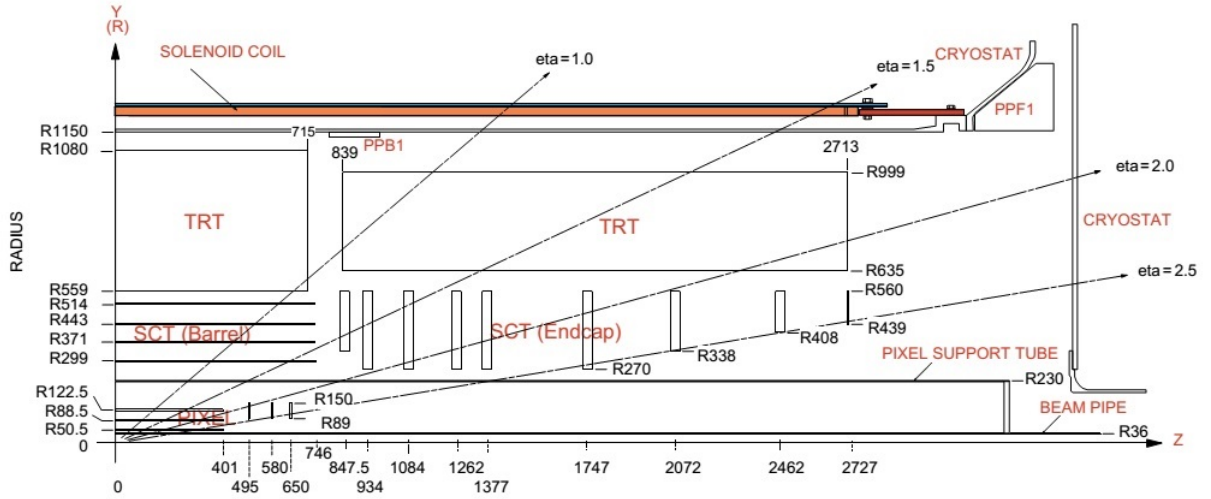
Figure 3.3.: A cross-section taken parallel to the beam pipe of one quadrant of the SCT and its positioning relative to the PIXEL Detector and TRT. The positions of the barrel layers (horizontal lines) and end-cap disks (vertical rectangles) are shown in radial and longitudinal coordinates, with their exact coordinates labelled. Various values of η are shown for orientation. Figure taken from Ref. [91].

Moving on to the other silicon detector, the SCT consists of silicon modules which are arranged in four concentric barrels and two end-caps consisting of nine layers each comprised of silicon microchip sensors called strips[5]. The innermost barrel has a coverage of $|\eta| < 1.4$ while the outermost barrel has a coverage of $|\eta| < 1.1$ [92]. The barrel modules are of a uniform design, as shown in Figure 3.4. The two end-caps provide the remaining range of pseudo-rapidity coverage, reconstructing tracks of charged particles with $|\eta| \leq 2.5$ [93]. Each module is subdivided into two sides, side 0 and side 1.

---

[5]"Hitmaps" showing the locations of particle interactions with the detector for sides A and C of all layers of the barrel and end-caps are presented in Chapter 4.
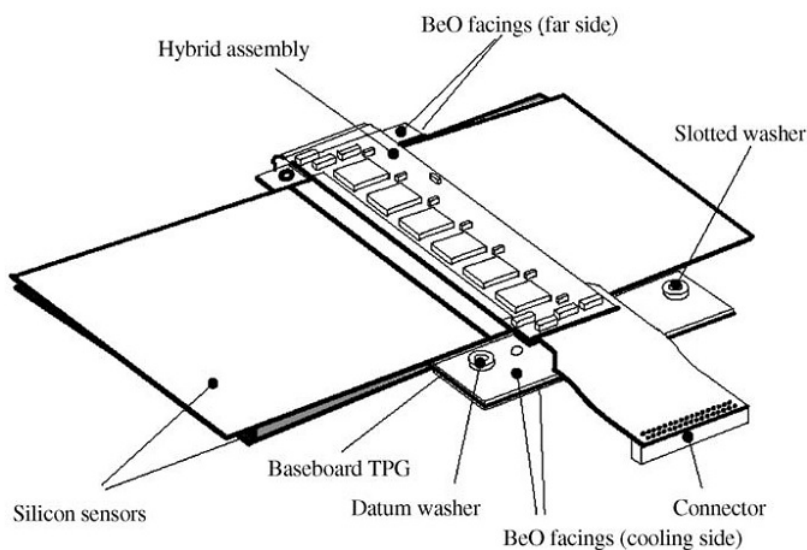
Figure 3.4.: A 3D diagram of an SCT barrel module. Figure taken from Ref. [91].

The silicon Read-Out Driver (ROD) is a fundamental constituent of the TDAQ and the two silicon-based ATLAS tracking systems, the PIXEL Detector and the SCT. The TDAQ is comprised of the L1, L2 and EF and is described in Section 3.5. The main purposes of the silicon RODs are configuration of the aforementioned modules, trigger propagation and data formatting. The RODs are also used for detector calibration and monitoring. Serial data streams are used to send control commands from the RODs to the modules. Examples of the commands that are often sent are L1 trigger, as well as Bunch-Crossing (BC) and event counter resets. The configuration and readout of the SCT modules can be handled by a single ROD board [94].

The correlation between the number of SCT strips recording a hit and the number of inelastic collisions per proton BC is an important statistic of the extent to which the SCT could be used as a luminometer, as shall be explained in Chapter 4. RODs can become "busy", which means that all information that was sent to that ROD from the modules that are connected to it, will be blocked off, which in turn means that all the data produced by the strips associated with that ROD is lost. This will affect the correlation between the number of strips recording hits and the number of inelastic collisions per BC. The effects of dead RODs are investigated by looking for blank spaces shown in the hitmaps in Section 4.3.2.

The SCT is enveloped by the TRT, providing continuous tracking to improve pattern recognition and momentum resolution over $|\eta| \leq 2.0$ [6]. It also complements the calorimetry system (see Section 3.3) in the task of electron identification [13]. Its operation is based on taking advantage of transition radiation. Transition radiation is emitted when a charged particle traverses the interface between two media of different dielectric constants [95]. The TRT can provide continuous tracking as its basic components are highly modular, thin walled, proportional drift tubes termed straws. Straws were chosen because, without compromising the continuous tracking requirement, they can be easily be integrated into a medium producing transition radiation [96].

3.3. Calorimeters

In the context of particle physics, a calorimeter is a device designed to measure the energy and direction of a particle or jet by measuring the cascade of particles resulting from the electromagnetic or hadronic shower that the initial particle induced [28,97]. EM showers are parametrised by the radiation length, the distance over which the number of particles in the shower approximately doubles, while hadronic showers are characterised by the mean distance between nuclear interactions, the nuclear interaction length. The nuclear interaction length is typically significantly greater than the radiation length, hence, hadronic calorimeters need to be composed of much more material than EM calorimeters [28]. Calorimeters play a crucial role in the performance of the LHC – many physics processes that are studied in detail (or expected to be discovered by the LHC, such as SUSY decays), that manifest themselves through final states involving electromagnetic and hadronically interacting particles [98]. A sampling calorimeter consists of layers of active material, that generate signal, which are sandwiched between metallic absorber layers [30]. ATLAS utilises sampling calorimeters, which means that the energy deposited by the minimum ionising particles in the active layers of the calorimeter is small compared to the total energy deposited by such particles in the calorimeter [99]. The performance of the calorimeter is dictated by the resolutions of each of the sub-detectors (detailed in [13]) of which it is comprised. Each of these sub-detectors are described below and a diagram of the ATLAS calorimeter as a whole is shown in Figure 3.5.

The calorimeter provides full ϕ-symmetry and coverage around the beam axis. As Figure 3.5 shows, it is divided into the ECAL (split into a barrel region and two end-cap

---

[6]Except for the region $0.8 < |\eta| < 1.0$, which lies between the barrel and the end-caps.
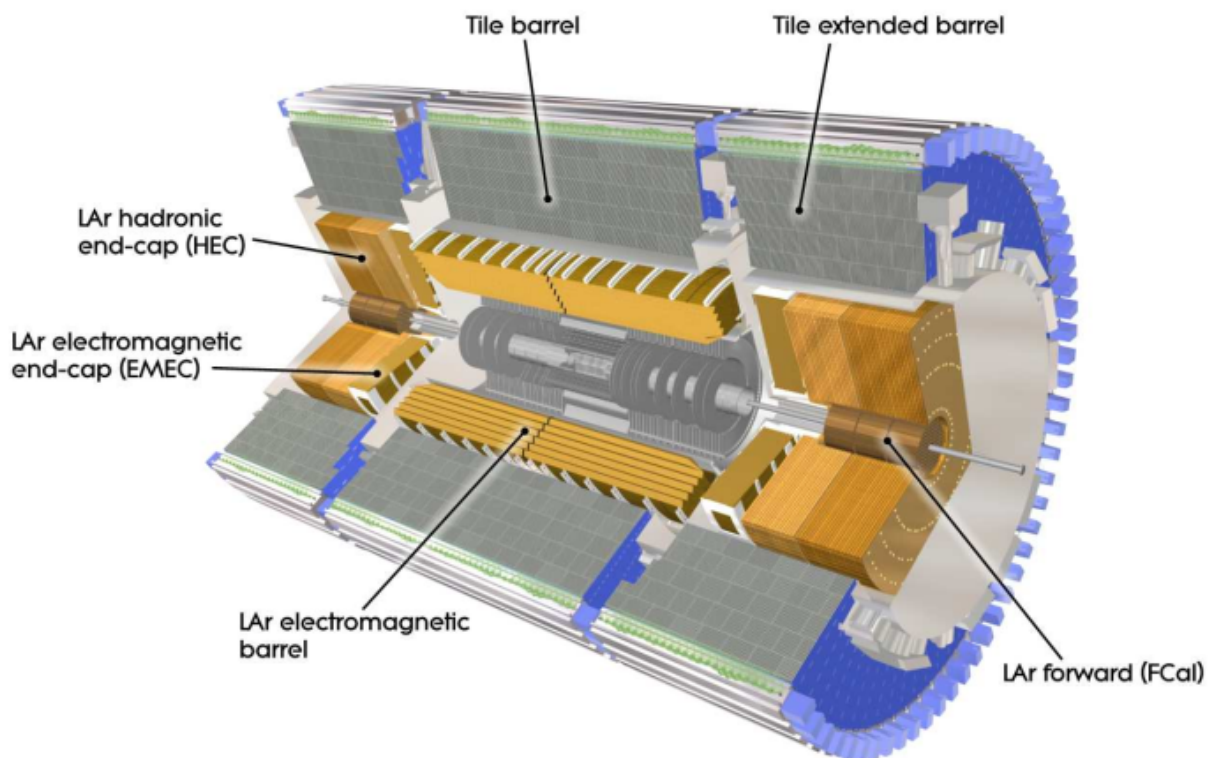
Figure 3.5.: A cut-away view of the ATLAS calorimeter. Figure taken from Ref. [13].

regions) and the HCAL (which consists of the TileCal, the liquid-argon Hadronic End-cap Calorimeter (HEC) calorimeter and the liquid-argon FCal) [13].

EM calorimeters detect electrons primarily through the bremsstrahlung process leading to a cascade of electrons, positrons, and photons called and EM shower [7] [28]. Similarly, photons are detected through e^+e^- pair production in the field of the nucleus of the atoms comprising the detector material, also producing an EM shower. The ATLAS ECAL is divided into a barrel region with a pseudo-rapidity coverage of $|\eta| < 1.5$ as well as two end-cap regions with $1.4 < |\eta| < 3.2$, each accommodated in their own cryostat [13]. The barrel is divided into two halves, with one half covering $z > 0$ and pseudorapidty $0 < \eta < 1.5$ and the other half covering $z < 0$ and pseudo-rapidity $0 > \eta > -1.5$ [13, 100]. On each side of the ECAL there are the two wheels of the Electromagnetic End-cap calorimeter (EMEC). They cover a pseudo-rapidity range of $1.4 < |\eta| \leq 3.2$ [13, 98]. Liquid-argon was chosen as the material for the ECAL (as well as for the FCal) because

---

[7]A single isolated electron (or muon) is one of the key characteristics of the final state of the SUSY decays discussed in Chapter 5 and Chapter 6.

of its intrinsic linear behaviour when a EM shower is triggered as well as the stability of its response over time and its radiation tolerance [100].

Moving on to hadronic calorimetry, in ATLAS this is performed by three sub-detectors called the TileCal, the liquid-argon HEC and the liquid-argon FCal. Hadronic showers are inherently less uniform than electromagnetic showers because of the wide variety of final states that hadronic interactions result in. Both charged and neutral hadrons undergo reactions with the detector material via the strong interaction [28].

Unlike the other sub-detectors in the ATLAS calorimeter, the TileCal is constructed out of steel absorber and scintillating tiles for the active material. Being placed directly outside the envelope of the ECAL, it is subdivided into one barrel region and two extended barrel regions and covers a pseudo rapidity range of $0.8 < |\eta| < 1.7$. It also works in conjunction with the HEC and FCal to provide accurate measurements of MET, which is essential in almost all searches for SUSY. In addition to the EMEC discussed above, ATLAS also has a copper-liquid argon sampling calorimeter for the detection of hadrons, the HEC with a range of $1.5 < |\eta| < 3.2$.

The final sub-detector of the ATLAS calorimeter is the FCal, also a liquid argon calorimeter, integrated into the cryostat of the end-cap covering the region $3.1 < |\eta| < 4.9$. Its function is also crucial to the effective measurement of MET as the presence of neutrinos (and other particles that are in invisible to the detector) can be inferred by observing a large energy imbalance in the direction transverse to the beam. The FCal is optimised to perform this measurement because it covers as much of the beam hole as is possible, therefore completing the almost hermetic calorimeter system [101].

3.4. Muon Spectrometer and Magnets

Accurate measurement of high momentum final state muons provides robust detection of physics signatures that are of interest to the ATLAS program [102]. The outermost component of the ATLAS detector is the MS, responsible for measuring the momentum of charged particles exiting the detector in the pseudo-rapidity range $|\eta| < 2.7$. The MS also provides triggering on these particles in the region $|\eta| < 2.4$ [13]. It operates on the principle of deflection of the tracks of the charged particles using three superconducting, toroidal magnets (one in the barrel region and one in each end-cap), interspersed with

high-precision tracking chambers and trigger chambers [102] (see Section 3.5 for a description of the ATLAS trigger system).

The ATLAS magnet system is an essential part of the experiment because it forces the trajectories of charged particles to be deflected, enabling their identification and measurement of their momentum perpendicular to the direction of the magnetic field. The field required is achieved by using four large superconducting magnet systems, which are arranged in the geometry shown in Figure 3.6. The central, 2 Tesla, solenoid which is aligned with the beam axis and provides a longitudinal magnetic field for the ID. The barrel toroid consists of a vacuum vessel running parallel to the beam producing a magnetic field of 0.5 Tesla. The final two of the four large superconducting magnets are the end-cap toroids each with a 1 Tesla magnetic field [13, 103]. The eight coils of the barrel toroid are each housed in their own cryostat. Each of the two end-cap toroids have eight flat coils assembled radially around the beam axis. All eight coils of a single end-cap are housed in a cryostat together [13, 102].
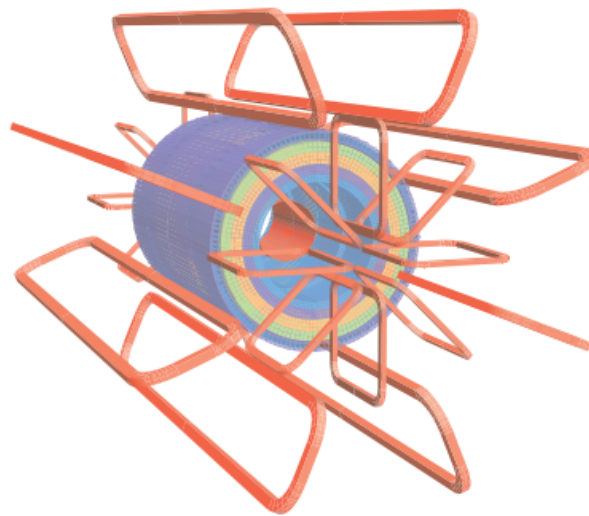
**Figure 3.6.:** Geometry of the eight barrel toroid coils along with the end-cap coils. The central solenoid is situated inside the steel TileCal which is also depicted here. Figure taken from Ref. [13].

3.5. The Trigger and Data AcQuisition System

The TDAQ is responsible for the collection and storage of the data from all the other sub-detectors of ATLAS that have been discussed. It is an essential part of the ATLAS

detector because it filters through the vast quantity of data produced by the *pp* collisions (an interaction rate of approximately 40 MHz at a luminosity of 10^{34} cm^{-2}s^{-1} [104]) down to only those events that result in final states that are of interest to the physics goals of the experiment given at the start of this chapter. Thus, data is stored for analysis at a rate (200 Hz) which is within the capabilities of the technological resources available. It has a three-level structure: L1, L2 and the EF (the L2 and the EF are collectively known as the HLT[8]), with different layers associated with separate sub-detectors. Each level of the trigger refines the decisions made at the previous level, and if necessary, applies additional selection criteria. Information from the calorimetry system and MS is used by the hardware-based L1. Meanwhile, information provided by all sub-detectors can be accessed by L2 and EF that are both software-based systems [74, 75]. Events that have been stored by the ATLAS Data AcQuisition system (DAQ) are read from the detector in categories called *streams*, depending on if the event is to be used for physics analysis, trigger level analysis, monitoring or detector calibration.

The L1 searches for high-p_T muons, photons, electrons, jets, and taus decaying to hadrons [13]. The L1 makes use of the reduced-granularity information from the calorimeters and the MS. The L1 identifies so-called Regions of Interest (RoI), regions of the detector where it has found features in an event that might be of interest in terms of η and ϕ coordinates. The RoI are used to seed the L2 with information on coordinates, energy and types of signatures in an event. The L2 consequently can reduce the event rate to below 3.5 kHz, using information from all sub-detectors. Events are then reconstructed by the EF which functions at the L2 acceptance rate to reduce the event rate to approximately 200 Hz, a rate that events can be recorded for analysis. It uses the full granularity and precision of the calorimeter as well as the MS data in addition to data from the ID to refine its trigger selections [13, 74].

When an event is accepted by the L1, the data are transferred from the detector to the RODs. These are detector-specific functional elements of the front end systems capable of achieving high levels of data concentration and multiplexing as they gather information from several front end streams. These digital signals are formatted as raw data before being transferred to the DAQ. In the initial stage of the DAQ, the readout system receives and temporarily stores the data in local buffers. The L2 then acquires the event data that is associated to the RoI. The events that are selected by the L2 are

---

[8]In Run 2 the TDAQ was upgraded to consist only of the L1 and HLT as the computer clusters for the L2 and EF were merged [105].

transferred to the event building system and then onto the EF for final selection. The CERN computing centre stores events that are selected by the EF [13].

After the physics objects have been identified by the L1 and HLT, the data are reconstructed using the ATHENA framework, in order to produce the physics objects and then stored in one of several data formats, as dictated by the ATLAS Event Data Model [106].

3.6. Detector Simulation

To understand and interpret the behaviour of the ATLAS detector, and hence to understand the data it collects, the detector and it's interactions with particles must be modelled in great detail. This is in addition to the simulation of the particles themselves that result from the *pp* collisions and their decays, which is discussed in Section 6.3.1. The GEANT4 [107] toolkit has been developed to simulate the passage of particles through matter and hence is used for this purpose. GEANT4 accomplishes this by breaking the detector volume down into a series of 3 dimensional shapes, each of which has a series of physical properties of the detector materials associated with it [108]. The drawback of making use of the extremely detailed simulation provided by GEANT4 is the computing time requirement, 90% of which is taken by modelling the passage of particles inside the calorimeter systems. To circumvent this issue, the FastCaloSim package [109] was developed to provide a parametrised simulation of particle energy response as well as the energy distribution in the calorimeter, thus reducing the time needed to simulate the calorimeter to a few seconds per event. The resulting *fast simulation* is particularly well suited to modelling processes where the highest level of precision in the simulation of the calorimeter response is not required, such as the production of the SUSY MC samples used in Chapter 6.

3.7. Physics Object Definitions

An overview of each of the ATLAS sub-detectors has been given. In this section each of the physics objects, as well as MET, that are used in the analysis that is presented in this thesis, shall be introduced.

3.7.1. Electrons

Electrons, like photons, deposit a large proportion of their energy in the ECAL and consequently no signal is anticipated for these particles in the HCAL or MS. The presence of an electron is identified by matching the energy cluster in the ECAL to a track measured in the ID. Electrons are required to satisfy $p_T > 4.5$ GeV and a pseudo-rapidity of $|\eta| < 2.47$ as well as the loose electron identification requirement defined in [110]. Electron candidates that satisfy such conditions are referred to as baseline electrons and are used to remove overlap between jet and electron candidates, see Section 3.7.6. Photons, on the other hand, do not leave tracks in the ID but the differentiation of electrons and photons is complicated due to bremsstrahlung of electrons and conversions of photons into electron-positron pairs. If no ID track can be matched to a cluster in the MC, the presence of an unconverted photon is inferred. Conversely, if a vertex in the ID is found that is consistent with a conversion, and this vertex is matched to a track, a converted photon is assumed.

If an electron candidate is to be eligible for inclusion in analysis selections, it must satisfy additional criteria. As decays in the targeted region of parameter space examined in this thesis are expected to have very soft (low-p_T) electrons, the signal electron p_T requirement is retained at $p_T > 4.5$ GeV, as well as the tight requirements for identification and tight requirements for isolation (see [110]). Electrons are defined by d_0 significance < 5 where this quantity is defined as $d_0/\sigma(d_0)$, where $\sigma(d_0)$ is the uncertainty of the transverse impact parameter d_0 (the shortest distance between the track and the beamline in the transverse plane) [111]. Electrons also must satisfy $z_0 \sin \theta < 0.5$ mm, where z_0 is the longitudinal impact parameter defined as the value of z of the point on the track that determines d_0 [112].

3.7.2. Muons

As explained in Section 3.4, muons are the most likely particles to reach the outer layer of ATLAS where the MS is situated. ATLAS reconstructs muon candidates by combining information from the MS, ID and the calorimeters. Information from the MS and ID is combined to reconstruct muons categorised into four different "types": *combined* muons, *segment-tagged* muons, *Calo-tagged* muons and *extrapolated* muons, details of which can be found in Ref. [113].

In this analysis, muon candidates are required to satisfy $p_\mathrm{T} > 4$ GeV and $|\eta| < 2.7$ in addition to $z_0 \sin\theta < 0.5$ mm and the medium muon identification requirements. Muon candidates that fulfil the above criteria are referred to as baseline muons [113]. The requirement for signal muons is kept at $p_\mathrm{T} > 4$ GeV as well as the tight isolation requirements, $z_0 \sin\theta < 0.5$ mm and d_0 significance < 3 [114].

3.7.3. Jets

When considering the exchange of gluons between two quarks at relatively large distances, the energy density in the gluons field between the quarks is constant [28]. Quarks produced in high energy collisions (such as those created within the LHC) will result in collimated sprays of hadrons (through the fragmentation of quarks and gluons) called jets [115]. This happens via a process called hadronisation: as the distance between the quarks increases, the energy density stored in the colour field connecting them becomes sufficient for the creation of $q\bar{q}$ pairs. It is thus energetically favourable for the colour field to break into smaller segments between the $q\bar{q}$ pairs. This process repeats itself until all the quarks and antiquarks have formed colourless hadrons. The formation of these hadrons traces out two jets, one formed in the direction of the initial quark and the other in the direction of the antiquark [9] [28].

Due to the complex structure of jets, clustering algorithms must be used to reconstruct them from measurements taken by the HCAL. In this analysis, jets are reconstructed from topological clusters using the anti-k_t algorithm [116], with $\Delta R = 0.4$. Baseline jets are required to have $p_\mathrm{T} > 20$ GeV, whereas signal jets are required to have $p_\mathrm{T} > 25$ GeV and lie in the range $|\eta| < 2.5$. If the jet has $p_\mathrm{T} < 120$ GeV and is found within $|\eta| < 2.4$, an additional Jet Vertex Tagger (JVT) cut is in place (JVT > 0.59). The JVT is a two-dimensional likelihood based on the the Jet Vertex Fraction (JVF)[10] to suppress pileup jets. The derivation of the JVT variable can be found in Ref. [117].

---

[9]Hadronisation also occurs between gluon-gluon (gg) quark-gluon (qg) as well as quark-quark (qq) pairs, which are formed at the LHC

[10]The JVF is sum of the p_T of the tracks associated with the jet that originates from the hard scatter vertex, divided by the scalar sum of all the tracks associated with that jet [117].

3.7.4. *b*-jets

Though it is not generally possible to deduce the flavour of a quark, or even whether a jet originated from a quark or a gluon, there are a few features of jets from *b* hadrons that allow them to be distinguished. When a *b*-quark is produced, leading to hadronisation, one of the resulting jets will also contain a *b*-quark. The *b* hadrons in this jet possesses a relatively long lifetime ($\approx$ 1.5 ps), which combined with its relatively large mass, results in decay products that can be produced at a large angle to the direction of the original *b*-quark. Hence, *b*-quarks can be identified by an experimental signature consisting of a Primary Vertex (PV) that originates from the collision and a SV (the *b*-jet) that is displaced by a few millimetres corresponding to the distance that the *b* hadron travelled [28]. The PV defines a reference point from which the track and vertex displacement are computed. At least one PV is required per event and the primary interaction point is selected from the PV comprised of tracks with the highest sum of the squared transverse momenta. *B* hadrons are then identified from charged particle tracks that are displaced this PV by placing requirements on $|d_0|$ and $|z_0 \sin \theta|$ [118].

The identification of *b*-jets is accomplished through the use of a multivariate algorithm called MV2c10, which is described in Ref. [119]. The input variables to MV2c10 are obtained from algorithms that are divided into three distinct classes: lifetime-based algorithms that take advantage of the relatively long lifetime of hadrons containing *b*-quarks; muon-based tagging algorithms which employ either the direct decay $b \to \mu^-$ or the cascade decay $b \to c \to \mu^+$; or the *b*-jet trigger algorithm which identifies *b*-jets at trigger level. The details of these three classes of algorithm are given in [120].

The value of MV2c10 that is used to define the *b*-jet objects is determined by the desired *b*-jet identification efficiency and the light-jet rejection rate. *b*-tagging models that are commonly used throughout the ATLAS collaboration are defined in Table 3.1 in terms of the value of MV2c10 and the efficiency that can be achieved by using that requirement. For most of the results presented in this analysis, *b*-jets are required to pass a cut of MV2c10 > 0.6459, corresponding to an average efficiency of 77%[11]. This efficiency has been calculated using simulated samples of $t\bar{t}$ events generated using MC@NLO v3.41 [122] interfaced with HERWIG v6.520[12] [123]. This translates into rejection rates for light-flavour jets, *c*-jets and τ-jets of 134.34, 6.21 and 22.04 respectively [54].

---

[11]Efficiency is a function of jet p_{T} as shown in Ref. [121]
[12]The MC@NLO and HERWIG MC generators are discussed in Section 6.3.1.

Mv2c10 value	Efficiency
0.934906	60%
0.8244273	70%
0.6459	77%
0.1758475	85%

Table 3.1.: Commonly used *b*-tagging working points defined in terms of their MV2c10 value and associated *b*-tagging efficiency.

Soft *b*-jets

The ATLAS calorimeter is unable to precisely reconstruct jets with a transverse momenta of less than 20 GeV. Calorimeter jets are one of the key objects that are used as input to the *b*-tagging algorithms which are mentioned above [120]. Therefore the applicability of standard *b*-tagging techniques is currently limited to calorimeter jets that have $p_\text{T} >$ 20 GeV [124]. This is a significant limitation in analyses where low-p_T, soft *b*-jets are a feature of the final state, as is the case with the analysis that is the subject of this thesis. By the time this analysis reached completion, the capability of ATLAS to reconstruct *b*-jets had been had been extended down to 15 GeV, but even after this improvement, the limitations on a search for compressed stop decays are not lifted. However techniques for "soft-*b*-tagging" can be used to extend the scope of *b*-jet identification.

It has been shown in Ref. [124] that vertexing algorithms can be employed to perform soft-*b*-tagging. The soft-*b*-tagging algorithm used is taken from an existing vertexing algorithm which was developed in a search for long lived particles with displaced vertices, details of which are given in Ref. [125]. This algorithm is effective for searching for *stop* decays with a small mass splitting between the *stop* and the $\tilde{\chi}_1^0$ because in this decay, the system is boosted by an Initial State Radiation (ISR) jet, which gives a similar signature to a long lived particle.

Tracks are constructed by the ID and are the input to the vertexing algorithm. Tracks in the ID are created from any charged particle, not just *b*-jets. Therefore, a way to separate the SVs found by this algorithm that originate from *b*-jets from those SVs originating from other charged particles is required.

The first step of the algorithm is to make requirements on tracks, in addition to those employed in standard track reconstruction. Considering the transverse and longitudinal impact parameters of the SV with respect to the primary vertex, d_0 and z_0 respectively,

the following selections are applied: $z_0/\sigma(z_0) > 0.5$ and $d_0/\sigma(d_0) > 1.7$. The algorithm proceeds by considering all possible track pairs which have to satisfy $\cos(\theta) > 0.95$, where θ is the angle between the three-vector obtained from the vectorial sum of the track momenta and the vector pointing from the PV to the SV. The pairs of tracks that pass this condition are then used to form multi-track vertices, by employing an incompatibility graph, details of which are found in [125]. Nearby vertices are merged and lower quality tracks that were not initially pre-selected are attached to compatible vertices to improve certain kinematic properties of the vertices and a final list of SVs is produced. Finally, a collection of observable that are given in [124] are used to reject vertices that are unlikely to be from b hadron decays, thus acting as overlap removal for SVs (see Section 3.7.6 for a definition of overlap removal). Details of the calibration and validation procedures used to apply this algorithm to search for compressed SUSY decays can also be found in Ref. [124] . The analysis presented in Ref. [124] introduces a number of algorithms to identify low-p_T b-jets and in order to quantify their performance, the product of the algorithm acceptance and tagging efficiency is given. This quantity is dependant on the p_T of the b hadron but on average both the acceptance multiplied by the tagging efficiency and the c-hadron fake rejection rate was found to be 7.2%.

3.7.5. MET

In a collider experiment, conservation of momentum implies that the transverse momentum of all the collision products should sum to zero. Accurate measurements of the momentum of the invisible decay products in the longitudinal direction cannot be made in a hadron collider experiment. Any imbalance of momentum in the transverse plane is referred to as missing transverse momentum [126]. A popular convention in the particle physics community is to refer to the missing transverse momentum as Missing Transverse Energy (MET), which is often denoted $E_T^{\mathrm{miss}} = |\boldsymbol{p}_T^{\mathrm{miss}}|$. When considering the event as a whole the MET can be expressed as:

$$\boldsymbol{p}_T^{\mathrm{miss}} = \sum_i \boldsymbol{p}_T^{\mathrm{invisible}}(i) = -\sum_i \boldsymbol{p}_T(i) \, , \qquad (3.1)$$

where $\boldsymbol{p}_T(i)$ is the transverse momentum of the ith visible particle. This makes reference to the fact that MET is an energy-like quantity that can be written in terms of the transverse momentum of a particle. The undetected particles are known as the invisible decay products, hence their transverse momentum can be denoted as $p_T^{\mathrm{invisible}}$. Within the

SM, MET arises from neutrinos as they do not interact with the detector material and hence are not registered. Many SUSY models conjecture that the LSP at the end of the SUSY decay chain would be the neutralino, mass eigenstates formed from combinations higgsinos and gauginos. The LSP would not be detected and hence also contributes to the MET.

The MET is reconstructed from two contributions: the hard term and the soft term. The hard term corresponds to hard objects comprising fully reconstructed and calibrated physics objects: jets, electrons, muons, taus and photons. The soft term is reconstructed from measurements from the ID or calorimeters that are not associated with any of the hard objects [126]. When SM particles escape the acceptance of the detector and hence are poorly reconstructed, or are not reconstructed at all, their p_T does not contribute to the overall p_T of the event as well. This is known as *fake* MET which can contribute a part of the soft MET term. Hence a lot of information about the event and its reconstruction is stored in its MET. In practice, MET is calculated as the negative vectorial sum of the physics objects discussed below (the hard objects) and the soft term [127]:

$$
\begin{aligned}
\boldsymbol{p}_T^{\text{miss}} \;=\; & -\left(\sum_{i \in \text{muons}} \boldsymbol{p}_T(i) + \sum_{i \in \text{electrons}} \boldsymbol{p}_T(i) + \sum_{i \in \text{photons}} \boldsymbol{p}_T(i) \right. \\
& \left. + \sum_{i \in \text{hadronic } \tau} \boldsymbol{p}_T(i) + \sum_{i \in \text{jets}} \boldsymbol{p}_T(i) + \sum_{i \in \text{Soft Term}} \boldsymbol{p}_T(i) \right) .
\end{aligned}
\tag{3.2}
$$

For this analysis, only the soft term from the ID, the so called track-soft-term, is considered. The soft term is the only place in the analysis where photons and hadronically decaying taus are considered, unless the latter is reconsidered through the jets that its decay produces. The MET is calculated using the default ATLAS tool, the METUtilities tool.

3.7.6. Overlap Removal

When a candidate object meets the selection criteria of two or more of the physics objects defined above, a procedure is required to avoid double-counting the candidate as more than one type of object. This procedure must also be capable of retaining two objects that are distinct but recorded physically close to each other. This procedure is known as overlap removal. There are variations on the specifics of the overlap procedure that can

be applied, but, for the pairs of objects considered in this analysis, the procedure is as follows.

Electron/Muon A subset of the muons meeting the loose selection criteria defined in Ref. [113] with $\eta \approx 0$, which are reconstructed from Calo-tagged muons, can also be reconstructed as electrons. Additionally, if the electron and muon candidates satisfy $\Delta R < 0.01$, the muon is removed if it is Calo-tagged, otherwise the electron is removed.

Electron/Jet If a baseline jet and a baseline electron satisfy $\Delta R < 0.2$, assuming the jet is not b-tagged, the object is interpreted as an electron and the overlapping jet candidate is removed. However, if the separation between the baseline jet and the baseline electron satisfies $0.2 < \Delta R < 0.4$, the jet is retained and the electron discarded to minimize contamination from jets misidentified as electrons.

Muon/Jet "Ghost-matching" is defined in [128]. If a baseline muon is ghost-matched to a baseline jet satisfying $\Delta R < 0.4$, assuming the jet is not b-tagged, the object is interpreted as a muon if the jet has less than three tracks with $p_T > 500$ MeV. The equivalent criteria as identified above for separations satisfying $0.2 < \Delta R < 0.4$ holds for the overlap procedure applied between muons and jets.

SV/Lepton and light flavour jets as detailed in [124], a set of variables was devised to reject SVs that were unlikely to have originated from b hadron decays. These variables included: the displacement in the transverse plane of the SV with respect to the PV; the angle between the vertex pointing from the PV to the SV and the vectorial sum of the track momenta as well as the mass of the SV calculated from the associated tracks.

3.8. Summary and Outlook

In this chapter a brief description of how the components of the ATLAS detector operate to detect the fundamental particles of the SM introduced in Chapter 2. However, as was also explained in Chapter 2, the SM cannot call itself a complete theory of nature. One of the most promising theories of BSM physics is offered by SUSY, a search for which is presented in Chapter 5 and Chapter 6.

In order to continue to search for SUSY in the as-yet unexplored regions of parameter space, more data provided by collisions taking place with higher luminosity beams are needed, as well as collisions with higher centre of mass energies. With the advent of Run 2, the luminosity of pp collisions at the LHC was increased such that some of

the algorithms that ATLAS relied on to measure the luminosity became increasingly ineffectual. An alternative approach to luminosity measurement, which uses the ATLAS SCT described in Section 3.2, that is intended to supplement the existing luminosity determination algorithms, is presented in Chapter 4. Unless otherwise stated, all plots from this point onwards were produced by the author.

Chapter 4.

Luminosity Determination

" Tapestries are made by many artisans working together. The contributions of separate workers cannot be discerned in the completed work, and the loose and false threads have been covered over. So it is in our picture of particle physics. "
— Sheldon L. Glashow

The word luminosity is derived from the Latin word "luminosus" which means "full of light" [129] The concept of luminosity is more commonly associated with astronomy, where it means the "total amount of energy emitted by a star per second in all wavelengths" [130]. It was first introduced into the field of particle physics in the context of e^+e^- collisions at the the Anello Di Accumulazione collider (AdA) collider in the late 1950s to relate the electron-positron annihilation cross-section to the number of annihilations per unit time [129,131]. It is still being used to date to describe the proportionality factor between the event rate and the cross-section in a particle collider [79].

Two of the main distinguishing quantities for any particle accelerator are the centre of mass energy of the colliding particles and the beam luminosity that it can attain. The probability that collisions produced by the accelerator lead to the discovery of new physics is to some extent a function of both these quantities. An accelerator that can attain a higher centre of mass energy is able to produce heavier particles and probe smaller distance scales. Moreover, the higher the luminosities that are attained, the greater the potential for delivering a statistically significant sample of a given class of events [79].

4.1. Background and Motivation

Precise measurements of the luminosity of the *pp* beam at the LHC underpin the accuracy of all measurements made by the ATLAS experiment. In fact, the uncertainty on the delivered luminosity is one of the main systematic uncertainties in all cross-section measurements [129]. A key strategy ATLAS employs to control the systematic uncertainties in the luminosity measurement is to compare the readings from several luminometers, most of which use more than one algorithm to determine the luminosity. These luminometers and their algorithms differ in terms of their acceptance, response to pileup, as well as sensitivity to instrumental effects and beam-induced backgrounds. This strategy is crucial, as the calibration of the absolute luminosity is carried out at most three times a year and so must remain valid in the intervening periods under varying machine conditions and also be corrected for long-term drifts [84].

As explained in Section 3.1, LUCID and BCM are ATLAS' two main luminometers, which use event-counting algorithms [84]. Event-counting algorithms provide a luminosity measurement by recording the number of BCs containing inelastic collisions [87]. μ_{vis} is the average number of observed interactions per BC. As μ_{vis} increases to be much greater than 1, more BCs in a given time interval contain one or more observed interactions. As a consequence, event-counting algorithms reach a saturation point and lose their sensitivity. For LUCID, this point is reached when $\mu_{\mathrm{vis}} \sim 20 - 30$ over a one-minute interval. LUCID is also limited by saturation, lifetime and radiation hardness of its PMTs [132]. However, during the operation of the LHC in 2012, shortly before the study presented in this chapter was first formulated, μ_{vis} peaked at ~ 40, rendering LUCID's event-counting algorithms beyond saturation point [84]. To address these problems, a new LUCID detector was built for the start of Run 2 [133]. As μ_{vis} increases, the probability of an BC containing more than two inelastic collisions will no longer be negligible, as is explained in Section 4.2.1. Event-counting algorithms will increase in complexity when bunch crossings contain more than one inelastic collision. This will become a more common problem when higher luminosities are reached in Run 2 [87] – in 2017 and 2018, the number of inelastic interactions per bunch crossing peaked at 60 [134].

The measurements obtained from the event-counting algorithm are then compared to results from track counting algorithms which are implemented in the SCT. In Section 3.2 it was explained that barrel and end-cap modules consist of microstrip sensors known as strips. If a group of adjacent strips are activated, an SCT cluster is recorded. Clusters are then combined, assuming additional requirements on p_{T}, $|\eta|$ and the number of

hits produced, to construct tracks [135]. Tracking algorithms using the SCT to make a luminosity measurement operate on the principle that the luminosity is proportional to the number of reconstructed charged-particle tracks. Therefore, when using the SCT's tracking algorithms, μ_{vis} is equivalent to the number of tracks per BC, typically averaged over one Luminosity Block (LB)[1]. The default track selection used makes no attempt to distinguish tracks originating from PV from those produced by secondary interactions, as the yields of both are expected to be proportional to luminosity [84].

Measurements obtained from the methods discussed above are supplemented by those obtained from hit-counting algorithms, which are currently employed by LUCID in addition to event-counting algorithms. In the context of detector physics, a hit is defined as a pulse in a readout channel with an amplitude above a preset threshold [132]. Hit-counting algorithms utilise the number of detector readout channels with signals above a predefined threshold, rather than the number of BCs containing at least one inelastic interaction.

As shall be shown in Section 4.2.1, the value of μ_{vis} at which hit-counting algorithms reach saturation[2] and break down is higher than that of event-counting algorithms. The saturation of event-counting algorithms, which prevents effective luminosity measurement, could be circumvented by making increased use of hit-counting algorithms. Pixel cluster counting algorithms, an example of hit-counting algorithms, are already the primary technique used for luminosity determination by CMS [136, 137].

In Ref. [24], preliminary results are presented on the feasibility of using cluster counting (an implementation of hit-counting) with the PIXEL Detector, to provide a robust luminosity measurement. There are three distinct contributions to the background of a luminosity signal: afterglow, instrumental noise and single-beam backgrounds[3]. During a typical run intended for physics analysis, the second two contributions become negligible compared to the luminosity, making the afterglow the only significant background [84]. Therefore, to make a reliable luminosity measurement, the effects of afterglow must be understood and eliminated. Afterglow is thought to result from photons from nuclear de-excitation of the detector material that were induced by hadronic cascades initiated by the *pp* collisions [84]. The starting point of [24] was the observation that, in the PIXEL Detector, the signatures of the physics objects (that can be used for a luminosity

---

[1]The LB is the basic unit of time for storing luminosity information for use in physics analysis. The boundaries of each LB are defined by the ATLAS Central Trigger Processor and are typically approximately one minute apart.

[2]Meaning that μ_{vis} will no longer be linearly related to the raw event count.

[3]The background caused by unpaired protons that were not involved in a collision [138].

measurement) are characterised by streaks, while the signatures of afterglow resemble localised spots. From these observations, an algorithm to select strip-like clusters and reject spot-like clusters was developed. The algorithm was based on the requirements that clusters must include more than two hits in the PIXEL Detector in the z-direction and the total number of hits per cluster must be within three hits of the number of hits along that cluster in the z-direction. Analysis of the origin of the objects responsible for these strip-like clusters confirmed that they originate from the IP and hence are physics objects. This analysis also showed that the maximum impact on the efficiency of recording clusters from dead modules within the PIXEL Detector was less than 0.75%. It was shown that, by application of the algorithm developed by this preliminary study, there is a strong correlation between the number of strip-like clusters recorded by the PIXEL Detector and the luminosity measurement made by TileCal. Therefore, this preliminary result, though at the time subject to further investigations to fully understand and calibrate this relationship, was taken to be indicative of the feasibility of using the PIXEL Detector as a luminometer.

In the light of these findings it is proposed that the SCT could similarly be used to provide a luminosity measurement, complementary to those of ATLAS' other luminometers, described above. To use the SCT to make a luminosity measurement, the relationship between the number of strips - or alternatively clusters - recorded by the SCT and the number of inelastic collisions per BC has to be studied. The effectiveness of using strips, compared to clusters, is evaluated. It shall be seen that, as in the context of the PIXEL Detector, hits on two or more adjacent strips in the SCT are merged to form a cluster once "noisy" or faulty strips have been removed from consideration. Noisy strips are identified using a specific data stream triggered on BCs such that no collision hits are present and are defined as having an average occupation of more than 1.5% [68]. Hitmaps of each region of the SCT are scrutinised to analyse the effects of "noisy modules". Additionally, the ratio between the number of SCT tracks and the number of clusters was considered, with the aim of studying to what extent the detection of clusters is affected by background noise in comparison to the detection of tracks. The effectiveness of this technique depends on the more stringent requirements that are imposed on track candidates relative to clusters, which were discussed previously. Clusters can, on the one hand, be part of the tracks from the pp collisions, that is, contributing to luminosity, whereas on the other hand they can originate from other sources such as afterglow, or electronic noise.

As the research presented here pertains to the development of a new technique for luminosity measurement, intended to complement those currently existing, a review of luminosity determination in ATLAS shall follow in Section 4.2. This is preceded by a brief description of the algorithms that ATLAS currently uses to make luminosity measurements, before presenting the results of this feasibility study in Section 4.3. The findings of this study are summarised in Section 4.4 whilst the future implications are outlined in Section 4.5.

4.2. Measurements of Luminosity

To place in context the development of the SCT as a luminometer, the standard method of determining the luminosity of the proton beams within ATLAS is reviewed. The instantaneous luminosity $\mathcal{L}$ of a *pp* collider can be written as

$$\mathcal{L} = \frac{R_{\text{inel}}}{\sigma_{\text{inel}}} \quad , \tag{4.1}$$

where R_{inel} represents the rate of inelastic collisions and σ_{inel} gives the *pp* inelastic cross-section. $\mathcal{L}$ reflects the instantaneous performance of the collider and its value may vary on time scales from tens of nanoseconds to minutes [129]. For a collider with n_b bunches of protons crossing at the IP and a revolution frequency of f_r, the luminosity can also be expressed as

$$\mathcal{L} = \frac{\mu n_b f_r}{\sigma_{\text{inel}}} \quad , \tag{4.2}$$

where μ is the average number of inelastic interactions per BC [80]. The luminosity which is actually delivered to ATLAS is measured using the observed interaction rate per BC μ_{vis} by writing $\mathcal{L}$ as

$$\mathcal{L} = \frac{\mu_{\text{vis}} n_b f_{\tau}}{\sigma_{\text{vis}}} \quad , \tag{4.3}$$

where $\sigma_{\text{vis}} = \varepsilon \sigma_{\text{inel}}$ gives the product of the total inelastic cross-section with the efficiency ε depending on the detector and algorithm, and likewise $\mu_{\text{vis}} = \varepsilon \mu_{\text{inel}}$ [87].

The calibration of σ_{vis} is achieved by using dedicated beam separated scans called van der Meer (vdM) scans, a technique introduced in [139]. The vdM scans, or μ-scans, can determine the size and shape of the interaction region between the two intersecting

beams of protons by recording the relative interaction rate as a function of transverse beam separation. The first vdM scans that were performed at the LHC are documented in Ref. [140].

Introducing the label $I = \{x, y\}$ together with $dI = \{dx, dy\}$, and assigning $R_I(\delta_I)$ as the rate at which the beams are moved across each other, where δ_I is the difference in the I-direction, the profile Σ_I in the I-direction is defined as:

$$\Sigma_I = \frac{1}{\sqrt{2\pi}} \frac{\int R_I(\delta_I) d\delta_I}{R_I(0)} \quad . \tag{4.4}$$

To perform a scan, the two beams must be first separated by up to $\pm 6\Sigma_I$ in the I-direction. This transverse displacement is generated using an orbit bump, a technique used to facilitate beam injection and extraction [141]. The beams are then moved in a stepwise fashion across each other in the x-direction and data is recorded at each step for 20 to 30 seconds. This method is then repeated in the other transverse plane [87, 140].

Assuming, for simplicity, that the beams collide with zero crossing angle, the bunch luminosity $\mathcal{L}_b$ is given by [80]:

$$\mathcal{L}_b = f_r n_1 n_2 \int \rho_1(x, y) \rho_2(x, y) dx \, dy \quad . \tag{4.5}$$

Presuming that the particle densities $\rho_{1(2)}(x, y)$ can be factorized into independent horizontal and vertical components, so $\rho(x, y) = \hat{\rho}_x(x)\hat{\rho}_y(y)$, Equation 4.5 can be rewritten as [87]

$$\mathcal{L}_b = f_r n_1 n_2 \Omega_x(\hat{\rho}_{x1}, \hat{\rho}_{x2}) \Omega_y(\hat{\rho}_{y1}, \hat{\rho}_{y2}) \quad , \tag{4.6}$$

where

$$\Omega_y(\hat{\rho}_{y1}, \hat{\rho}_{y2}) = \int \hat{\rho}_{y1}(y) \hat{\rho}_{y2}(y) \, dy \tag{4.7}$$

is the beam overlap integral in the y-direction (and similarly for the x-direction). Using the same notation as previously for I, dI and $R_I(\delta_I)$, the overlap integral Ω_I is given by

$$\Omega_I(\hat{\rho}_{I_1}, \hat{\rho}_{I_2}) = \frac{R_I(0)}{\int R_I(\delta_I) d\delta_I} \quad , \tag{4.8}$$

with $R_I(0)$ being the monitor rate when the beam has zero displacement in the I-direction [129, 139]. Thus, $R_I(\delta_I)$ and μ_{vis} are measured during a vdM scan when the two beams are separated by the vertical distance δ_I [129].

The luminosity can be calculated by only considering measured accelerator parameters and thus can be re-written in the form [87]

$$\mathcal{L} = \frac{n_b f_r n_1 n_2}{2\pi\Sigma_x\Sigma_y} \quad , \tag{4.9}$$

where $\Sigma_{x,y}$ are as in Equation 4.4. This is the general formula used when extracting the luminosity from the machine parameters, i.e. $n_b, n_1, n_2, f_r, \Sigma_I$, after a vdM scan has been performed.

4.2.1. Luminosity Algorithms

This section discusses the luminosity determination algorithm that is proposed for use by the SCT in the context of the luminosity algorithms used by the other ATLAS luminometers. The most common method used by ATLAS to determine luminosity is the event-counting algorithm. The defining feature of event-counting algorithms is that they count the number of BCs containing inelastic collisions in a given time interval N, where at least one of the pp interactions satisfies the event selection criteria. There are two distinct types of algorithm, EventOR (inclusive counting) and EventAND (coincidence counting).

In an EventOR algorithm a BC is considered to contain an event if at least one hit is recorded on either the A or C side. The probability of observing k events with the mean μ_{vis} is given by the Poisson distribution. Therefore, the probability of observing at least one event in a BC is:

$$P_{\mathrm{EventOR}}(\mu_{\mathrm{vis}}^{\mathrm{OR}}) = \frac{N_{\mathrm{OR}}}{N_{\mathrm{BC}}} = 1 - \exp(-\mu_{\mathrm{vis}}^{\mathrm{OR}}) \quad . \tag{4.10}$$

For an EventAND algorithm, the relationship between μ_{vis} and N is more complex. In this case, a BC is counted only if there is at least one hit on both the A and C sides. This condition can either be satisfied by a single pp interaction or by individual hits on either side of the detector from different pp interactions in the same BC. Therefore, the probability for having at least one hit is no longer dependent on a single efficiency

and must be written in terms of: the efficiency of observing at least one hit on the A side, ε^{A}; the efficiency of observing at least one hit on the C side, ε^{C}; and the efficiency of observing at least one hit on both sides simultaneously, $\varepsilon^{\mathrm{AND}}$. These efficiencies are related to $\varepsilon^{\mathrm{OR}}$ of the EventOR algorithm through

$$\varepsilon^{\mathrm{OR}} = \varepsilon^{\mathrm{A}} + \varepsilon^{\mathrm{C}} - \varepsilon^{\mathrm{AND}} \ . \tag{4.11}$$

Assuming that $\varepsilon^{\mathrm{A}} \approx \varepsilon^{\mathrm{C}}$ and writing $\varepsilon^{\mathrm{AND}}$ and $\varepsilon^{\mathrm{OR}}$ in terms of their respective cross-sections, i.e. $\varepsilon^{\mathrm{AND}} \equiv \sigma_{\mathrm{vis}}^{\mathrm{AND}}/\sigma_{\mathrm{inel}}$ $\varepsilon^{\mathrm{OR}} \equiv \sigma_{\mathrm{vis}}^{\mathrm{OR}}/\sigma_{\mathrm{inel}}$, the probability of observing at least one event is [129]

$$P_{\mathrm{EventAND}}(\mu_{\mathrm{vis}}^{\mathrm{AND}}) = \frac{N_{\mathrm{AND}}}{N_{BC}} \tag{4.12}$$
$$= 1 - 2\exp\left(-\frac{\mu_{\mathrm{vis}}^{\mathrm{AND}}}{\sigma_{\mathrm{vis}}^{\mathrm{AND}}}\right)\left[\exp\left(\frac{\sigma_{\mathrm{vis}}^{\mathrm{AND}} + \sigma_{\mathrm{vis}}^{\mathrm{OR}}}{2}\right) + \exp\left(\sigma_{\mathrm{vis}}^{\mathrm{OR}}\right)\right] \ .$$

It can be seen that Equation 4.12 cannot be inverted analytically to obtain $\mu_{\mathrm{vis}}^{\mathrm{AND}}$ as a function of N_{AND}/N_{BC}. Instead the number of inelastic collisions per BC is determined using the values of $\sigma_{\mathrm{vis}}^{\mathrm{AND}}$ and $\sigma_{\mathrm{vis}}^{\mathrm{OR}}$ which are extracted from vdM scans [80].

As μ_{vis} increases there is no longer a negligible probability that each BC will only contain one *pp* interaction so μ_{vis} will not be linearly related to the raw event count. When there are multiple *pp* collisions in the same BC, this is known as pileup. In this case μ_{vis} must be calculated by modelling the probability that a BC will contain at least one *pp* interaction using a Poisson distribution, as well as considering instrumental or other pileup related effects. Eventually, event-counting no longer provides any useable information about the interaction rate when all BCs contain at least one inelastic collision, which occurs when $N/N_{BC} = 1$ [87]. Here N is the number of BCs, in a given time interval, in which one *pp* interaction satisfies the event selection criteria of either the EventOR or EventAND algorithms.

By contrast, in the work presented here it is intended that the SCT should be used with a *hit* counting algorithm to measure the luminosity. In the hit-counting algorithm, rather than considering how many BCs pass the criteria of having at least one inelastic collision, the number of readout channels in the detector with signals above a predefined threshold is considered [80, 87]. In this algorithm it is assumed that the probability of having a hit on a given readout channel per *pp* interaction follows a binomial distribution, but the number of interactions per BC follows a Poisson distribution.

Therefore, if N_{hit} is the total number of hits in one detector channel during a time interval, and N_{CH} is the number of detector channels, the average probability of having a hit in one of the detector channels per BC is

$$P_{\mathrm{hit}}(\mu_{\mathrm{vis}}^{\mathrm{hit}}) = \frac{N_{\mathrm{hit}}}{N_{BC}N_{CH}} = 1 - \exp(-\mu_{\mathrm{vis}}^{\mathrm{hit}}) \quad . \tag{4.13}$$

Hit-counting algorithms are often more sensitive than event-counting to instrumental uncertainties. In particular, the binomial assumption only holds if the probability of observing a hit in a single channel is independent of the number of hits observed in the other channels. Nevertheless, preliminary results show that algorithms like the pixel-cluster counting method used in Ref. [24] can be applied successfully in the hostile experimental environment of the LHC, where the high values of μ make it impractical to use event-counting in large-acceptance luminometers [129].

Hit-counting can be taken to its limit by using particle counting algorithms, where the number of individual particles entering a given detector is counted directly, which is only achievable in detectors with a very fine segmentation [80]. Even though the TileCal and FCal (which are introduced in the context of luminosity measurement in Section 3.1) use the proportionality between the current drawn by the PMTs and the total number of particles interacting with the PMTs, their measurements of the luminosity cannot be said to be made using particle counting algorithms, as individual particles are not being counted [87].

4.3. Results and Discussion

4.3.1. Samples

The data presented in Section 4.3.2 was collected in Run 1 during Run 206962, representing a typical run for collecting data to be used in physics analysis. The structure of the proton beams at the LHC is discussed in Section 3.1. The time difference between the trains for this run was 50 ns and these trains are considered separately when the background effects are investigated in Section 4.3.2. In Section 4.3.3, Run 2 data from the μ-scan conducted during Run 280520 is presented. Data from Run 266904, which was configured specifically to examine the afterglow, was also used to determine whether a requirement in the number of strips per SCT cluster was necessary to reduce the effects of noise, as

is explained in Section 4.3.3 Run 266904 had two BCs that contained collisions, and this analysis focused on the one occurring at a Bunch-Crossing Identification (BCID)[4] of 1786.

4.3.2. Run 1 Results

Hitmaps

Hitmaps have been made to show the locations that the SCT recorded hits in the $\eta - \phi$ plane for both sides of the four barrel layers mentioned in Section 3.2, which are shown in Figure 4.1. The hitmaps in Figure 4.2 were produced using a dataset where one of the RODs had been deliberately excluded, for reasons that are explained below. The binning in the hitmaps for the barrel shown in Figs. 4.1 and 4.2 is chosen such that each bin represents one module.

The inner layers of the barrel region contain fewer modules than the outer layers. However they cover a larger pseudo-rapidity range as they extend the same length in the beam direction but at a smaller radius. The coordinate scheme used on the η and ϕ axes in Figure 4.1 and Figure 4.2 corresponds to the numbering of the modules in the $\eta - \phi$ plane in the SCT, denoted by $(N_\eta^{\mathrm{mod}}, N_\phi^{\mathrm{mod}})$.

Studying hitmaps can alert one to the presence of problems with modules. For example on side 0 of layer 3, in the bin representing the module with coordinates $N_\eta^{\mathrm{mod}} = -2$ and $N_\phi^{\mathrm{mod}} = 12$ it can be seen there is a point that has a much higher density of clusters than the rest of the side (see Figure 4.1g). This indicates a module is recording a significant amount of noise in addition to the signals generated by a charged particle. Corrections to account for excluding these modules will need to be made before cluster counting in the SCT can be considered a reliable method of measuring luminosity.

As well as reading hits from the SCT modules without being triggered by a cluster, modules can also become unresponsive. If a module becomes unresponsive, it will block all the information that was sent from the trigger that it is associated with, resulting in a blank space on the hitmap; for example on side 0 of layer 0 for $N_\eta^{\mathrm{mod}} \in \{5, 6\}$ and $N_\phi^{\mathrm{mod}} = 14$ (see Figure 4.1). This means that all the data from the strips that comprise the unresponsive module are lost. As with "noisy modules", it is also important to assess the impact that unresponsive modules will have on the proposed method of measuring

---

[4]The integer given to each successive BC

(a) Hitmap for barrel, side 0, layer 0

(b) Hitmap for barrel, side 1, layer 0

(c) Hitmap for barrel, side 0, layer 1

(d) Hitmap for barrel, side 1, layer 1

(e) Hitmap for barrel, side 0, layer 2

(f) Hitmap for barrel, side 1, layer 2

(g) Hitmap for barrel, side 0, layer 3

(h) Hitmap for barrel, side 1, layer 3
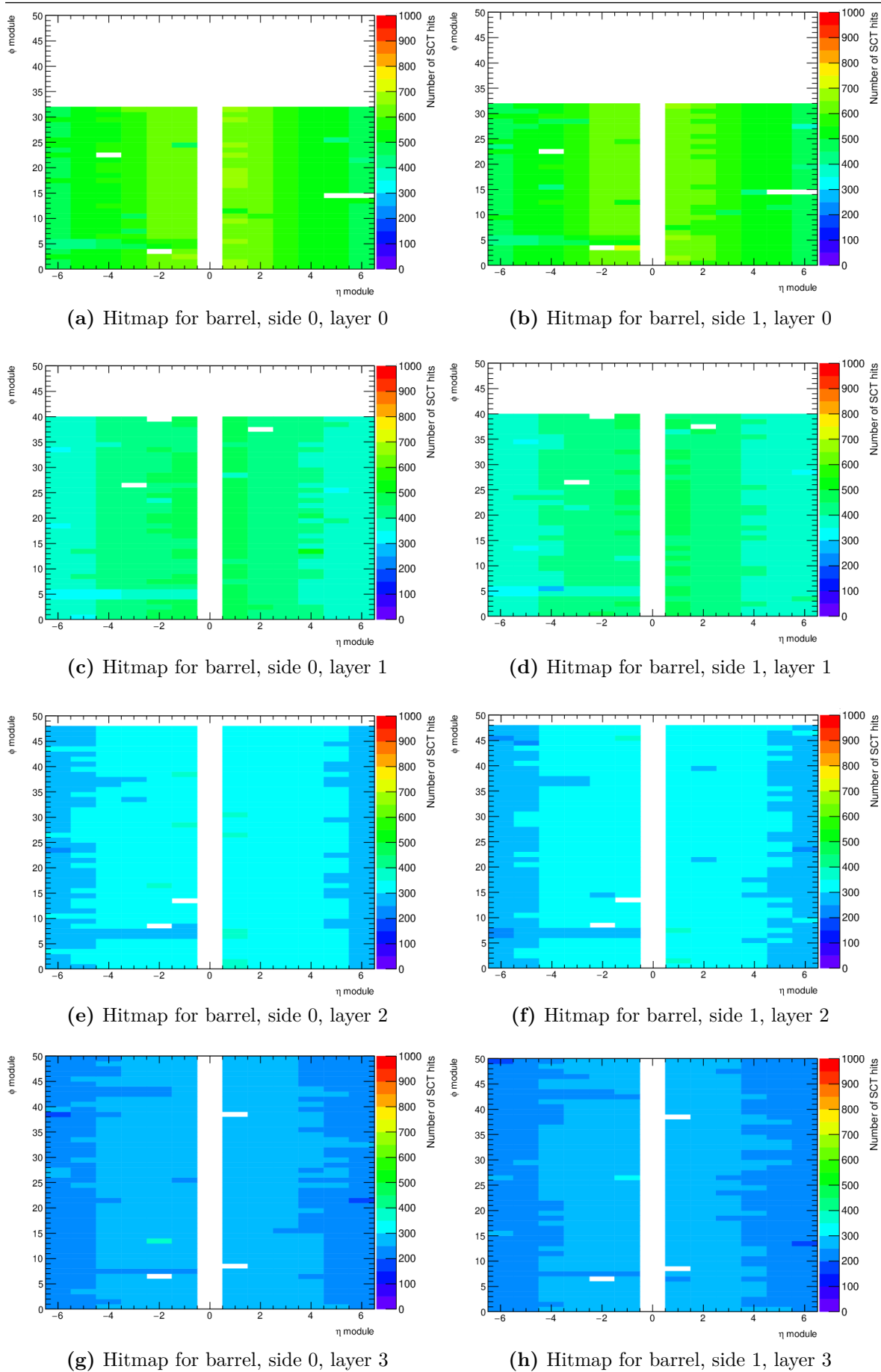
Figure 4.1.: Hitmaps in the $\eta - \phi$ plane for side 0 and side 1 of the four layers of the barrel region of the SCT for Run 206962 calibration pixel beam stream.

(a) Hitmap for barrel, side 0, layer 0

(b) Hitmap for barrel, side 1, layer 0

(c) Hitmap for barrel, side 0, layer 1

(d) Hitmap for barrel, side 1, layer 1

(e) Hitmap for barrel, side 0, layer 2

(f) Hitmap for barrel, side 1, layer 2

(g) Hitmap for barrel, side 0, layer 3

(h) Hitmap for barrel, side 1, layer 3
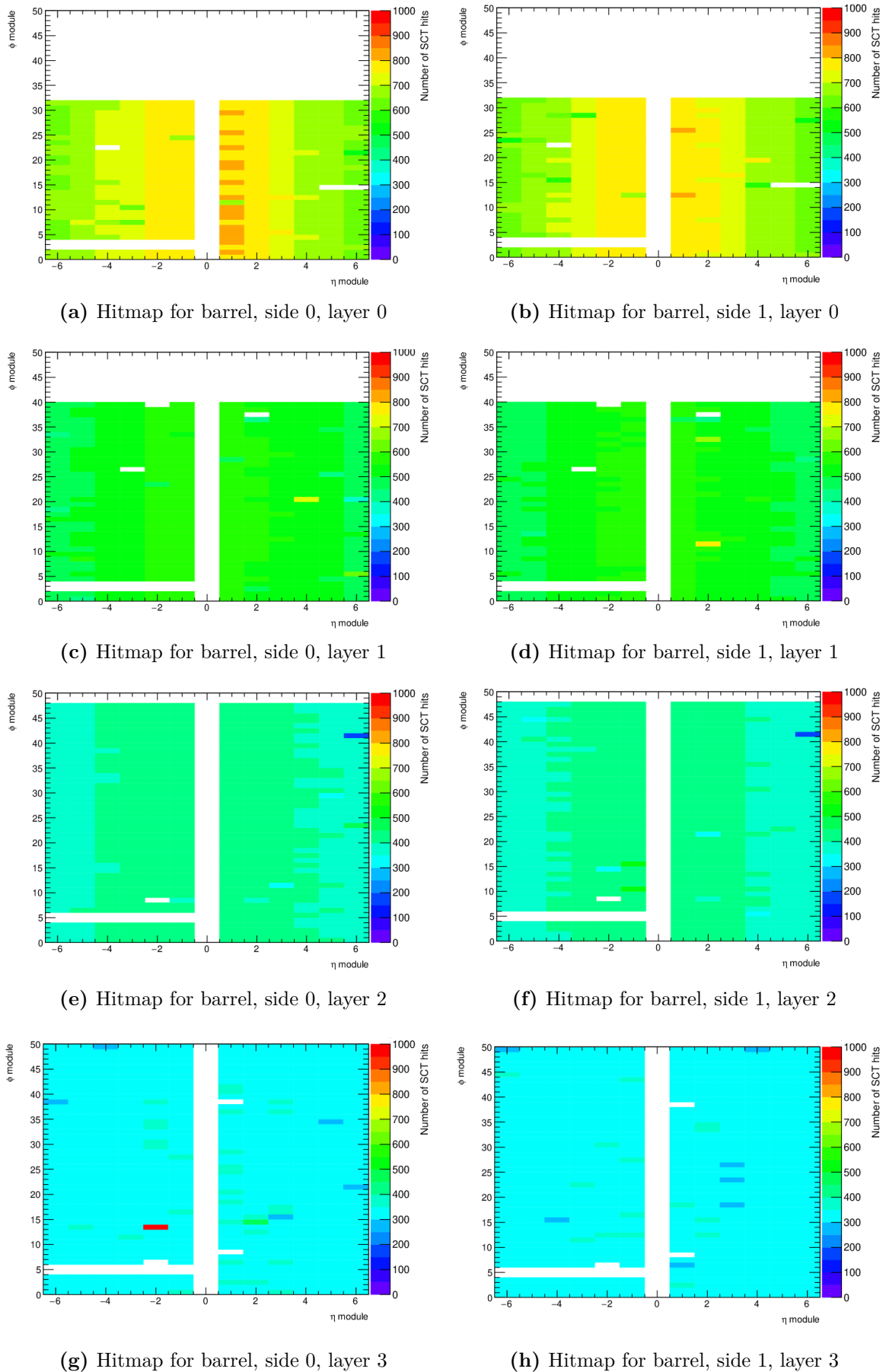
Figure 4.2.: Hitmaps in the $\eta - \phi$ plane for side 0 and side 1 of the four layers of the barrel region of the SCT excluding a barrel rod for Run 206962 calibration pixel beam stream.

the luminosity, which shall be explained in Section 4.3.2. Figure 4.2 shows hitmaps for the barrel using data where a ROD has been deliberately excluded at $N_\phi^{\mathrm{mod}} = 5$ for $-7 < N_\eta^{\mathrm{mod}} < 0$. It is intended that this data can be used to investigate how a problematic ROD in the barrel can affect the relationship between the average number of strips and the average number of clusters with μ. However, in the results that follow, the focus is shifted to establishing that there exists a relationship between the average number of SCT clusters and μ and the implications that relationship would have on using the SCT to make a luminosity measurement. On the basis of the low number of noisy and dead modules observed, their effect on the luminosity measurement is neglected and left as the subject of future investigations.

Relationship Between Average Number of Clusters and μ

If the SCT were to be used as a luminometer, there would need to be a relationship between the number of clusters or strips it records and μ. To obtain the value of μ for a particular detector, each detector and algorithm must first be calibrated to determine its visible cross-section σ_{vis}. The vdM scan method that was described in Section 4.2 is the main technique used to find the absolute luminosity scale of each detector and algorithm, by first calculating σ_{vis}. Subsequently, Equation 4.3 and the relationship $\mu_{\mathrm{vis}} \equiv \varepsilon\mu$ are used to find a value for the luminosity and then cross-calibration is used to find μ, again taking the inferred luminosity and σ_{vis} as inputs to Equation 4.3. These values of μ have been obtained using the BCM's vertical sensor with the EventOR algorithm.

Figure 4.3a and Figure 4.4a show the relationships between the number of clusters and the number of strips with μ for each layer of the SCT barrel. It should be noted that the number of activated strips is always greater than the number of recorded clusters by a factor of 2-3 as each cluster comprises this number of strips on average (evidence of this can be seen by looking ahead to Figure 4.9). The data for each layer of the barrel was fitted with a linear fit $y = mx + c$ and the fitting parameters m and c together with the reduced χ^2, χ_R^2 are shown in Table 4.1. It can be seen from Figure 4.3 and Figure 4.4 that the relationship between detected clusters and activated strips with μ is approximately linear for $\mu \in (12, 25)$. This is evidence of the fact that before the effect of afterglow becomes significant (for $\mu > 25$), there is a correspondence between quantities that can be measured by the SCT (clusters and activated strips) and μ. It was anticipated that afterglow and electronic noise would be proportional to μ because both sources of background result directly from inelastic collisions. The low values of

χ^2_R also support the fact that there is a strong linear relationship between μ and the number of clusters recorded/strips activated for this range of μ. In order to calculate χ^2_R, the number of degrees of freedom[5] must be considered. The strong linear relationship is good initial evidence that the SCT would be an effective luminometer.

Layer	Strips			Clusters		
	χ^2_R	c	m	χ^2_R	c	m
Layer 0	3.1	306.0	113.1	1.4	155.8	51.8
Layer 1	3.6	306.7	106.1	1.4	152.7	47.4
Layer 2	3.4	280.6	99.3	1.4	145.0	43.5
Layer 3	3.5	275.3	91.9	1.4	140.6	40.6

Table 4.1.: The χ^2 values, y-axis intercepts (c) and gradients (m) for the linear fits for $\mu = [13, 25]$ of the plots of the number of strips and number of clusters vs. μ

A possible explanation of why the ratio of the number of strips or clusters to μ is not constant over the entire range of μ (as can be most clearly seen from Figure 4.3b and Figure 4.4b) is because these results were produced using data from the calibration pixel beam stream, using triggers that were intended to facilitate the study of afterglow rather than random triggers. Random triggers sample each BCID with equal probability which makes their use more suited to making a luminosity measurement [84]. This is achieved by the EF selecting events at random from the L1, regardless of whether a RoI is present [142]. Data that has been selected by the trigger system was categorised into one of two types of *stream*, the physics stream and the calibration stream. Data from the calibration pixel beam stream has been specifically collected for the calibration of the PIXEL Detector [143]. The data from Run 2, presented in Section 4.3.3, was collected from the calibration pixel beam stream with a random trigger.

---

[5]The degrees of freedom corresponds to the number of bins the contained in the fitted range minus the free parameters and is equal to 24.
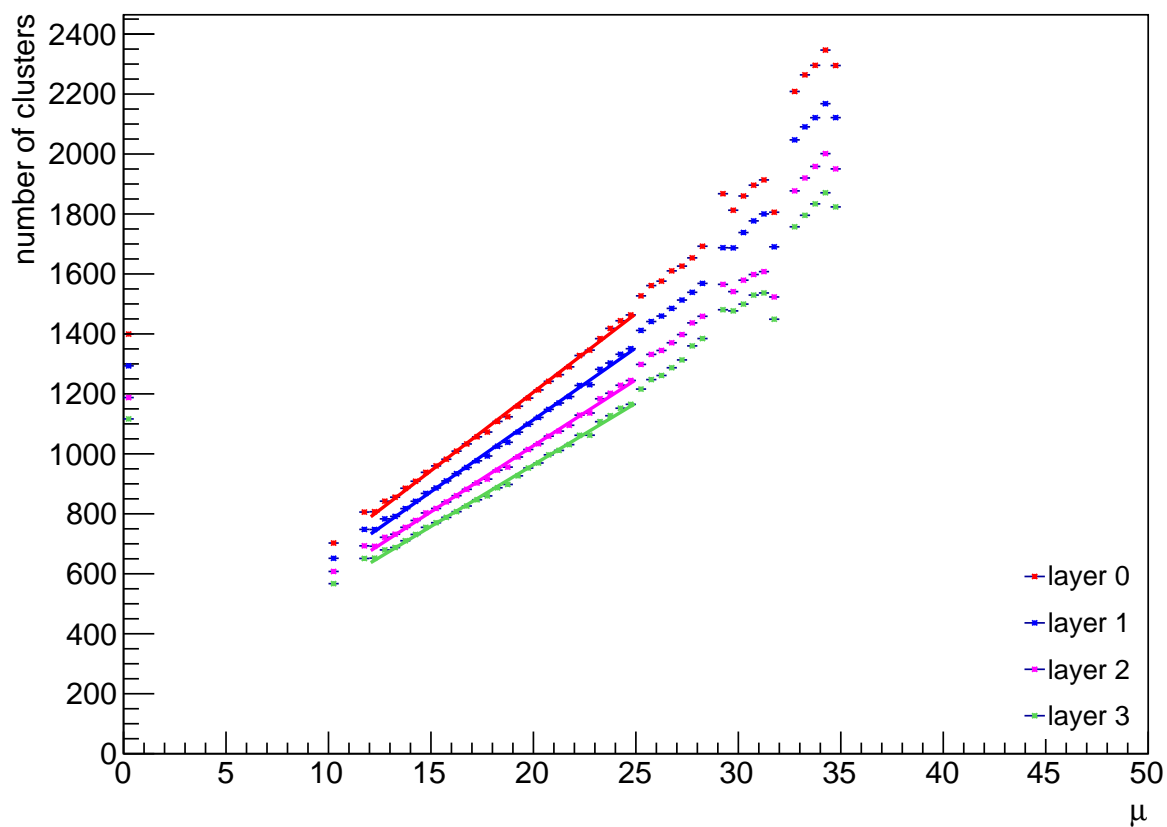
(a) Number of clusters vs. μ for each layer of the barrel region
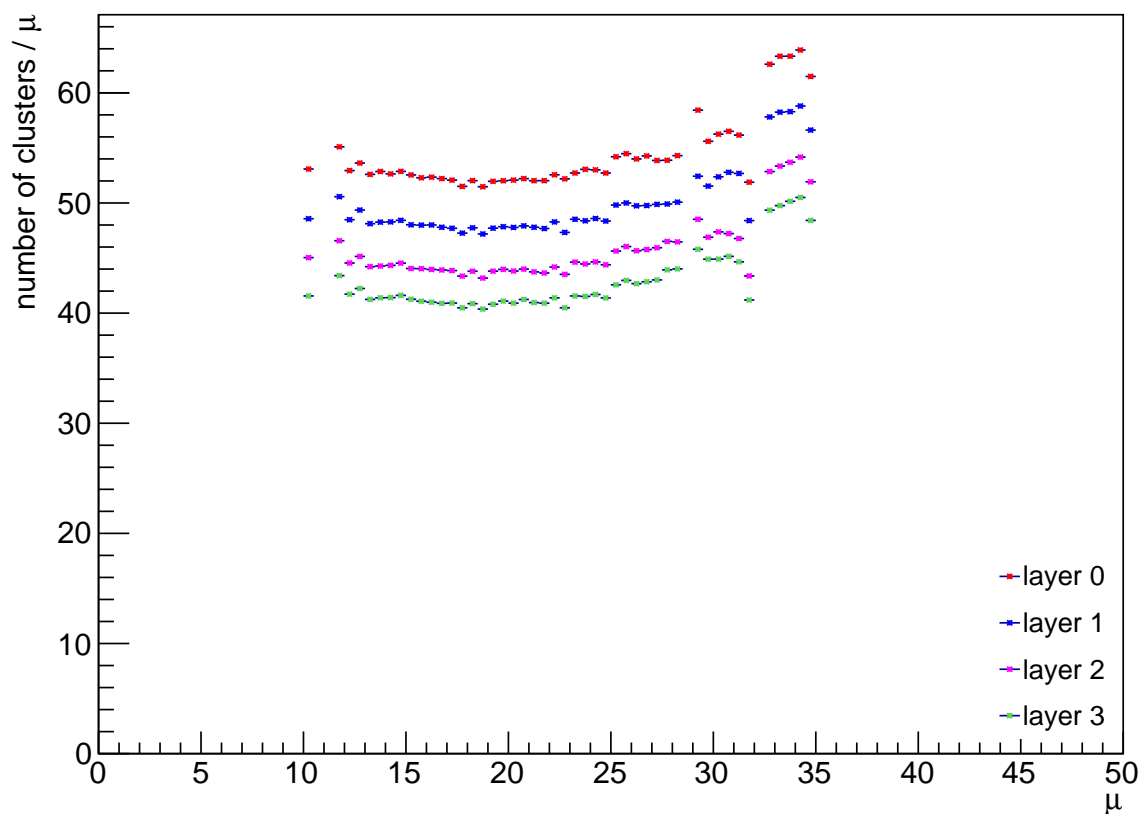
(b) Ratio of number of clusters to μ vs. μ for each layer of the barrel region

Figure 4.3.: The relationship between the number of clusters recorded by the SCT and μ for Run 206962 calibration pixel beam stream.
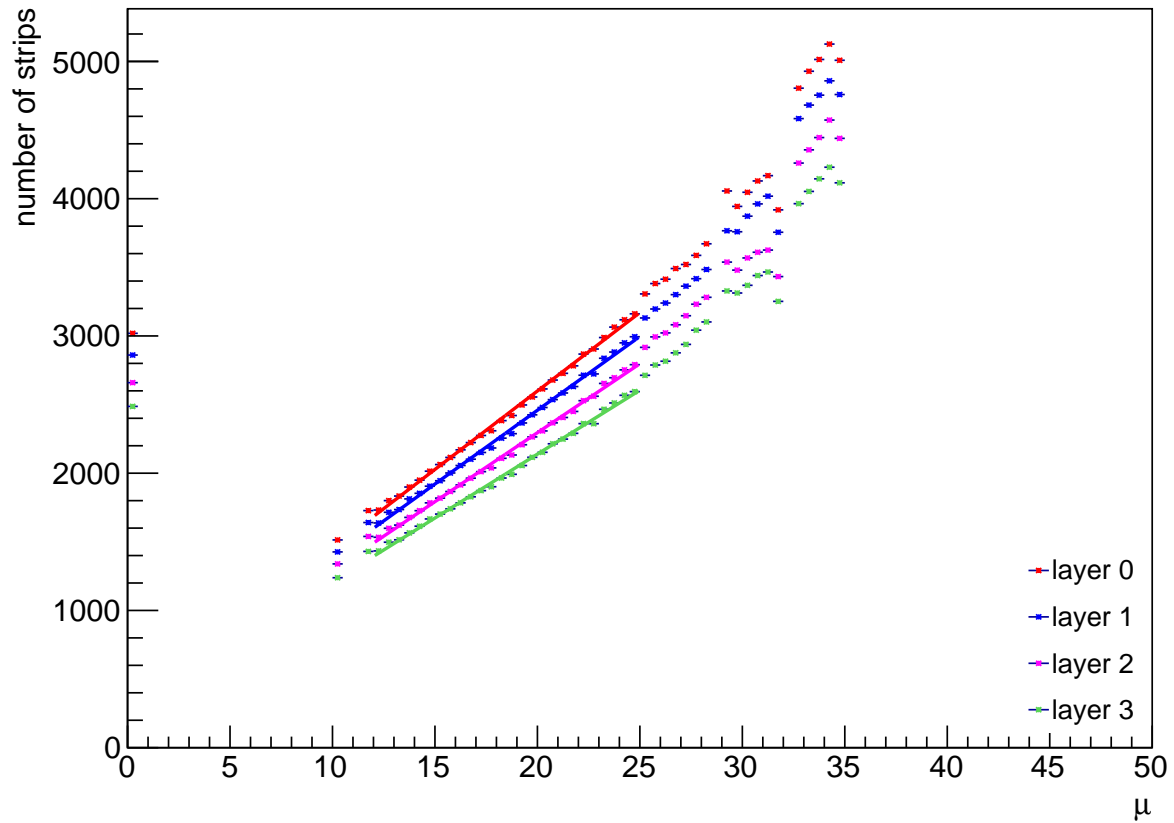
(a) Number of strips vs. μ for each layer of the barrel region
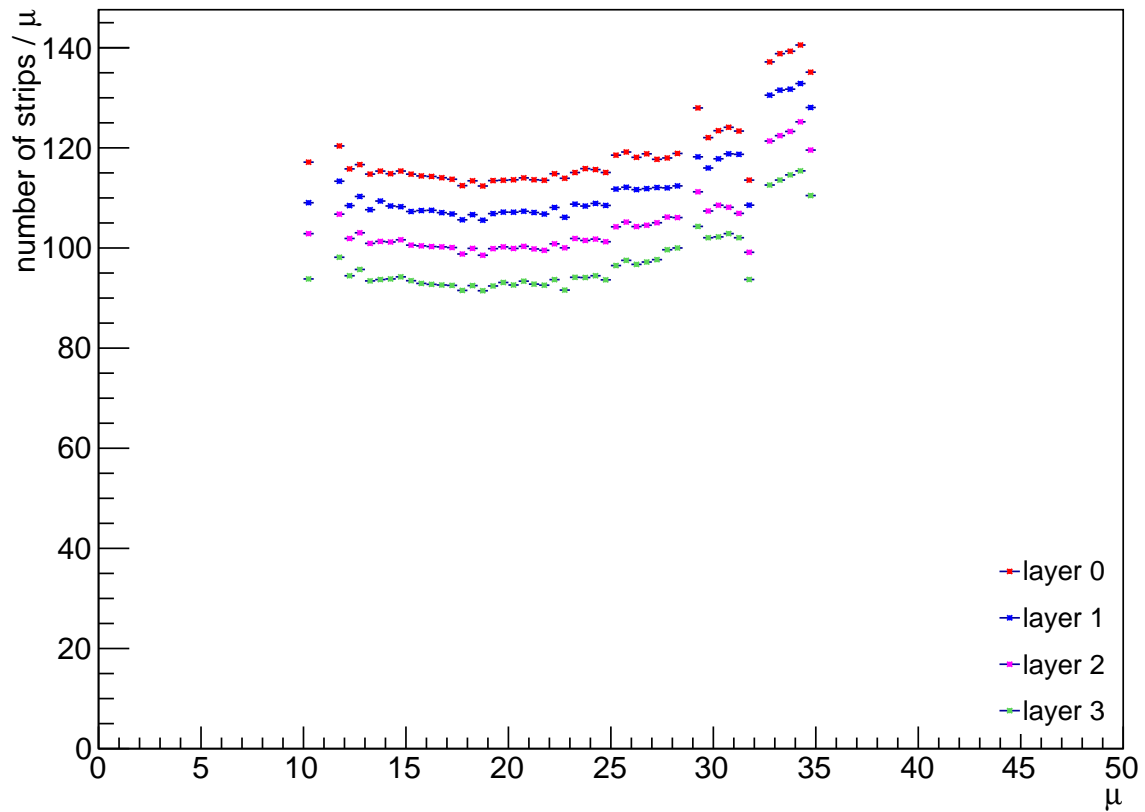
(b) Ratio of number of strips to μ vs. μ for each layer of the barrel region

Figure 4.4.: The relationship between the number of strips recorded by the SCT and μ for Run 206962 calibration pixel beam stream.

Relationship Between Average Number of Tracks and Average Number of Clusters

To ascertain whether the sources of background are well understood, the ratio between the average number of tracks and the average number of clusters recorded by the SCT is considered. Again, for ease of analysis, only the results from the barrel region were used.

As mentioned in Section 4.1, clusters can originate from sources such as afterglow, or electronic noise, as well as from pp collisions. In addition, the requirements on track recognition are much more stringent than those on cluster recognition. This can be seen from just the requirement on the number of hits alone - as shall be seen in Section 4.3.3, only two or three silicon hits are required to define a cluster, whereas even the loose track selection requires at least seven silicon hits to define a track. Track candidates also have to pass selection criteria on p_{T}, $|\eta|$ and the number of silicon holes, which are not applied to clusters [135, 144]. Therefore any substantial deviation from an approximately constant ratio between average number of tracks and average number of clusters would indicate that some of the clusters were coming from the background sources. For clarity, average number of tracks and average number of clusters measured as a function of BCID are shown separately in Figure 4.5. As the overall shape of the distribution of the ratio is informative for studying the afterglow, this histogram was normalised to make its area equal to unity.

Figure 4.6 shows the ratio of the average number of tracks to average number of clusters. It can be seen, in general terms, that the distribution of the ratio is similar for the four trains in the run and increases towards the end of the train. As the value of this ratio has been plotted for each of the 3564 values of BCID, it is much easier to see how it varies over the course of the four trains in this run from Figure 4.7, where each of the trains are examined separately.

It may be expected that the ratio shown in Figure 4.7 would be higher for the outer barrel layers as they have more modules. However, the ratio from each layer has been normalised to make the areas under the histograms of clusters and the histograms of tracks equal to one, so that the shapes of the distributions versus BCID can be compared. Therefore, the ratio recorded by the outer layers will not have a higher value compared to the ratio recorded by the lower layers.

Figure 4.7 also shows that the ratio between number of tracks and number of clusters plotted as a function of BCID is not constant. Therefore, a proportion of the clusters
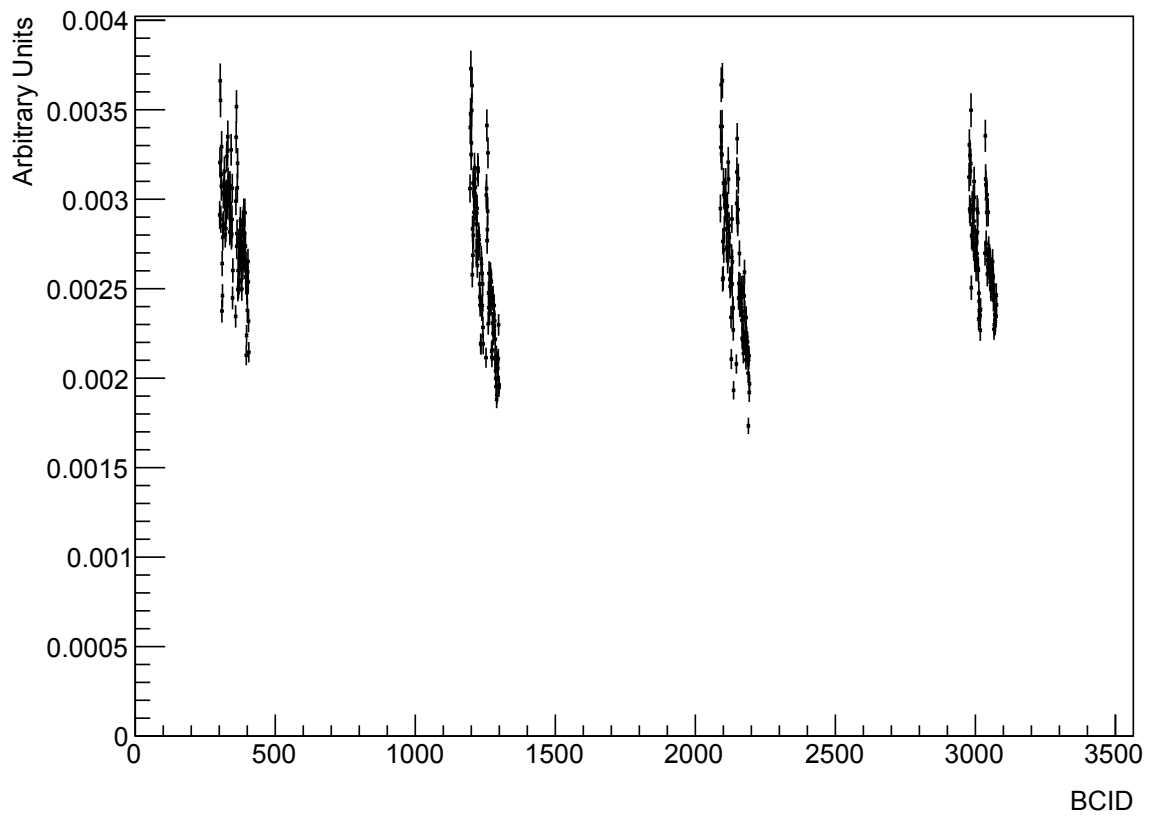
(a) Average number of tracks vs. BCID
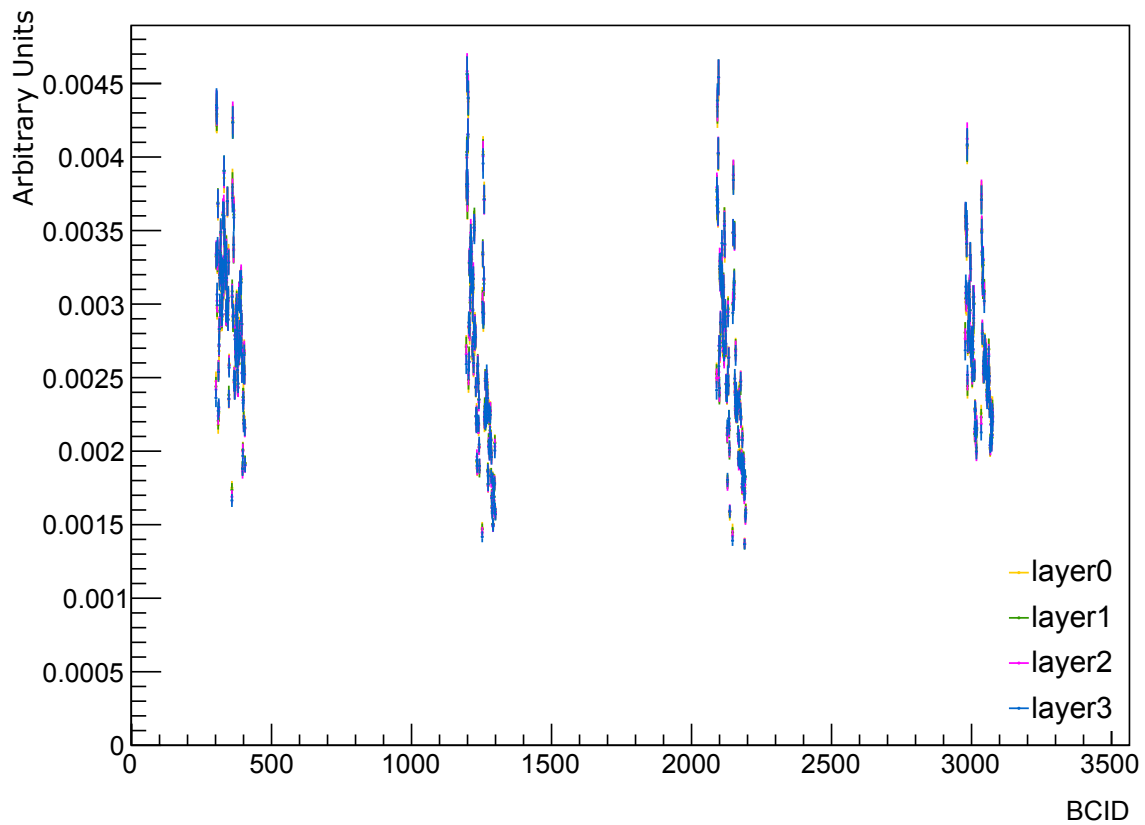
(b) Average number of clusters vs. BCID for each layer of the barrel

**Figure 4.5.:** Run 206962 calibration pixel beam stream.
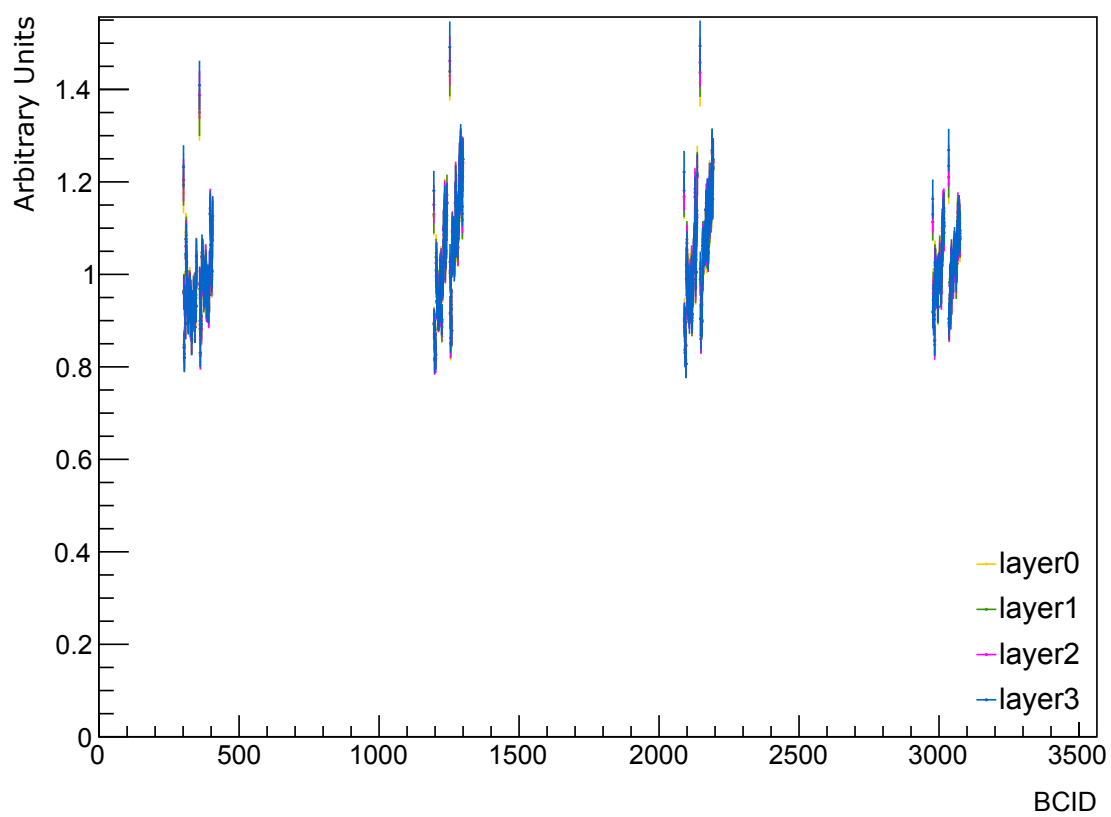
Figure 4.6.: The ratio of the average number of tracks to average number of clusters vs. BCID for the barrel for all four trains in Run 206962 calibration pixel beam stream.
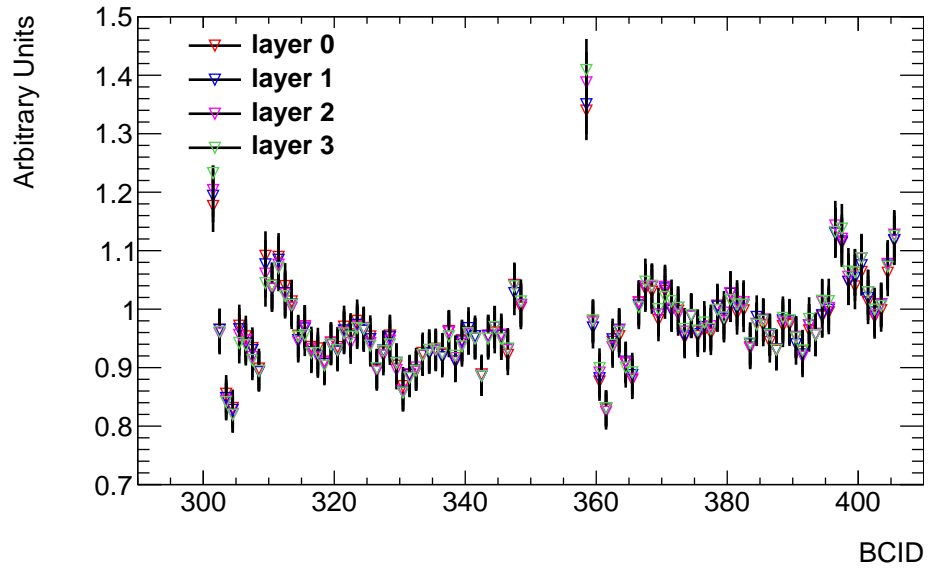
(a) First Train
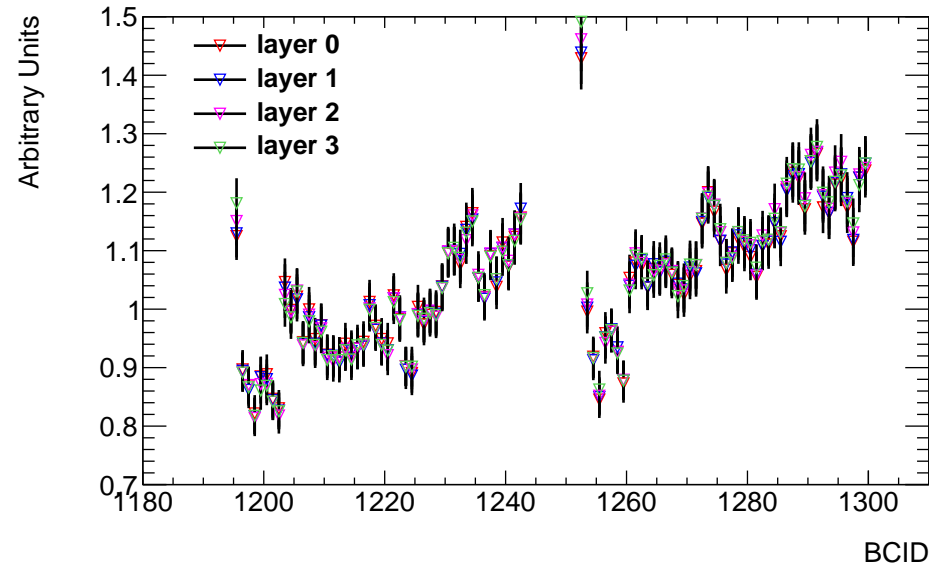
(b) Second Train
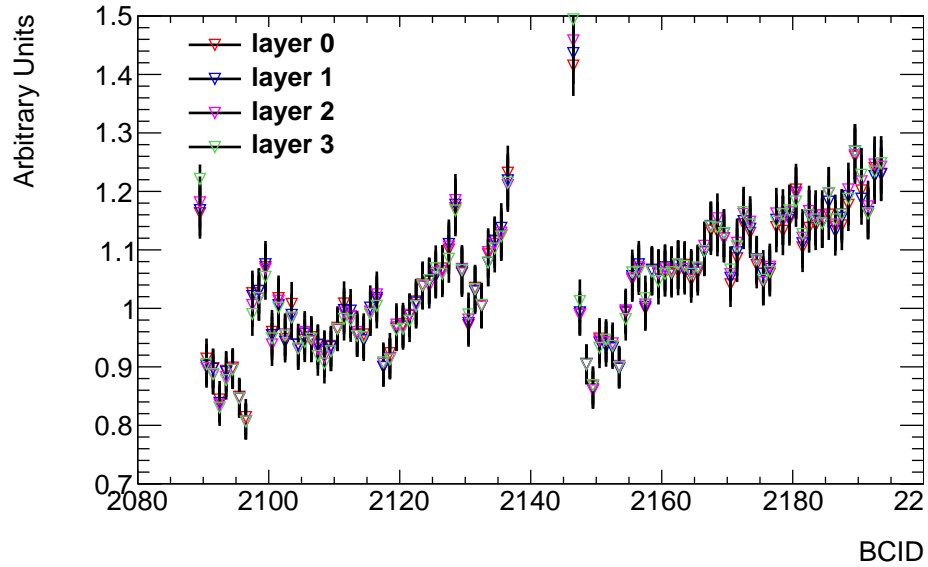
(c) Third Train
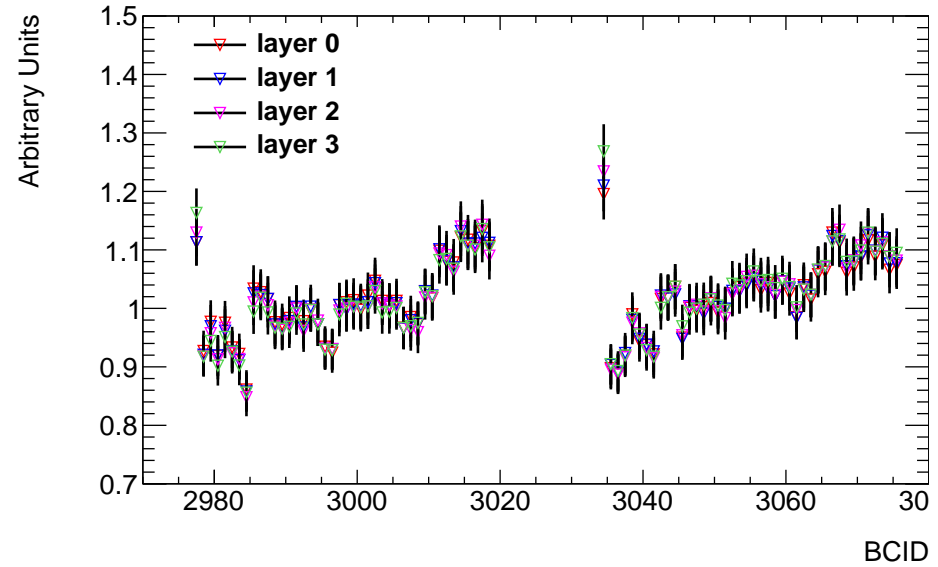
(d) Fourth Train

Figure 4.7.: The ratio of the average number of tracks to average number of clusters vs. BCID for the barrel, for each train for Run 206962 calibration pixel beam stream. Error bars have been calculated by adding the uncertainty on the average number of tracks and the average number of clusters in quadrature and scaling to the ratio.

recorded by the SCT are from sources other than the primary collisions. These sources need to be the subject of further investigation if the SCT is to produce accurate measurements of the luminosity. As explained in Section 4.1, afterglow is the only non-negligible source of background in a luminosity measurement. Therefore, the upward trend at the end of each train can be attributed to the afterglow of the collisions from the rest of the train.

It is noteworthy that the first BCID in every train has a higher value of the ratio than its successors. A possible explanation for this can be obtained by considering that the SCT is read out in 01X binary readout mode. The SCT uses binary readout of three successive BCIDs of the form $X_1 X_2 X_3$ where $X_i \in \{0, 1\}$, to record timing information. It should be noted that the BCID before the start of the train is empty by definition. The second binary digit in the group of three is in time with the trigger whilst the first and last represent the BCIDs before and after the trigger respectively. Therefore, the ratio is higher in the first BCID in the train because the 01X requirement is always met by virtue of the empty proceeding BCID - before the start of the train. For successive BCIDs in the train, some of the events fail the 01X requirement, if X_1 (X_2) is registered as a 1 (0) due to out of time hits. It may be possible to attribute this effect to afterglow which is the subject the next section.

4.3.3. Run 2 Results

Results from "Afterglow Runs"

One of the most important steps to determine whether the SCT could be used as a luminometer is to isolate the effect of afterglow. SCT clusters that result from collisions are more likely to consist of a higher number of strips than clusters, which result from afterglow and other types of noise. It was therefore determined that a requirement on the number of strips that a cluster must contain in order to be considered as part of the luminosity measurement would be an effective way to reduce the influence of afterglow on the measurement.

Figure 4.8 shows how the number of clusters changes around the colliding BCID and for the BCIDs in the tail if requirements are placed on the number of strips in a cluster, compared with no requirements in place. It was assumed that noise was responsible for the clusters recorded in the tail region, from the BCID of 1789 to 1794 shown in Figure 4.8. A compromise must be made between retaining the maximum number of

clusters in the colliding BCID and minimising the number of clusters in subsequent BCIDs in order to achieve the most signal with which to make a luminosity measurement for the least noise. It can be seen that the requirement that clusters contain two or more strips greatly reduces the number of clusters in the tail region. Meanwhile, requiring that clusters contain three or more strips only produces a small further reduction in the number of clusters recorded in this region. In comparison, in the region around the peak, a requirement of two or more strip clusters reduces the signal recorded around the colliding BCID by just under half, whereas requiring three or more strip clusters reduces the signal in the region of the peak by approximately three quarters. Therefore it was concluded that a requirement of two or more strips in the cluster was sufficient to reduce the effect of noise (attributed mostly to afterglow) whilst minimising the reduction in signal.

This is illustrated by the plot shown in Figure 4.9 where the size of the SCT clusters recorded is shown as a function of BCID. It can be seen that the clusters recorded with a
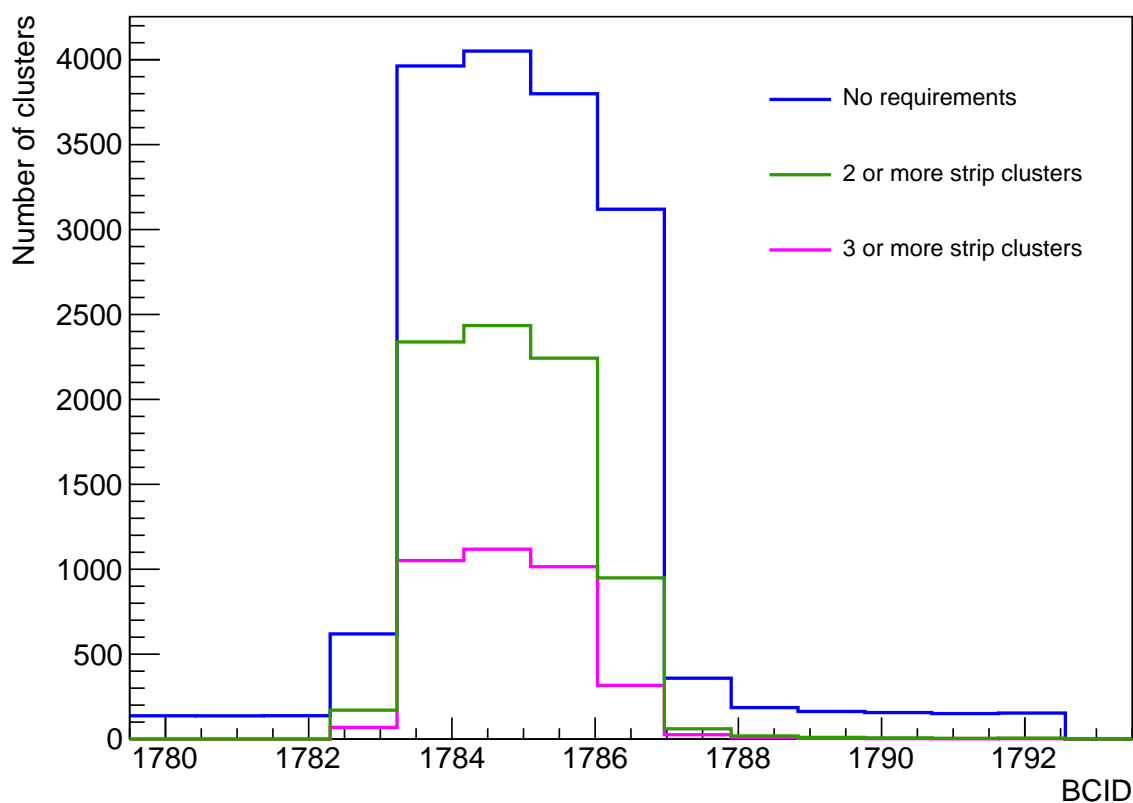
Figure 4.8.: Number of clusters vs. BCID for the barrel region of the SCT for: no requirements on the number of strips in a cluster; clusters consisting of two or more strips and clusters of consisting of three or more strips for afterglow Run 266904 calibration pixel beam stream.
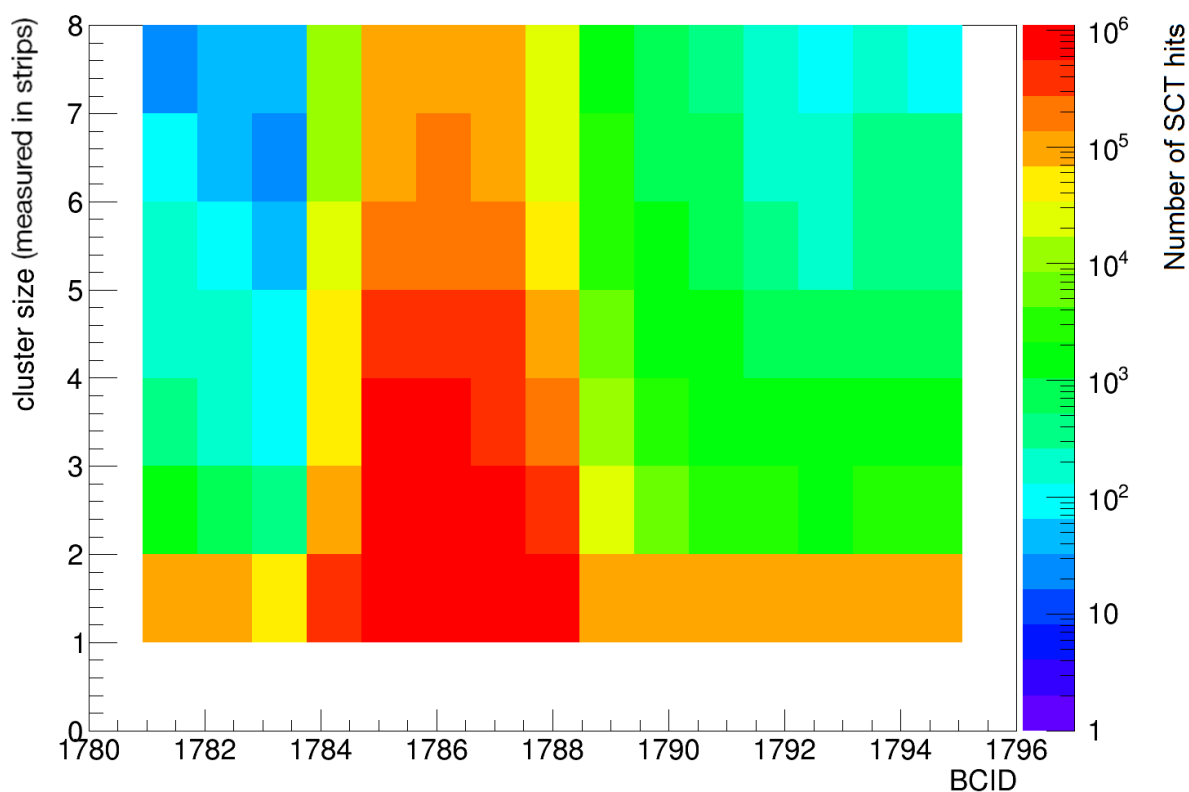
Figure 4.9.: SCT cluster size as a function of BCID for Run 266904 calibration pixel beam stream.

BCID of 1784 are most likely to be one strip wide, which is typical of a cluster caused by noise. In comparison, a greater proportion of clusters that contain two or more strips can be found at the colliding BCID. After the colliding BCID, the typical size of a cluster decreases again, which is to be expected if the clusters were caused by noise.

Further requirements to reduce the effects of afterglow can be enforced by considering timing information from the SCT. Figure 4.10 shows timing information for the "afterglow run" 266904 that included two colliding BCIDs. The following analysis focuses on the collision which occurred at a BCID of 1786.

Figure 4.10a shows timing information only from the colliding BCID after the requirement that clusters contain two or more strips is imposed. It can be seen that a large proportion of the hits are in the 010 bin, which corresponds to hits being recorded in time with the trigger being fired. There is also a large number of hits in the 011 bin, which is expected due to the shape of the output pulses from the amplifiers used to amplify the SCT signals. In fact, 71% of hits-on-track are 011 hits [68]. Figure 4.10b depicts the readout for the BCID 1785 prior to the colliding bunch BCID. The majority of hits

(a) Timing information for the colliding bunch at a BCID of 1786

(b) Timing information for the BCID of 1785

(c) Timing information for the BCIDs from 1787 to 1792

(d) Timing information for the BCIDs from 2100 to 2200, pure noise
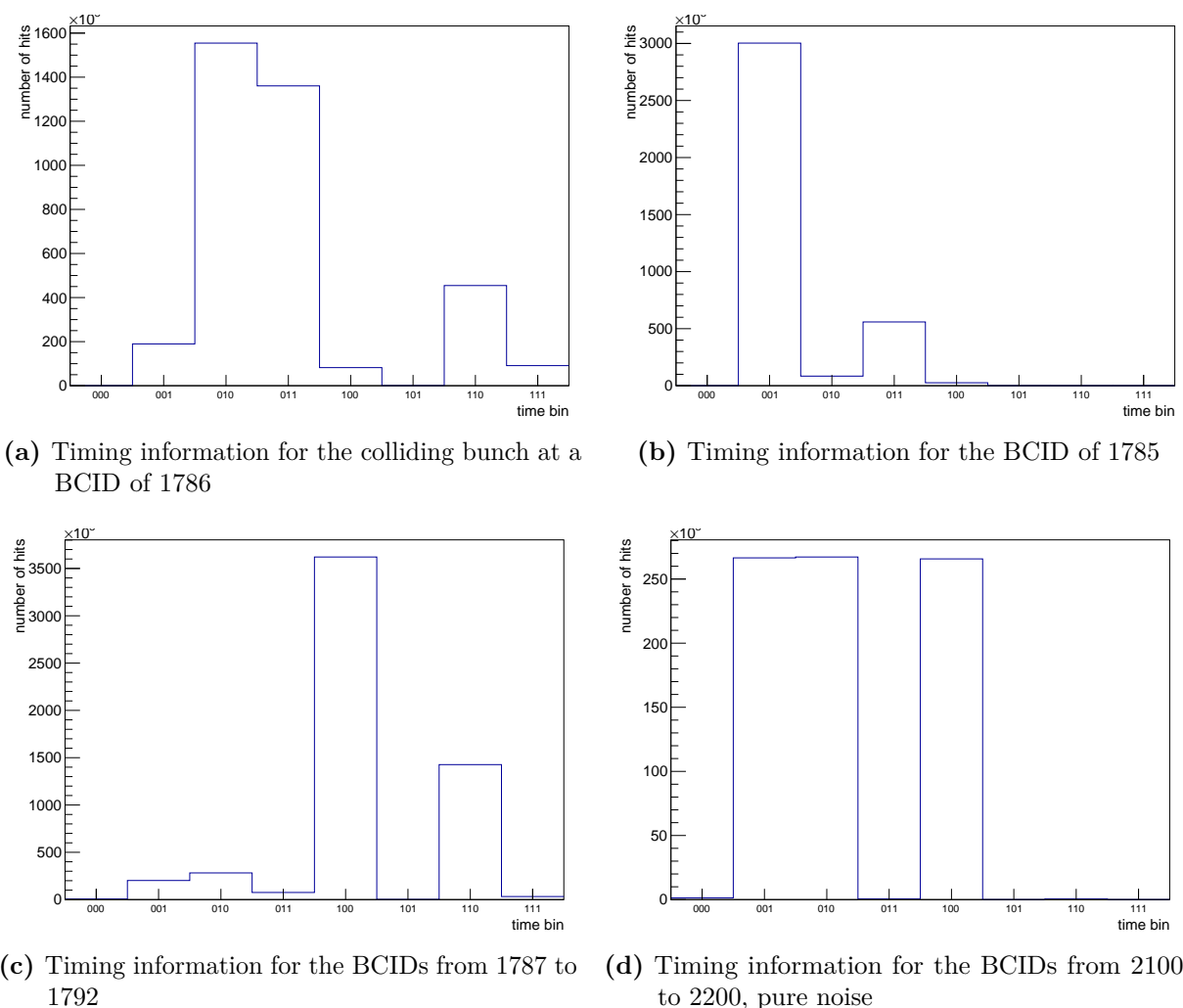
Figure 4.10.: SCT Timing information for the "afterglow run" 266904 calibration pixel beam stream that included two colliding BCIDs, one of which occurred at 1786.

are in bin labelled 001 which means that the hits are recorded for the following BCID i.e. BCID of the colliding bunch pair. The timing information shown in Figure 4.10c relates to the BCIDs 1787 to 1792, corresponding to the tail region of Figure 4.8. The majority of the hits in this plot are in the 100 bin, corresponding to hits from the BCID of the colliding bunch. The 110 bin also has a relatively high number of hits, some of which were recorded at the BCID of the colliding bunch pair. The 110 hits can also be attributed to the aforementioned fact that the SCT recorded 71% of hits-on-track as 011 hits. The 001 and the 010 bin also contain hits from the tail. These hits can be attributed to out-of-time hits or possibly to afterglow. It is therefore recommended that a 01X requirement is applied to the data collected by the SCT to make a luminosity measurement in order to mitigate the effects of afterglow. Figure 4.10d is included here
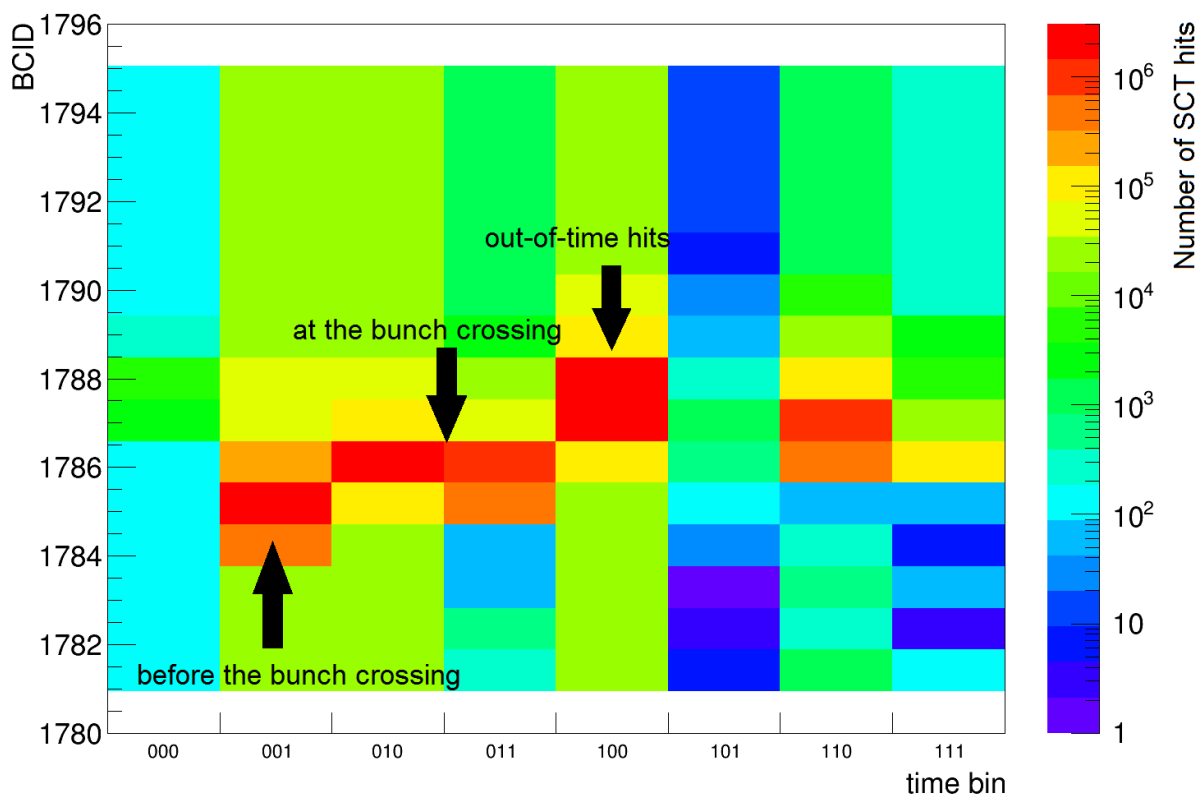
Figure 4.11.: SCT timing information for BCIDs surrounding the BCID of the collision at 1786 (Run 266904 calibration pixel beam stream).

for reference. The plot shows timing information for BCIDs 2100 to 2200 which are separated from the BCID of the colliding bunch pair at 1786. There are approximately equal numbers of hits recorded in the 001, 010 and 100 bin meaning that the trigger threshold has the same probability of being exceeded in time with, before, or after the trigger. Therefore pure noise was recorded for this range of BCIDs.

This is summarised in Figure 4.11 where timing information is shown for the range of BCIDs surrounding the BCID of the collision at 1786. It can be seen that there is a large quantity of hits for the 001 bin at BCID of 1785, corresponding to the out-of-time hits mentioned above. The BCID of the colliding bunch pair is shown with in-time as well as out-of-time hits. The BCIDs following 1786 exhibit out-of-time hits, discussed previously, that can be attributed to noise or afterglow.

Results from μ-scans

The relationship between the number of clusters recorded in the barrel of the SCT and the entire range of LB for the μ-scan in Run 280520 is shown in Figure 4.12 and Figure 4.13. It can be seen that the data presented in Figure 4.13 was taken just from the period with LBs from 400 to 450 in Figure 4.12 as this period represents one complete scan (as well as a proportion of the previous scan for reference), as can be seen from the Gaussian in Figure 4.12. The same scale of reductions in the number of clusters can be seen when the requirements on the number of strips per cluster are imposed on this data, as can be seen from Figure 4.13. The 01X timing requirement has also been applied.

To test the accuracy of the luminosity measurement that the SCT can produce, a comparison was made between the number of clusters recorded by the SCT and the luminosity measurements made by LUCID operating with an EventOR algorithm (denoted LUCID_OR) and TileCal, for this μ-scan, as shown in Figure 4.14. It can be seen that the comparison was made for a similar range of LBs as in Figure 4.13. In the centre of the scan, the ratio between the number of clusters recorded to the luminosity measurements of LUCID_OR and TileCal is constant to within 10%. This is further evidence that the SCT could be used as a luminometer.
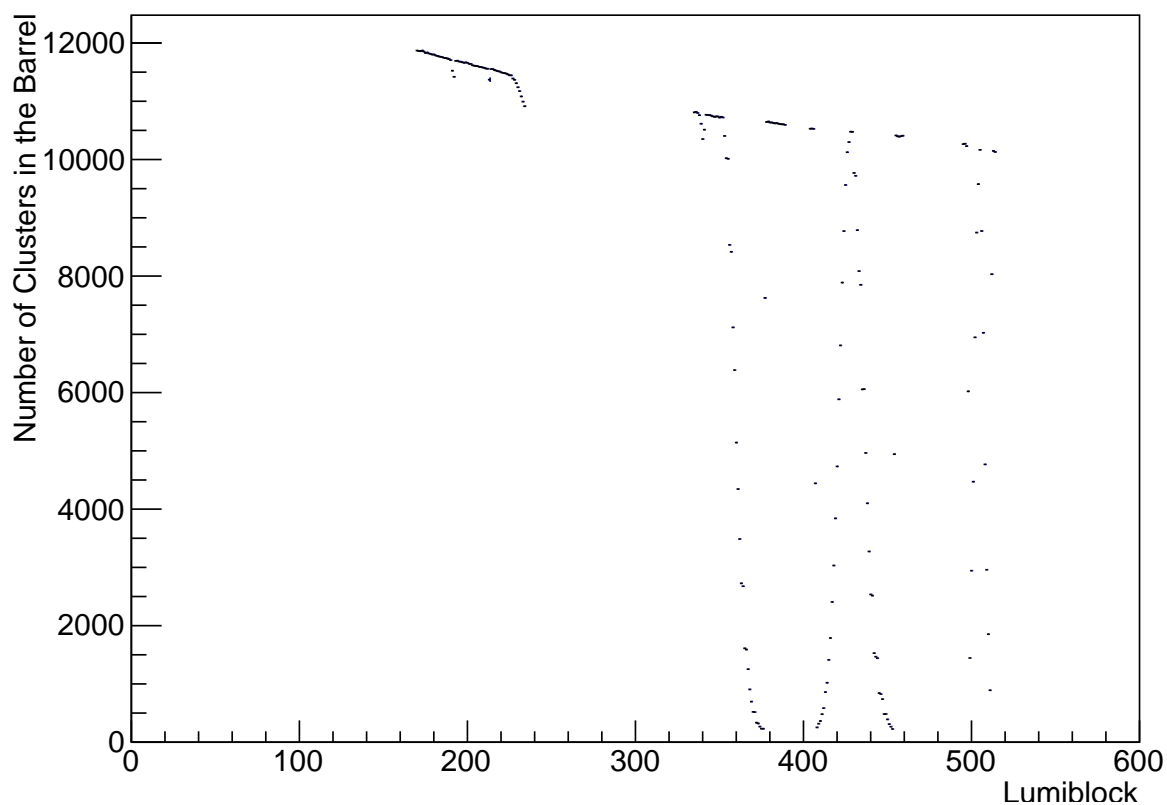
Figure 4.12.: Number of clusters vs. lumiblock for the barrel region of the SCT for the μ-scan run taken in Run 280520 calibration pixel beam stream.
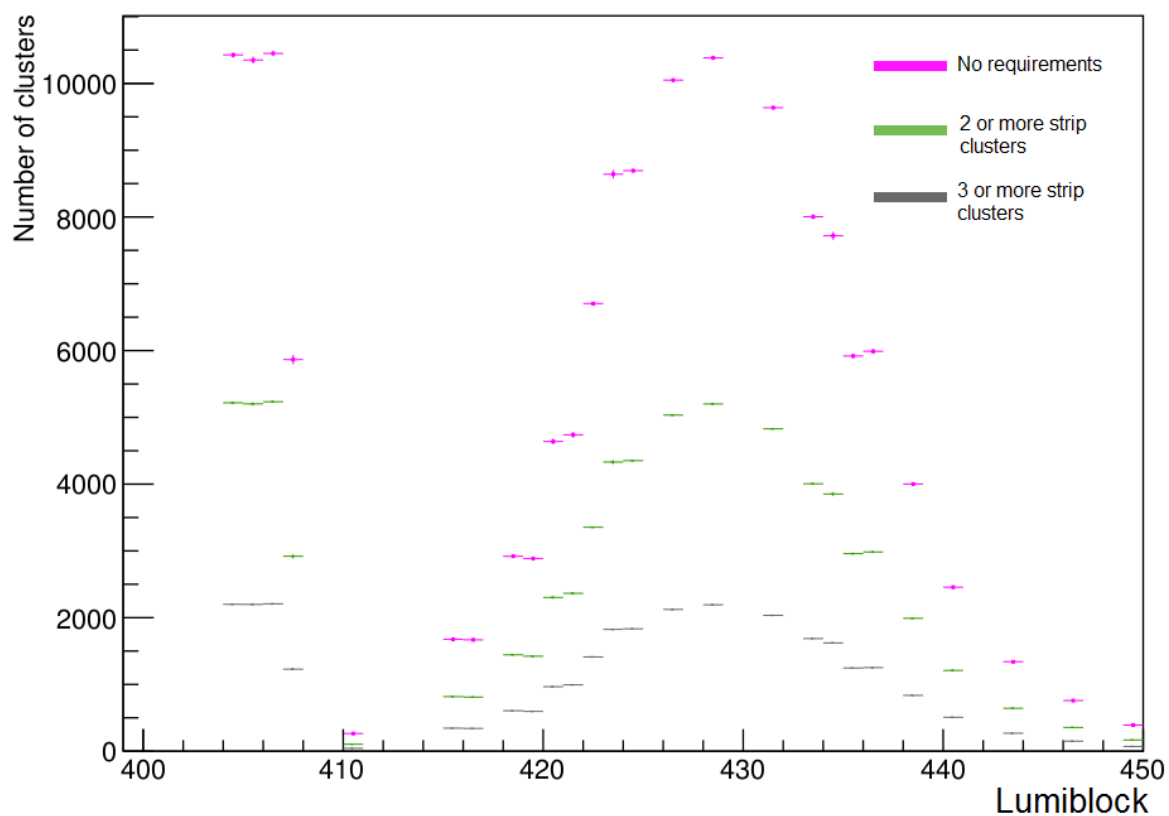
Figure 4.13.: Number of clusters vs. lumiblock for the barrel region of the SCT for: no requirements on the number of strips in a cluster; clusters consisting of two or more strips and clusters consisting of three or more strips for the μ-scan run taken in Run 280520 calibration pixel beam stream.
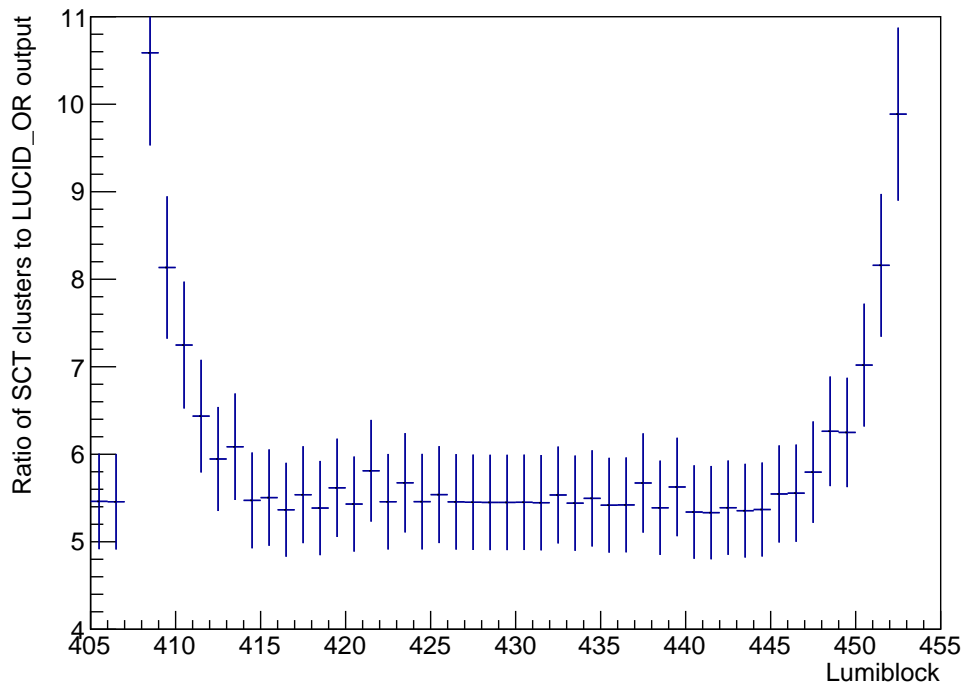
(a) The ratio of the number of SCT clusters recorded in the barrel region to the luminosity measurements from LUCID_OR as a function of lumiblock
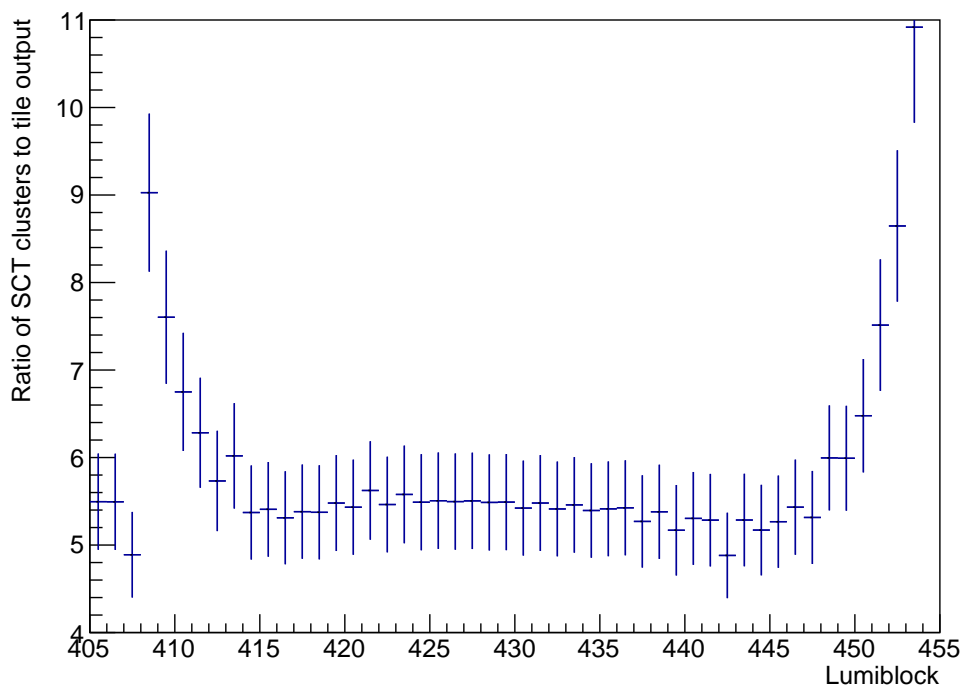
(b) The ratio of the number of SCT clusters recorded in the barrel region to the luminosity measurements from TileCal as a function of lumiblock

Figure 4.14.: The ratio of the number of SCT clusters recorded in the barrel region to the luminosity measurements from (a) LUCID_OR and (b) TileCal as a function of lumiblock in Run 280520 calibration pixel beam stream. A 10% uncertainty was assumed.

4.4. Conclusions

The goal of this project is to determine if the SCT of the ATLAS detector can be used to reliably measure the luminosity of the proton beams at the LHC. As explained in Section 4.2.1, hit-counting algorithms reach saturation at a higher value of μ_{vis} than event-counting algorithms. Therefore, if the SCT were to be used as a luminometer, it would employ a hit-counting algorithm. The SCT's luminosity measurements would complement the currently used luminometers of the ATLAS detector. Using the SCT to make a luminosity measurement would hence help to minimise the systematic uncertainty on the overall luminosity measurement that ATLAS uses, in accordance with the strategy of comparing the readings from multiple luminometers and algorithms.

Hitmaps of the entire SCT were produced. These can be used to identify "noisy modules" which would affect the number of clusters recorded, which would in turn adversely affect the luminosity measurements. Unresponsive modules would also have a detrimental effect on this measurement. As a first step towards negating this effect, hitmaps were produced using data which had a ROD deliberately excluded and compared to those produced using the whole data set.

To assess whether the SCT could provide an accurate measurement of the luminosity of the LHC's pp beam, the relationship between the average number of clusters measured by the SCT and the average number of interactions per bunch crossing, μ, was analysed. It was found that the relationship between the average number of clusters and μ, for each layer of the barrel region, of the SCT could be modelled by a linear function.

To make an accurate measurement of the luminosity using the SCT, a precise understanding of all sources of the clusters that are recorded is needed. If a proportion of the measured clusters did not originate from the primary pp collisions, the ratio of the average number of tracks to the average number of clusters would not be constant with BCID. This is because the majority of sources of background affect clusters more than tracks as they can be part of the tracks from the pp collision or instigated by afterglow. It was found that the ratio between the average number of tracks and the average number of clusters is not constant with the BCID. Therefore the sources of background that are contributing to the average number of clusters measured could be a subject of further investigation. A possible explanation for the upward trend in this ratio, shown at the end of the bunch trains in Figure 4.7, is that it could be attributed to the afterglow of the collisions from the rest of the train.

In order to identify SCT hits that may be attributed to afterglow, timing information was considered. It was found that enforcing a 01X requirement would reduce the effects of noise and afterglow. The analysis of the data from the "afterglow run", as well as from the μ run, also show that the requirement of two-or-more-strip clusters greatly reduce the noise (observed after the colliding bunch in Figure 4.8) whilst keeping the diminishment of the signal to a minimum (Figure 4.8 and Figure 4.13).

The number of clusters recorded by the SCT during a μ-scan was compared to measurements made by LUCID_OR and TileCal. It was found that the number of clusters recorded for the SCT (which is intended to be used as a luminosity measurement) was consistent with those of the other two detectors to within 10%, even before applying any corrections (Figure 4.14). This result provides good initial evidence that the SCT could be used as a luminometer for the ATLAS detector. To produce an exact measurement of the luminosity, a value of the *pp* cross section according to the SCT must be extracted by cross calibrating data from at least two LHC runs. Discussion of the continuation of this study after the author's direct involvement with the project had ceased is briefly documented in the next section for completeness.

4.5. The Continuation of the Implementation of the SCT as a luminometer

Continuing to use the requirement of two-or-more-strip clusters, the SCT's luminosity measurement was calibrated with a track-counting algorithm, which is also implemented using the SCT as was discussed in Section 4.1. The calibration was conducted using Run 299584, a so-called 'anchor run', and compared to runs 307732, 310249 and 310738. An anchor run is used to translate beam parameters from the vdM regime to the regime used for physics analysis. Consequently, the anchor run is the run against which the luminosity of all other runs are calibrated. At the time of writing, the resulting calibration agrees with the SCT's track-counting algorithm to within 10%. This uncertainty was quantified by studying the ratio between the SCTs's luminosity measurement and that of the track-counting algorithm, and was found not to be constant between the aforementioned runs; hence it is subject to ongoing investigations [145].

4.6. Outlook

The focus of the work presented in this chapter was to provide a robust technique for luminosity measurements, particularly looking to the future as increasingly high luminosities are attained at the LHC. The motivation for striving towards ever higher luminosities is that this provides a greater ability to attain a statistically significant sample of a given class of events. This is due to the fact that the instantaneous luminosity is directly proportional to the number of particle collisions and hence to the amount of data that has to be collected and analysed. This is particularly useful when probing difficult-to-reach regions of phase space in the hunt for BSM. As was explained in Chapter 2, SUSY is one of the most promising candidates of BSM, offering solutions to some of the open questions in particle physics such as the hierarchy problem and the nature of dark matter. In Chapter 6, a search for SUSY in one of the more inaccessible regions of parameter space is undertaken. In order to complete such an endeavour effectively, it is often very beneficial to design new variables that are optimised to differentiate between events that include particle decays predicted by the SM and those that do not as well, as techniques that extend the detector's capability to reconstruct particles whose physical properties lie at the edges of the detector's acceptance. Implementation of such analysis strategies are the subject of the next chapter.

Chapter 5.

Techniques for Searching for Compressed SUSY at ATLAS

"What is the path? There is no path. On into the unknown."
— Johann Wolfgang von Goethe

The *stop*-quark has a unique role to play in solving the hierarchy problem, as a consequence of the relatively large mass of the *top*-quark compared to other fermions, as explained in Chapter 2. The rich phenomenology of *stop* processes leads to a variety of final states and represents a challenge for the experimental search programs. An overview of this phenomenological landscape was given in Section 2.4. Alas, at the time of writing, no evidence for supersymmetric particles has yet been found. Hence, given the vast amount of data that has been collected by the experiments at CERN, the best outcome that can currently be achieved is to rule out regions of parameter space where SUSY is known not to be i.e. set limits on properties of SUSY particles such as their masses.

In Section 5.1 the analysis presented in this thesis is put into context compared with the previous limits which have set on the mass of the *stop*. This analysis targets a relatively inaccessible region of SUSY parameter space, where the SUSY mass spectrum is compressed. In this context, compressed means that the mass of the *stop* and the LSP, a neutralino, are very close together, separated by 7 GeV to 80 GeV with benchmark points that have mass splittings of 50 GeV.

The M_{T2} variable (otherwise known as the "Cambridge M_{T2} Variable" or the "Strans-verse mass") [26, 146–148], has been developed specifically to measure the mass of

pair-produced particles at hadron colliders. It shall be shown that the application of M_{T2} to measure the mass of *stops* can be used very effectively and indeed the variable is widely used in many analyses to measure the mass of the *stop* as well as other pair-produced particles (see for example Ref. [149–153]). As shall be seen, due to its definition M_{T2} is normally used to provide a lower bound on the mass of a particle. However, one of the focuses of this thesis is the use of M_{T2} in the unconventional application of selecting events *below* (rather than above) a certain value of M_{T2}, in order to select events which could contain *stop* processes. This investigation is described in Section 5.2, where is explained that the variable is termed aM_{T2} if the invisible daughter product of the decay under consideration have unequal masses[1]. It is also shown that aM_{T2} has the potential to be a particularly powerful discriminatory variable in BSM searches such as one that will be discussed in Chapter 6.

One of the products of *stop* processes where the SUSY mass spectrum is compressed are low-pt *b*-jets. Section 3.7.4 reviewed the techniques that are available to identify *b*-jets that fall below the detection capabilities of the ATLAS calorimeter of 20 GeV. In Section 5.3 the applicability of these soft-*b*-tagging techniques in a search for *stop*-quarks that uses aM_{T2} is critiqued, and it is found that these techniques may be used to enhance the scope of the analysis presented in Chapter 6.

5.1. A Brief History of *Stop* Searches[2]

A full account of searches for the *stop* quark can be found in Ref. [29], though the highlights are given here to place the search presented here in context. At the Large Electron-Positron Collider (LEP) collider in 2002, the Omni-Purpose Apparatus at LEP (OPAL) experiment at CERN set a lower limit on the *stop* mass of $t_1 = 98$ GeV [155]. The experiments at the Tevatron performed several searches for *stop*-quarks, commonly assuming direct pair production [55]. In the searches where the *stop* is assumed to decay to a lepton, a sneutrino ($\tilde{\nu}$) and a *b*-quark with 100% branching fraction, limits on the *stop* and sneutrino masses are set at $m_{\tilde{t}_1} > 210$ GeV if $m_{\tilde{\nu}} < 110$ GeV and $m_{\tilde{t}_1} - m_{\tilde{\nu}} > 30$ GeV [156] or $m_{\tilde{t}_1} > 180$ GeV with $m_{\tilde{\nu}} < 50$ GeV [157]. The *DØ* experiment excluded *stops* with masses below 180 GeV, assuming the *stop* decays via $\tilde{t} \to c\tilde{\chi}^0$ and $m_{\tilde{\chi}^0} < 95$ GeV [55, 158]. In the $\tilde{t} \to b\tilde{\chi}_1^\pm$ channel, the Collider Detector at Fermilab (CDF) experiment excluded stops with masses between 128 and 135 GeV, independent of

---

[1]The use of the word "invisible" is the context of particle decays was introduced in Section 3.7.5.
[2]Inspiration for this title was taken from Ref. [154]

the value of the branching fraction of chargino to lepton decays [159], while the *D∅* experiment excluded *stops* with masses between 130-190 GeV for chargino masses between 90-150 GeV [160].
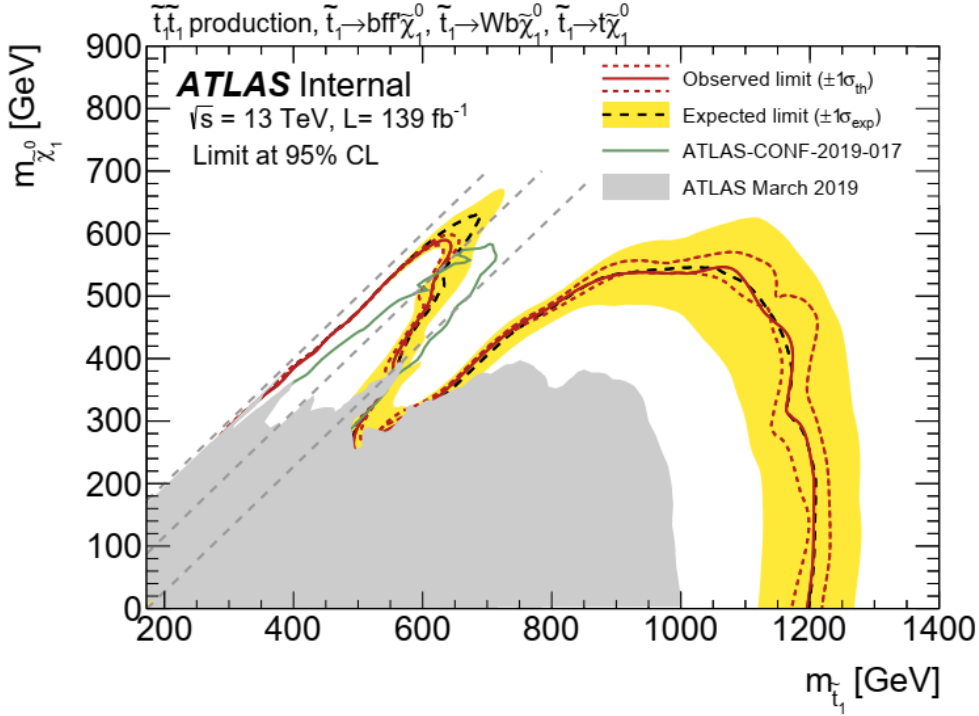

Figure 5.1.: Exclusion contour for a simplified model of the process shown in Figure 6.1. Figure taken from Ref. [114].

The limits on the *stop* mass were improved substantially when the LHC started operation. The ATLAS limits in the $m_{\tilde{t}_1} - m\tilde{\chi}_1^0$ mass plane are given in the exclusion contour shown in Figure 5.1. Some of the most promising *stop* searches currently being undertaken are those dedicated to final decays including zero-or-one- isolated lepton, E_T^{miss} and four or more jets, with at least one being reconstructed as a *b*-jet. The search presented here goes along the one-isolated-lepton route.

Regarding other limits placed on the *stop* mass by the ATLAS and CMS experiments: if the *stop* is assumed to decay via $\tilde{t}_1 \to t\tilde{\chi}_1^0$ the exclusion limits depend strongly on the $\tilde{t} - \tilde{\chi}_1^\pm - \tilde{\chi}_1^0$ mass hierarchy. For example, Ref. [27] excludes *stop* masses below 1200 GeV for the process $\tilde{t}_1 \to t\tilde{\chi}_1^0$. These limits can change substantially under certain assumptions about the mass hierarchy [55]. If the *stop* mass and the mass of the chargino in the decay chain are close to each other, the final state turns from hadronic to multi-leptonic (see for example Ref. [161]).

(a) Stop production from quark-antiquark annihilation

(b) Stop production from gluon fusion
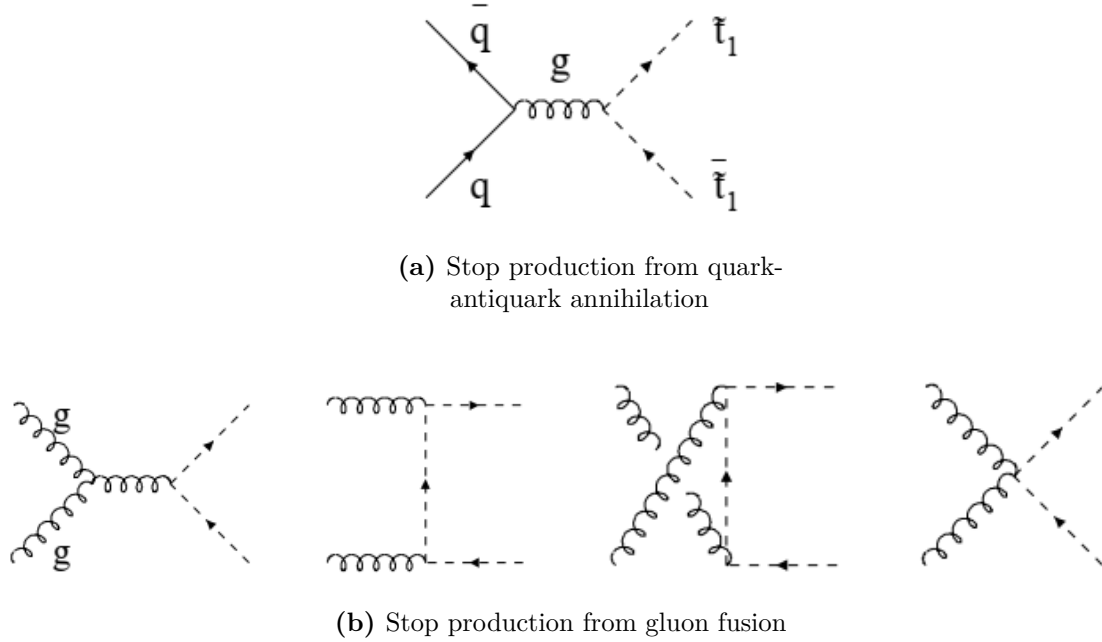
Figure 5.2.: Leading order Feymann diagrams for stop production at hadron colliders via (a) quark-antiquark annihilation and (b) gluon fusion.

Stop decay modes and their relation to the SUSY mass spectrum was discussed in Section 2.4. As Figure 2.1 shows, if the decay $\tilde{t}_1 \to t\tilde{\chi}_1^0$ is kinematically forbidden, the decay $\tilde{t}_1 \to bW\tilde{\chi}_1^0$ as well as $\tilde{t}_1 \to c\tilde{\chi}_1^0$ and $\tilde{t}_1 \to bff'\tilde{\chi}_1^0$ become relevant. Focusing on $\tilde{t}_1 \to bW\tilde{\chi}_1^0$, ATLAS excludes *stops* with $m_{\tilde{t}_1} < 710$ GeV. This kinematic region is also targeted in Refs. [162–167]

If $\Delta m(\tilde{t}_1, \tilde{\chi}_1^0) < m_t$, the production of on shell W bosons is kinematically allowed. ATLAS and CMS substantially improve on the limits that the Tevatron placed on $\tilde{t}_1 \to c\tilde{\chi}_1^0$. The analysis in [27] presents one possible method to exclude $\tilde{t}_1 \to bff' + \tilde{\chi}_1^0$ up to $m_{\tilde{t}_1} \approx 640$ GeV, whilst the analysis presented here is intended to be complementary to that result, whilst relying on the novel use of the aM_{T2} variable as a upper bound to isolate signal (see Section 6.1 for further details). The ATLAS mono-jet search excludes $m_{\tilde{t}_1} < 430$ GeV, assuming $\tilde{t}_1 \to c\tilde{\chi}_1^0$ or $\tilde{t}_1 \to bff' + \tilde{\chi}_1^0$ [168]. CMS places a constraint of $m_{\tilde{t}_1} > 550$ GeV in this region assuming $m_{\tilde{\chi}_1^0} < 450$ GeV using hadronic searches [164].

The generic leading order Feynman diagrams for stop pair production at hadron colliders via quark-antiquark annihilation and gluon fusion are shown in Figure 5.2

5.2. The Use of the M_{T2} Variable

In this section, an investigation of the use of M_{T2} to search for compressed *stop* processes is presented. However, to understand the construction of the M_{T2} variable, the transverse mass, M_{T}, must first be examined.

A consideration that must be made in most colliding-beam experiments is that the analysis should not be sensitive to components of the momentum along the direction of the beam because their value has to be inferred analytically rather than measured directly. These are the components of the quarks and gluons that collide in the 'hard' (high-p_{T}) interactions of the protons. Contamination from pileup also makes a much greater contribution in the longitudinal rather than in the transverse directions [147]. Therefore, any attempt to make measurements involving the longitudinal components of the momenta will be subject to a relatively high uncertainty.

A more accurate approach is to construct variables which eliminate the degree of freedom in the longitudinal plane, projecting onto the plane transverse to the colliding beams instead [169]. Objects and variables that represent a "projection" of energy or momentum into the plane transverse to the colliding beams, are commonly used in analyses of data from hadron colliders [147]. Hence, this so-called "transverse mass" is defined as Ref. [97]:

$$M_T(m_1, s_1, m_2, s_2) = \sqrt{m_1^2 + m_2^2 + 2\left(E_{T.1} E_{T.2} - s_1 \cdot s_2\right)}, \qquad (5.1)$$

where m_1, m_2 are the invariant masses of the particles with momentum components (transverse energies) of s_1, s_2 ($E_{T.1}$, $E_{T.2}$) respectively in the (x,y) plane, perpendicular to the beam direction. As mentioned in Section 2.4, SUSY particles are pair produced as a consequence of R-parity. It is common for both SM and SUSY particles to decay into particles whose presence can be directly detected (visible decay products), as well as those whose presence can only be inferred through considerations of conservation of momentum (invisible decay products). Therefore, SUSY decays commonly result in more than one invisible daughter product. For these processes, the detector can only infer the sum of the p_{T} of these particles as only the total MET of an event can be measured. So in the context of measuring particle processes, it is common to identify one of the particles as the visible decay products (with a momentum 2-vector of *s*) and the other as

the invisible decay products (with a momentum 2-vector of $\displaystyle{\not}{p}$).[3] A well-known example of such an application of M_T was the measurement of the mass of the W boson [34–36]. Hence, Equation 5.1 can be rewritten as:

$$M_T(m, s, \chi, \displaystyle{\not}{p}) = \sqrt{m^2 + \chi^2 + 2\left(E_{T.vis}E_{T.ivis} - s \cdot \displaystyle{\not}{p}\right)}\,, \tag{5.2}$$

where m and $E_{T.vis}$ (χ and $E_{T.ivis}$) are the mass and transverse energies of the visible (invisible) particles respectively. Under most circumstances, the masses of the invisible daughter particles are unlikely to be known or known with limited precision. Therefore χ is a free parameter used to denote these masses to emphasise the lack of knowledge [148]. This is also necessary in order to define the $M_{\mathrm{T}2}$ variable.

To ascertain information about the mass of the parent particles, assumptions can be made regarding the topology of the decay under consideration [170]. As mentioned at the start of this chapter, the $M_{\mathrm{T}2}$ variable (Ref. [26]) was developed to measure the mass of particles that are pair-produced in hadron colliders, in events where each particle decays to one visible daughter product and an invisible daughter product whose existence is inferred from the MET of the event. A diagram of the generic process considered is shown in Figure 5.3. $M_{\mathrm{T}2}$ can be used in supersymmetric analysis to provide a lower bound on the masses of particles that are pair produced in hadron colliders. In SUSY analyses, the masses of the invisible particles are not known as they are dependent on the theory under consideration (see Section 2.4). $M_{\mathrm{T}2}$ is given by the following minimisation procedure:

$$M_{T2}^2 \equiv \min_{\displaystyle{\not}{p}_1 + \displaystyle{\not}{p}_2 = \displaystyle{\not}{p}_T} \left\{ \max\left[M_T^2(m_1, s_1, \chi_1, \displaystyle{\not}{p}_1), M_T^2(m_2, s_2, \chi_2, \displaystyle{\not}{p}_2) \right] \right\} \tag{5.3}$$

Here, the subscripts 1 and 2 are used to denote which side of the decay is being referred to. The function is known as asymmetric $M_{\mathrm{T}2}$ ($aM_{\mathrm{T}2}$) for the case where the invisible particles can be assumed to have different masses, i.e. $\chi_1 \neq \chi_2$ [171]. In the case where an event has only one non-interacting invisible daughter product, it is safe to assume that all of the $p_\mathrm{T}^\mathrm{invisible}$ can be assigned to that daughter product. The minimisation is performed by considering all the possible ways to split up the total MET between the two invisible daughter particles in the sum $\displaystyle{\not}{p}_1 + \displaystyle{\not}{p}_2 = \displaystyle{\not}{p}_T$. For any given event there is

---

[3]If there is more than one visible (invisible) decay product, $s(\displaystyle{\not}{p})$ would be the momentum 2- vector of the composite particle.
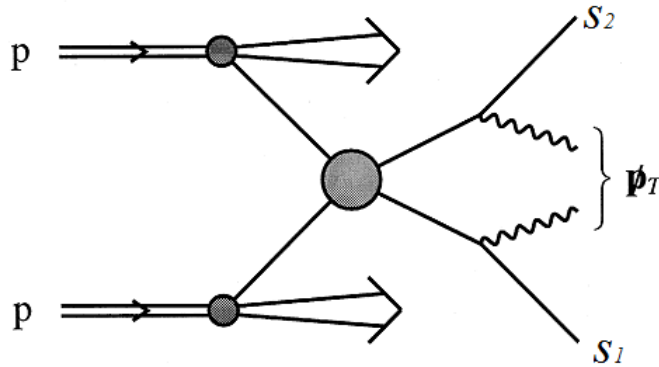
Figure 5.3.: The generic process considered in this study. The *pp* collision results in the pair production of particles that subsequently decay into visible particles (with momenta s_1 and s_2) as well as invisible particles whose presence is inferred by the MET of the event, $\not{p}_T$. Figure adapted from Ref. [26].

an infinite number of pairs of $\{\not{t}_1, \not{t}_2\}$ that satisfy this sum. The way that $\not{p}_T$ was split between the two invisible particles for a given event in reality can never be known. The value of M_{T2} associated with the actual outcome of the splitting shall be called $M_{\text{T2}.truth}$. The minimisation procedure defined in Equation 5.3 will pick out the lowest possible value of M_{T2} that could have occurred due to the splitting of MET and hence define a lower bound on the mass M of the parent particle, so $M_{\text{T2}} \leq M_{\text{T2}.truth}$. Hence to separate signal from background, events above a certain value of M_{T2} can be selected - effectively placing a lower bound on the mass of the sparticles being searched for[4].

Indeed, this is how many analyses use M_{T2}, see for example Refs. [164, 172, 173]. However there are very few examples of the use of M_{T2} as an upper bound to define analysis selections (see for example Refs. [174–176]) and where it is used in this way, the bound is often considerably higher than the kinematic minimum of the variable. The use of aM_{T2} in Ref. [176] was particularly noteworthy as the variable was used as an *upper* limit of 90 GeV that was just 10 GeV greater than the kinematic minimum to differentiate SUSY processes from $t\bar{t}$ processes – the dominant background in this analysis.

---

[4]Assuming the analysis is searching for SUSY

5.2.1. The Use of aM_{T2} as an Upper Bound

A study was performed to determine the utility of aM_{T2} to separate the SUSY processes of the type shown in Figure 5.4 (and similar) from the dominant background process of single lepton direct *stop* searches, $t\bar{t}$. In the decay considered for this study, the *stop* decays to a bottom quark and a neutralino $\tilde{t}_1 \rightarrow b + \ell\nu + \tilde{\chi}_1^0$, via an off-shell *top* quark $(t \rightarrow b + W \rightarrow b + l\nu)$. It is assumed that all of the pair-produced *stops* resulted in one leptonically decaying and one hadronically decaying W. Here, $\tilde{t}_1$ is the lighter of the two *stop* eigenstates. In the *stop* decays considered, one of the masses of the invisible particles is defined to be zero and the mass of the other invisible particle is taken to be equal to that of the undetected W boson. This decay is characterised by final states that have one isolated lepton, at least one b-jet and a large amount of MET Ref. [176], which is consistent with the experimental signature searched for in the rest of this chapter and Chapter 6. The dileptonic $t\bar{t}$ decay has to be considered for events where one lepton is either not identified, outside the detector acceptance, or a hadronically decaying tau-lepton. In each of these cases, the products of the $t\bar{t}$ include two or more high-p_{T} neutrinos which result in elevated MET [177], similar to the experimental signature of the SUSY decay. Hence, the power of aM_{T2} to isolate this decay from the signal events is very much sought after.
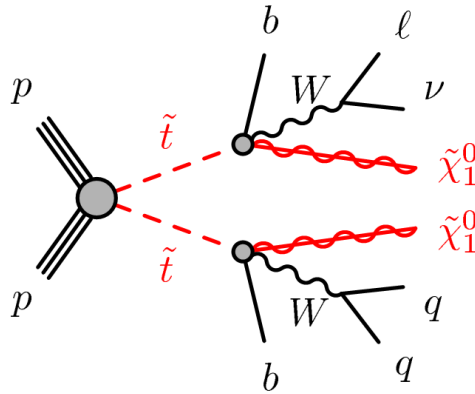
Figure 5.4.: The decay scenario considered in this part of the analysis. In contrast to the decay considered in the next chapter, the intermediary *top* quark will not be on the mass shell so the *stop* will decay directly to the bottom quark, W boson and LSP. In this analysis, the W from one branch is assumed to decay leptonically and the one from the other branch is assumed to decay hadronically, leading to the one-lepton final state. Figure taken from Ref. [176].

There is a degree of flexibility in the implementation of the calculation of aM_{T2}. This stems from the fact that there is a choice in how the b-jets are paired with the visible

lepton to construct the b-jet-lepton system, in both the SUSY decay under consideration and the $t\bar{t}$-decay. This can be seen in Figure 5.5, which takes the slightly simpler example of the dileptonic $t\bar{t}$ decay (compared to the SUSY decay shown in Figure 5.4) to illustrate the visible and invisible inputs to aM_{T2}. In theory, the lepton should always be paired with the b-jet from its own side, in accordance with Equation 5.3, but in reality (and in reconstructed MC) there is no way of knowing which "side" of the decay the lepton, or any particle for that matter, originated from. Therefore, for every event, there is a choice of two values of aM_{T2} that can be used. Figure 5.5 illustrates how a dileptonic $t\bar{t}$ event is considered to choose the inputs to aM_{T2}. The b-jet from one side of the decay and the combined b-jet-lepton system from the other side are selected as the two visible particles. Hence, their transverse (2+1) momenta would be assigned to s_1 and s_2 in Equation 5.3. The two invisible inputs are taken to be the lepton-neutrino system from the upper branch and the neutrino from the lower branch. As the lepton-neutrino system originated from the decay of a W boson, χ_1 is taken to be M_W. The neutrino is assumed to be massless so $\chi_2 = 0$. Therefore, aM_{T2} for the dileptonic $t\bar{t}$ decay will be bounded from below by M_W as it is the lower kinematic end point. The use of aM_{T2} by Ref. [176] to remove the $t\bar{t}$ background hinges on the fact that the vast majority of signal events will exhibit a lower value of aM_{T2} (below 90 GeV) compared to the $t\bar{t}$ events.
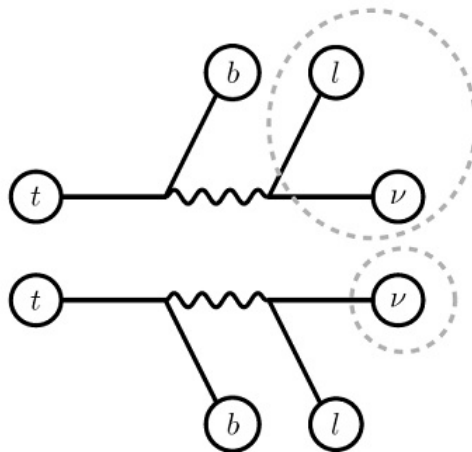
Figure 5.5.: The use of the aM_{T2} variable. The visible objects are considered to be the b-jet from one side of the decay and the b-jet-lepton system from the other side. The dashed circles indicate which particles are considered to be the invisible inputs to aM_{T2}, i.e. the lepton-neutrino system on one side and the neutrino from the other side. Figure taken from Ref. [176].

The requirement that $aM_{\mathrm{T2}} \leq 90$ GeV used in Ref. [176] was determined by considering the aM_{T2} distributions produced by a toy model for the decay shown in Figure 5.4 as well as for a $t\bar{t}$ decay. The aforementioned toy model was produced by generating events using the ROOT[5] class TGenPhaseSpace, a MC generator of n-body events with a constant cross-section or with a Fermi energy dependence [179]. The results are shown in Figure 5.6a. The same distributions were also produced using the TRUTH record to verify the results obtained by the toy model. These distributions are shown in Figure 5.6b. The invariant mass of the system comprising the lepton and the b-jet with which it is paired, m_{bl}, is also plotted for the SUSY and $t\bar{t}$ processes in both Figure 5.6a and Figure 5.6b. aMC@NLO [122] was used to generate the $t\bar{t}$ process, whilst HERWIG++ [180] was used to simulate the SUSY decay (see Chapter 6.3.1 for details of the MC generators). In this figure, as in the remainder of this thesis, $\sqrt{s}$ is used to denote the center-of-mass energy of the pp collisions whilst $\int \mathcal{L}dx$ denotes the total integrated luminosity used. In this analysis, jets and b-jets are ordered by p_{T} unless otherwise stated, so the leading jet corresponds to the highest-p_{T} jet. It should also be noted that b-jets were treated as particles rather than jets in this study.

Several methods of matching b-jets to leptons were reported to have been investigated in Ref. [176], including ΔR matching, but the most effective strategy was to take the minimum of the two values of aM_{T2} yielded for every event. This assumes that the b-jets have first been ordered in terms of their MV2c10 values in order to determine the correct two b-jets to consider.

From Equation 5.3 it can be seen that for a two-sided decay, each side possesses a distinct value of M_{T}. By considering the value of aM_{T2} over all possible events, the minimal value of the variable is found to be equal to the sum of the visible and invisible daughter products from the side of the decay that had the higher value for M_{T}. In the case of a $t\bar{t}$ decay, this occurs on the side which the undetected lepton originated from. Therefore the lower bound on aM_{T2} would be given by the sum of the W-boson and the b-quark masses. The mass of the b (4.2 GeV) can be taken to be negligible compared to the mass of the W boson (80.4 GeV) so aM_{T2} values for $t\bar{t}$ processes are bounded from below by M_W.

One of the main features that should be noted from the M_{T2} distributions in Figure 5.6 is that the majority of the aM_{T2} distributions of the SUSY decay lies below 90 GeV, in the peak, whereas the majority of the $t\bar{t}$ aM_{T2} distribution is found above 90 GeV.

---

[5]ROOT is a C++ based object-orientated framework for large-scale data analysis that was developed at CERN [178]
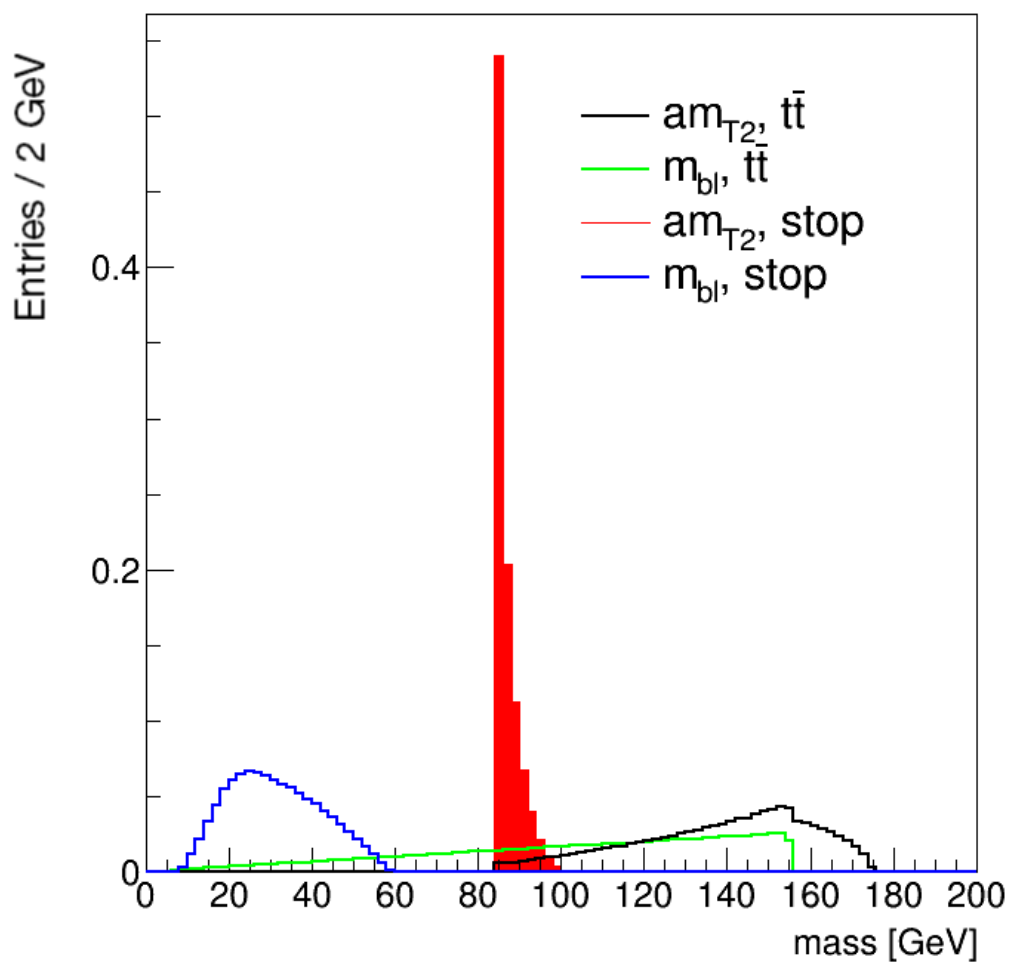
(a) Toy model
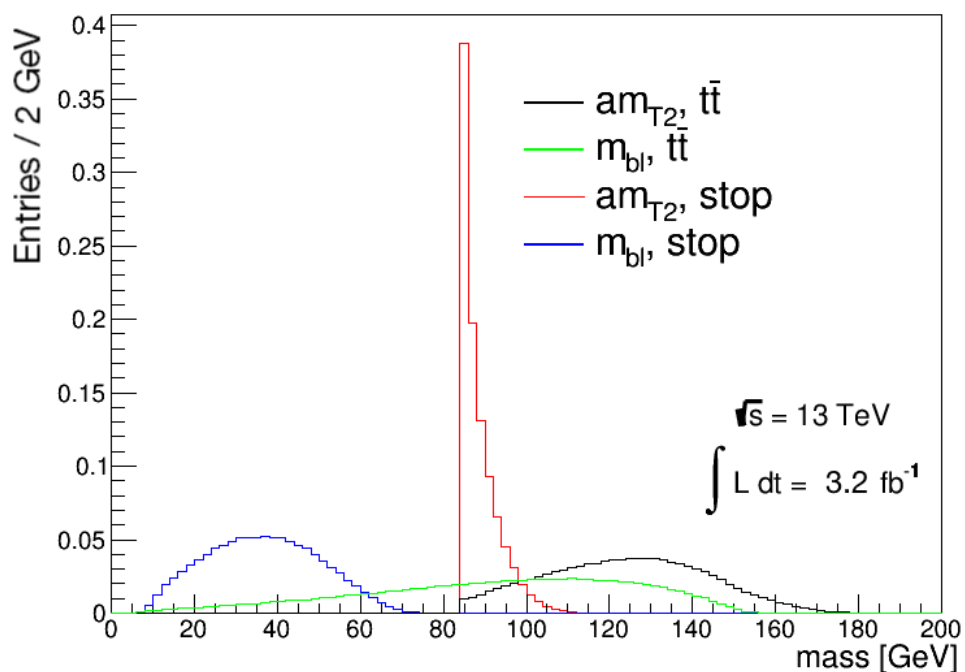
(b) TRUTH MC

Figure 5.6.: Distributions of aM_{T2} and m_{bl} produced using the (a) Toy model and (b) TRUTH MC, for the $t\bar{t}$ process and the SUSY decay given in Figure 5.4.

This is true for both the toy model and TRUTH distributions and provides evidence that employing an upper bound of 90 GeV on aM_{T2} is an effective method of removing $t\bar{t}$ background events from signal events. The other notable feature when comparing Figure 5.6a and Figure 5.6b is that the toy model predicts that the m_{bl} distribution for $t\bar{t}$ should take the triangular form shown whereas the same distribution made by considering the TRUTH record exhibits a much smoother shape. It was found that the discrepancy in the m_{bl} distribution for $t\bar{t}$ between the toy and the TRUTH was a consequence of the toy model not including any spin effects, as shall be explained in the next section.

5.2.2. The Effect of Spin

As mentioned in Chapter 2, the *top* quark has such a short lifetime that it decays before it hadronises and during its decay, it imparts its spin information to its decay products. Consider a leptonically decaying *top* quark: in the rest frame of the W boson, the distribution of the angle between the lepton and the b-quark, θ_{lb}, is given by Ref. [181]:

$$\frac{1}{\Gamma}\frac{d\Gamma}{d(\cos\theta_{lb})} = \frac{3}{4}\frac{m_t^2\sin^2\theta_{lb} + m_W^2(1+\cos\theta_{lb})^2}{m_t^2 + 2m_W^2} \ , \tag{5.4}$$

where Γ is the decay rate of the *top* quark and m_t is its mass.[6]

The distribution of $\cos\theta_{lb}$ was plotted for the toy model (Figure 5.7a) and for the TRUTH MC (Figure 5.7b). Both the toy model and the TRUTH MC boost the final state particles into the rest frame of the original particle, although the events are generated in the rest frame of the centre of mass. This means that the decay of the top quark to the W boson and the b-quark was generated in the centre of mass frame of the event and then boosted into the rest frame of the top. Likewise, the decay of the W boson was also generated in the event centre of mass frame and then boosted into the W boson rest frame. The calculation of these boosts is not shown explicitly, but their consideration accounts for the fact that Equation 5.4 cannot be made to go to zero by any angle of θ_{lb} in contrast with the shape of the distribution Figure 5.7b. The distribution of $\cos\theta_{lb}$ presented in Figure 5.7a can be fitted with a linear function and hence does not bear any resemblance to the distribution given by Equation 5.4 (a quadratic function in $\cos\theta_{lb}$). Therefore only the distribution of $\cos\theta_{lb}$ obtained from the TRUTH MC in Figure 5.7b was fitted with Equation 5.4 in the rest frame of the top, multiplied by a constant whose

---

[6]To produce the results presented below, the mass of the *top* quark obtained by direct measurements, 1.73×10^5 MeV was used.

value was optimised by the fit. This is indicative of the fact that spin effects were only taken into account in the TRUTH MC, not the toy model.
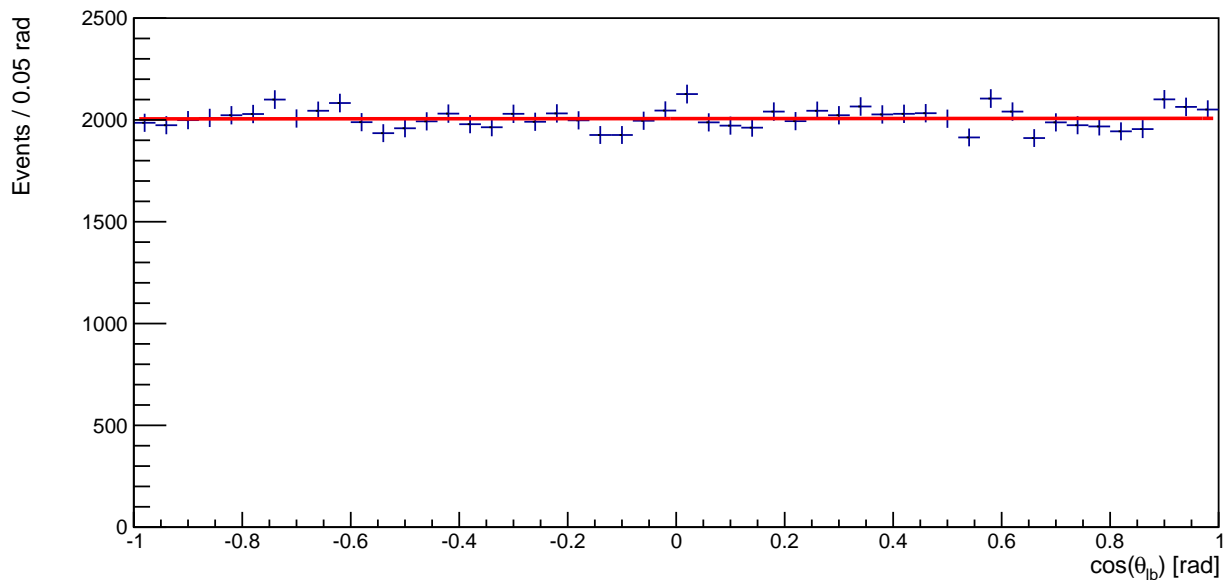
(a) Toy model
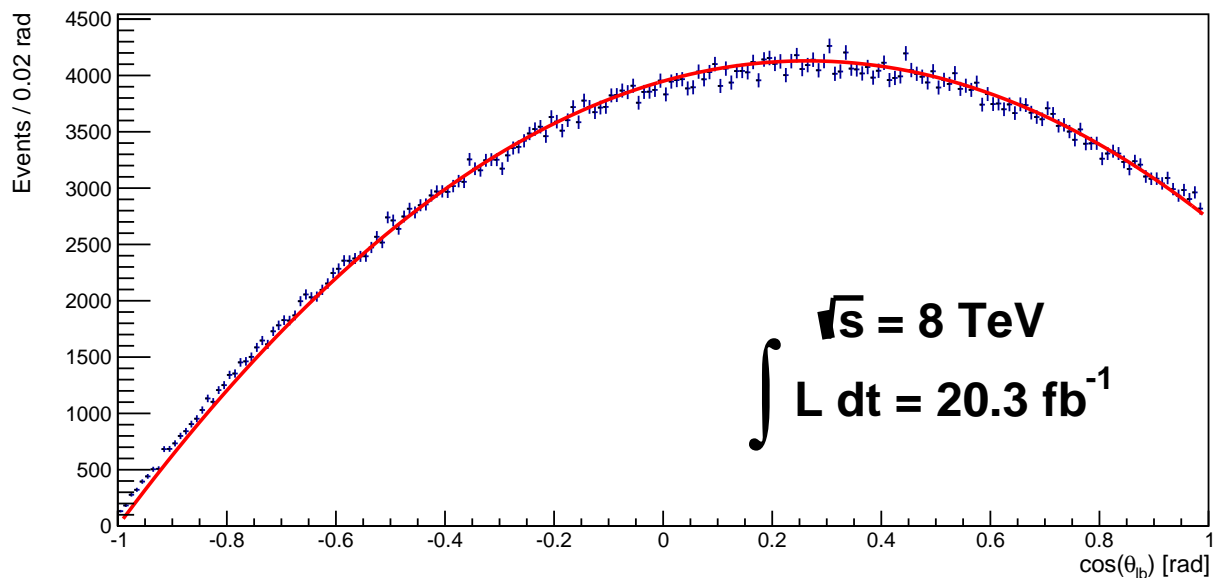
(b) TRUTH MC

Figure 5.7.: Distributions of $\cos\theta_{lb}$ produced using the (a) Toy model and (b) TRUTH MC, for a $t\bar{t}$ decay.

The distribution of $\cos\theta_{lb}$ for the TRUTH MC provides an explanation for the difference in the shape of the $t\bar{t}$ m_{bl} distribution between Figure 5.6a and Figure 5.6b.

It can be seen in Figure 5.7b that the $\cos\theta_{lb}$ distribution is suppressed as $\cos\theta_{lb} \to -1$ ($\theta_{lb} \to \pi$). As θ_{lb} is the angle between the b-jet and the lepton, if $\theta_{lb} = \pi$, the b-jet and the lepton are formed back-to-back and travel away from the decaying *top* quark in opposite directions. It should be remembered that m_{bl} takes the form of a transverse mass, which is given in Equation 5.1, so if there is a suppression of events where the b-jet and the lepton are formed back to back, this is translated into a suppression of events with large transverse masses. Hence, comparing the two m_{bl} distributions in Figure 5.6, it can be seen that events are not concentrated at the higher values of m_{bl} in the TRUTH MC distribution because of the suppression caused by spin effects. If these effects are not included in the toy model, high values of m_{bl} are not suppressed for the $t\bar{t}$ decay, producing the "cliff" in the m_{bl} distribution, which is situated at approximately 155 GeV.

5.2.3. Optimization of aM_{T2} Requirement in Run 2 Analysis

As was shown in Ref. [146], there are a number of event topologies that can give rise to values of aM_{T2} that are close to the kinematic minimum. In particular when the difference between the *stop* mass ($m_{\tilde{t}_1}$) is relatively close to $m_{\tilde{\chi}_1^0}$, (approximately 50 GeV), the aM_{T2} distribution is peaked at the kinematic minimum. To see evidence of this consider Figure 5.8, where the scenario $(m_{\tilde{t}_1}, m_{\tilde{\chi}_1^0}) = (450, 400)$ GeV is compared to a model with a much greater mass splitting of 350 GeV. It can be seen that the aM_{T2} distribution for this model is not peaked at the kinematic minimum. This feature of the aM_{T2} is exploited in the search for compressed *stop* processes presented in the next chapter.
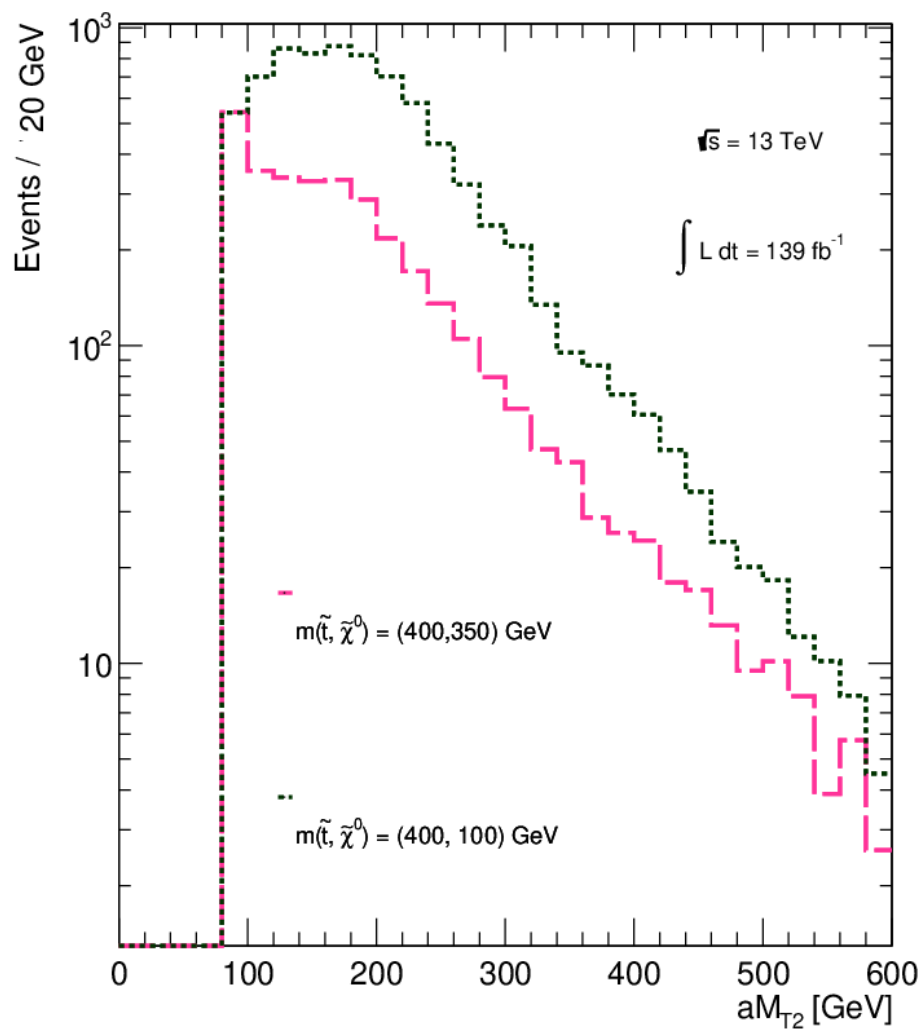
Figure 5.8.: The distribution of aM_{T2} for the decay shown in Figure 6.1 for SUSY mass splittings of $\Delta m(\tilde{t}_1, \tilde{\chi}^0_1) = (400, 350)$ and $(400, 100)$ GeV.

5.3. Secondary Vertices

The b-jets which are included in the final state of the processes focused on in this thesis have low p_T due to the fact that the SUSY spectrum is compressed. It was explained, in Section 3.7.4, that there is a lower limit of 20 GeV on the p_T on jets which the ATLAS calorimeter is able to precisely reconstruct and as Figure 5.9 shows, a large proportion of the p_T spectrum of b hadrons from compressed SUSY processes lies below this 20 GeV threshold[7]. Moreover, the p_T spectrum shows that as the mass splitting decreases, the p_T of the b hadrons also decreases because less energy is imparted to the decay products. Therefore, the lower the mass splitting of the decay, the less likely it is that the calorimeter will be able detect b-jets in its final state.

Soft b-tagging techniques extend the detector's capability to identify b-jets to below 20 GeV. Therefore the extent to which it was possible to make use of information from soft b-tagging algorithms was investigated with the hope of incorporating the technique into the search for compressed SUSY processes. Considering the final states of the signal and background processes, a proportion of the events which are reported to not contain b-jets, may instead contain b-jets that are not detected through traditional b-tagging techniques, such as those discussed in Section 3.7.4. It was therefore thought that soft b-tagging techniques would be specifically targeted at those events with a reported b-jet multiplicity of zero. In this section, the use of the word "jets" is taken to mean light flavoured jets, i.e. those originating form a *up*-quark, *down*-quark or *strange*-quark as opposed to originating from a *charm*-quark or a *bottom*-quark (heavy flavour quarks).

---

[7]Figure 5.9 shows a suppression of events in the $\Delta m(\tilde{t_1}, \tilde{\chi}_1^0) = (450, 443)$ GeV scenario as, prior to the application of pre-selection requirements (given in Section 6.4), a requirement of MET > 50 GeV was present to suppress SM backgrounds.
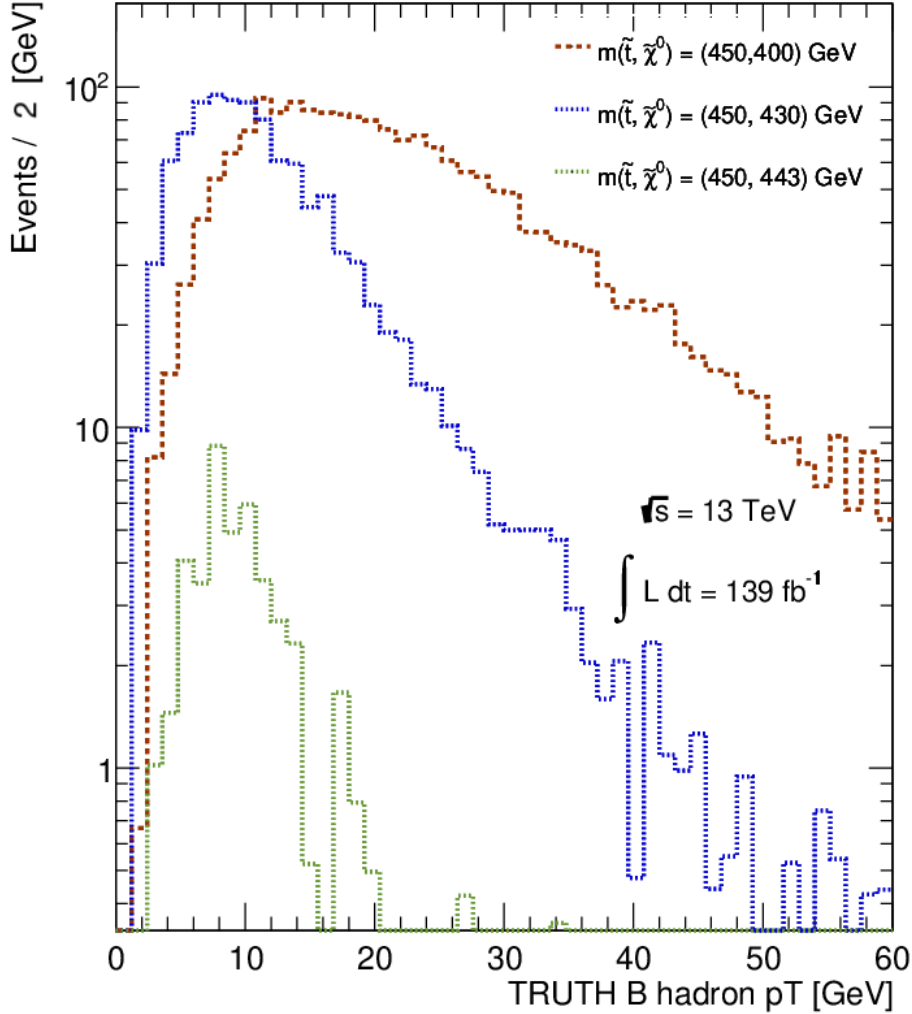
Figure 5.9.: TRUTH p_T distributions of b hadrons in *stop* processes where the *stop* mass is 450 GeV and the mass splitting is 7 GeV, 20 GeV or 50 GeV.

As explained in Section 3.7.4, the secondary vertexing algorithm identifies SVs that could be associated with any physics object, not just b-jets. Therefore, if the algorithm is to be used to identify soft b-jets, an initial consideration is to determine what proportion of SVs are associated with b-jets. In order to validate overlap removal developed in [124] (outlined in Section 3.7.6) for use in this analysis, the geometric distance ΔR (as defined in Chapter 3) between each of the SVs in an event and the physics objects b-jets, jets and leptons are shown in Figure 5.10a, Figure 5.10b and Figure 5.10c. Figure 5.10a shows that it is approximately a hundred times more likely for a b-jet than a lepton to be within $\Delta R < 0.4$ of a SV. It also shows that b-jets are approximately ten times more likely to be within $\Delta R < 0.4$ rad of a SV than jets. Therefore, one can proceed with some confidence that SVs are more likely to be associated with b-jets then with other physics objects such as light flavour jets or leptons.

(a)

(b)

(c)
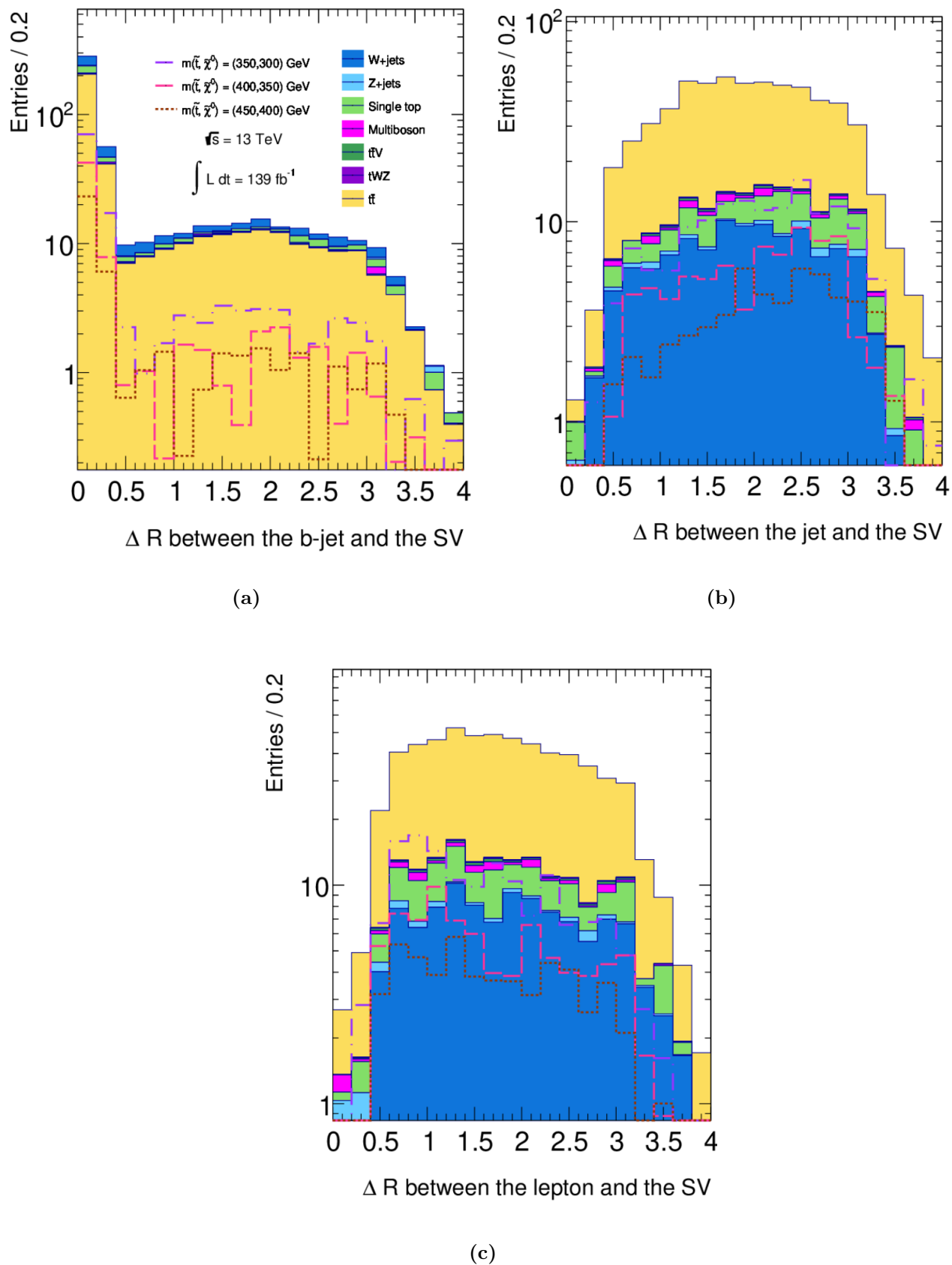
Figure 5.10.: Geometric distance ΔR between SVs and (a) b-jets, (b) jets and (c) leptons.

(a)

(b)

(c)

(d)
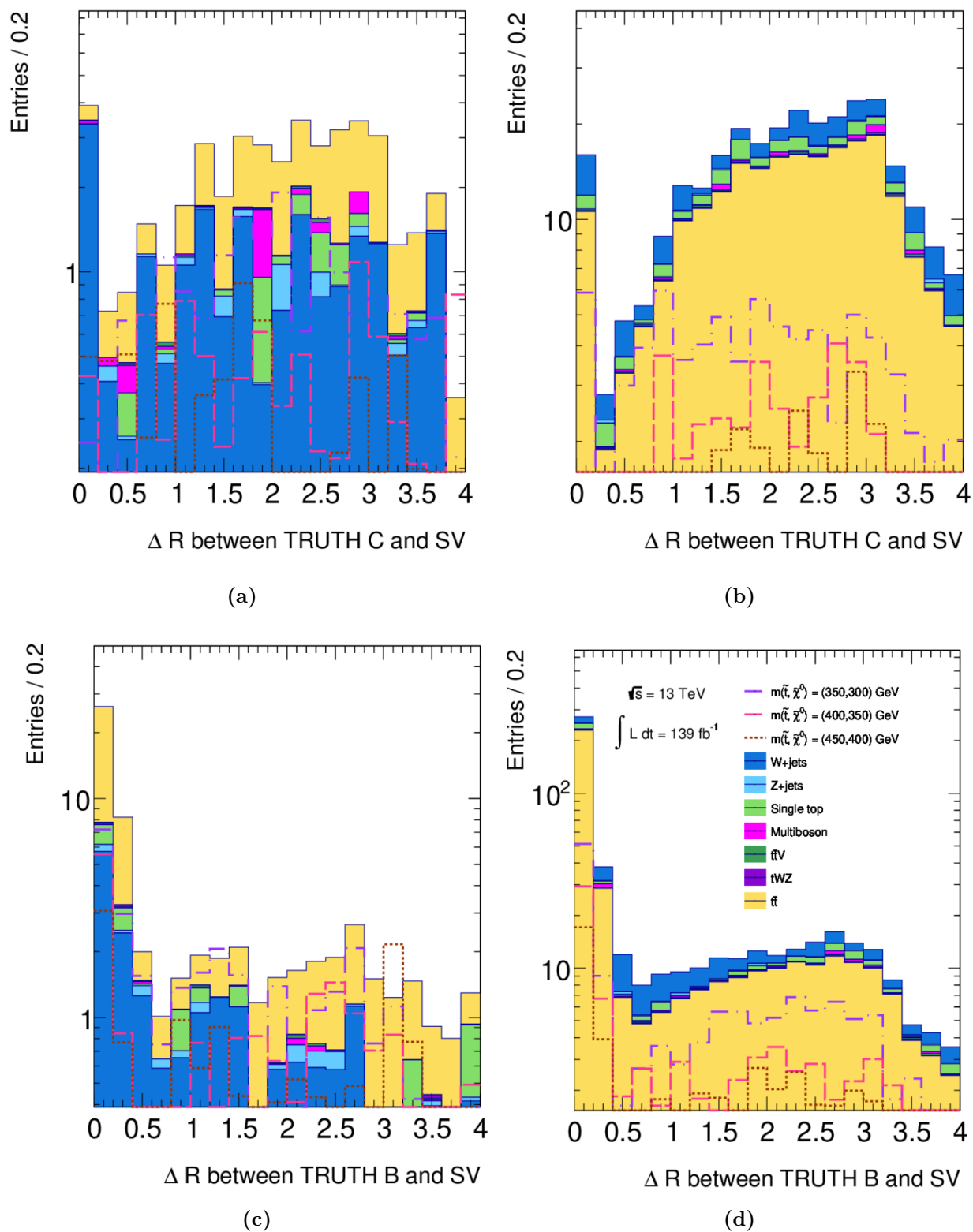
Figure 5.11.: Geometric distance ΔR between SVs and (a) c hadrons, (b) c hadrons, (c) b hadrons and (d) b hadrons. (a) and (c) assume that the events had 0 b-tagged jets while (b) and (d) assume 1 b-tagged jet.

However, it should be verified that SVs are originating from *b*-jets rather than *c*-jets by using the TRUTH record to investigate the proximity of secondary vertices to *c* hadrons. Instead, for each SV, the distance ΔR between each b and *c* hadrons in the TRUTH record for that event is studied. In Figure 5.11 ΔR between b and c hadrons and SVs were plotted both for events that have no b-tagged jets and for events that have one or more b-tagged jets. One of the first things to note about these plots is the difference in an order of magnitude of the scales on the *y*-axis. This indicates that there are approximately ten times fewer TRUTH *c* hadrons expected in this region of phase space compared to TRUTH *b* hadrons. Of the *c* hadrons that are recorded in the TRUTH record, although a small number of them are reported to lie close to a SV, the majority of them are shown to have a large value of ΔR with respect to SVs, as shown in Figure 5.11a and Figure 5.11b This is in contrast to the equivalent distribution for *b* hadrons are shown in Figure 5.11c and Figure 5.11d, where the majority of TRUTH *b* hadrons are shown to align with secondary vertices. Finally confirmation of the close alignment of the SVs of *b* hadrons rather than *c* hadrons can be seen very easily by considering Figure 5.12 and Figure 5.13. Here, the ΔR between each SV and b and *c* hadrons, both for events with zero b-tagged jets and one or more b-tagged jets are shown plotted on a 2D plane for $t\bar{t}$ events, W+jet events and events of two of the signal models. It can be seen that it is most common for a SV to have a very small separation from the *b* hadron for types of events shown, whereas the separation between SVs and *c* hadrons is much more varied.

The types of physics objects that can be found in close proximity to a SV is summarised by considering Figure 5.14a. This plot shows the identity of objects that are within ΔR < 0.4 rad of the SV. It can be seen that the object is approximately ten times more likely to be a *b*-jet than a jet and approximately a hundred times more likely to be a muon or an electron confirming the results shown in Figure 5.10.

Now that it has been established that the presence of a SV more than likely indicates the presence of a *b*-jet, the possibility of using SV algorithms to increase sensitivity for events where traditional *b*-tagging techniques have failed to detect any of the *b*-jets in the event, can be evaluated. This can be conducted by placing events in the following categories by considering the recorded topology of their final states:

1. 0 *b*-jets, 0 SVs: events have no b-tagged jets and no recorded SVs. These events are unlikely to be useful for the analysis as SVs can not be used to detect the existence of *b*-jets.
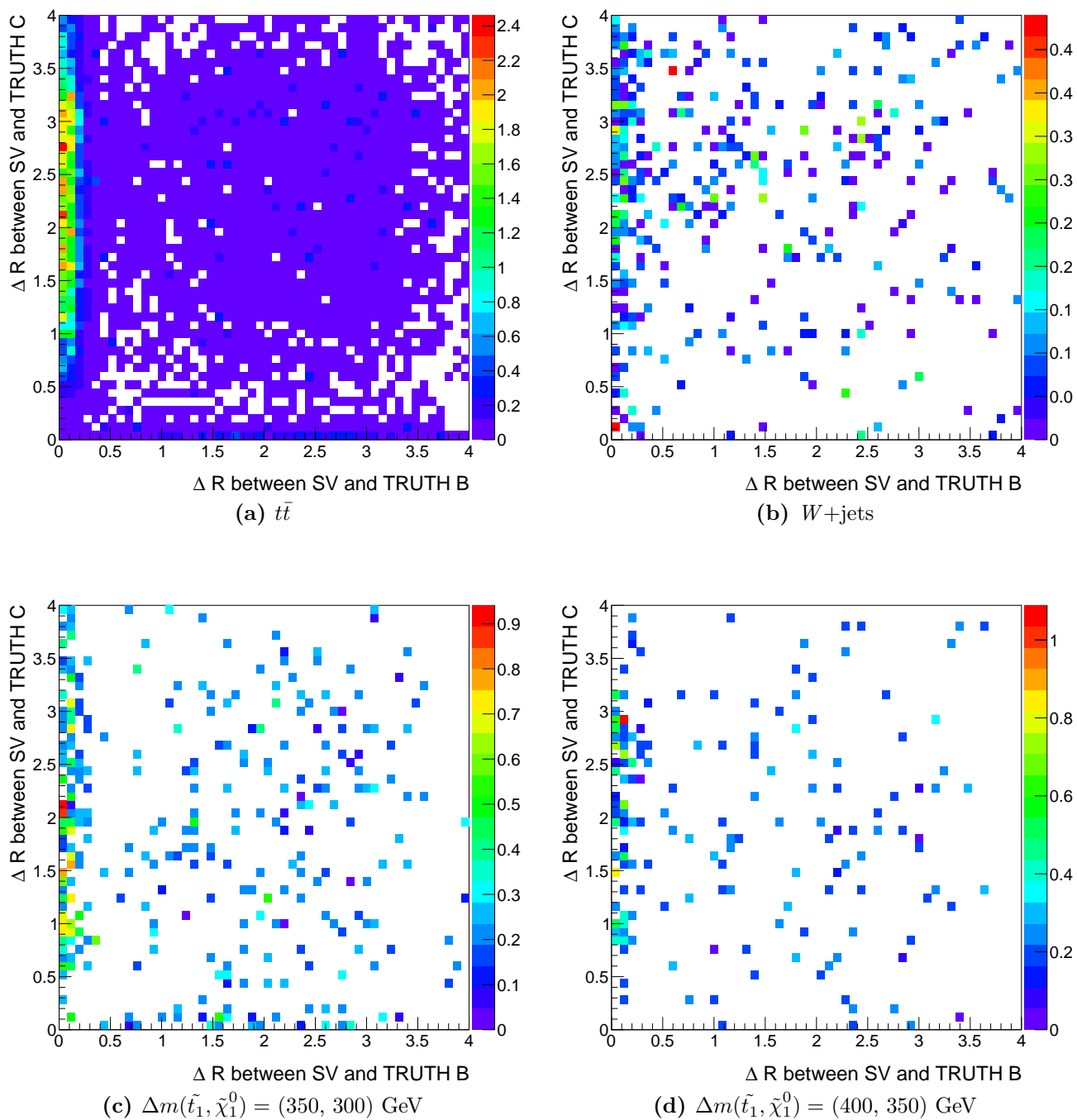
Figure 5.12.: ΔR between secondary vertices and TRUTH B hadrons vs. ΔR between secondary vertices and TRUTH C hadrons when the events have one or more b-tagged jets. MC simulation assumes $\sqrt{s} = 13$ TeV and $\int \mathcal{L}dt = 139$ fb^{-1}
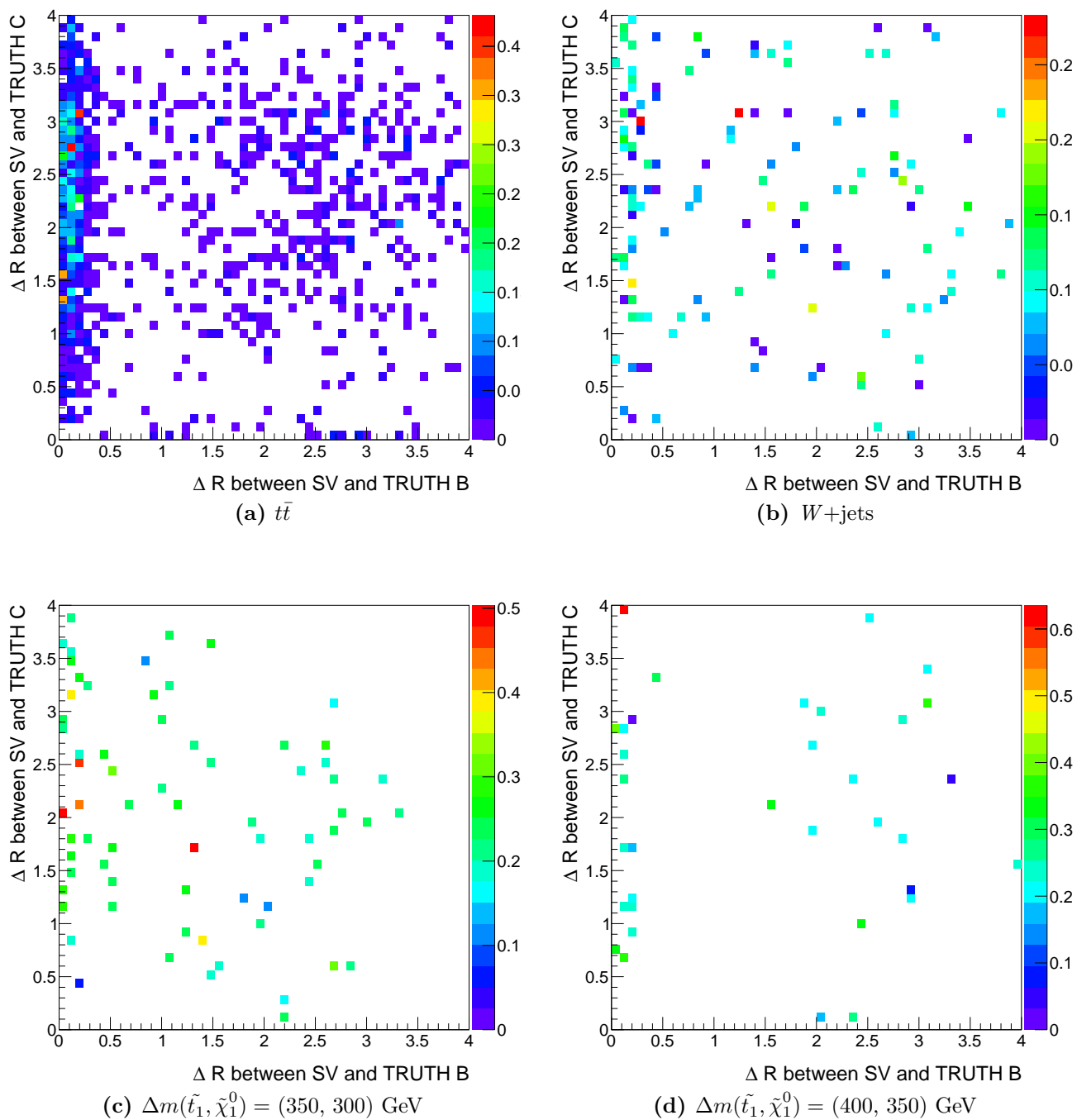
(a) $t\bar{t}$

(b) W+jets

(c) $\Delta m(\tilde{t}_1, \tilde{\chi}_1^0) = (350, 300)$ GeV

(d) $\Delta m(\tilde{t}_1, \tilde{\chi}_1^0) = (400, 350)$ GeV

Figure 5.13.: ΔR between secondary vertices and TRUTH B hadrons vs. ΔR between secondary vertices and TRUTH C hadrons when the events have no b-tagged jets. MC simulation assumes $\sqrt{s} = 13$ TeV and $\int \mathcal{L}dt = 139$ fb^{-1}.
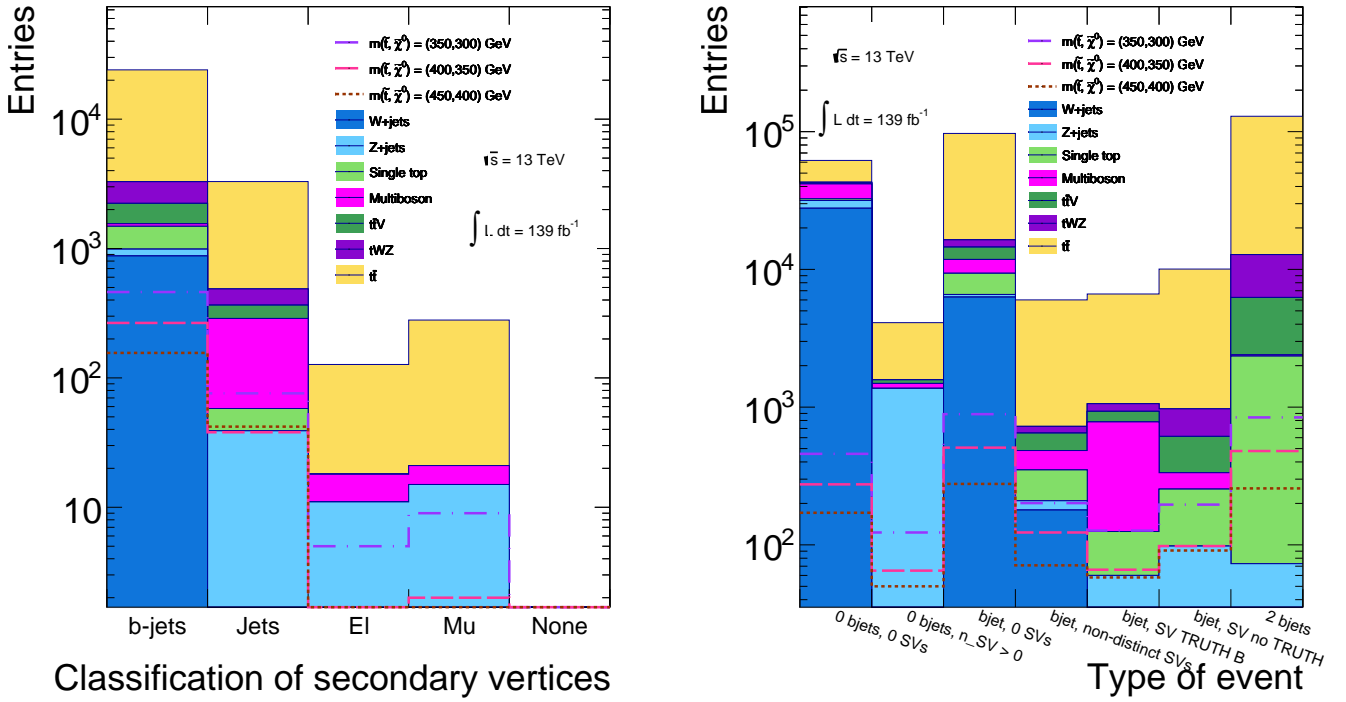
(a) Classification of the types of particles found within a radius of $\Delta R = 0.4$ of each SV

(b) Topology of events in terms of b-jet multiplicity, SV multiplicity and the proximity of each SV to a TRUTH b hadron

Figure 5.14.: Investigations of the types of physics objects found within $\Delta R = 0.4$ of an SV.

2. 0 b-jets, > 0 SVs: These are the events that could be detected, if it was found that SV information could supplement other b-tagging techniques. The types of objects that are associated with SVs in this type of event is shown in Figure 5.13.

3. 1 b-jet, 0 SVs: These events already have a b tagged jet and there are no SVs to examine.

4. 1 b-jet, > 0 SVs This class of event is broken down into three categories. TRUTH information is used here to examine which events fall into each category.

   - 1 b-jet where the only SVs found are within $\Delta R = 0.4$ of the b-jet: This means that the SV was probably caused by the b-jet and so recording it doesn't give additional information to the analysis.

   - 1 b-jet where a SV is found that is further than $\Delta R = 0.4$ rad from the b-jet: In this case TRUTH information is used to determine if:

     – The SV is within $\Delta R = 0.4$ of a b hadron and hence is probably associated with it

    – The SV is further than $\Delta R = 0.4$ from a b hadron and hence was probably associated with a jet or lepton.

5. 2 b-jets : b-tagging has identified both b-jets that are associated with the event and hence it is not necessary to fall back on soft b-tagging.

The result of breaking down events in the way described above is displayed in Figure 5.14b[8]. It should be noted that the area of this histogram has no relationship with the normalised number of events as this histogram is not normalised and the categories are not mutually exclusive. In fact, if one were to use TRUTH information to *stop* the algorithm when a distinct SV close to a b hadron was found, this would make the results meaningless because in reality the TRUTH information obviously cannot be used in the search. Hence the presence of every SV must be recorded in this plot, which will mean that events will naturally be double counted if they contain multiple SVs. Also, given the results shown in Figure 5.11 to Figure 5.13, information about the proximity of SVs to c-quarks was not included in Figure 5.14 for the sake of clarity.

It can be seen that the majority of events do not contain SVs (or contain two b-jets in which case the number of SVs is not recorded). As would be expected given the final state of a $t\bar{t}$ process, the two b-jets bin is dominated by $t\bar{t}$ events. Attention should be focused on the fourth, fifth and sixth bins where events with one b-jet and one or more SVs are considered. It can be seen that this category of events is also dominated by $t\bar{t}$ and out of those events, an approximately equal number of instances are recorded where the SV is not distinct from the b-jet or it is distinct and close to where the TRUTH record would indicate a b hadron would lie. The sixth bin indicates secondary vertices that are not associated with a b-jet or a b hadron. However, as the sum of the number of incidents where an SV is non distinct from a b-jet or in close proximity to a TRUTH b hadron is greater than the instances where the SV is not associated with a b hadron, it can be concluded that SVs are more likely to be associated with b-jets than with other physics objects such as leptons or jets. From the investigation of the nature of SVs presented here it can be concluded that soft b-tagging techniques have potential to enhance the scope of a search for compressed *stop* processes. Therefore, the development of an analysis that uses SV information is documented in the analysis presented in the next chapter.

---

[8]Figure 5.14 could have been extended to include subcategories for events with 0 b-jets and > 0 SVs. However such an extension would possibly decrease the interpretability of Figure 5.14 and duplicate the information shown in Figure 5.13 without enhancing clarity.

5.4. Conclusions

This chapter places the analysis presented in Chapter 6 in context in terms of the phenomenology of stop processes as well as previous searches which have attempted to find evidence of *stops*. It also introduces the underlying tools and concepts that are used in this analysis, in terms of one of the main discriminatory variables, aM_{T2}, and the use of SV information.

It was explained that one of the motivating factors for constructing kinematic variables is that any attempt to make measurements involving the longitudinal component of the momenta of the invisible decay products in a collider such as the LHC is subject to a great amount of uncertainty, and hence it was seen that discriminatory variables used in SUSY analyses are commonly constructed in the transverse plane. Indeed, this is a case for the M_{T2} variable, which was specifically designed to measure the mass of pair-produced particles in hadron colliders and hence is particularly useful in searches for the *stop*-quark. It was seen that, due to its definition, M_{T2} is typically used as a lower limit on the mass of a SUSY particle. The validity of using the variable as an upper limit was examined and the variable was found to be effective in this capacity, assuming *stop* processes of the form $\tilde{t}_1 \to b + \ell\nu + \tilde{\chi}_1^0$. The motivation to use M_{T2} in this way was based on the predictions of a toy model which showed that the majority of events containing the *stop* process satisfy $aM_{\text{T2}} < 90$ GeV. The toy model was used to plot distributions of aM_{T2} and M_{T} for the *stop* process and its dominant background, $t\bar{t}$, and these were compared to the equivalent distributions produced by MC generators operating at TRUTH level. There was found to be a discrepancy between the M_{T} distribution produced by the toy model and those produced by the MC. This discrepancy was explained by the fact that the toy model omitted the effect of the spin of the top quark, as was ascertained by analysing the angular distribution of the b-jet and the lepton from the process. It was also shown that the distributions of aM_{T2} in *stop* processes are greatly dependant on the mass difference between $m_{\tilde{t}_1}$ and $m_{\tilde{\chi}_1^0}$. This feature of the variable shall be explored further in the search for BSM presented in the following chapter.

This thesis focuses particularly on *stop* processes where the SUSY mass spectrum is compressed and hence b-jets are produced which have a low-p_{T} – rendering them too soft to be detected by the normal b-tagging techniques. A soft-b-tagging algorithm, employing SV information, has been proposed as a method of detecting these low p_{T} b-jets. The potential of using SV information in this way was evaluated by determining which objects SVs are most closely aligned to and hence were produced by. Not only was

it found that SVs are more closely aligned with b-jets than jets or leptons, by examining the TRUTH record, it was found that SVs are much more likely to be found close to b hadrons than c hadrons. Hence, SV information, alongside aM_{T2}, is another tool with which compressed SUSY processes are hunted for in the analysis presented in the next chapter.

Chapter 6.

Searching for Compressed SUSY

"I would rather have questions that can't be answered than answers that can't be questioned"

— Richard Feynman

In this chapter, the innovative technique of using aM_{T2} as an upper bound to separate signal events from background and the use of SV information to identify soft b-jets, are combined in a search for compressed *stop* decays. It is explained how specific regions of parameter space can be designated to search for evidence of deviations from the SM in the data collected from the LHC, whilst others are designed to provide estimates of the SM background and to quantify the uncertainties in the measurement of the events in the former regions. The design of the analysis must be conducted whilst being blinded to the LHC data as to eliminate possible biases. The analysis was performed using 139 fb^{-1} of ATLAS data, building on investigations of which kinematic variables were most effective at searching for SUSY in the compressed area of parameter space in a feasibility study using 36.1 fb^{-1} of ATLAS data. Finally, it is shown that, given the absence of any significant deviations from the SM predictions, this analysis confirms that the SUSY simplified models can be excluded from certain areas of parameter space.

6.1. Motivation for This Search

This analysis focuses specifically on SUSY models that have a compressed SUSY mass spectrum. If $\Delta m(\tilde{t}_1, \tilde{\chi}_1^0)$ is just 50 GeV, the decay of the *stop* has little additional

energy to give momenta to its daughter products. Therefore, soft (low-p_T) final state objects are produced with lower MET. The softness of the decay products make this an experimentally difficult region to perform a search for BSM. However, the lack of momentum given to the $\tilde{\chi}_1^0$ can be taken advantage of when searching for decays in this region. In these decays, the $\tilde{\chi}_1^0$ gain their momentum by recoiling from ISR jets. Given such a low-p_T regime, signal events can be distinguished from SM background events if a high-p_T jet boosts the di-*stop* system and enhances the MET while the visible decay products remain soft. Three SUSY benchmark points, $(m_{\tilde{t}_1}, m_{\tilde{\chi}_1^0}) = (450, 400)$, (400, 350) and (350, 300) GeV are used to optimize the analysis. This search was initially conceived with only 36.1 fb^{-1} of LHC data, at which point there was poor sensitivity to the $\tilde{t}_1 \to bff' + \tilde{\chi}_1^0$ decay with compressed SUSY mass spectra. The Feynman diagram for this process is shown in Figure 6.1. These benchmark points were a sample of the range of *stop* masses in the area of low sensitivity and in the middle of the range of mass splittings analysed in this thesis. From Table 6.1 it can be seen that the NLO cross sections are inversely proportional to $m_{\tilde{t}_1}$.

SUSY scenario	Cross section
$(m_{\tilde{t}_1}, m_{\tilde{\chi}_1^0}) = (350, 300)$ GeV	3.79 pb
$(m_{\tilde{t}_1}, m_{\tilde{\chi}_1^0}) = (400, 350)$ GeV	1.84 pb
$(m_{\tilde{t}_1}, m_{\tilde{\chi}_1^0}) = (450, 400)$ GeV	0.94 pb

Table 6.1.: The NLO cross sections for the decay in Figure 6.1 of the SUSY scenarios considered in this analysis, taken from Ref. [182].

In a previous iteration of the analysis detailed in Ref. [52], this region of SUSY parameter space has been targeted specifically, constructing a branch of the analysis tailored to searching for events where the MET has been enhanced by high-p_T ISR jets. The research effort towards this analysis was then used as a feasibility study to assist with implementing the search with the full Run 2 dataset, as explained in Section 6.5. Meanwhile, in the most recent iteration, Ref. [114], soft b-tagging is used to target *stop* decays with mass splittings approximately equal to the acceptance limit in p_T of the calorimeter, and is based around the discriminatory power of the ratio of lepton p_T to MET. *Stop* decays with mass splittings > 20 GeV are differentiated from background decays using the variable C_{T2} (defined as $\min(p_T^{\mathrm{miss}}, p_T(\mathrm{ISR}))$, for further details see Ref. [183]). Neither the ratio of the lepton p_T to MET nor C_{T2} are used in this analysis.

Instead, this analysis employs the discriminatory power of the aM_{T2} variable in an unconventional use case, as demonstrated in Section 5.2.1, as well as other kinematic variables with high discriminatory power such as H_{T} significance. Moreover, the current analysis proposes Signal Regions (SRs) targeting decays with and without a b-tagged jet, constructed with the same set of kinematic variables allowing for increased ease of physical interpretation. This analysis is also emphatically distinct from that in Ref. [114] because the presence of an ISR jet, and hence enhanced MET, is not relied upon to search for the decay.
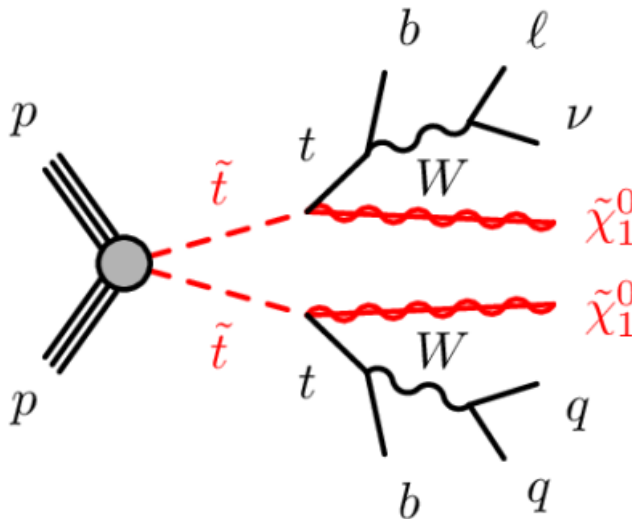
Figure 6.1.: Feynman diagram of the SUSY decay scenario considered for the main analysis presented in this thesis. The *stop* decays to a *top* and a lightest neutralino because $\Delta m(\tilde{t}_1, \tilde{\chi}_1^0) < m_W + m_b$ as explained in Section 2.4.

6.2. Analysis Strategy

As was discussed in Chapter 2, despite the huge success of the SM at explaining the behaviour of observed particle phenomena, there is much evidence that the model is not yet complete. Hence when a search for BSM is performed, there are two possible outcomes; the data is either consistent or inconsistent with the SM. If the data is found to be inconsistent with the SM, it then needs to be determined whether there is a BSM model that provides a good description of the data or if the SM needs to be revised. To determine which outcome is supported by the experiment, one performs a hypothesis test, a statistical tool for drawing conclusions based on acquired sets of measurements [76]. In

a hypothesis test one starts with a null hypothesis, H_0, which is considered to be true by default and in the case of a BSM analysis is taken to be the SM. This is tested against the alternative hypothesis, H_1, which in this context, is a model that includes both the SM and the BSM model under consideration [184]. The p-value quantifies how often an experiment would result in an outcome that was at least as far away from the result predicted by the H_0 as the measured outcome of the experiment [76].

SUSY cannot be described by a single model. Thus to search the parameter space available for SUSY, analyses are divided, within the ATLAS and CMS collaborations at least, into searches that are categorised by the final states of the process under consideration. This thesis focuses on the search for SUSY processes where the final state includes one isolated lepton. Within any SUSY search, regardless of the final state under consideration, the phase space can be further divided into SRs in order to search for a particular process. A SR (in this analysis) is defined by applying selections to a set of kinematic observables such that, in the resulting region, a significant excess of signal events compared to background events is predicted by the theoretical model employed; the SR is said to be enriched with signal events [185].

In order to estimate the SM background in the SRs, reducing the dependence on MC, it is normal to define control regions - regions of parameter space where the normalisation of the dominant background(s) can be controlled by comparison to the data. The requirements on the kinematic variables that define the Control Regions (CRs) are selected to identify a region of phase space where the purity of the considered background is high and the number of signal events is minimised. The purity of a CR is calculated as the percentage of the total number of SM events that the background process under consideration accounts for. It is common to design a CR for each of the most dominant SM backgrounds, so in this analysis CRs are designed for $t\bar{t}$ and W+jets - the Top Control Region (TCR) and the W+jets Control Region (WCR). In this way the MC predictions of the SM backgrounds in the SRs can be constrained. CRs must be *disjoint* or *orthogonal* from SRs. This is commonly achieved by reversing the cut on one or more of the variables that define the SRs. SRs are designed to search for deviations from the SM in areas of parameter space that have not yet been excluded, which typically have very low statistics. A compromise must be struck between defining CRs that are close enough to the SRs to reduce experimental systematic uncertainties but separated enough to reduce statistical uncertainties.

In order to check or *validate* the model used to predict the number of background events in the SRs it is typical to define one or more Validation Regions (VRs) and analyse

the data/MC agreement in these regions. In this analysis, a Top Validation Region (TVR) and a W+jets Validation Region (WVR) are used. VRs are commonly placed between the SRs and the CRs, in the phase space of the observables that define the distinctions between the regions. Therefore the positioning of the VRs is often a compromise between maximising the yield of the VR and minimising the signal contamination, whilst controlling the assumptions implicit in the extrapolation for the SRs and CRs. A general schematic representation of an analysis strategy using multiple SRs, CRs and VRs is shown in Figure 6.2[1].
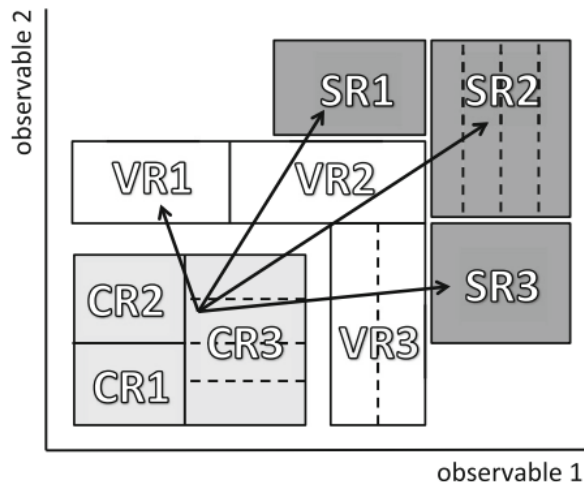
Figure 6.2.: A schematic representation of an analysis strategy that uses multiple SRs, CRs and VRs. The dashed lines indicate the binning in observable 1, 2. Extrapolation from the CRs to the SRs is validated by the VRs, which normally lie between the CRs and SRs in terms of the phase space of observable 1, 2. Figure taken from Ref. [185]

A so-called "cut-and-count" technique is used to identify the optimal values of the requirements on the kinematic variables determined in the analysis presented in this thesis, a technique which is often employed in BSM searches. The main advantage of analysis strategies based on kinematic considerations is that they make relatively few assumptions about the details of the BSM model under investigation and hence can be an effective step towards understanding scenarios that have not been considered in detail [186]. The two factors that were considered when optimizing the kinematic requirements were the signal yields compared to the background yields produced by a particular set of requirements, and the significance of the signal. The significance of an SR is calculated by obtaining the $\mathcal{Z}$-value, which can be written in terms of the p-value.

---

[1]A schematic representation of the the regions specific to the analysis presented in this thesis is shown in Figure 6.8.

The relationship between the $\mathcal{Z}$-value and the p-value is given as [187]:

$$\mathcal{Z} = \Phi^{-1}(1 - p) , \tag{6.1}$$

where Φ^{-1} is the inverse cumulative distribution function of a unit Gaussian. In the context of particle physics, an alternative hypothesis can be taken to be excluded if $\mathcal{Z} \geq 1.64$ and the threshold of discovery that the alternative hypothesis is correct is $\mathcal{Z} \geq 5$. For the analysis presented here the RooStats toolkit [188] is employed (specifically the BinomialExpZ distribution with an uncertainty of 30% assumed) for the calculation of the $\mathcal{Z}$-value.

The size of the MC data sets used in this analysis, given in Section 6.3, dictates that the workflow must utilise a batch system to keep running times on a practical scale of hours rather than days or weeks. With this in mind, the computational task-management tool GANGA [189, 190] was employed. Central to the functioning of GANGA is the concept of a *job*, which is a full description of the computational task used to run the analysis: including the code for execution; the input MC or data to be processed; the outputted results; the specification of the required processing environment; the post-processing tasks; and the metadata needed for book-keeping [189]. GANGA's book-keeping abilities, in particular, make it ideally suited for facilitating this analysis as they enable the jobs created during the process of identifying the optimum values for the requirements defining the SRs, CRs and VRs to be automatically catalogued. These requirements were found by systematically changing the value of one kinematic variable at a time, thus using GANGA's book-keeping abilities to their full extent by allocating one job to each combination. The bespoke software written by the author specifically for this analysis was run by GANGA as an executable, to make the entire process, from selecting the values of the requirements to processing the input MC datasets to producing the plots and yield tables presented in this chapter, highly automated and efficient. This is in contrast with the typical use case of GANGA within ATLAS in conjunction with the ATHENA framework, as well as providing an interface for analysers to collaborate and exchange jobs.

6.3. Monte Carlo samples

6.3.1. Monte Carlo Event Generators

At the core of the event simulation of most LHC processes is the simulation of subprocesses with large momentum transfer. This requires the calculation of the cross section of the hard scattering process between the two incoming partons, which can be computed using collinear factorisation. Factorisation is the mathematical tool that allows the description of a process to be separated into different regimes depending on the scales of the momentum transfer involved and is employed by most MC generators [191].

The energy scale of the hard scattering process is between 100 GeV and several TeV whilst the hadron scale is approximately 1 GeV. This energy difference leaves a large phase space for parton showers to develop in both the initial and final states [192]. Whilst the perturbative short distance physics of a hard scattering process can be described at a first order this is not possible for the long distance. non-perturbative QCD effects required to describe the parton showers and hence a parton shower algorithm must be used to accomplish this. Parton shower algorithms describe the non-perturbative QCD effects that are not included in the matrix element calculations for the hard scattering process. As described in Section 2.1, the confinement property of QCD implies that the fragmentation of quarks in high energy collisions will result in jets. The modelling of this hadronisation step is based on phenomenological models, which fall into two classes; string models and cluster models [191]. Finally, additional soft hadronic activity resulting from multiple proton interaction, called pileup, is included in the MC event generation by overlaying the simulated event with general *pp* collisions [192]. Below, the MC generators that are most relevant to this thesis are introduced and details of their implementation are given in Section 6.3.2.

POWHEG The POWHEG BOX is a computational framework that combines NLO calculations with the description of showering in MC event generators. This is necessary because other MC generators for showering do not have NLO accuracy, important when a precision measurement is to be made such as refinements to the accuracy to which physical parameters of the *top* quark are known [193].

PYTHIA 8 is a general purpose event generator with libraries whose capabilities include the modelling of hard processes, initial- and final- state parton showers, multi-parton interactions and particle decays [194].

HERWIG++ is a general purpose event generator with a special emphasis on the accurate generation of QCD radiation [180, 191].

SHERPA Simulation of High-Energy Reactions of PArticles (SHERPA) is also a general purpose generator with very flexible tree-level matrix-element generator for the calculation of hard scattering processes within the SM and various BSM models [195].

aMC@NLO [122] is a package, based on the HERWIG++ generator, that allows the incorporation of NLO QCD matrix elements consistently into a framework for parton showering in order to calculate hard processes at NLO.

MADGRAPH [196] is a leading order matrix generator which has been extended to permit the inclusion of loop diagrams [197].

6.3.2. Samples Used in this Analysis

When searching for SUSY decays, or indeed any decay from a BSM model, the background events are from SM processes. The dominant SM processes for the decay shown in Figure 6.1 are $t\bar{t}$, W+jets, Z+jets, multiboson, $t\bar{t}$W, $t\bar{t}$Z, tWZ and single-top. Representative Feynman diagrams for each process are shown in Figure 6.3. It can be seen that each of the processes results in the final state involving at least one lepton, energetic jet(s) and MET, like the SUSY decay under consideration. Events that do not contain exactly one lepton in their final state are vetoed. For these SM processes, the MET is constituted by the undetected neutrino, as well as any leptons additional to one lepton required for this analysis. It is assumed that any additional leptons will be vetoed.

Signal samples were generated with MADGRAPH interfaced with PYTHIA 6 for parton showering and hadronisation. Meanwhile, the $t\bar{t}$ and single-top samples were generated with POWHEG interfaced with PYTHIA 6, again for parton showering and hadronisation, the Z+jets and W+jets by SHERPA 2.2.1. Meanwhile the alternative $t\bar{t}$ samples used to calculate the theoretical uncertainties were generated with either POWHEG interfaced with HERWIG++ or aMC@NLO interfaced with PYTHIA 8 and alternative W+jet samples were generated with MADGRAPH[2]. The multiboson samples were generated by a combination of SHERPA 2.2.1 and SHERPA 2.2.2. Finally the $t\bar{t}+V$ background was modelled by aMC@NLO. The MADGRAPH samples used the A14 underlying event tune [202] with the NNPDF23LO parton distribution function set,

---

[2]Alternative samples are used to calculate the $t\bar{t}$ and W+jets uncertainties, as explained in Section 6.12.2.

(a) Single-top

(b) W+jets with one and two jets that could be b-jets respectively

(c) Multiboson

(d) Z+jets

(e) $t\bar{t}$

(f) $t\bar{t}+W$ and $t\bar{t}+Z$

(g) tWZ
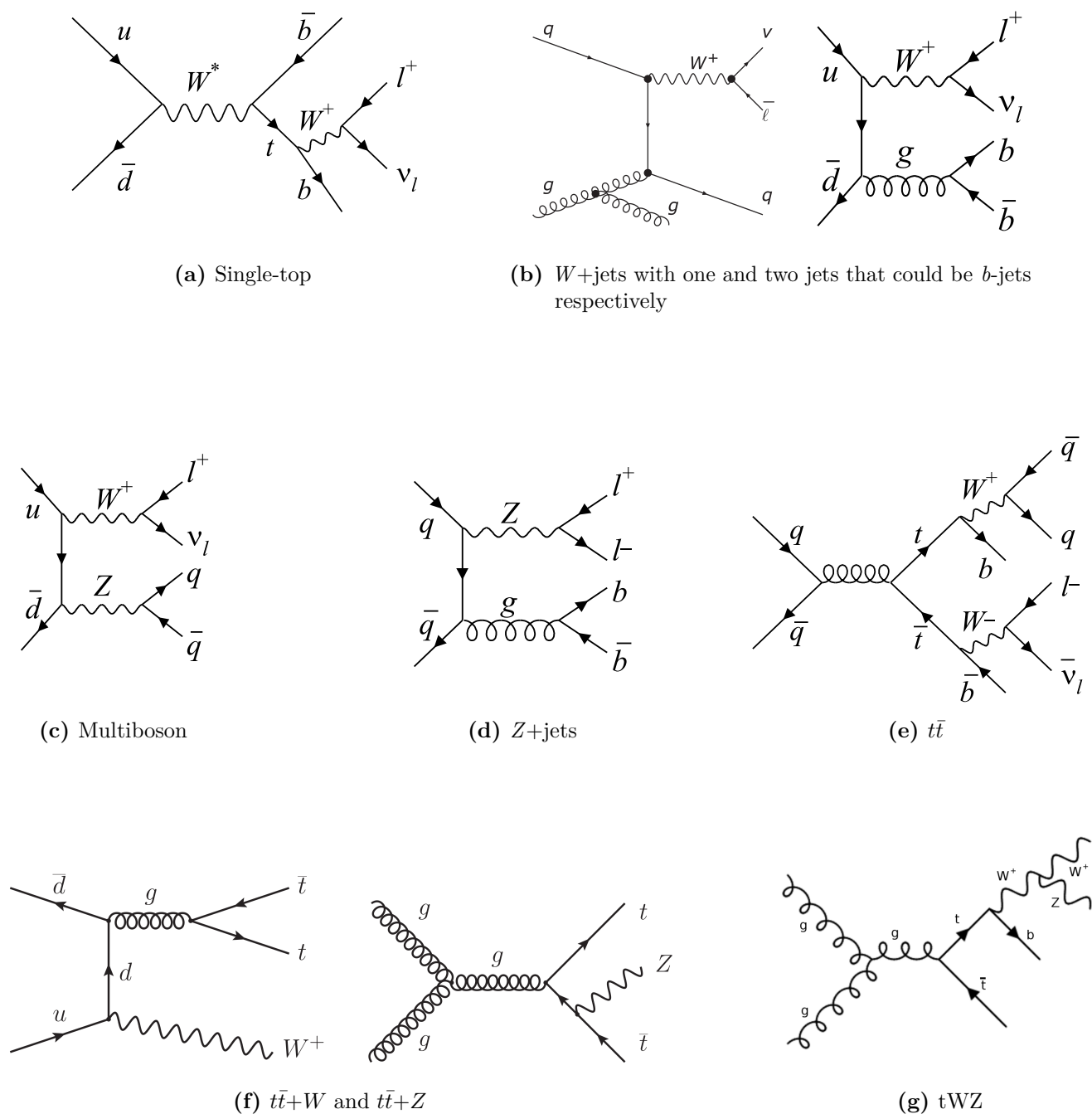
Figure 6.3.: Representative Feynman diagrams for each of the SM background processes considered. Figures reproduced from Refs. [198–201].

whilst the NNPDF3.0 parton density function set was used by the SHERPA samples and the CT10 parton distribution function set by the POWHEG samples (see Ref. [203] for details of the parton distribution function sets). The SUSY signal samples were processed with fast simulation [109], whereas the background samples were processed with full simulation of the ATLAS detector (see Section 3.6). All of the samples are produced with differing numbers of simulated minimum-bias interactions[3] overlaid on the hard-scattering events to account for pileup. As well as correcting for pileup, samples are re-weighted for lepton efficiency, b-tagging efficiency, trigger efficiency, scale factors and the integrated luminosity of 139 fb^{-1} to match the distributions in the data (except where an alternative luminosity is stated).

6.4. Pre-selection Criteria

Table 6.2 gives the pre-selections used in this analysis. The pre-selection is optimised to give a very high efficiency for the signal and greatly reduces the minor backgrounds such as tWZ and $t\bar{t}+V$.

In the names of the triggers given in Table 6.2, "HLT" stands for High Level Trigger whilst "xe" indicates a MET trigger. The integer (denoted X_{HLT} for the purpose of discussion) following "xe" is a notification that the trigger requires the MET $> X_{HLT}$ GeV whilst the integer "L1XE", X_{L1}, signifies that the Level 1 trigger applies a requirement of MET$>$ L1 [206]. HLT_xe70_L1XE50 is calculated using measurements from the calorimeter. MET triggers labelled with "mht" are calculated by summing over all anti-k_t jets after calibration whilst those labelled with "pufit" are calculated using the data collected by the calorimeter to correct for pileup [114]. The requirement that MET$>$ 230 GeV is the offline threshold, used to ensure that all the triggers used are on the efficiency plateau (operating at maximum efficiency). Events containing jets that do not pass jet quality requirements ('jet cleaning') detailed in Ref. [207, 208] are vetoed to suppress detector noise and non-collision backgrounds. The requirement on $|\Delta\phi_{j_{1,2},E_{\mathrm{T}}^{\mathrm{miss}}}|$, the minimum azimuthal angular distance between the MET and the direction of the two leading jets, is an effective technique to reject multi-jet events with mismeasured

---

[3]Minimum-bias interactions are generally associated with low-p_{T} particles in the central region of ATLAS and are caused by the leading inelastic process. They are suppressed using a trigger which removes empty BCs thus introducing a minimum bias [204].

Selection	
Trigger	MET triggers only
	HLT_xe70_L1XE50
	HLT_xe90_mht_L1XE50
	HLT_xe100_mht_L1XE50
	HLT_xe110_mht_L1XE50
	HLT_xe110_pufit_L1XE55
	HLT_xe110_pufit_L1XE50
	HLT_xe110_pufit_xe70_L1XE50
	HLT_xe110_pufit_xe65_L1XE50
Data quality	Jet cleaning, primary vertex
Second-lepton veto	No additional baseline leptons
Number of leptons, tightness	1 "tight" [†] lepton
Lepton p_T GeV	> 4 for μ
	> 4.5 for e
Jet p_T of leading jet GeV	> 200
MET GeV	> 230
$\lvert \Delta\phi_{j_{1,2}, E_\mathrm{T}^\mathrm{miss}} \rvert$ rad	> 0.4

[†] The "tight" selection on leptons as defined in [205]

Table 6.2.: Pre-selection used in the SRs, CRs and VRs.

momenta [27]. The requirements on the p_T of the leptons are in line with the definitions of electrons and muons given in Section 3.7.

Plots of data vs. MC for the main variables used in this analysis can be found in Figure 6.4 and Figure 6.5 and show good agreement between data and MC. From Figure 6.4, it can be seen that kinematic variables used in this analysis are well modelled[4] thus supporting there use as the main tools employed to discriminate background events from signal events. It should be noted that the double peak structure in Figure 6.5c is caused by the requirement that the high-p_T jet must have a $p_\mathrm{T} > 200$ GeV. The requirement was included to suppress the presence of pileup jets. b-jets are a subset of jets and are identified using the MV2c10 discriminant introduced in Section 3.7.4 so any

---

[4]The calculation of M_T and aM_T2 was discussed in Section 5.2.1 whilst the definition of H_T significance shall be given in Section 6.5.2.

b-jet that could not correspond to the highest-p_T jet and had a $p_\mathrm{T} < 200$ GeV would populate the area of plot to the left of the artificially created peak.

6.5. Choice of Kinematic Variables

Due to the fact that the compressed SUSY spectra of these processes makes them experimentally difficult to search for, a feasibility study was initially performed with 36.1 fb^{-1} of ATLAS data to determine which kinematic variables, if any, may have a high discriminatory power in this region of phase space[5]. The feasibility study with the ATLAS data collected in the period from 2015 to 2016 provided an opportunity to examine the discriminatory power of a large range of kinematic variables and select those which are best suited to performing a search for compressed SUSY decays.

Variable	LSR	TSR	TCR	WCR	WCR loose
$aM_{\mathrm{T}2}$ [GeV]	< 100	< 100	< 100	< 100	< 100
No. b-jets	≥ 1	≥ 1	≥ 1	$= 0$	$= 0$
$|\Delta\phi_{b,E_T^{miss}}|$ [rads]	< 1.5	< 1.5	< 1.5	< 1.5	< 1.5
Leading 1st, 2nd b-jet p_T [GeV]	< 100	< 100	< 100	< 100	< 100
H_T significance	> 26	> 30	< 26	> 14	-
Purity [%]	-	-	83	82	80

Table 6.3.: Overview of event selection used in feasibility study. The common event pre-selection defined in Table 6.2 was applied in all cases. The purities of the control regions are also given.

Table 6.3 displays the definitions of the regions proposed by the study while Appendix A discusses the design of the CRs and a schematic of the regions used. It was thought that two types of SR could be defined; a *general*, Loose Signal Region (LSR) and a *targeted* Tight Signal Region (TSR). General regions are designed such that the values of the requirements are chosen to allow for the possibility of detecting the signatures of models that are similar to the model under consideration. This approach is favourable

---

[5]It should also be noted that, due to the prolonged timescale of the study necessitated by the author's access requirements, the analysis was conceived at a time when 36.1 fb^{-1} of data was available, but came to fruition once 139 fb^{-1} of data was available
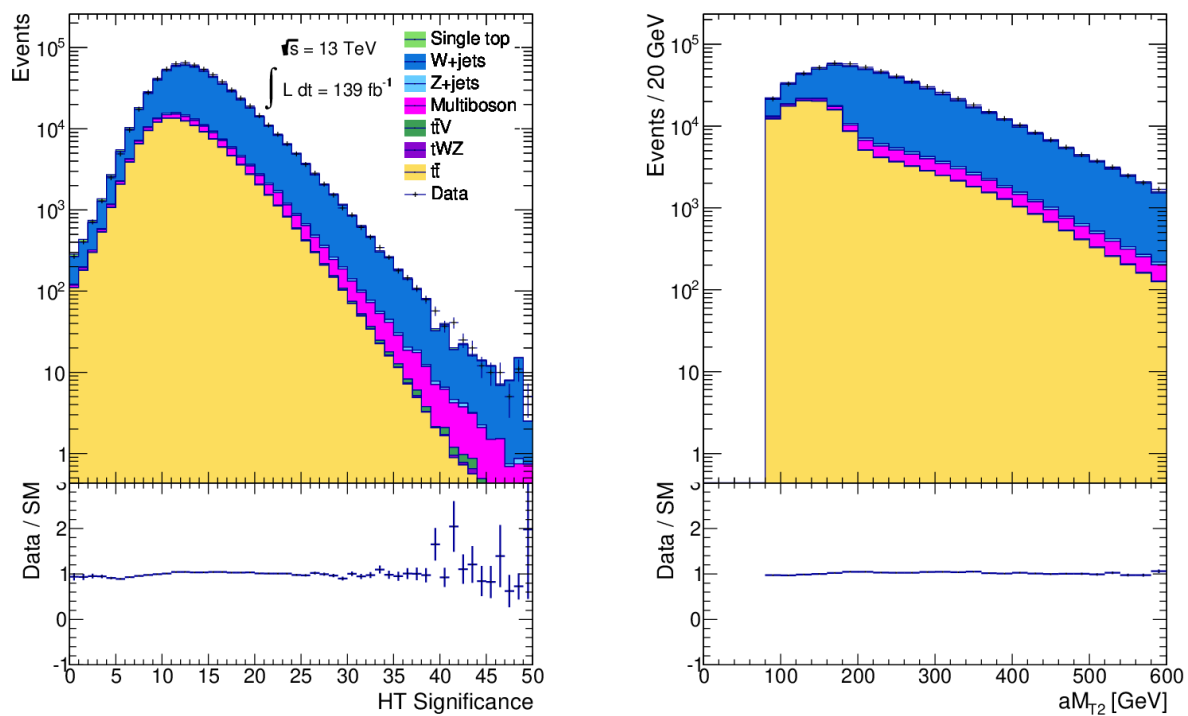
(a)

(b)
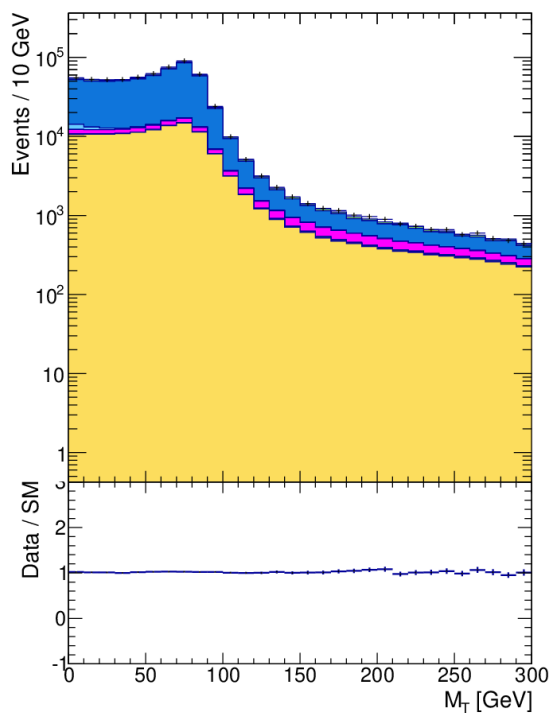
(c)

Figure 6.4.: Data/MC comparison plots for the main kinematic variables used in this analysis with pre-selection requirements applied.
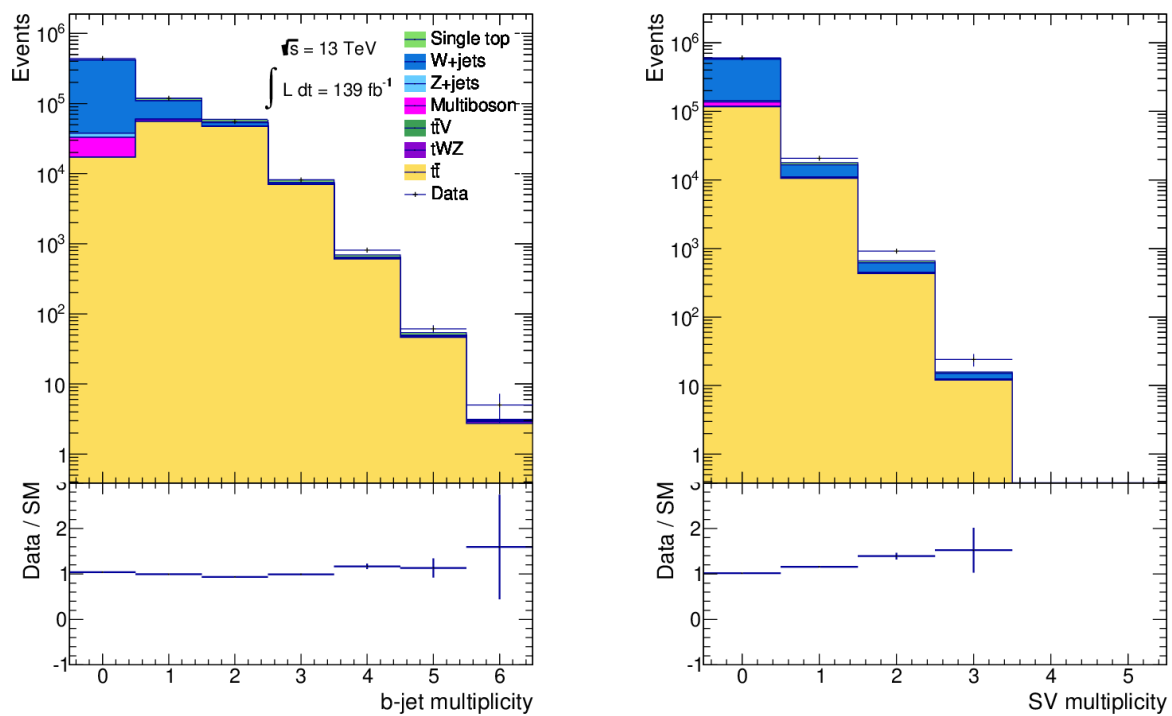
(a)

(b)
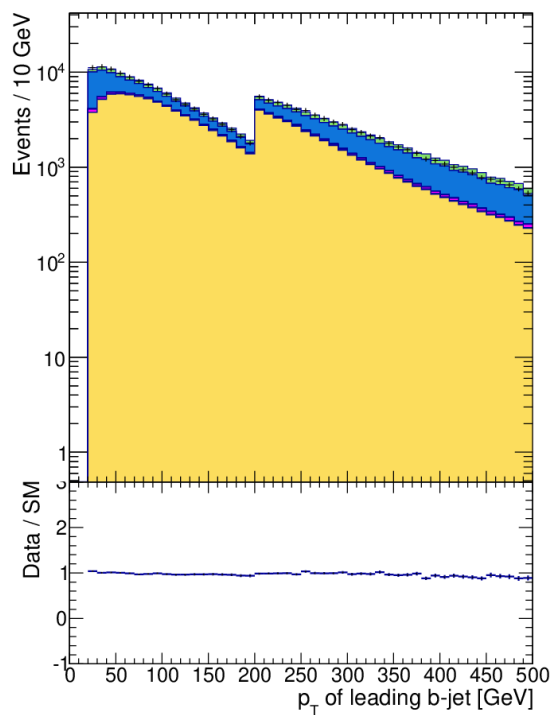
(c)

Figure 6.5.: Data/MC comparison plots for the variables used in this analysis to study b-jets with pre-selection requirements applied.

given the plethora of possible SUSY models that could be realised in nature. If more models can be tested in a single experiment, it follows that the chances of discovering new physics are increased. On the other hand, targeted regions are useful for focusing a search on a particular SUSY model. The use of a LSR and a TSR was investigated in the full analysis but was found not to be optimal.

The utility of a maximum aM_{T2} requirement has already been motivated in the search for SUSY processes with compressed mass spectra[6]. In Section 6.7 the effectiveness of requiring one or more b-jets when removing W+jets, Z-jets and multiboson backgrounds shall be demonstrated. This section discusses whether angular distributions between the decay products may provide useful discriminatory variables as well as comparing the utility of the significance variables MET significance and H_{T} significance.

6.5.1. Requirements on Angular Distributions

The findings from the feasibility study motivated the implementation of a requirement on the angle between the MET and the b-jets, $\Delta\phi_{b,E_T^{miss}}$ as a so-called "clean up" requirement. Figure 6.6 shows that the signal events typically have low values of $\Delta\phi_{b,E_{\mathrm{T}}^{\mathrm{miss}}}$ whereas the region of the distribution above 1.5 rad is background heavy. Therefore, a requirement that events must have a separation angle between the MET and the b-jets greater than 1.5 rad can be imposed without a large reduction in signal events. The physical interpretation of this result is that very few signal events produce b-jets back-to-back with the particles contributing to the MET. The $\mathcal{Z}$-value is plotted in the lower panel and denoted significance. The statistical interpretation of the negative significance values in Figure 6.6 is that the results do not support either the null hypothesis of the SM or the alternative hypothesis of the SUSY model under consideration. This is due to the fact that from Equation 6.1 a negative $\mathcal{Z}$-value corresponds to a p-value p$\geq$0.5. It can be seen from Figure 6.6 that the majority of background events have values of $\Delta\phi_{b,E_{\mathrm{T}}^{\mathrm{miss}}}$ that are close to 0 or π rad which means that most of the background events produce a b-jet which is either aligned or back-to-back with the direction of the MET. When the b-jet and the MET are arranged in this configuration, increased mismeasurement of hadronic objects such as b-jets[7] will result in the miscalculation of the MET and hence the recording of "fake" MET in the event, as was discussed in Section 3.7. This possible

---

[6]In this initial study, the requirement on aM_{T2} was slightly looser at a maximum of 100 GeV due to the reduced amount of data analysed with respect to the full Run 2 analysis.

[7]This is due to jets being collimated sprays of hadronic objects produced by the fragmentation of quarks and gluons [115], as explained in Section 2.1.
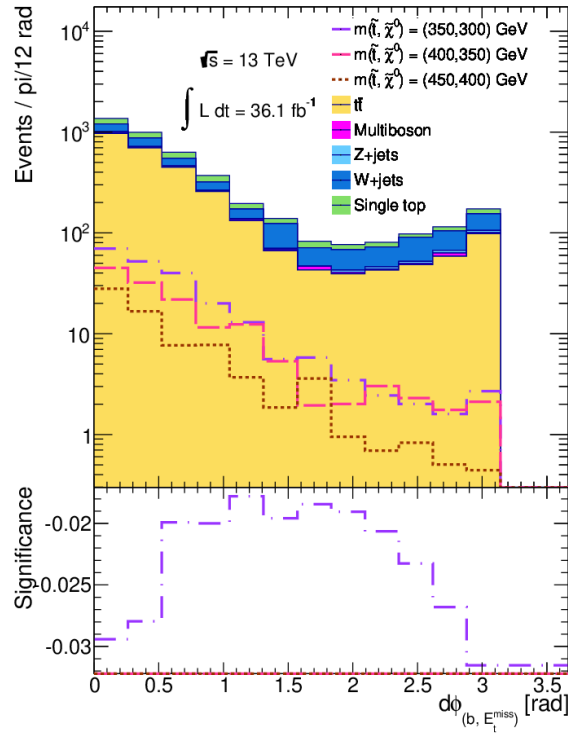
Figure 6.6.: Distribution of $\Delta\phi_{b,E_T^{miss}}$ with pre-selection applied as well as requirements of $aM_{T2} < 100$ GeV and one or more b-jets.

mismeasurement gives further motivation to using the "clean-up" requirement and was used in the 36.1 fb^{-1} study (see Appendix A).

6.5.2. The Utility of MET significance Compared to H_{T} significance

Two variables that are often considered in SUSY searches are the MET significance and H_T significance. As discussed in Section 3.7.5, a very important technique for detecting SUSY particles is to infer their presence from the MET in an event. However, it is known that many SM processes also produce particles, for example neutrinos in $t\bar{t}$ events, that go undetected and hence contribute to the MET. A complication is that experimental effects such as finite energy resolution of jets and gaps in the coverage of the detector can also mimic the effects of MET. A solution is to use the quantity MET significance, defined as

$$E_{T,sig}^{\mathrm{miss}} = \frac{E_T^{\mathrm{miss}}}{\sqrt{|\vec{H}_T^{\mathrm{miss}}|}} \, , \tag{6.2}$$

where $|\vec{H}_T^{\text{miss}}|$ is the negative sum of the jet and lepton vectors. MET significance quantifies the degree to which the reconstructed MET is consistent with the momentum resolution of the detector and the particle identification efficiencies, by equating $\sqrt{|\vec{H}_T^{\text{miss}}|}$ to the event-based approximation of the total MET resolution. Hence this variable allows evaluation of the log-likelihood that an event's MET is due to a resolution fluctuation or is consistent with the null hypothesis of the event having no real MET, thus accounting for the topology of the process and objects that are measured. Therefore a high value of $E_{T,sig}^{\text{miss}}$ indicates that MET in an event cannot be explained from momentum resolution effects suggesting that the events could contain undetected objects [127]. A variable that indicates this is particularly useful in a search for sparticles.

The discriminating power of kinematic variables can often be improved by taking detector resolution into account in their definitions [209]. This was the motivation for introducing the variable known as H_T significance:

$$H_{\text{T},sig}^{\text{miss}} = \frac{|\vec{H}_\text{T}^{\text{miss}}| - M}{\sigma_{|\vec{H}_\text{T}^{\text{miss}}|}} \, , \tag{6.3}$$

where $\sigma_{|\vec{H}_\text{T}^{\text{miss}}|}$ is the per-event resolution of the jets, assuming the lepton is well measured, which is found through the procedure given in [176]. M is the characteristic scale of the background, which is fixed, for the purpose of the analysis presented here, at 100 GeV by optimisation studies also outlined in [176].

In Figure 6.7 it can be seen from the distribution of the $\mathcal{Z}$-value that the MET significance and the H_T significance show strong separation between signal and background events. Relatively high significances can also be achieved using selections on these variables. Therefore, the possibility of defining signal regions using either MET significance or H_T significance was investigated. Figure 6.7 shows that a requirement on H_T significance in the range 22 to 32 (or 22 GeV$^{1/2}$ to 32 GeV$^{1/2}$ in the case of MET significance) could be effective. These variables can be used to define two non-orthogonal SRs, the LSR and the TSR.

Analysis strategies described in Section 6.2 demonstrate that imposing a minimum on MET significance of 24 GeV$^{1/2}$ reduces the background yields of $t\bar{t}$, Z+jets and multiboson by at least a factor of ten. In comparison, just under half of the signal yields are maintained after implementing the requirement. Thus, with a requirement of MET significance > 24 GeV$^{1/2}$, an LSR can be defined as a loose, general region. If the minimum requirement on MET significance is increased to 30 GeV$^{1/2}$, the W+jets,

Z+jets, multiboson and single *top* backgrounds can be removed almost entirely, to create an almost background-free region (disregarding the $t\bar{t}$ events). This is achieved despite maintaining the signal yields up to a third of their original value before the cut was implemented and significances up to 2.39 can be achieved. Increasing the MET significance requirement further could make results too sensitive to statistical fluctuations in the MC. Therefore, a second, targeted TSR was defined with a requirement that MET significance is greater than 28 GeV$^{1/2}$.
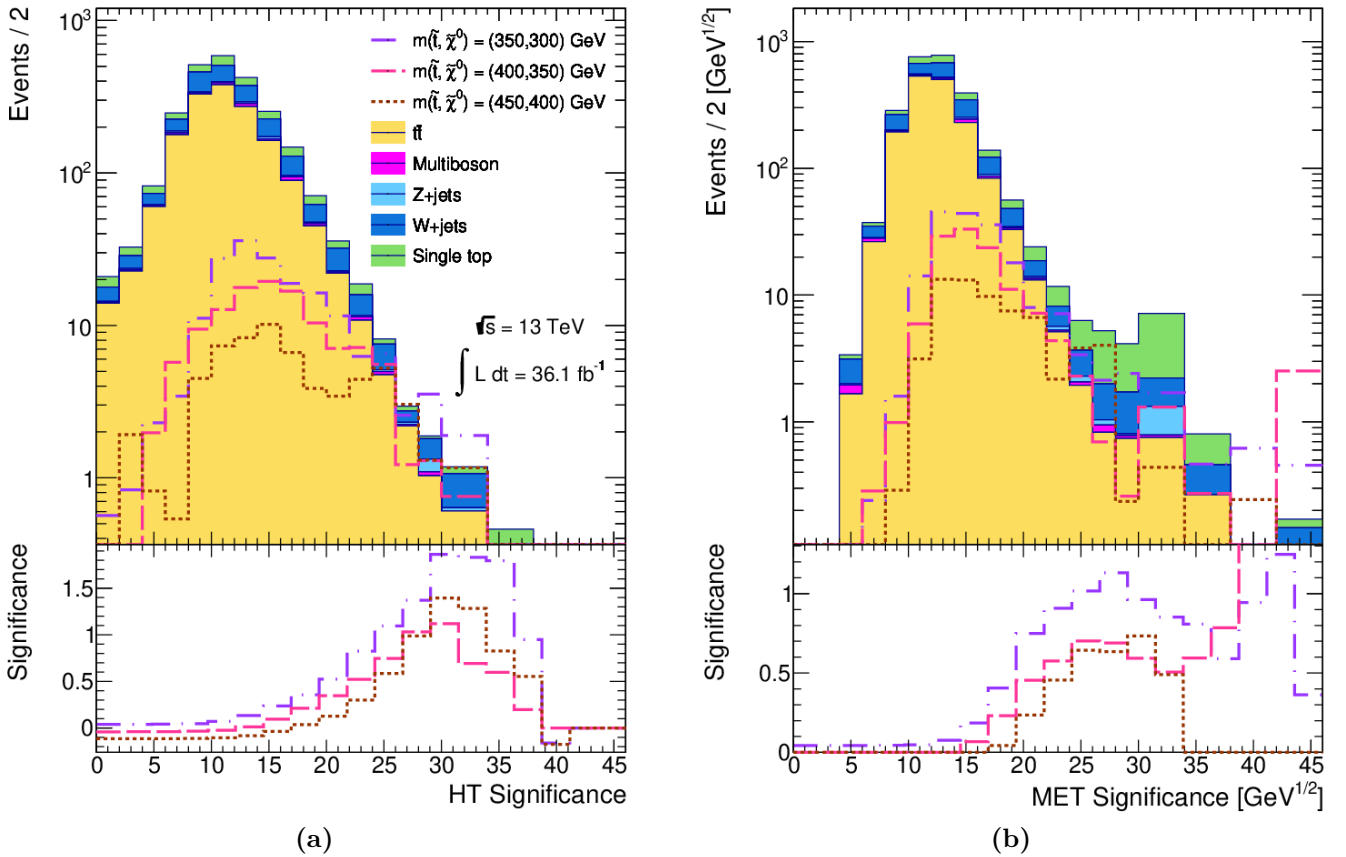
Figure 6.7.: The distribution of H_T and MET significance for the process shown in Figure 6.1 as well as for its SM backgrounds. Requirements on aM_{T2}, the number of *b*-jets, $\Delta\phi_{b,E_T^{\mathrm{miss}}}$, the p_T of the two leading *b*-jets and the pre-selection defined in Table 6.2 are applied.

Similar reasoning can be applied when considering potential values for a lower bound on H_T significance by studying Figure 6.7. Requiring H_T significance to be at least 26 reduces all SM backgrounds by a approximately a factor 20 whilst returning at least a third of the signal events. Therefore, a viable alternative to using the lower bound of 24 GeV$^{1/2}$ on the MET significance to define the LSR would be to require that H_T

LSR	MET significance > 24 GeV$^{1/2}$	H_T significance > 26
$(m_{\tilde{t}_1}, m_{\tilde{\chi}_1^0}) = (350, 300)$ GeV	1.31	1.66
$(m_{\tilde{t}_1}, m_{\tilde{\chi}_1^0}) = (400, 350)$ GeV	1.32	1.16
$(m_{\tilde{t}_1}, m_{\tilde{\chi}_1^0}) = (450, 400)$ GeV	0.75	1.18
TSR	MET significance > 28 GeV$^{1/2}$	H_T significance > 30
$(m_{\tilde{t}_1}, m_{\tilde{\chi}_1^0}) = (350, 300)$ GeV	1.21	2.05
$(m_{\tilde{t}_1}, m_{\tilde{\chi}_1^0}) = (400, 350)$ GeV	2.39	1.34
$(m_{\tilde{t}_1}, m_{\tilde{\chi}_1^0}) = (450, 400)$ GeV	1.19	1.61

Table 6.4.: $\mathcal{Z}$-values achieved in the LSR and TSR for each SUSY scenario considering the requirements on H_T significance and MET significance shown. Requirements on variables other than H_T significance and MET significance are applied as stated in Table 6.3 with MC representing 36.1 fb^{-1} of data collected from ATLAS.

significance be > 26. It can also be seen that the signal significance peaks when a minimum requirement for H_T significance > 30 is imposed, implying that this cut could be used to define a TSR. This requirement also was found to create a very low background region, disregarding the $t\bar{t}$ background, supporting its use as a targeted region.

Table 6.4 summarises the $\mathcal{Z}$-values that can be achieved using either MET significance or H_T significance to define the SRs for each SUSY benchmark point analysed. It can be seen that for the LSR, higher significances were achieved for most SUSY models when H_T significance is used. Likewise, for the TSR, higher significances were achieved for two of the mass points when H_T significance is used. So overall, higher significances can be achieved when H_T significance is used to define the SRs. This concurs with the prediction that H_T significance should be a more powerful discriminatory variable than MET significance due to its use of event resolution information. The details presented here concerning the impacts that changing the values of the requirements had on signal and background yields and the significances of the SRs, illustrate the calculations made throughout the design of the regions used in this analysis, by employing the GANGA toolkit as described in Section 6.2.

6.6. *Stop* Search with 139 fb^{-1} of ATLAS Data

A search for compressed *stop* decays with 1 isolated lepton in the final state was devised using the requirements stated in Table 6.5 and the positioning of these regions relative

to one another is illustrated in the schematic Figure 6.8. Potential SUSY events where b-tagging has identified at least one of the b-jets are searched for with the region termed Signal Region with 1 or more b-tagged jets (SRB1). As was motivated in Chapter 5, SV information can be used to search for events where b-tagging has failed to identify one or both of the b-jets in the final state, which is desirable given the softness of the decay products - the p_T of the b-jets can frequently be below 20 GeV, the lower limit at which jets can be precisely calibrated. Hence the analysis includes a second SR taking advantage of the gains in sensitivity provided by SV information, termed Signal Region with 0 b-tagged jets (SRB0). Background estimates for the two dominant backgrounds are provided by orthogonal CRs and VRs - the TCR and TVR for the $t\bar{t}$ background and the WCR and the WVR for the W+jets background.

Variable	SRB1	SRB0	TCR	TVR	WCR	WVR
aM_{T2} GeV	< 90	< 90	< 90	< 90	< 90	< 90
No. b-jets	≥ 1	$= 0$	≥ 1	≥ 1	$= 0$	$= 0$
No. SVs	-	≥ 1	-	-	$= 0$	$= 0$
M_T GeV	< 100	-	< 80	-	-	-
Leading 1st, 2nd b-jet p_T GeV	< 75	-	-	-	-	-
H_T significance	> 26	> 20	< 20	$20 < x < 26$	> 10	< 10

Table 6.5.: Overview of region definitions used in full Run 2 analysis with 139 fb^{-1} of data, applied in addition to the pre-selections listed in Table 6.2.

Figure 6.8 shows the H_T significance vs. b-jet multiplicity plane (upper) parallel to the H_T significance vs. SV multiplicity plane (lower). These planes are represented parallel to each other to highlight the relationship between b-jets and SVs motivated in Chapter 5. Only the requirements on these variables are represented in the schematic because they are the ones that ensure the orthogonality of all the regions. For example, there is a requirement that events in SRB1 have one or more b-jets - so SRB1 is represented in the upper plane by the region containing one b-jet and with a value of H_T significance > 26. However, the definition of SRB1 does not include a requirement on SV multiplicity, so in the lower plane this region includes any point as long as it meets the requirement on H_T significance and is shown by the hashed rectangle to the right of the lower plane. Events that have one or more b-tagged jets and relatively high values of H_T significance can only be present in this region as it is orthogonal to every other region. Similarly, events in SRB0 do not contain b-tagged jets (the lower part of the upper plane) but must contain one or more SV (the upper part of the lower plane) as well as the requirement

that H_T significance > 20. There is no requirement on SV multiplicity in the TCR or TVR which is why these regions extend the length of the y-axis in the lower plane but the requirement of 1 or more b-jets places these regions in the upper half of the upper plane. Finally the WCR and WVR have vetos on both b-jets and SVs and hence occupy the lower part of both planes. To recognise the orthogonality of SRB0 from Figure 6.8 consider that despite the overlap between this SR and the WCR in the upper plane, the requirements of SV multiplicity dictate that events are either in SRB0 if they possess SVs, otherwise they would be in the WCR. Events with one or more b-tagged jets can be in either the TCR or TVR (depending on the precise value of H_T significance) whilst only the WCR and WVR contain those events with neither b-tagged jets nor SVs. In the next section, the requirements used to define the SRs are justified by examining their N-1 plots and the yields and significances obtained from their application.
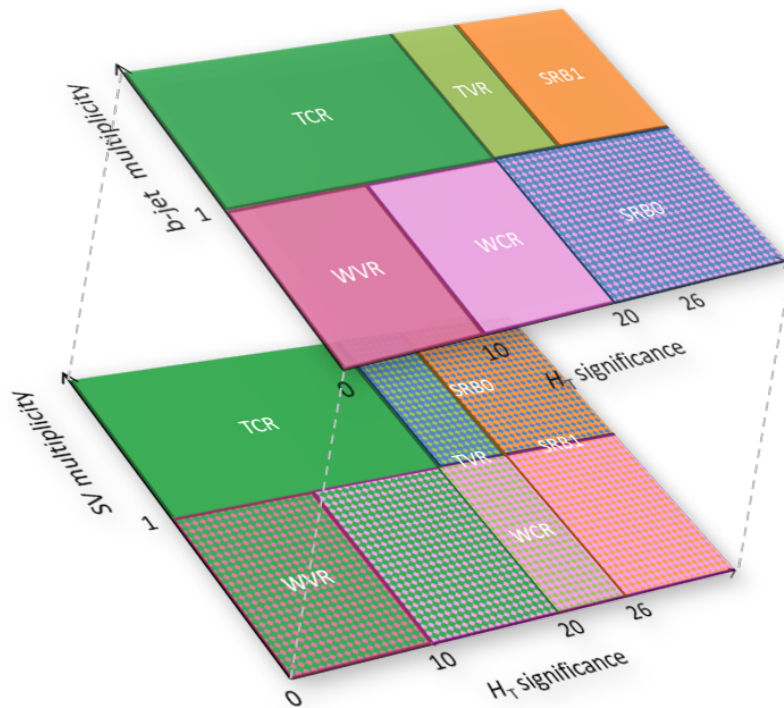
Figure 6.8.: Schematic of the regions defined in Table 6.5 showing their relative positions in the H_T significance vs. b-jet multiplicity as H_T significance vs. SV multiplicity planes. When both planes are considered together, it can be seen that the regions are orthogonal to each other.

6.7. The Use Of aM_{T2}, b-jets and SV

As was shown in Chapter 5, SUSY decays with mass splittings of around 50 GeV typically have events with low values of aM_{T2} - just above the kinematic minimum of aM_{T2} which is M_W. Background processes generally have events where the value of aM_{T2} is approximately 200 GeV as shown in Figure 6.9a where only the pre-selection requirements are applied. This provides strong motivation for placing an upper bound on aM_{T2} where the significance of the variable is shown to peak (90 GeV) and, indeed, Table 6.6 shows that this requirement reduces all backgrounds to approximately 1-3% of the original whilst retaining approximately 10% of signal events. To increase the resolution of the binning used in order to more precisely determine the location of the aM_{T2} peaks above the kinematic minimum of 80 GeV would increase the vulnerability of this relatively low statistic analysis to statistical fluctuations in the MC. The N-1 plot in Figure 6.9b (showing distributions produced by applying all the SRB1 requirements listed in Table 6.5 except for the requirement on aM_{T2}) confirms that 90 GeV was the optimum value of the upper bound in this region as this is where the $\mathcal{Z}$-value peaks. Figure 6.10 shows the distribution of MC weights in the first bin in Figure 6.9b above the kinematic minimum of aM_{T2} for the benchmark signal samples. It can be seen that all signal events in this bin received a weight between 0 and 0.5, indicating that there were no signal events that were significantly weighted with respect the others. This in turn implies that the peak in the aM_{T2} distribution in the first non-empty bin of Figure 6.9b is a result of the aM_{T2} distribution of the signal itself and not an artefact of how the signal events were weighted.

As explained in Section 2.4, b-jets are included in the final state of the process under consideration. In the SM, the *top* decays to a W and a b-quark with a branching ratio of 96% [29]. This implies that 92% of signal events should have 2 b-jets, and 99.8% of signal events should have at least one b-jet. As explained in Section 3.7.4, b-jets were tagged with an efficiency of 77% which corresponds to a value of the MV2c10 discriminant of 0.6459, as given in Table 3.1. This efficiency was measured using the $t\bar{t}$ MC sample that is used throughout this analysis [121]. This analysis only selects events with one lepton in the final state so if a W+jets or multiboson event is selected, the W must have decayed leptonically. The jets of the W+jets events are mainly contributed by gluon emission from the quarks involved in the hard process of the decay, as shown in the first Feynman diagram of Figure 6.3b. By considering which mesons are created during the hadronisation that occurs after the gluon decay, it can be shown that the W+jets

background will be composed mainly of light flavoured jets instead of b-jets. Therefore, most of the W+jets events will have 0 b-jets, so a very effective way to remove this background would be by raising the threshold on the minimum number of b-jets.

Furthermore, the W+jets events with 1 or more b-jets result from $W+$ heavy-flavour decays (as is shown in the second Feynman diagram of Figure 6.3b) as well as events containing mis-tagged b-jets. Meanwhile Figure 6.3c shows that if a multi-boson event is present in the analysis then the Z-boson must have decayed hadronically. The branching ratio of Z-boson to light quark flavours sums to approximately 30% in comparison to the ratio of Z-boson $\to b\bar{b}$ at approximately 12% which explains the relatively high proportion of multiboson events in the 0 b-jet bin in Figure 6.13a [29]. Indeed Table 6.6 shows that the requirement on b-jet multiplicity reduces the W and Z jets and multiboson backgrounds to approximately 20-30% of the yields before the requirement was applied whilst maintaining 75% of signal. Moreover, the N-1 plot of b-jet multiplicity shows that the 0 b-jet bin is dominated by W+jets and multiboson events and the $\mathcal{Z}$-value of the variable peaks in the 1 b-jet bin.
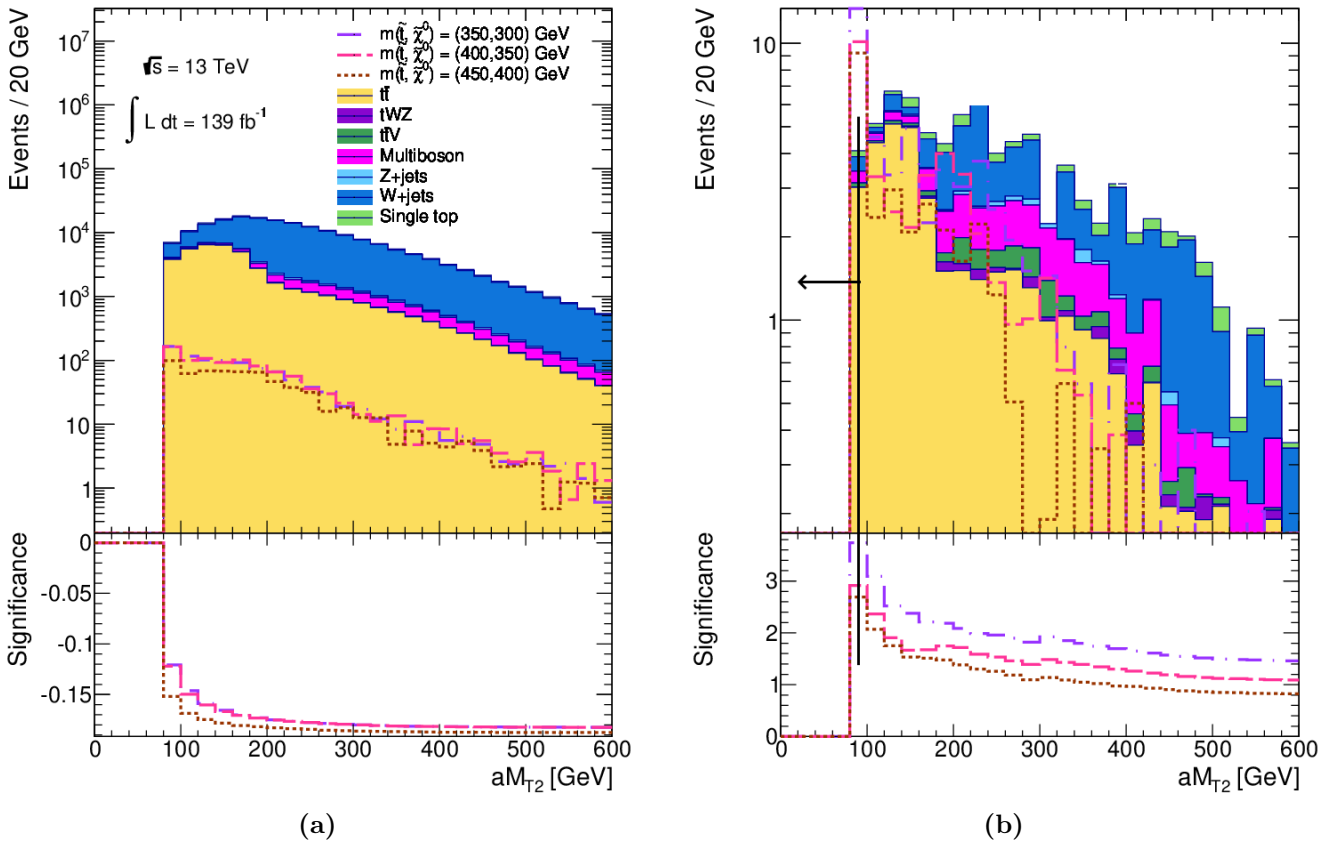
Figure 6.9.: Distributions of aM_{T2} (a) at pre-selection and (b) as an N-1 plot for SRB1
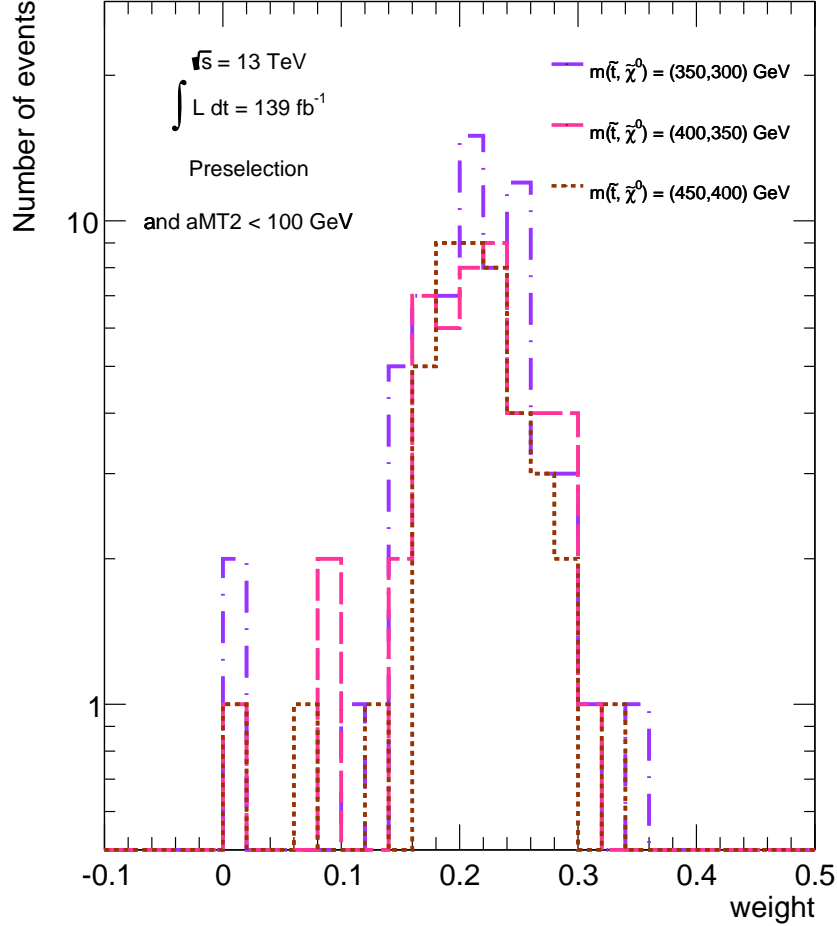
Figure 6.10.: Distribution of MC weigths of the signal samples in the first bin above the kinematic minimum of aM_{T2} from Figure 6.9b

The region SRB0 is designed to search for SUSY events where neither of the b-jets have been identified using b-tagging. Instead SV information is used to define a region with sensitivity to such events. A requirement of $aM_{\mathrm{T2}} < 90$ GeV was used to define the SRB0 for the reasons discussed in Section 6.8. The N-1 plot of aM_{T2} in Figure 6.11b shows that the significance of aM_{T2} in this region is also peaked just above the kinematic minimum of this variable. As Figure 5.14b shows, there are of order a hundred signal events where the b-jets are not identified but which contained one or more SVs - it is these events that this region was defined to have sensitivity to. In order for the region to target events where b-tagging has failed, it was therefore necessary to impose a b-veto in SRB0.
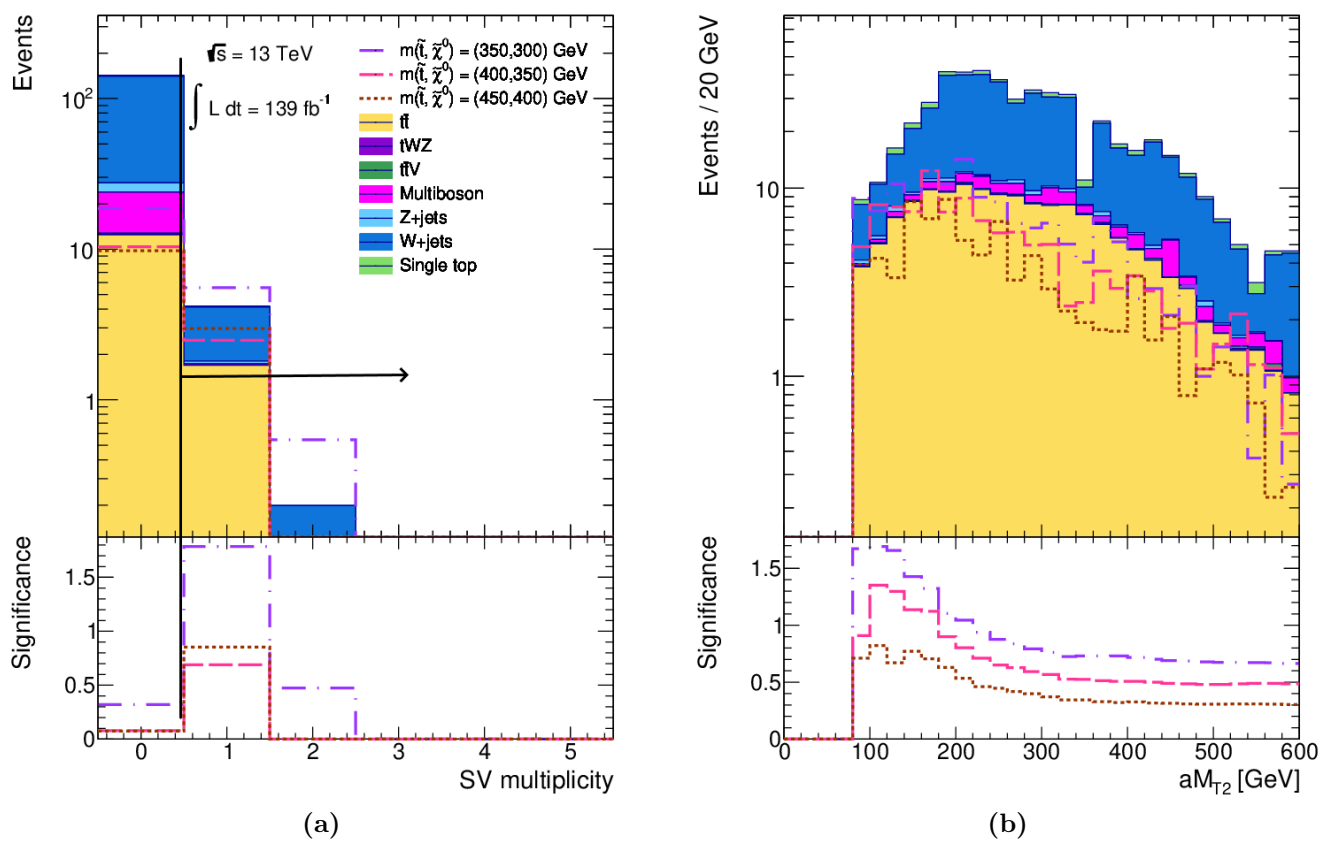
Figure 6.11.: N-1 plots of (a) SV multiplicity and (b) aM_{T2} in SRB0

	pre-selection	aM_{T2}	b-jets	M_{T}	b-jet p_{T}	H_{T} significance
$\Delta m(\tilde{t}_1, \tilde{\chi}_1^0) =$ (350, 300) GeV	5113 ± 35	577 ± 12	442 ± 10	119 ± 5	110 ± 5	9.5 ± 1.5
$\Delta m(\tilde{t}_1, \tilde{\chi}_1^0) =$ (400, 350) GeV	3237 ± 28	329 ± 9	253 ± 8	67 ± 4	62 ± 4	6.2 ± 1.2
$\Delta m(\tilde{t}_1, \tilde{\chi}_1^0) =$ (450, 400) GeV	2083 ± 22	192 ± 7	141 ± 6	41.2 ± 3.0	38.6 ± 2.9	6.6 ± 1.2
SM Background						
$t\bar{t}$	127343 ± 68	3973 ± 12	3576 ± 12	456 ± 4	253.2 ± 3.4	1.21 ± 0.09
W+jets	435731 ± 788	3363 ± 45	673 ± 19	24 ± 4	21 ± 4	0.045 ± 0.022
Z+jets	5787 ± 171	141 ± 5	33.0 ± 3.5	0.77 ± 0.22	0.65 ± 0.21	0.006 ± 0.006
single top	20586 ± 38	390 ± 5	330 ± 5	22.4 ± 1.3	13.2 ± 1.0	0.10 ± 0.04
Multiboson	18910 ± 106	208 ± 5	62.4 ± 3.1	7.2 ± 0.7	5.9 ± 0.7	0.11 ± 0.03
$t\bar{t}+V$	1137 ± 5	26.5 ± 0.8	23.7 ± 0.8	6.2 ± 0.4	3.43 ± 0.28	0.06 ± 0.03
tWZ	187.1 ± 2.7	2.7 ± 0.4	2.3 ± 0.4	0.77 ± 0.24	0.68 ± 0.19	$0.00^{+0.02}_{-0.00}$
Total bkg	609681 ± 817	8103 ± 47	4701 ± 23	517 ± 6	298 ± 5	1.50 ± 0.11

Table 6.6.: Cut flow table of the requirements used to define the SRB1. An integrated luminosity of 139 fb^{-1} was used to normalise the MC simulation. Only statistical uncertainties are shown.

	pre-selection	aM_{T2}	b-jets veto	No. SV	H_{T} significance
$\Delta m(\tilde{t}_1, \tilde{\chi}_1^0) =$ (350, 300) GeV	5113 ± 35	577 ± 12	135 ± 6	27.7 ± 2.6	6.1 ± 1.2
$\Delta m(\tilde{t}_1, \tilde{\chi}_1^0) =$ (400, 350) GeV	3237 ± 28	329 ± 9	76 ± 4	14.9 ± 1.9	2.5 ± 0.8
$\Delta m(\tilde{t}_1, \tilde{\chi}_1^0) =$ (450, 400) GeV	2083 ± 22	192 ± 7	51 ± 4	12.1 ± 1.8	3.0 ± 0.9
$t\bar{t}$	127343 ± 68	3973 ± 12	396 ± 4	43.9 ± 1.3	1.82 ± 0.14
W+jets	435731 ± 788	3363 ± 45	2690 ± 40	41 ± 4	2.4 ± 0.7
Z+jets	5787 ± 171	141 ± 5	108 ± 4	1.8 ± 0.4	0.08 ± 0.04
single top	20586 ± 38	390 ± 5	59.5 ± 2.1	4.3 ± 0.5	0.068 ± 0.035
Multiboson	18910 ± 106	208 ± 5	145 ± 4	1.8 ± 0.4	0.066 ± 0.034
$t\bar{t}+V$	1137 ± 5	26.5 ± 0.8	2.84 ± 0.27	0.38 ± 0.08	$0.00^{+0.01}_{-0.00}$
tWZ	187.1 ± 2.7	2.7 ± 0.4	0.44 ± 0.17	$0.04^{+0.05}_{-0.04}$	$0.00^{+0.02}_{-0.00}$
Total bkg	609681 ± 817	8103 ± 47	3403 ± 41	93 ± 4	4.4 ± 0.7

Table 6.7.: Cut flow table of the requirements used to define the SRB0. An integrated luminosity of 139 fb^{-1} was used to normalise the MC simulation. Only statistical uncertainties are shown.

6.8. Optimising SRB1

The feasibility study, presented in Section 6.5, used a "clean-up" requirement on $\Delta\phi_{b,E_T^{miss}}$. An alternative to using this "clean-up" cut would be to use a lower bound on the transverse mass M_T, which was defined in Section 5.2[8]. Figure 6.12 shows that requiring $M_T \gtrsim 100$ GeV would increase the significance of the region whilst compromising between retaining a large proportion of signal events and rejecting the background events that compose the peak of the distribution. Comparing Figure 6.6 and Figure 6.12a shows that when the full ATLAS dataset was used, the distributions of the significance of $\Delta\phi_{b,E_T^{miss}}$ had a less pronounced peak than in the feasibility study and hence placing a requirement on this variable would achieve less discriminatory power. In contrast the distribution of the significance of the M_T shows a very pronounced peak at approximately 100 GeV (Figure 6.12b). A requirement on M_T was also investigated in the feasibility study, however, it was found not to be as effective as a "clean-up" requirement on $\Delta\phi_{b,E_T^{miss}}$. The differences in the distributions in the two studies were due to updated MC simulation and the increased number of events. Note that it would not be optimal to use both a requirement of $\Delta\phi_{b,E_T^{miss}}$ and M_T, as this would give too small a sample events for which to employ a requirement on a more discriminatory variable, such as H_T significance. Indeed the fact there are arguments in favour of the use of requirements on $\Delta\phi_{b,E_T^{miss}}$ and M_T points to the flexibility of the "cut-and-count" approach to designing searches for BSM physics.

Hence, the SRB1 is also defined by a requirement that $M_T > 100$ GeV. This requirement maintains 25-30% of signal whilst being particularly effective at reducing W and Z jets to between 2-3% percent of original and most other backgrounds reduce to approximately 10% of original. The N-1 plot in Figure 6.13b confirms that the requirement is well placed as it is situated at the peak of the distribution of the $\mathcal{Z}$ distribution and removes a background heavy region below the 100 GeV requirement. It was confirmed that the distributions of signal events in Figure 6.12b was not caused by a small proportion of events that were significantly weighted but instead by statistical fluctuations by plotting the distribution of weigths for these events, analogous to Figure 6.10.

Table 6.6 shows that after the requirements on aM_{T2}, b-jet multiplicity and M_T has been applied, $t\bar{t}$ background accounts for approximately 90% of the background events in the region under consideration. Given that the compressed *stop* decays are expected

---

[8]Again the negative significances for some values of M_T suggest that at this stage in the analysis there is not enough evidence to support the null hypothesis.

(a) $\Delta\phi_{b,E_T^{miss}}$ distribution using 139.0 fb^{-1} of ATLAS data

(b) M_T distribution using 139.0 fb^{-1} of ATLAS data
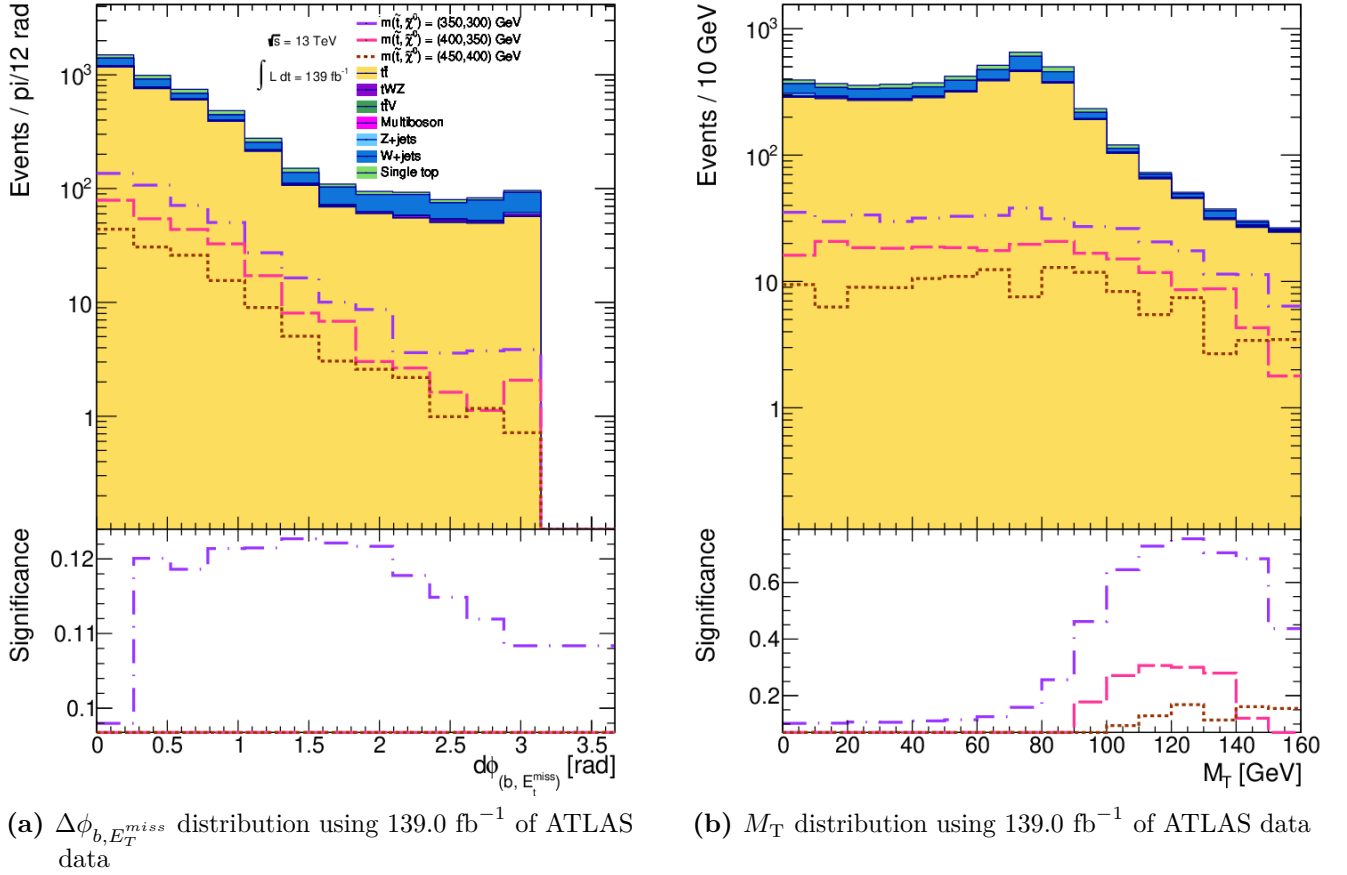
Figure 6.12.: Distributions of $\Delta\phi_{b,E_T^{miss}}$ and M_T - two kinematic variables on which requirements could be placed to design SRB1s to search for compressed *stop* decays. Requirements of $aM_{T2} < 90$ GeV and one or more b-jets have been applied in addition to pre-selection.

to have low p_T b-jets in their final states, an upper limit on the p_T of the b-jet can be justified. Indeed as can be seen from Figure 6.14, the distribution of the b-jet p_T has a long tail which consists mainly of $t\bar{t}$ events and the majority of signal events are peaked at lower end of the distribution. The most advantageous upper bound on b-jet p_T in terms of retaining signal and removing background was found to be 75 GeV and as Table 6.6 shows, this has the effect of reducing $t\bar{t}$ and $t\bar{t}+V$ backgrounds by approximately 50% for whilst retaining over 90% of the signal. It can also be seen that the distributions of the $\mathcal{Z}$ value of the two p_T distributions presented in Figure 6.14 are both peaked below 75 GeV.

Finally, Table 6.6 shows that the H_T significance requirement reduces the $t\bar{t}$ background to below 1% of the yield before the requirement was applied whilst reducing the single *top*, Z-jets, multiboson and tWZ to nearly 0 events. Moreover the N-1 plot
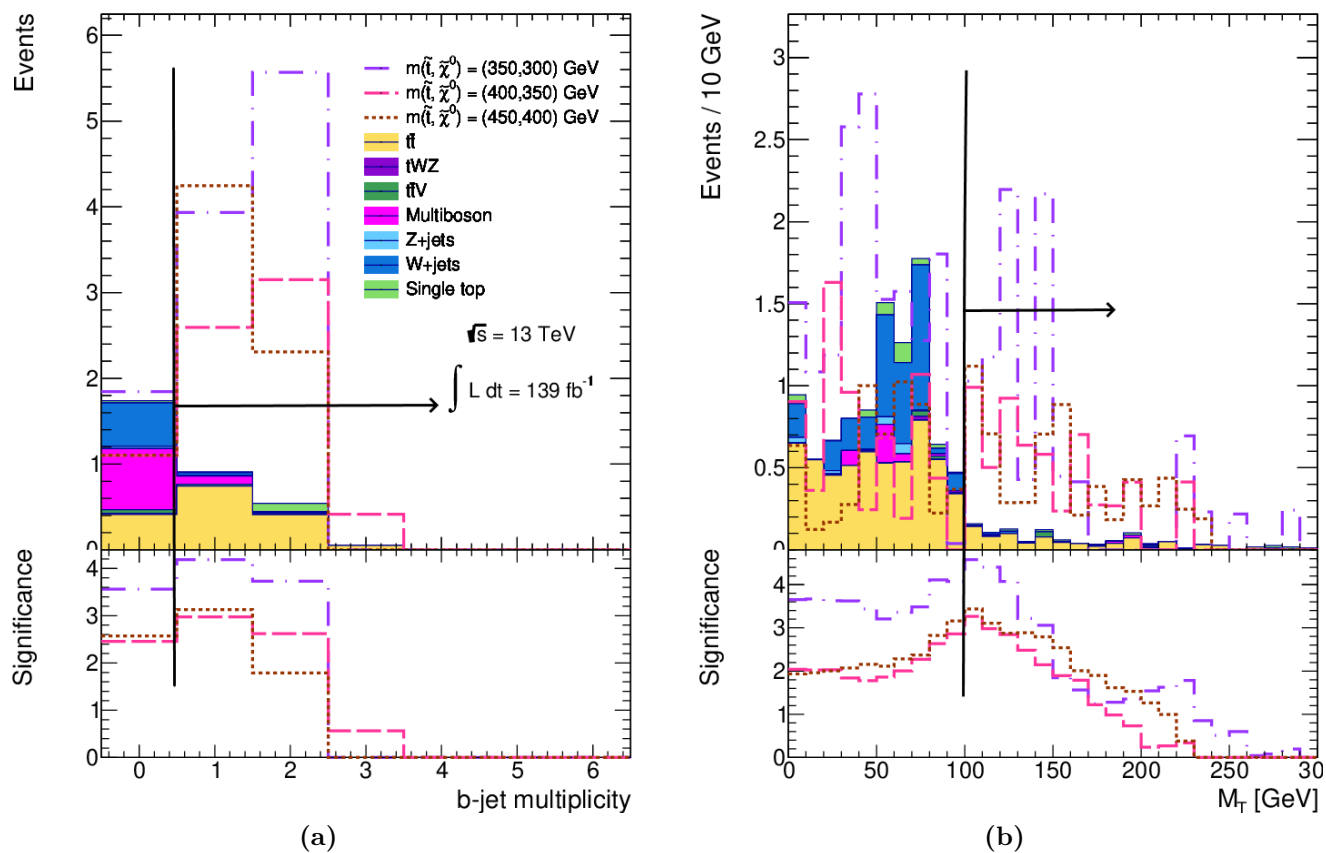
Figure 6.13.: N-1 plot of (a) *b*-jet multiplicity and (b) M_{T} in SRB1

in Figure 6.15a confirms that the H_{T} significance requirement is well placed at H_{T} significance > 26 as this is where the $\mathcal{Z}$-value peaks.
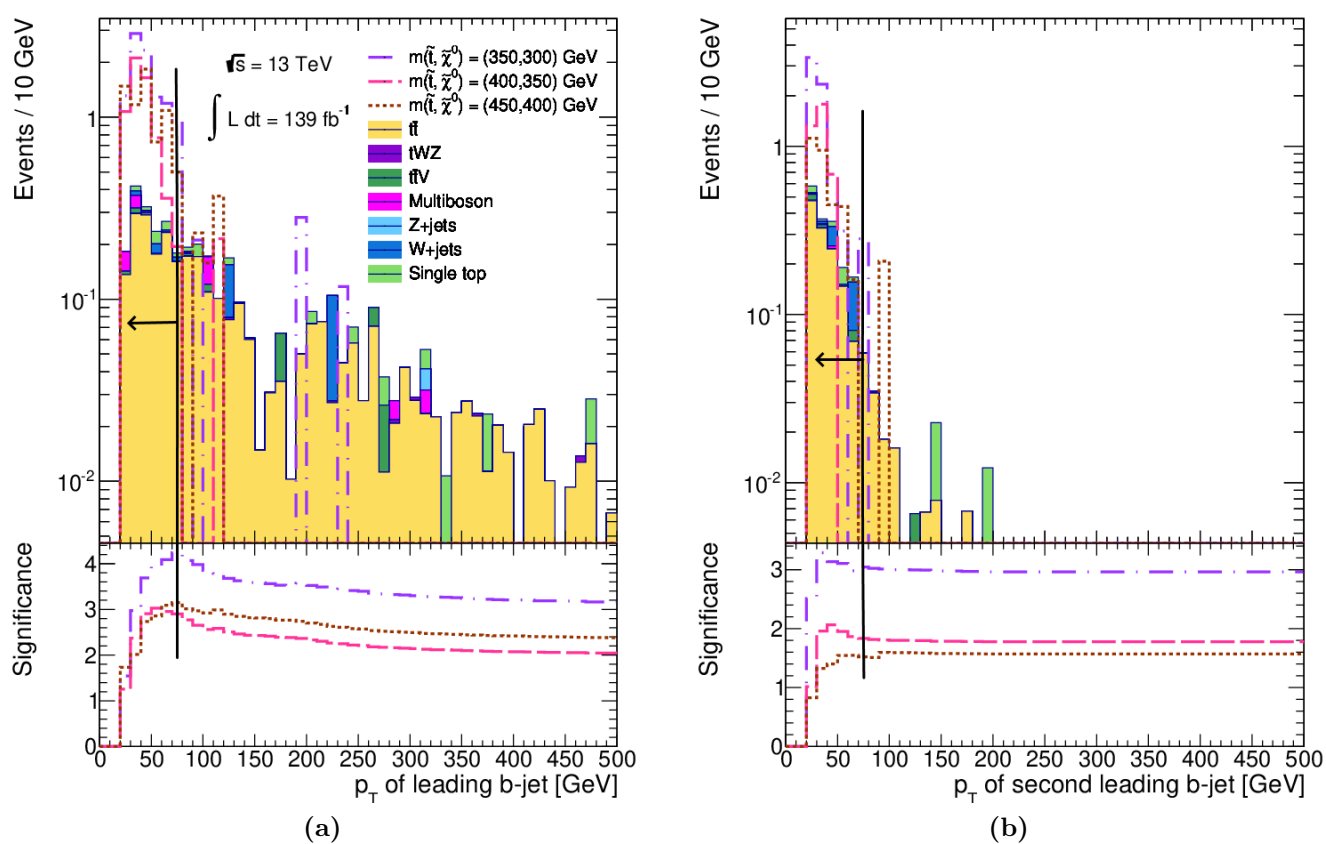
Figure 6.14.: N-1 plots of the (a) p_T of the first and (b) second leading b-jet in SRB1

6.9. Optimising SRB0

Once the *b*-veto has been applied, the fifth column of Table 6.7 shows that requiring one or more SV is an effective way to reduce all backgrounds by at least 85% whilst retaining approximately a quarter of signal events in this particularly experimentally difficult region of parameter space. Indeed the N-1 plot of SV multiplicity in Figure 6.11 shows that the significance of this variable has a substantial peak in the SV multiplicity N-1 plot.

Finally Figure 6.15b shows that a requirement of at least 20 on H_{T} significance is needed to mostly eradicate all backgrounds except $t\bar{t}$ and W+jets and to complete the definition of a region to search for *stop* decays where *b*-tagging cannot identify the *b*-jets in the final state.

(a) SRB1   **(b)** SRB0
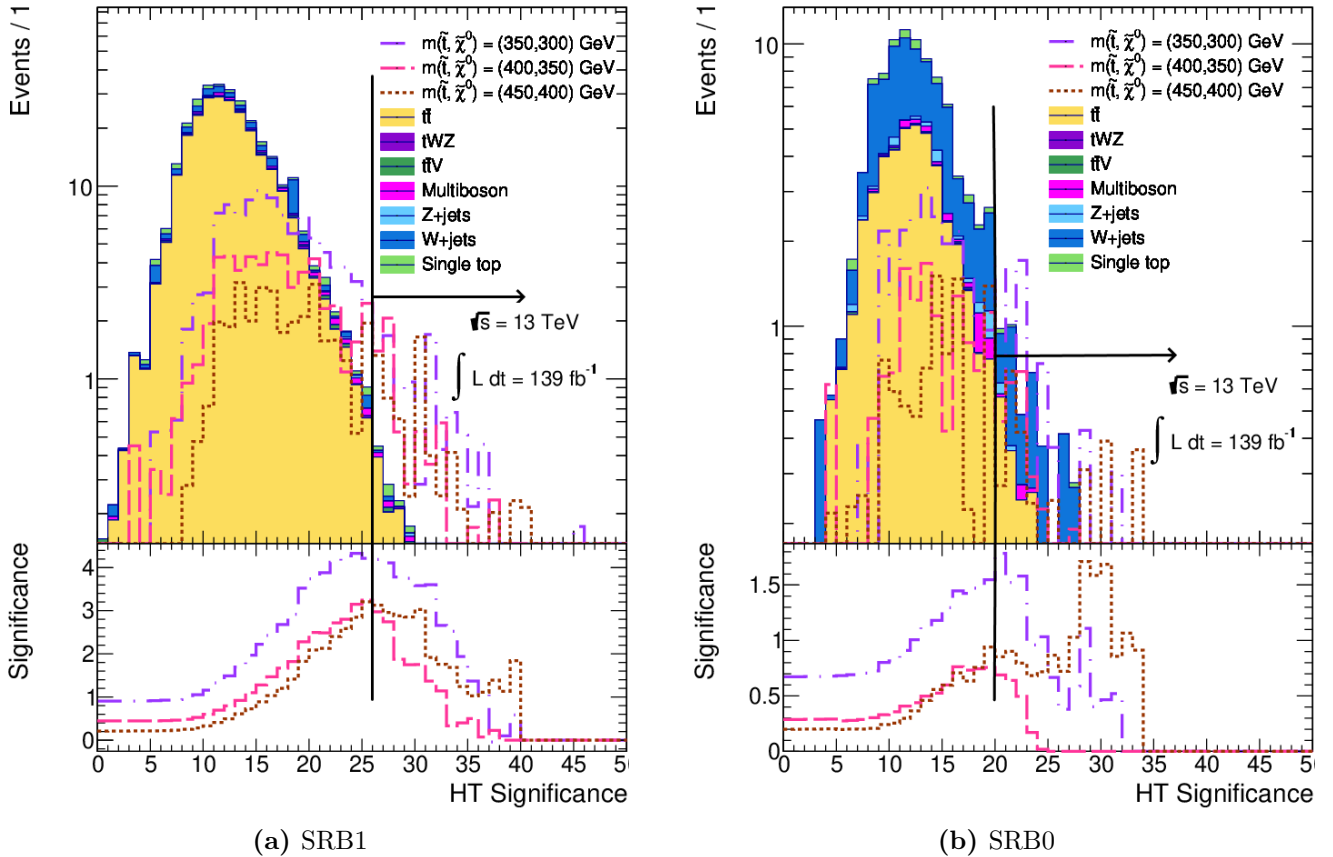
Figure 6.15.: N-1 plot of H_{T} significance in (a) SRB1 and (b) SRB0.

6.10. Effectiveness of Signal Regions

It is a testament to the effectiveness of the requirements that the total background is reduced to of order $10^{-4}\%$ of the number of events at pre-selection, thus almost eradicating all but the dominant $t\bar{t}$ background (W+jets in SRB0), as shown in Table 6.8. Hence, in both SRs the reduction in the background is approximately 3 times that of the reduction in the signal. The fact that these impressive reductions in the background yields come at the cost of retaining at most approximately 0.1% of signal events is a consequence of the difficulties searching for the signatures of such compressed decays leading to very soft final states. Table 6.8 also shows that the $\mathcal{Z}$-values for most benchmark models are also higher than the 1.64 threshold of exclusion of the null hypothesis, although $\mathcal{Z}$-values are lower in SRB0 due to experimental difficulties in identifying events where b-tagging has failed despite the use of SV information.

scenario/decay	Acceptance SRB1 (%)	Acceptance SRB0 (%)	$\mathcal{Z}$-values SRB1	$\mathcal{Z}$-values SRB0
$\Delta m(\tilde{t}_1, \tilde{\chi}_1^0) =$ (350, 300) GeV	0.19	0.12	4.18	1.79
$\Delta m(\tilde{t}_1, \tilde{\chi}_1^0) =$ (400, 350) GeV	0.19	0.08	2.98	0.69
$\Delta m(\tilde{t}_1, \tilde{\chi}_1^0) =$ 450, 400) GeV	0.32	0.14	3.31	0.85
$t\bar{t}$	9.4×10^{-4}	1.4×10^{-3}	-	-
W+jets	9.2×10^{-6}	5.5×10^{-4}	-	-
Z+jets	1×10^{-4}	1.4×10^{-4}	-	-
single top	4.9×10^{-4}	3.4×10^{-4}	-	-
Multiboson	5.8×10^{-4}	3.7×10^{-4}	-	-
$t\bar{t}$+V	5.3×10^{-3}	0.0	-	-
tWZ	0.0	0.0	-	-
Tot. norm. bgd	2.2×10^{-4}	7.2×10^{-4}	-	-

Table 6.8.: Acceptance of SRB1 and SRB0 of each SUSY scenario and background process relative to the yields obtained when only the pre-selection defined in Table 6.2 is applied as well as the $\mathcal{Z}$-values achieved for each SUSY benchmark point.

Another measure of the effectiveness of the SRs would be to examine the expected $\mathcal{Z}$-values for each region as a function of $m_{\tilde{t}_1}$ and $\Delta m(\tilde{t}_1, \tilde{\chi}_1^0)$, before any simultaneous fits have been performed (see Section 6.13). Such plots are shown in Figure 6.16. The binning of these plots is such that the centre of each bin represents a point on the signal grid - hence the coarse nature of the plots. The signal grid was constructed to concentrate the signal point around the edges of the exclusion contour shown in Figure 6.22. As to be expected it can be seen that the $\mathcal{Z}$-value decreases with the $m_{\tilde{t}_1}$ because the cross-section of the process decreases, as was explained in Section 6.1. It has been explained that the area of the phase space where $\Delta m(\tilde{t}_1, \tilde{\chi}_1^0) < 20$ GeV is experimentally more difficult than areas with higher values of $\Delta m(\tilde{t}_1, \tilde{\chi}_1^0)$ calling for the region SRB0 to be designed specifically to search for processes in the former area. Indeed it can be seen that SRB0 is expected to have enhanced $\mathcal{Z}$-values compared to SRB1 for $\Delta m(\tilde{t}_1, \tilde{\chi}_1^0)$ approximately 7 GeV.
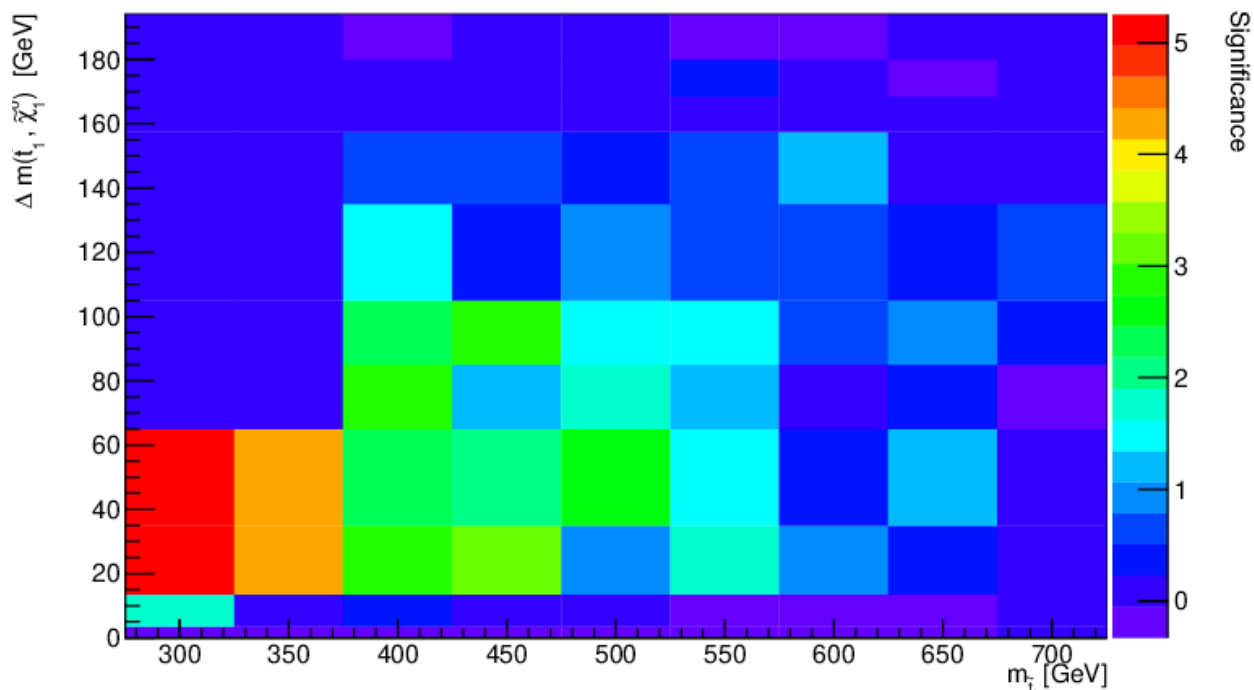
(a) SRB1
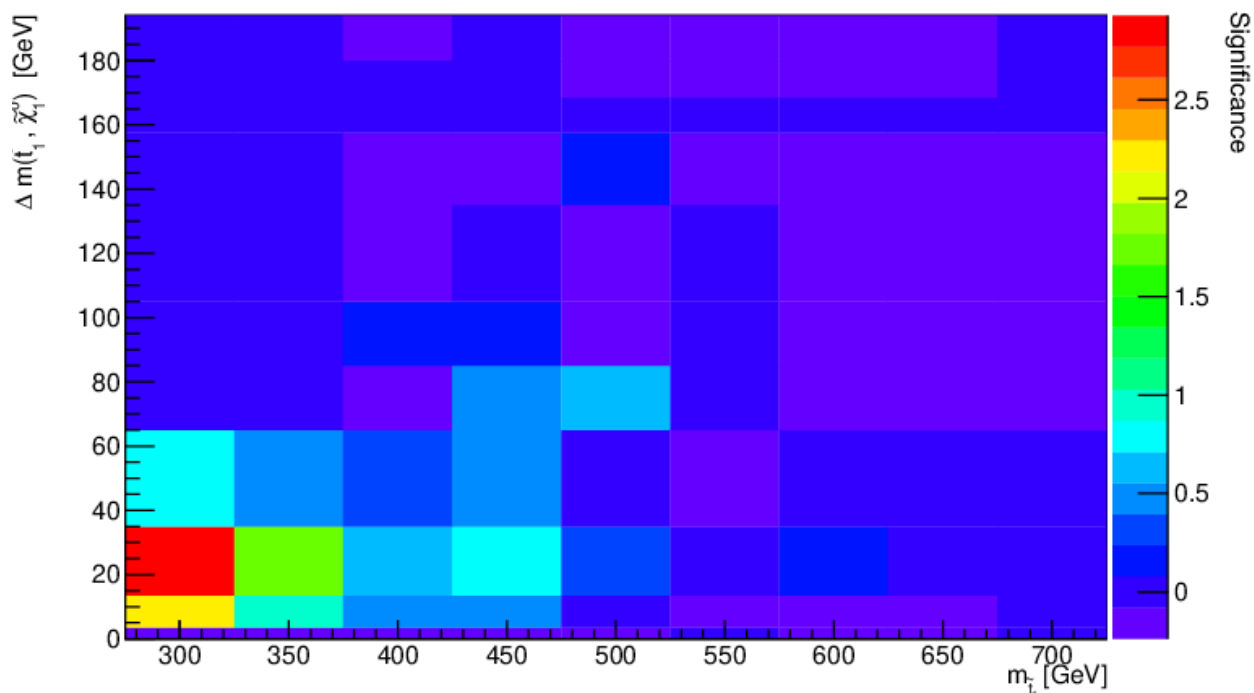
(b) SRB0

Figure 6.16.: Expected $\mathcal{Z}$-values for (a) SRB1 and (b) SRB0 as a function of $m_{\tilde{t}_1}$ and $\Delta m(\tilde{t}_1, \tilde{\chi}_1^0)$.

6.11. Background Estimation Techniques

The two dominant SM backgrounds in this analysis are $t\bar{t}$ and W+jets. As explained in Section 6.2, it is necessary to ensure that CRs and VRs are disjoint from their associated SRs. This can be done by reversing the requirements on one or more variables that define the SRs and then placing the VRs between the phase space of the SR and CR. Hence, to define the CR for $t\bar{t}$, TCR, this is accomplished by reversing the requirement on H_T significance and dividing the parameter space such that $20 < H_T$ significance < 26 corresponded to a TVR and a TCR was defined by H_T significance < 20. This produces a TCR and TVR with a purity of approximately 87% and 74% respectively.

Given that the majority of W+jets events contain light flavour rather than heavy flavour jets, one might think to define high purity WCR and WVR by imposing a b-veto. However this region of parameter space is occupied by SRB0 so cannot be used to define disjoint CRs or VRs. Therefore, given aforementioned relationship between b-jets and SVs a WCR and a WVR may instead be defined by imposing a veto on SVs as well as a veto on b-jets. This region design successfully gives a WCR with 79% purity and a WVR with 76% purity. Figure 6.17 and Figure 6.18 shows a comparison between data and MC in the two VRs and confirms that the data is well modelled in these regions (except in the low statistics tails).

6.12. Systematic Uncertainties

Up to this point only the statistical uncertainties have been taken into consideration - this is an oversimplification. Performing an experiment using such sophisticated apparatus as the ATLAS detector leads to a variety of sources of experimental systematic uncertainties. Moreover even though the SM provides a very accurate description of almost every observed phenomena at a sub-atomic level, some parameters within the model are known to a greater level of precision that others, leading to a source of theoretical uncertainty. There are also theoretical uncertainties implicit in the theoretical framework such as how many orders of Feynman diagrams to include in a calculation. This section discusses the sources of systematic uncertainties in this analysis and how they were addressed.
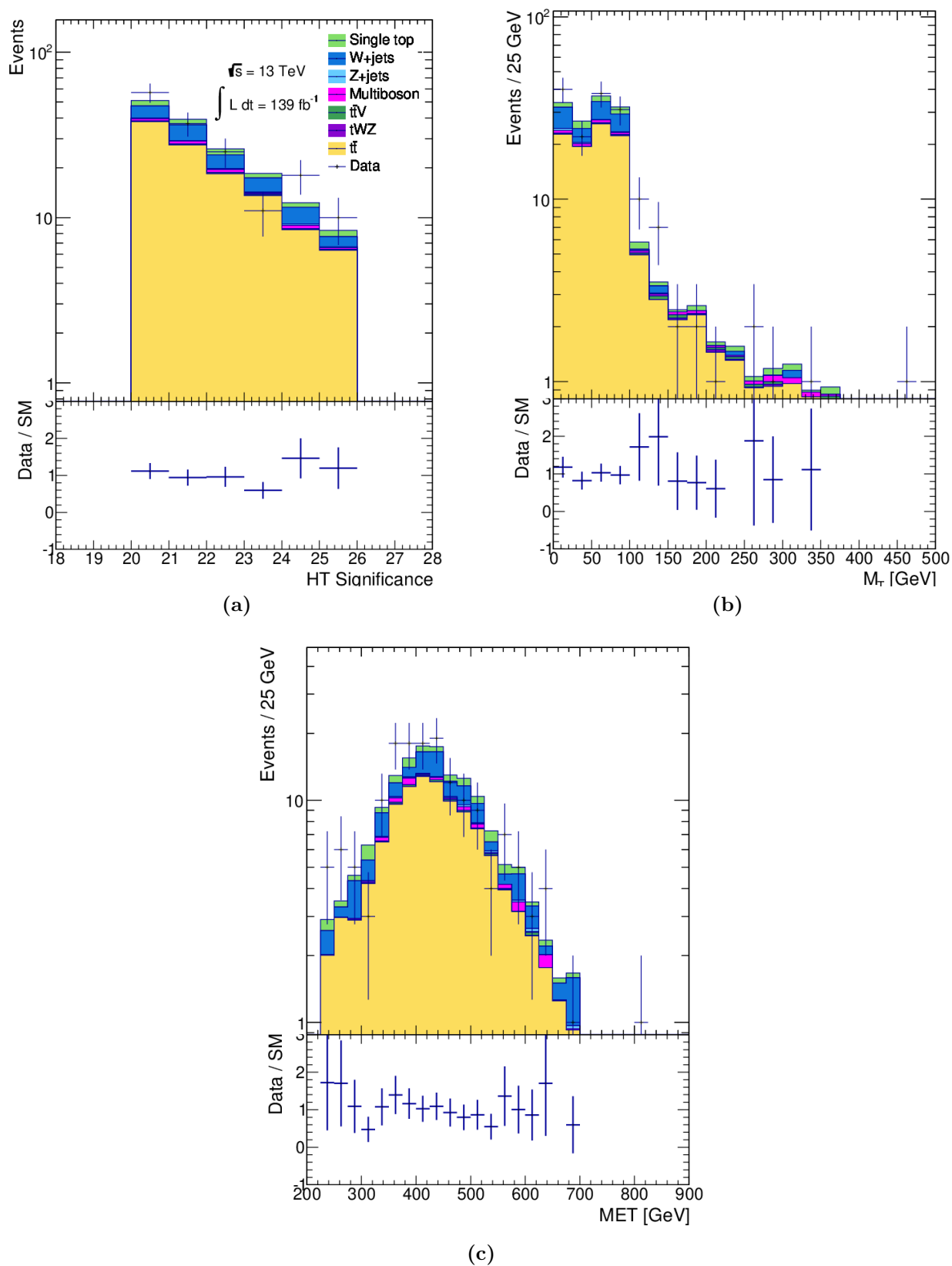
Figure 6.17.: Distributions of (a) H_{T} significance, (b) M_{T} and (c) MET plotted in the TVR showing the agreement between data and MC prediction.

(a)

(b)

(c)
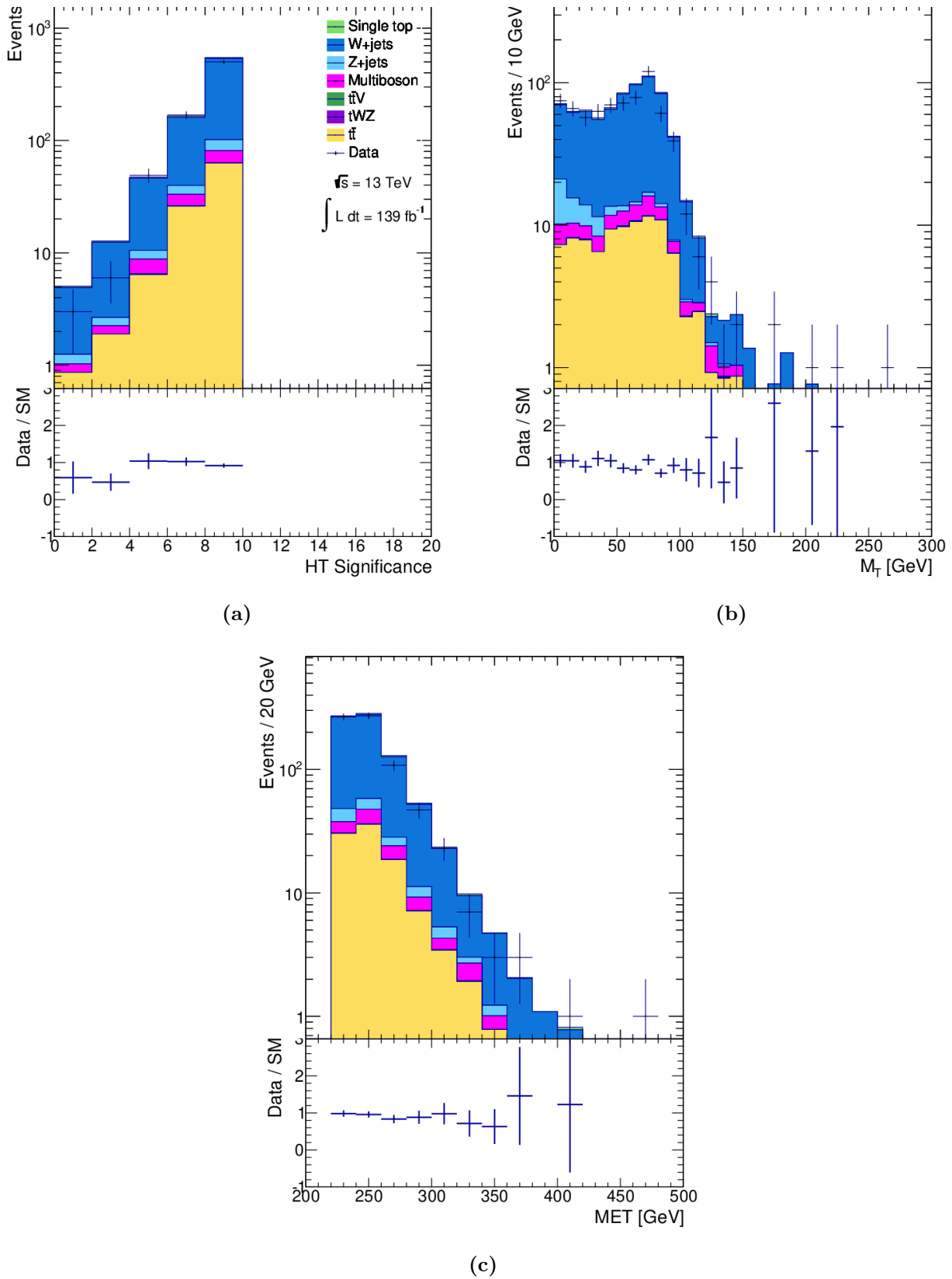
Figure 6.18.: Distributions of (a) H_T significance, (b) M_T and (c) MET plotted in the WVR showing the agreement between data and MC prediction.

6.12.1. Experimental Uncertainties

No experimental apparatus provides measurements that are free from experimental systematic errors and hence for each of the physics objects introduced in Section 3.7, the associated experimental systematic uncertainty must be taken into account. These are summarised in Table 6.9. In Section 6.13, its explained that these systematic uncertainties are estimated by representing them in the general likelihood function of the analysis in the form of Nuisance Parameters (NPs). In order to perform the estimate of each systematic uncertainty, alternative distributions are produced of the quantity of relevance, but in the alternative samples, the quantity of interest, e.g. the Jet Energy Scale (JES), has its central quantity shifted up or down by 1 standard deviation away from the nominal value. The difference between the yields produced from these "variations" is used to calculate the uncertainty. These object-based variations are propagated to event-level variables such as MET and H_{T} significance.

6.12.2. Theoretical Uncertainties

An overview of the anatomy of an event simulated in an MC generator was given in Section 6.3 where a brief introduction to the types of calculations and physical phenomena that are the sources of the theoretical uncertainties that are discussed in this section was given. In order to estimate the theoretical uncertainties in each region used in the analysis, the yields obtained from using different MC generators are compared as the precise theoretical treatment of the process differs between generators. This section gives the estimates of the theoretical uncertainties calculated from making such comparisons for the two dominant SM backgrounds: $t\bar{t}$ and W+jets. During the calculation of the theoretical uncertainties, requirements used to define the regions may be loosened or removed to prevent the calculations being overly subject to statistical fluctuations in regions where a low number of events is expected (details given in the table captions). $t\bar{t}$ theoretical uncertainties are calculated in the WCR and WVR and visa versa as the CRs and VRs do not have 100% purity with respect to the backgrounds they were designed to estimate.

For the $t\bar{t}$ background the theoretical uncertainties are associated with the modelling of the hard scatter process, the parton showers and the factorization and normalization scales (the uncertainty due to these two scales being jointly denoted as additional

Physics Object	Source of experimental systematic uncertainty
Jets	
	Jet Energy Scale (JES)
	Jet Energy Resolution (JER)
b-jets	
	Flavour Tagging
Soft *b*-jets	
	Soft *b*-tagging (see Section 3.7.4)
Electron	
	Efficiency
	Resolution
	Energy Scale
Muon	
	Efficiency
	Resolution
	Momentum Scale
MET	
	Soft Term (defined in Section 3.7.5)
Pileup	Reweighting (see Section 4.2.1 for a discussion of the origin of pileup)

Table 6.9.: Types of experimental systematic uncertainty considered in the full set of NPs.

radiation). To calculate the uncertainty associated with hard scattering, yields produced when using POWHEG interfaced with PYTHIA 8 are compared with those produced by aMC@NLO interface with PYTHIA 8. Similarly the uncertainty associated with fragmentation/hadronisation in $t\bar{t}$ events is found by comparing POWHEG interfaced with PYTHIA 8 with POWHEG interfaced with HERWIG++. Finally, the uncertainty due to additional radiation was calculated using POWHEG interfaced with PYTHIA 8 where the factorisation and normalisation scales had been modified (increased by a factor of 2 or 0.5) and the resulting yields produced are compared to calculate the uncertainty [210]. It can be seen in Table 6.10, that uncertainties due to the simulation of the hard scattering and the additional radiation are dominant in every region. Due to the use of a TCR and the renormalisation factor (defined in Section 6.13) the uncertainty due to the $t\bar{t}$ cross section was assumed to cancel between the SRs and the TCR.

	SRB1	SRB0	TCR	WCR	TVR	WVR
Theoretical uncertainty [%]						
Hard Scatter	$\pm 9.6 \pm 0.1$	$\pm 10.7 \pm 0.1$	$\pm 11.9 \pm 0.0$	$\pm 10.6 \pm 0.0$	$\pm 11.3 \pm 0.1$	$\pm 15.0 \pm 0.1$
Fragmentation/Hadronisation	$\pm 2.6 \pm 0.1$	$\pm 0.8 \pm 0.1$	$\pm 0.2 \pm 0.0$	$\pm 0.8 \pm 0.0$	$\pm 0.3 \pm 0.1$	$\pm 2.6 \pm 0.1$
Additional Radiation	$\pm 12.6 \pm 0.9$	$\pm 10.0 \pm 0.6$	$\pm 9.1 \pm 0.0$	$\pm 6.7 \pm 0.1$	$\pm 10.6 \pm 0.2$	$\pm 9.9 \pm 0.2$
Total theoretical uncertainty [%]						
Total	$\pm 16.0 \pm 1.0$	$\pm 14.6 \pm 0.7$	$\pm 14.9 \pm 0.0$	$\pm 12.5 \pm 0.1$	$\pm 14.9 \pm 0.5$	$\pm 18.2 \pm 0.4$

Table 6.10.: Theoretical systematic and statistical uncertainties for $t\bar{t}$, given in the form $\pm (\text{sys}) \pm (\text{stat})$. An integrated luminosity of 139 fb^{-1} of MC prediction was used. Total theoretical uncertainties were calculated by adding in quadrature. No M_T requirement was applied to avoid having too few events to perform the calculation with.

	SRB1	SRB0	TCR	WCR	TVR	WVR
Theoretical uncertainty [%]						
Choice of Generator	$\pm 21.9 \pm 0.1$	$\pm 4.3 \pm 0.1$	$\pm 15.2 \pm 0.0$	$\pm 5.5 \pm 0.0$	$\pm 8.1 \pm 0.0$	$\pm 16.3 \pm 0.0$
CKKW	$\pm 0.5 \pm 0.1$	$\pm 1.0 \pm 0.1$	$\pm 4.6 \pm 0.0$	$\pm 6.1 \pm 0.0$	$\pm 4.5 \pm 0.0$	$\pm 4.7 \pm 0.0$
Factorization	$\pm 3.8 \pm 0.1$	$\pm 3.4 \pm 0.1$	$\pm 2.3 \pm 0.0$	$\pm 3.3 \pm 0.0$	$\pm 4.0 \pm 0.0$	$\pm 2.1 \pm 0.0$
Renormalization	$\pm 28.6 \pm 0.1$	$\pm 26.4 \pm 0.1$	$\pm 29.9 \pm 0.0$	$\pm 2.0 \pm 0.0$	$\pm 2.3 \pm 0.0$	$\pm 2.0 \pm 0.0$
Resummation	$\pm 0.4 \pm 0.1$	$\pm 0.6 \pm 0.1$	$\pm 5.8 \pm 0.0$	$\pm 2.4 \pm 0.0$	$\pm 0.3 \pm 0.0$	$\pm 8.9 \pm 0.0$
Total theoretical uncertainty [%]						
Total	$\pm 36.2 \pm 0.2$	$\pm 27.0 \pm 0.2$	$\pm 34.4 \pm 0.0$	$\pm 9.4 \pm 0.0$	$\pm 10.4 \pm 0.0$	$\pm 19.4 \pm 0.0$

Table 6.11.: Theoretical systematic and statistical uncertainties for W+jets, given in the form $\pm (\text{sys}) \pm (\text{stat})$. An integrated luminosity of 139 fb^{-1} of MC prediction was used. Total theoretical uncertainties were calculated by adding in quadrature. Requirements on M_T and b-jet multiplicity were removed in SRB1, as well as a requirement on H_T significance being loosened to > 20. Additionally, the pre-selection was reduced only requiring that events have only one lepton. These changes avoid having too few events to perform the calculation with.

The theoretical uncertainties associated with the W+jets background are shown in Table 6.11, where the yields produced from simulating this background with SHERPA is compared to the yield produced when using MADGRAPH to calculate the uncertainty associated with choosing one generator over another[9]. It can be seen that across all regions where the uncertainty due to W+jets is relevant, the uncertainties due to the choice of generator and renormalisation are dominant. As with the $t\bar{t}$ cross section uncertainty, the W+jets cross section uncertainty is assumed to be cancelled between the SRs and the WCR.

---

[9]As was explained in Ref. [191], Catani-Kuhn-Krauss-Webber (CKKW) matching is concerned with combining calculations using matrix elements and parton showers. Meanwhile, resummation is a mathematical technique to handle poorly converging perturbative calculations in QCD [29].

6.13. Estimating the SM Background and Systematic Uncertainties

In Section 6.2, the concept of using CRs and VRs to provide estimates of the backgrounds in the SRs was introduced. In BSM searches conducted by ATLAS (and CMS) it is typical to obtain these methods by conducting a simultaneous fit, a mathematical procedure that also accounts for the sources of systematic (and statistical) uncertainties discussed in the previous section. The simultaneous fit is performed using the software framework HistFitter [185] and the main concept is outlined below.

The HistFitter framework is able to provide background estimates in the SRs accounting for the systematic and statistical uncertainties by constructing a probability distribution function. If one considers a binned counting experiment, the likelihood function can be written in terms the product of Poisson distributions, assuming that the measurements are statistically independent. One can write the Poisson distribution P of an SR as a function of n_i, which is the number of observed events in the signal region with i bins. The expectation value of the Poisson distribution can be written as $P(\lambda_i, \mu_p, \theta)$, a function of the parameter of interest μ_p which is used to find the normalisation factor for each background process p and the NPs θ that parametrises the systematic uncertainties. For each background process p, a separate normalisation factor is calculated from comparisons between data and MC, as explicitly shown in Equation 6.5 through Equation 6.7. One can denote the probability density function that represents the systematic uncertainties as $C_{\mathrm{SYST}}(\theta^0, \theta)$, where θ^0 is the nominal value around which the systematic uncertainties can be varied [185]. These probability density functions are generally assumed to be unit Gaussians. If the analysis includes statistically independent, orthogonal SRs (as this analysis does) a statistically combined fit can be performed over all SRs to increase the exclusion power of the analysis. Such a statistical combination was used to produce the final exclusion contour achieved by this analysis, shown in Figure 6.22 which is shown in the context of the contours achieved by the two SRs separately in Figure 6.21. Putting this together, the general likelihood function of an event-counting analysis can be written as:

$$\mathcal{L}(n, \theta^0|, \mu_p, \theta) = \prod_{s \in SR} P(n_s|\lambda_s(\mu_p, \theta)) \times \prod_{i \in CR} P(n_i|\lambda_i(\mu_p, \theta)) \times C_{\mathrm{syst}}(\theta^0, \theta) \qquad (6.4)$$

The subscripts s and i refer to the signal and control regions respectively. HistFitter is used to build and configure the parametric models using the likelihood function given in
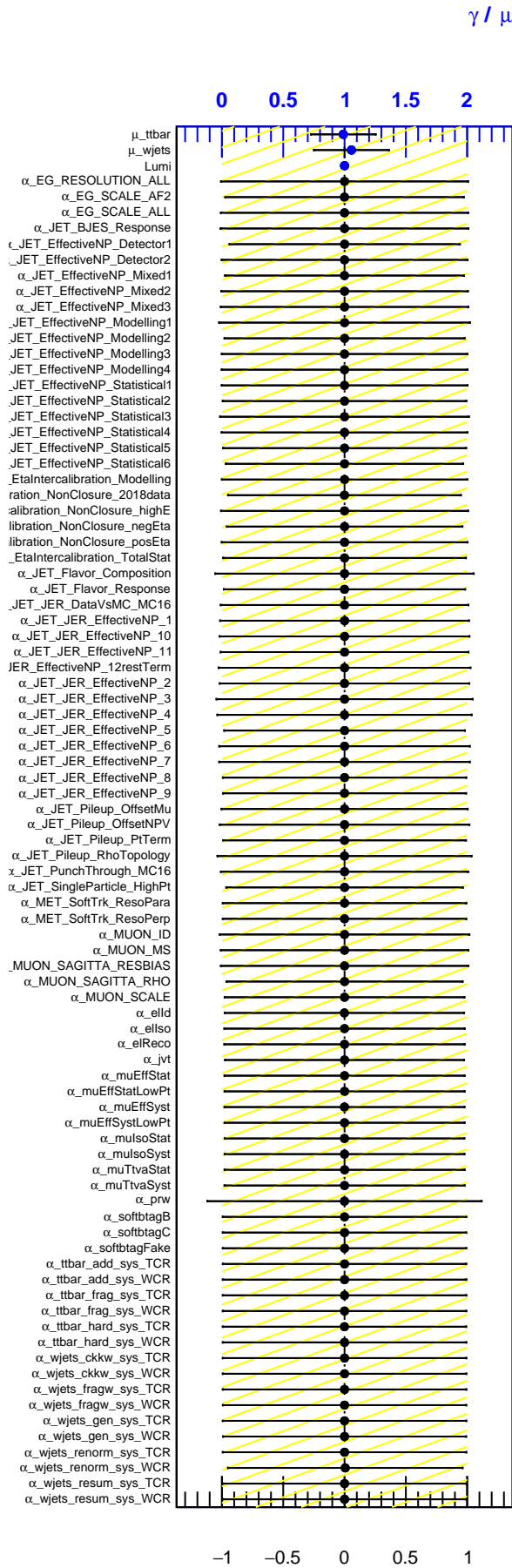
Figure 6.19.: NPs in background only fit.

Equation 6.4 to simultaneously fit the MC predictions to the data in order to estimate the quantity of background events, through the techniques described below.

The regions defined above in an analysis can be used to provide an estimate of the number of background events, by considering that for every SM background process p for which there is an associated CR and VR, one can write:

$$N_{p,SR} = \mu_p M_{p,SR} \tag{6.5}$$

where $N_{p,SR}$ is the number of estimated events of process p in the SR and $M_{p,SR}$ is the number of events for p obtained from MC simulation. The analogous expression can be written for the CR:

$$N_{p,CR} = \mu_p M_{p,CR} \tag{6.6}$$

Through a simple substitution of the parameter of interest μ_p, one obtains:

$$N_{p,SR} = \frac{M_{p,SR}}{M_{p,CR}} \times N_{p,CR} \tag{6.7}$$

where one defines the ratio of the MC estimates in Equation 6.7 as the Transfer Factor (TF) for process p [185]. The TF determines the number of fitted events in the SR after the simultaneous fit has been performed - as it is the constant of proportionality between $N_{p,SR}$ and $M_{p,CR}$.

Extensive checks were performed to validate that HistFitter was correctly processing the data and MC simulations as well as producing results consistent with those from the framework developed using GANGA, discussed above. Firstly, the agreement between the nominal yields recorded the two frameworks was verified, as well as checking that the yields produced from the alternative distributions (introduced in Section 6.12.1) were within a few percent of the yields as expected. This included confirming that the requirements used to define each region and the weights applied to the MC samples were implemented consistently and correctly. The inbuilt functionality of HistFitter to tabularise the yields recorded and the magnitude of each source of uncertainty in every region was extensively used. It was during this validation that the presence of a requirement on the distribution of M_{T} had been imposed on the alternative samples, which is not present in some of the regions used in this analysis and was therefore invalidating the results of the fits. Consequently, all of the results presented in this

chapter were produced from ntuples that were regenerated by the author without the requirement on M_{T} mentioned above.

HistFitter can perform several different types of fit. To provide estimates of the number of background events in the SRs and VRs, the background only fit is performed where only the MC simulation is used and the CRs and VRs are unblinded to the data to avoid biasing the analysis with knowledge of the quantity of data events in the SRs. For each type of background where CRs and VRs are provided μ_p connects the MC expected number of events to the fitted number of events, as shown in Equation 6.13. The values of $\mu_{t\bar{t}}$ and μ_{W+jets} are shown in Figure 6.19 as $\mu_{t\bar{t}} = 0.98 \pm 0.26$ and $\mu_{W+jets}=1.07 \pm 0.31$. This figure also confirms an assumption stated earlier in this section that the NPs are assumed to be well modelled by unit Gaussians.

From performing a background only fit one can also obtain the values of each of the systematic uncertainties, before and after the fit. It should be noted that a particular source of experimental systematic uncertainty (take the JES again for example) may need to be deconstructed into separate components and each of these needs to be modelled by a different NP. As noted in Table 6.9 the full set of nuisance parameters were used in this analysis, accounting for the multiple components associated with each of the sources of experimental systematic uncertainties mentioned in Table 6.9. The value of each component of every systematic in every region is given in Appendix B whilst Table 6.12 shows the largest components ($> 5\%$) of the total systematic uncertainties in in the two SRs, compared to the value of that component in the other SR. It can be seen that in both SRs (as well as in other regions) the total systematic uncertainty is below 30%. In the SRB1 the uncertainties are dominated by those associated with $\mu_{t\bar{t}}$, the JES, the statistical uncertainty of the region, the JER and pileup re-weighting. Similarly, the JES, JER and pileup uncertainties also dominate SRB0 as well as the uncertainty on μ_{W+jets} and $\mu_{t\bar{t}}$ as well as the statistical uncertainty in this region. It is thought that the higher systematic uncertainties in SRB0 compared to SRB1 are primarily introduced through the use of the SV finding algorithm, particularly due to the fact that Table 6.12 shows that the majority of the largest uncertainty components are associated with the JES or JER. It was shown in [27] to have relatively poor agreement between data and MC in some of the distributions of the variables that the algorithm uses, such as p_{T} of the SVs. It can be also seen from Appendix B that the WVR (which is defined using SV information) has a larger total systematic uncertainty at approximately 25% than the TVR (which is not defined using SV information) with a total systematic uncertainty of approximately 22%, despite the fact that Table 6.13 shows that the WVR has almost

3 times as many events than the TVR. Additionally, the analogous SRs in [27] that use SV information in their definitions are also shown to have larger total systematic uncertainties than shimilar regions using traditional b-tagging techniques.

Uncertainty of channel	SRB1	SRB0
Total background expectation	1.57	5.86
Total statistical ($\sqrt{N_{exp}}$)	± 1.25	± 2.42
Total background systematic	± 0.39 [24.84%]	± 1.74 [29.62%]
mu_ttbar	± 0.32 [20.5%]	± 0.58 [9.9%]
alpha_JET_EffectiveNP_Statistical4	± 0.18 [11.8%]	± 0.18 [3.1%]
gamma_stat_SRB1_cuts_bin_0	± 0.11 [7.1%]	± 0.00 [0.00%]
alpha_JET_Flavor_Composition	± 0.07 [4.2%]	± 0.58 [9.9%]
alpha_JET_JER_EffectiveNP_11	± 0.05 [3.2%]	± 0.70 [11.9%]
alpha_JET_JER_EffectiveNP_2	± 0.04 [2.8%]	± 0.43 [7.4%]
alpha_JET_EtaIntercalibration_TotalStat	± 0.03 [1.7%]	± 0.32 [5.5%]
alpha_JET_Pileup_OffsetNPV	± 0.02 [1.6%]	± 0.34 [5.7%]
alpha_JET_EffectiveNP_Mixed1	± 0.02 [1.5%]	± 0.61 [10.3%]
alpha_JET_JER_EffectiveNP_4	± 0.02 [1.5%]	± 0.59 [10.1%]
alpha_JET_EffectiveNP_Mixed3	± 0.02 [1.4%]	± 0.32 [5.5%]
alpha_JET_EtaIntercalibration_Modelling	± 0.02 [1.3%]	± 0.49 [8.4%]
alpha_JET_EffectiveNP_Statistical6	± 0.02 [1.3%]	± 0.60 [10.2%]
alpha_JET_JER_EffectiveNP_3	± 0.02 [1.2%]	± 0.53 [9.1%]
alpha_JET_Pileup_RhoTopology	± 0.02 [1.2%]	± 0.50 [8.6%]
alpha_JET_JER_EffectiveNP_3	± 0.02 [1.2%]	± 0.53 [9.1%]
alpha_JET_EtaIntercalibration_NonClosure_negEta	± 0.01 [0.71%]	± 0.29 [5.0%]
alpha_JET_JER_EffectiveNP_10	± 0.01 [0.60%]	± 0.36 [6.2%]
alpha_JET_EffectiveNP_Modelling1	± 0.01 [0.52%]	± 0.76 [13.0%]
alpha_JET_EffectiveNP_Modelling2	± 0.01 [0.50%]	± 0.56 [9.6%]
mu_wjets	± 0.01 [0.41%]	± 0.96 [16.4%]
alpha_JET_EffectiveNP_Modelling4	± 0.00 [0.21%]	± 0.57 [9.7%]
alpha_JET_JER_EffectiveNP_1	± 0.00 [0.25%]	± 0.44 [7.6%]
alpha_JET_EtaIntercalibration_NonClosure_posEta	± 0.00 [0.13%]	± 0.30 [5.1%]
gamma_stat_SRB0_cuts_bin_0	± 0.00 [0.00%]	± 0.98 [16.7%]

Table 6.12.: Comparison of the dominant systematic and statistical uncertainties in the two SRs above a threshold of 5% ordered with reference to SRB1. Components that contribute more than 5% to the total uncertainty of the SR are highlighted in red. The full table is shown in Appendix B. Note that the individual uncertainties can be correlated, and do not necessarily add up quadratically to the total background uncertainty, which includes all components given in Appendix B. The percentages show the size of the uncertainty relative to the total expected background.

6.14. Unblinding the Signal Regions

As mentioned, the analysis is designed and the simultaneous fits are performed with the SRs blinded as to not introduce bias. This section presents the results of unblinding the SRs after the two types of simultaneous fits had been performed. The *top* half of Table 6.13 shows the estimated number of each type of background event given the inputted number shown in the lower half of the table. The table shows that 1.6 $\pm$ 0.4 events were expected in the SRB1 according to the MC prediction after the fit and 2 events were observed in the data. Meanwhile in the SRB0, 5.9 $\pm$ 2.5 events were expected according to MC simulations after the fit was performed while 6 events were observed in data. Therefore, no significant excess was observed from this analysis above the SM background and limits on the *stop* and neutralino masses in processes with one isolated lepton in their final state were set at 95% confidence level, as is described in Section 6.15.

Figure 6.20 shows coarsely binned distributions of the two main variables used in this analysis - aM_{T2} and H_T significance - plotted in the two VRs with all sources of systematic and statistical uncertainties included in the error bands. It can therefore be seen that the sources of uncertainties are well modelled in the VRs in these distributions and the data/MC ratio is close to unity as observed previously.

Table 6.14 and Table 6.15 display the physical properties of the data events that were observed in SRB0s and SRB1. Despite the fact that the data collected does not provide any evidence for physics beyond the SM, it is interesting to examine the properties of these eight events in the context of a experimental signature searched for in this analysis. The final state that was searched for contained soft b-jets and the MET was enhanced due to a high-pt ISR jet. In Table 6.15 it can be seen that of the two events that contain b-jets, all of those b-jets are in the lower half of the list of jets ordered in p_T (note that the *b*-jets are highlighted in red). In addition, in the majority of events in both SRs the MET is at least a couple of hundred GeV above the minimum requirement of 230 GeV set in the pre-selection.

	SRB1	SRB0	TCR	WCR	TVR	WVR
Observed events	2	6	1186	2534	158	732
Fitted bkg events	1.6 ± 0.4	5.9 ± 2.5	1186 ± 34	2533 ± 50	157 ± 34	747 ± 50
Fitted ttbar events	1.2 ± 0.4	2.3 ± 0.8	949 ± 47	247 ± 44	114 ± 33	93 ± 17
Fitted wjets events	$0.02^{+0.05}_{-0.02}$	3.4 ± 2.1	122 ± 30	2030 ± 70	22 ± 8	580 ± 50
Fitted zjets events	0.01 ± 0.00	0.12 ± 0.02	2.26 ± 0.04	83.8 ± 1.4	1.49 ± 0.03	31.5 ± 0.5
Fitted singletop events	0.12 ± 0.07	$0.08^{+0.21}_{-0.08}$	85 ± 9	45 ± 5	13.2 ± 2.1	15.4 ± 2.6
Fitted multiboson events	0.11 ± 0.01	0.10 ± 0.02	16.40 ± 0.28	127.0 ± 2.2	4.33 ± 0.07	31.0 ± 0.5
Fitted ttV events	0.06 ± 0.03	0.00 ± 0.00	9.5 ± 0.8	2.2 ± 0.3	1.68 ± 0.25	0.48 ± 0.18
Fitted tWZ events	0.00 ± 0.00	0.00 ± 0.00	1.12 ± 0.02	0.32 ± 0.01	0.11 ± 0.00	0.12 ± 0.00
MC exp. SM events	1.58	5.78	1189.02	2424.67	156.93	716.88
MC exp. ttbar events	1.26	2.29	959.36	249.22	115.75	93.64
MC exp. wjets events	0.02	3.19	115.63	1917.00	20.41	544.73
MC exp. zjets events	0.01	0.12	2.26	83.84	1.49	31.53
MC exp. singletop events	0.12	0.08	84.74	45.10	13.16	15.40
MC exp. multiboson events	0.11	0.10	16.40	127.01	4.33	30.99
MC exp. ttV events	0.06	0.00	9.52	2.18	1.68	0.48
MC exp. tWZ events	0.00	0.00	1.12	0.32	0.11	0.12

Table 6.13.: Yields after unblinding the SRs showing no significant excesses.
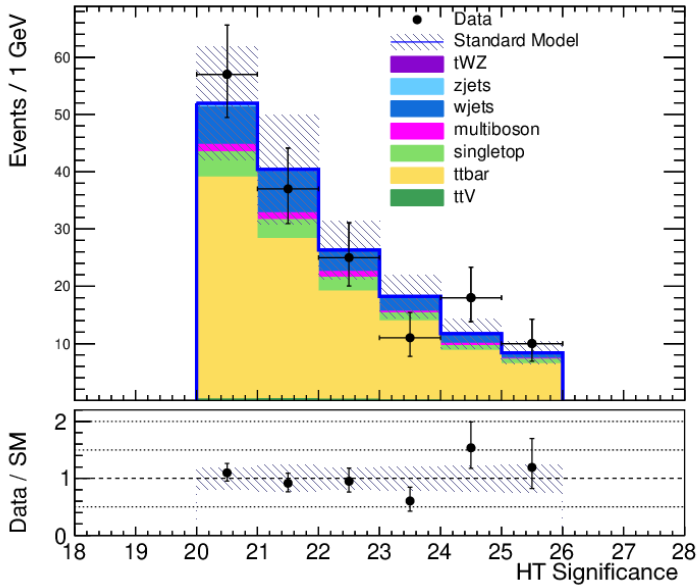
(a) H_T significance in the TVR after fit
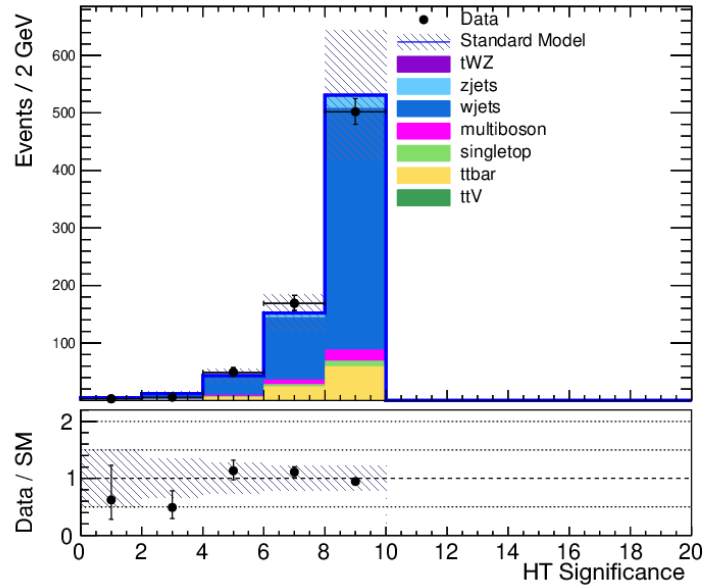
(b) H_T significance in the WVR after fit
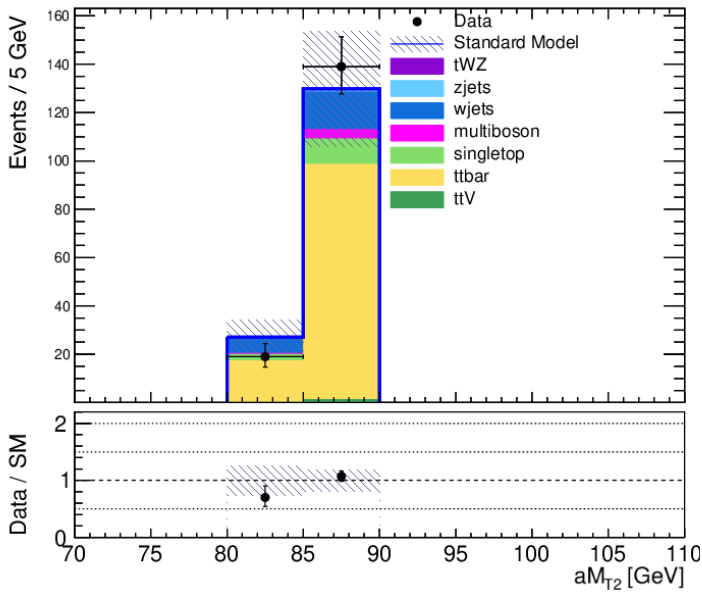
(c) aM_T2 in the TVR after fit
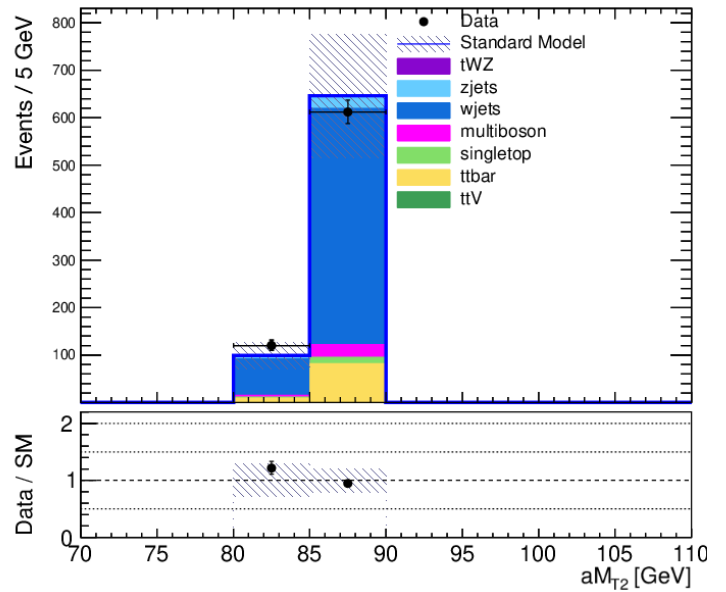
(d) aM_T2 in the WVR after fit

Figure 6.20.: aM_T2 and H_T significance distributions in the TVR and WVR after fit, with error bands incorporating all sources of systematic and statistical uncertainties

Event Properties	
Event number	1111403427
Run Number	329780
aM_{T2} [GeV]	85
MET [GeV]	458
H_T significance	23

Jet Properties	p_T [GeV]	η [rad]	ϕ [rad]	b-jet
jet 1	318	−0.8	0.5	False
jet 2	170	1.5	1.0	False
jet 3	30	0.15	−1.5	False
jet 4	30	−1.3	0.7	False
jet 5	30	−2.0	1.4	False
jet 6	24	0.13	−0.7	False
jet 7	22	0.31	1.5	False
jet 8	22	2.1	−2.7	False

Lepton Properties	p_T [GeV]	η [rad]	ϕ [rad]	Type
Lepton	54	0.17	−2.3	Muon

(a)

Event Properties	
Event number	4099423240
Run Number	302300
aM_{T2} [GeV]	83
MET [GeV]	583
H_T significance	21

Jet Properties	p_T [GeV]	η [rad]	ϕ [rad]	b-jet
jet 1	592	0.9	−1.9	False
jet 2	39	−0.6	−0.9	False
jet 3	37	1.5	2.7	False
jet 4	31	1.6	−2.3	False
jet 5	26	2.5	3.0	False
jet 6	25	−1.0	1.6	False
jet 7	24	1.4	−1.5	False

Lepton Properties	p_T [GeV]	η [rad]	ϕ [rad]	Type
Lepton	68	−1.4	1.4	Electron

(b)

Event Properties	
Event number	518657095
Run Number	334907
aM_{T2} [GeV]	89
MET [GeV]	231
H_T significance	21

Jet Properties	p_T [GeV]	η [rad]	ϕ [rad]	b-jet
jet 1	299	−0.07	−1.3	False
jet 2	65	−0.6	−1.1	False
jet 3	46	1.1	−0.6	False
jet 4	40	0.9	1.4	False
jet 5	22	0.7	−2.1	False

Lepton Properties	p_T [GeV]	η [rad]	ϕ [rad]	Type
Lepton	6.5	−0.7	−2.2	Muon

(c)

Event Properties	
Event number	1046694277
Run Number	350160
aM_{T2} [GeV]	84
MET [GeV]	406
H_T significance	23

Jet Properties	p_T [GeV]	η [rad]	ϕ [rad]	b-jet
jet 1	238	0.029	0.8	False
jet 2	151	0.4	−0.5	False
jet 3	140	−0.10	−1.3	False
jet 4	44	0.9	2.1	False
jet 5	20	1.4	2.0	False

Lepton Properties	p_T [GeV]	η [rad]	ϕ [rad]	Type
Lepton	46	1.3	2.8	Electron

(d)

Event Properties	
Event number	800793978
Run Number	363710
aM_{T2} [GeV]	88
MET [GeV]	429
H_T significance	21

Jet Properties	p_T [GeV]	η [rad]	ϕ [rad]	b-jet
jet 1	458	0.7	1.8	False
jet 2	86	−1.7	−3.0	False
jet 3	55	0.9	−1.5	False
jet 4	50	−2.2	3.1	False
jet 5	23	−2.2	1.7	False
jet 6	23	−2.5	0.5	False

Lepton Properties	p_T [GeV]	η [rad]	ϕ [rad]	Type
Lepton	10.2	−1.2	0.6	Electron

(e)

Event Properties	
Event number	2124237435
Run Number	359058
aM_{T2} [GeV]	85
MET [GeV]	429
H_T significance	20

Jet Properties	p_T [GeV]	η [rad]	ϕ [rad]	b-jet
jet 1	403	−0.9	−1.0	False
jet 2	87	1.0	−2.7	False
jet 3	85	−1.9	−1.8	False
jet 4	28	−0.5	1.7	False
jet 5	28	0.7	2.5	False
jet 6	26	−1.4	−0.7	False
jet 7	25	−2.4	−1.5	False

Lepton Properties	p_T [GeV]	η [rad]	ϕ [rad]	Type
Lepton	24	−1.1	1.1	Muon

(f)

Table 6.14.: Properties of data events in SRB0.

Event Properties	
Event number	2792280393
Run Number	303338
aM_{T2} [GeV]	85
MET [GeV]	607
H_T significance	29

Jet Properties	p_T [GeV]	η [rad]	ϕ [rad]	b-jet
jet 1	302	0.6	0.13	False
jet 2	225	1.2	0.25	False
jet 3	221	2.1	1.3	False
jet 4	59	−2.0	−2.2	True
jet 5	49	0.7	0.7	False
jet 6	33	0.07	−0.32	False
jet 7	29	−0.24	2.0	True

Lepton Properties	p_T [GeV]	η [rad]	ϕ [rad]	Type
Lepton	39	−0.7	2.4	Electron

(a)

Event Properties	
Event number	912129731
Run Number	309375
aM_{T2} [GeV]	85
MET [GeV]	326
H_T significance	26

Jet Properties	p_T [GeV]	η [rad]	ϕ [rad]	b-jet
jet 1	583	0.29	0.4	False
jet 2	26	0.4	1.6	False
jet 3	22	−0.4	−2.1	True
jet 4	21	0.5	−1.6	False

Lepton Properties	p_T [GeV]	η [rad]	ϕ [rad]	Type
Lepton	29	−1.0	2.2	Muon

(b)

Table 6.15.: Properties of data events in SRB1. b-tagged jets are highlighted in red.

6.15. Exclusion of a Hypothesis

Once the sources of backgrounds and the systematic uncertainties have been quantified in the analysis, as described in previous sections, another type of simultaneous fit is performed. Unlike the background only fit, this so-called *exclusion* fit sets limits on the compressed SUSY scenarios examined in this analysis and hence it can be determined if the analysis shows there is enough evidence to exclude the null hypothesis of the SM. To perform this fit, an additional parameter of interest, μ_{sig}, is included in the expression of the likelihood function in Equation 6.4. If $\mu_{\text{sig}} = 0$, this would signify the background only hypothesis H_0 was supported while $\mu_{\text{sig}} = 1$ corresponds to evidence supporting the background plus signal hypothesis H_1 [184]. The CL_S technique [211] provides a means of setting limits on which SUSY are scenarios are excluded. A review of the use of this technique within the ATLAS and CMS collaborations can be found in [212].

It is convenient to summarise which alternative hypotheses are excluded graphically using an exclusion contour plot with the masses of the *stop* and LSP on the axis of the plot. As the SUSY scenarios considered are compressed, it can be clearer to plot the exclusion in terms of the *stop* mass and the mass splitting between the *stop* and the LSP. Exclusion contour plots for both SRs can be seen in Figure 6.21 where the second parametrisation has been used and all limits are set to a confidence level of 95%. It can be seen that the majority of the sensitivity of this analysis is contributed by SRB1, although SRB0 is able to extend the sensitivity downwards on the scale of $\Delta m(\tilde{t}_1, \tilde{\chi}_1^0)$ by
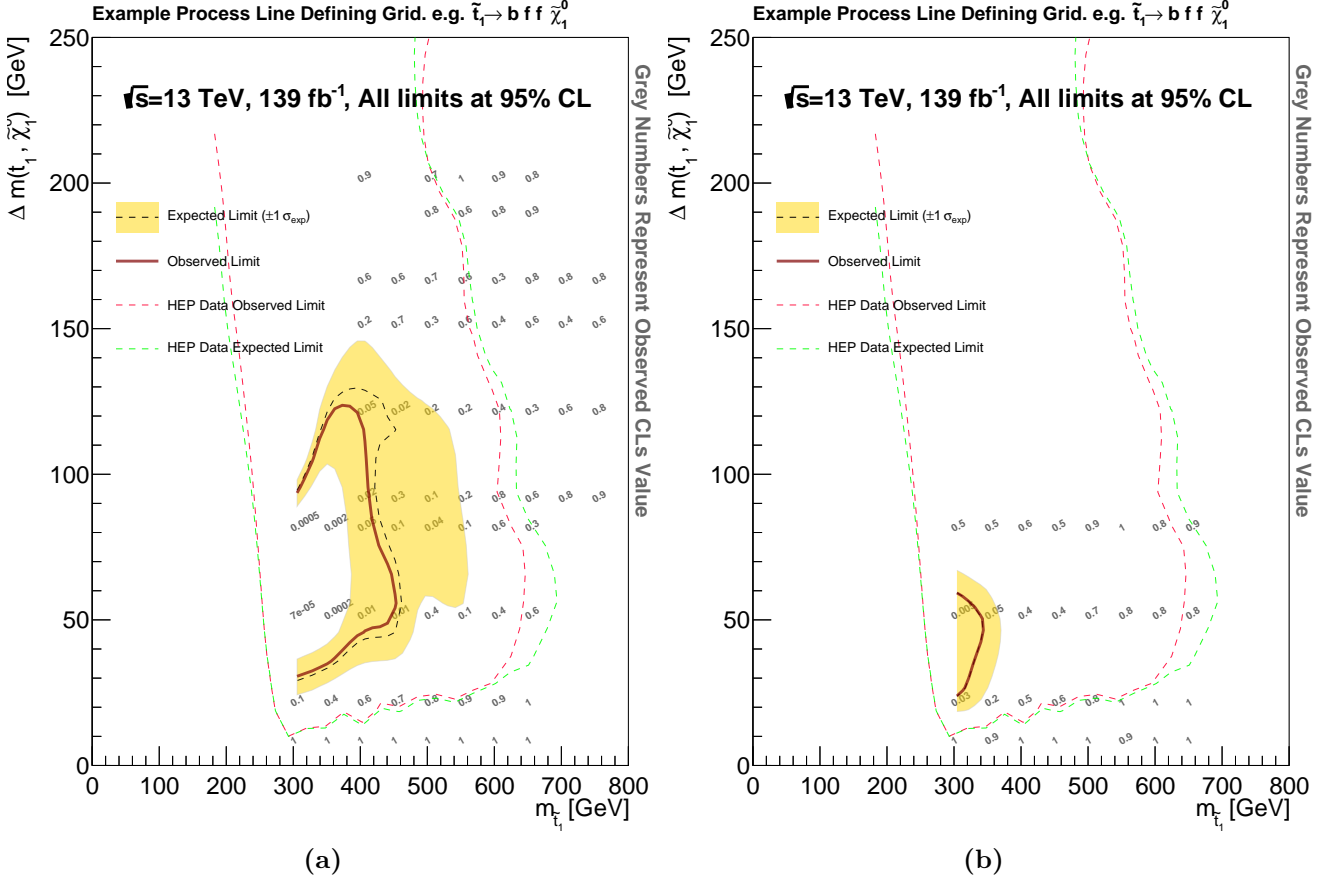
Figure 6.21.: Exclusion contours for (a) SRB1 and (b) SRB0 plotted with the $m_{\tilde{t}_1}$ vs. $\Delta m(\tilde{t}_1, \tilde{\chi}_1^0)$ parametrisation, where the black numbers denote the p-value of each point on the signal grid. Limits are shown in comparison with those found in Ref. [27].

approximately 5 GeV. These exclusion limits are shown in comparison to those presented in Ref. [27], found by a statistical combination of the SRs used to target *stop* decays with a compressed SUSY mass spectrum in that analysis. The depth of the exclusion achieved is also greater for SRB1.

A statistical combination contour of the SRB1 and SRB0, presented in both of the parametrisations, is shown in Figure 6.22. The statistical combination can be performed as the two SRs are orthogonal to each other. *Stop* quarks are found to be excluded up to 500 GeV and mass splittings between the *stop* and the neutralinos are found to be excluded up to 130 GeV. Thus it is concluded that these exclusion limits compliment those found in Ref. [27], by employing SRs invoking the unconventional requirement of an upper bound on the aM_{T2} variable close to its kinematic minimum. As to be

expected, there is far greater sensitivity to models with a lower mass splittings (up to the limit of 20 GeV where the precision of the reconstruction of jets is reduced) as this analysis depends on a requirement of low aM_{T2}. This is due to the fact that, as has been demonstrated, *stop* decays with a mass splitting of approximately 50 GeV have an associated distribution of aM_{T2} that is peaked just above the kinematic minimum, where as those with a greater mass splitting have a much higher peak in aM_{T2} and hence a low aM_{T2} requirement would not be optimal to search for them (see Chapter 5). The observed contour lies within the expected contour as in both SRs the observed number of events in data is slightly higher than the MC prediction, though well within the uncertainty bands so is consistent with the SM. Figure 6.22 also shows that the SUSY processes where the b-jet p_T is too low to be detected by the calorimeter, remain experimentally difficult to search for, as was predicted by the lower $\mathcal{Z}$-values obtained in SRB0 compared to SRB1 shown in Figure 6.16. The two "lobes" seen in the exclusion contours in Figure 6.22a result from the contour being a statistical combination of the exclusion contours of the two "lobes" shown in the contours of SRB1 and SRB0 in Figure 6.21.
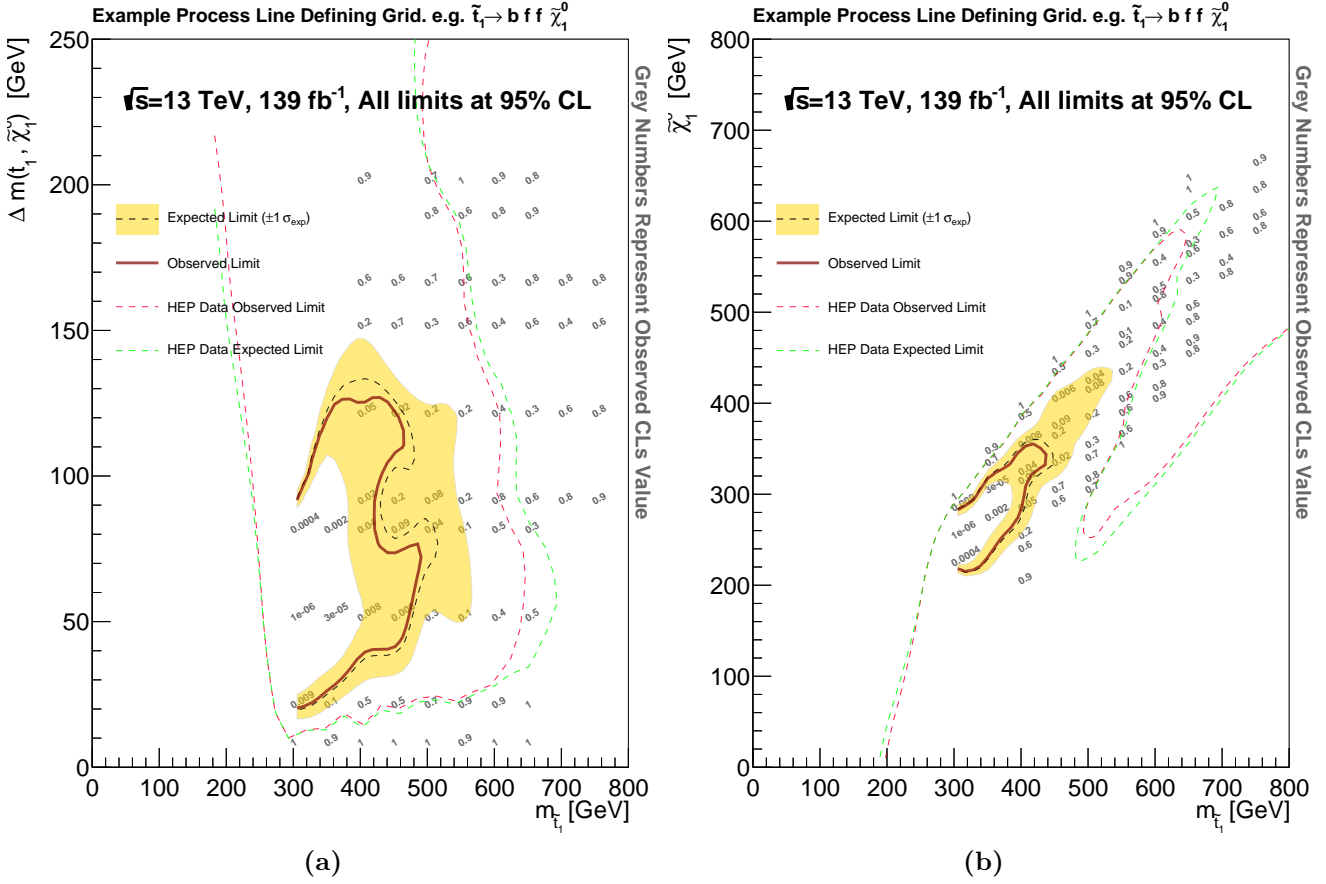
Figure 6.22.: Exclusion contours for a SRB1 and SRB0 combination plotted with the (a) $m_{\tilde{t}_1}$ vs. $m_{\tilde{\chi}_1^0}$ and (b) $m_{\tilde{t}_1}$ vs. $\Delta m(\tilde{t}_1, \tilde{\chi}_1^0)$ parametrisation, where the black numbers denote the p-valueof each point on the signal grid. Limits are shown in comparison with those found in Ref. [27].

6.16. Conclusions

In this chapter, the development and use of SRs to search for the *stop* decay $\tilde{t}_1 \to b f f' \tilde{\chi}_1^0$, with mass splittings between the *stop* and the LSP down to 7 GeV, is presented. The region of SUSY phase space that such decays occupy is relatively inaccessible due to the softness of the decay products caused by the compressed mass spectrum considered. Therefore, the experimental signature of this process is soft *b*-jets, elevated MET resulting from a high-p_{T} jet boosting the di-*stop* system and one isolated lepton is required in the final state.

To search for decays of this kind, two SRs were proposed - one targeting events where *b*-jet identification involving the calorimeter has tagged one or more *b*-jets in the final state and the other using a *b*-veto to target those events for which calorimeter based

b-tagging has failed. Instead, SV information is used to the infer the presence of *b*-jets in these events. Both SRs employ the aM_{T2} variable and upper bound to discriminate signal events from those of the SM background, an approach that was validated in the analysis presented in Chapter 5. In contrast, most analyses make use of aM_{T2} to place a *lower* bound on the mass of SUSY particles. The two dominant SM backgrounds in this analysis were $t\bar{t}$ and W+jets and dedicated CRs and VRs were used to estimate the levels of these backgrounds in the SRs. These regions were also used to perform simultaneous fits in order to calculate the experimental and theoretical systematic uncertainties associated with the SRs, as well as to perform a hypothesis test to determine whether the data showed any evidence for deviations from the SM prediction. No significant excess was observed above the SM background and limits at 95% confidence level are set. *Stop* quarks are found to be excluded up to 500 GeV and mass splittings between the *stop* and the neutralino are found to be excluded up to 130 GeV, complimenting the exclusion limits found in [27] and other searches for *stop* decays with one lepton final states.

Chapter 7.

Final Thoughts

"So Long, and Thanks for All the Fish."
— Douglas Adams

The beginning of the third decade of the 21$^{\text{st}}$ century is a very exciting (if unnerving) time to be conducting particle physics research. It is a very exciting period because, as discussed in Chapter 1 and Chapter 2, across the entire field, answers are being sought to profound questions, from the origins of dark matter to an explanation for the apparent fine-tuning of the Higgs mass. The phenomenological landscape of possible (and much-needed) extensions to the SM is vibrant and complex, handing experimentalists the thrilling task of determining which (if any) of the proposed theories are realised by nature. The need to design and build experiments to achieve this aim has also presented a huge instrumental challenge involving technologies as diverse as silicon microstrip sensors used for tracking, to liquid argon calorimeters [73, 98, 213]. A necessity to use such a range of technologies could be expected in a field where measurements of energies are made over a range of 24 orders of magnitude - from the cosmic microwave background to cosmic rays [214, 215]. A brief description of the technologies used in the context of the ATLAS detector was given in Chapter 3. As mentioned in Chapter 4, the higher the luminosity of a particle accelerator, the greater its potential for delivering a statistically significant sample of a given type of event, a fact that will become particularly relevant as ever-harder-to-reach regions of BSM phase space are probed. After Run 3 of the LHC[1], the statistical gain in operating the accelerator without a significant luminosity increase beyond its design values will become marginal [216]. With this in mind, the use of the

---

[1]Which is anticipated to last from 2022-2024.

ATLAS SCT as the luminometer operating with a hit-counting algorithm is proposed. Thus, the SCT's luminosity measurement would be compared to those of the existing luminometers, in line with ATLAS's strategy to control systematic uncertainties [84]. It was shown that, if the SCT is operated in the 01X binary readout mode, considering two-or-more-strip clusters, a luminosity measurement in agreement with LUCID and TileCal to within 10% can be made. This study could also be seen as an example of the technological lateral thinking that is demanded if BSM physics is to be searched for - in that the sub-detector, which was intended to provide ATLAS with tracking information, was tested for its utility in providing a luminosity measurement.

Despite this extremely optimistic picture, the current landscape of high-energy physics can still be described as unnerving. Throughout the second half of the 20th century, and up until the discovery of the Higgs boson in 2012, there was experimental verification of each fundamental particle that the SM predicted in turn. In such a climate, the particle physicist can be said to be aided by the no-lose theorem: where either the SM was experimentally validated, or much sought-after evidence of BSM physics was found. This is not the situation that the current community of particle physicists find themselves in. Where before there was a single theoretical framework to experimentally investigate, there is now a multitude of theoretically viable extensions to it that would complete our understanding of nature. Moreover, even SUSY, the BSM framework examined in this thesis, cannot be described as a single model but more a framework of many models, differing dramatically in key aspects of their predictions - such as the method by which SUSY is broken and the values of the masses of the hypothesised sparticles (see Section 2.4 for discussion).

Given the theoretical motivation that the existence of a supersymmetric partner to the top quark would provide an elegant solution to the hierarchy problem, an experimental search for the *stop*-quark is the subject of Chapter 5 and Chapter 6. As explained in Chapter 5, the analysis that has been presented targets a relatively inaccessible region of SUSY parameter space as the mass spectrum considered is compressed and, consequently, the products of the decay are soft. b-jets are a prominent feature of the final states of *stop* decays and are precisely reconstructed by the ATLAS calorimeter as long as their p_{T} is above 20 GeV. However, if the SUSY spectrum is compressed, b-jets are frequently produced with a p_{T} less than 20 GeV. Hence, as is shown in Chapter 5, the use of SV information can be used to extend the ATLAS detector's capability to identify such soft b-jets which is crucial when searching for compressed SUSY processes. This analysis focuses, in part, on the use of the aM_{T2} variable in the search for *stops*. In Chapter 5,

it was shown that the variable can effectively provide an upper limit on the mass of the *stop*, in addition to its more common usage of providing a lower limit on the mass of pair-produced particles. In Chapter 6, the unconventional technique of employing aM_{T2} as an upper bound in conjunction with SV information is used (along with other kinematic variables and those taking into account the detector resolution) to perform an analysis focused on *stop* decays with very compressed mass spectra. After considering all sources of experimental and theoretical systematic uncertainties, no significant excess was observed above the SM backgrounds and exclusion limits on *stop* and the mass splitting between the *stop* and the neutralino mass were set at 500 GeV and 130 GeV respectively at a 95% confidence level. Hence, this analysis with its novel use of the aM_{T2} variable, complements the results found in other *stop* searches such as [27].
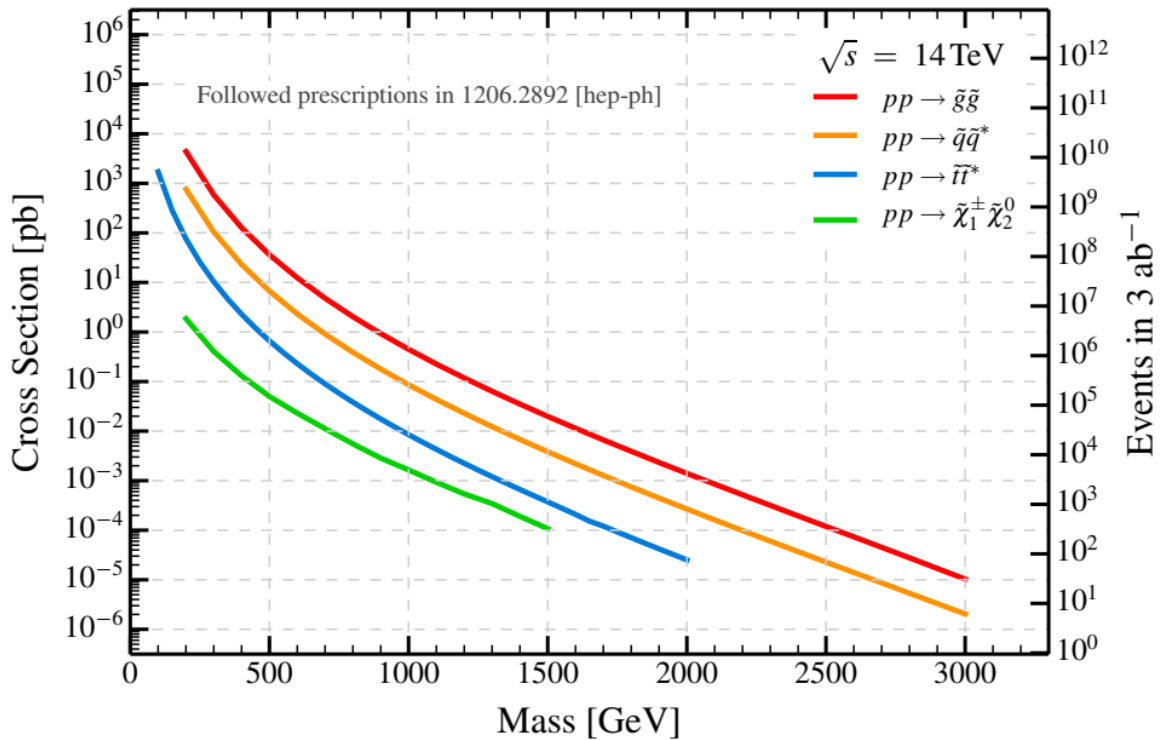
Figure 7.1.: NLO cross section for the production of SUSY particles at the LHC as a function of the average mass of pair produced sparticles. Figure taken from [217].

At the time of writing, the exclusion of the parameter space of *stop* decays that is currently within reach of the ATLAS detector has been maximised (as shown by the analysis presented here and [27]), assuming the *stop* decays to a neutralino and a *top* quark, where the final state includes one isolated lepton. Therefore, within the remit of
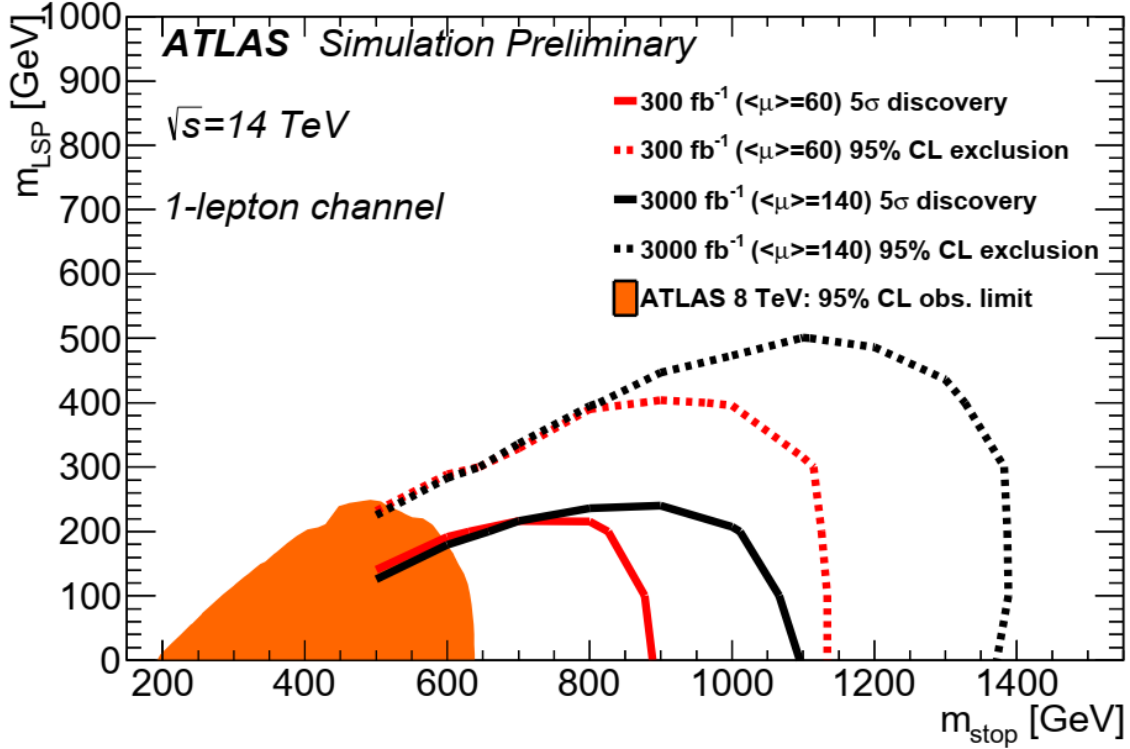
Figure 7.2.: ATLAS limits on the expected sensitivity of *stop* anti-*stop* production at the LHC for samples with 300 fb^{-1} and 3000 fb^{-1} of ATLAS data with 14 TeV *pp* collisions. Figure taken from [217].

this final state, the focus of investigation is now shifting within the ATLAS collaboration to search for evidence of pseudo-scalar dark matter particles in simplified models, both in events involving *top* pair production and single tops. It would, of course, be desirable to exclude or indeed discover stops with masses that were beyond the scope of the analysis presented here. As Figure 7.1 shows, the cross section of stop pair production is inversely proportional to the mass of the *stop* and therefore the significant increase in data provided by upcoming runs of the LHC will invaluable to search for theses processes. The upgrades to ATLAS concurrent with these runs will most probably produce further decreases of the minimum p_{T} at which b-jets can be reconstructed but it is still envisioned that the use of SV information would be beneficial to an analysis of this type given the b hadron p_{T} spectrum shown in Figure 5.9. The projected extent of exclusion in the $m_{\tilde{t}_1} - m_{\tilde{\chi}_1^0}$ plane after inclusion of 300 fb^{-1} and 3000 fb^{-1} of ATLAS data from future runs of the LHC is shown in Figure 7.2 which will greatly narrow down the parameter space in which SUSY could be living. It is intended that extensions to the analysis presented here

would continue to focus on benchmark points corresponding to compressed *stop* decays, at the limit of the exclusion achieved at the time of the analysis.

Without having a single theoretical framework to compare experimental findings against, physicists are dependent on their apparatus being capable of detecting, possibly incredibly small, deviations from the SM in order to determine which of the multitude of BSM models is realised by nature. In the event that no deviations are detected, only exclusion limits can be set on the parameter space in which BSM physics could be found. This bottom-up (data driven) approach is fundamentally different from the top-down (theory) approach that was needed to experimentally test the SM [213].

Despite the challenges and the seemingly unyielding mysteries, the particle physicist should not be discouraged by the lack of a definite direction in the field at the moment. After all, it is the prospect of discovering the unknown that is one of the thrills of scientific research.

Appendix A.

Stop Feasability Study

This appendix contains details of the feasability study conducted with 36.1 fb^{-1} of ATLAS data. The requirements used to define each of the regions in this study, as well as the purity of the proposed CRs and the total number of SM background events predicted by MC, is given in Table 6.3.

As mentioned in Chapter 6, the feasbility study proposed the use of a LSR and TSR both requiring events to have one or more b-tagged jets (the treatment of b-jets that failed detection by the calorimeter was not considered at this stage). To estimate the dominant $t\bar{t}$ and W+jets backgrounds, the study proposed a TCR, defined by reversing the requirement on H_{T} significance, as well as a WCR defined by implementing a b-veto and otherwise maintaining the requirements in the SRs. Whilst it is preferable to keep a CR as kinematically close to an SR as possible to maximise the accuracy of the background estimation in the SR, the accuracy of the estimation is also increased by using a CR with a large number of events. It was found that an alternative WCR (termed WCR loose) could be proposed with twice as many events as the WCR by removing the requirement on H_{T} significance whilst keeping the region relatively kinematically similar the SRs [1]. A schematic of the parameter space occupied by the SRs and CRs in this study is shown in Figure A.1.

---

[1]A conclusion on which WCR was more effective could have been made had the study been taken further to encompass a simulatenous fit.
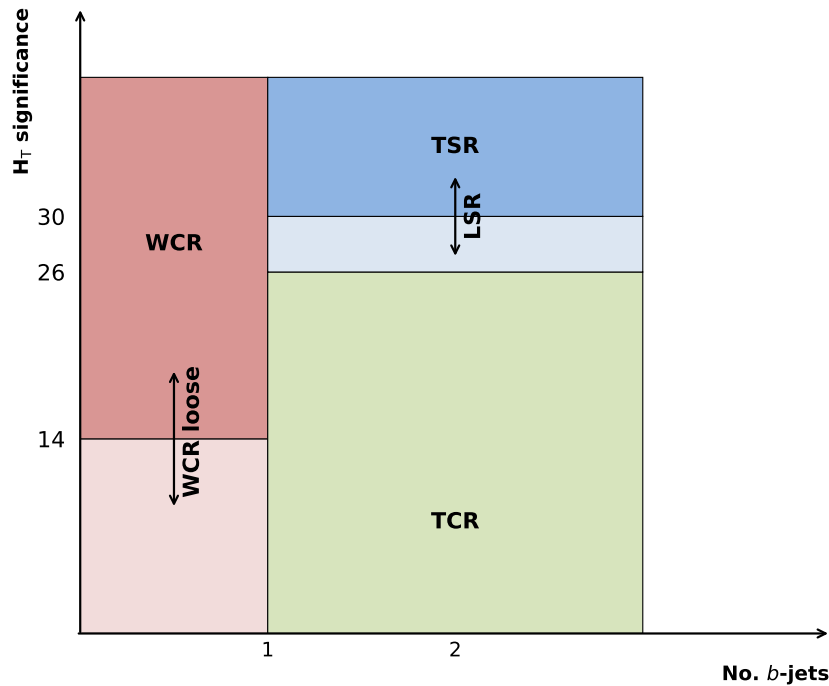
Figure A.1.: Schematic diagram of the parameter space occupied by the SRs and CRs designed by this analysis in the No. b-jets - H_T significance plane

A.1. *Top* Control Region

Signal events tend towards higher values of H_T significance while background events tend towards lower values. Therefore, a disjoint TCR could be defined by reversing the lower bound on H_T significance used to define the LSR. The upper bound on H_T significance used to define the TCR is therefore 26, with a relatively high purity of 65%.

A.2. *W*+jets Control Region

It has been explained that the majority of W+jets events result in light flavour jets. Therefore, a region with a high purity of W+jet events could be defined by imposing a veto on b-jets which would be disjoint from the SR. So a WCR was defined using the same requirements as those which define the LSR, but changing the requirement on the number of b-jets to a b-veto, as summarized in Table 6.3. It was also found that the total normalised background of the WCR was increased by approximately a factor of three by reducing the lower bound on H_T significance from 18 to 14 whilst keeping the purity of the region approximately equal, $\pm 1\%$. This would thus decrease statistical

uncertainties. An alternative CR for the W+jet background, termed WCR loose, can be defined by removing the requirement on H_T significance completely and thus increasing the total normalized background by approximately a further factor of two (from 173 ± 8 normalised events to 387 ± 14 normalised events). From Table 6.3 it can be seen that high purities of 81% and 80% can be obtained for the WCR and WCR loose, respectively.

Appendix B.

Full systematics after simultaneous fit

This appendix shows the values of every nuisance parameter in every region of the analysis presented in Chapter 6. Individual uncertainites can be correlated and do not necessarily add up quadratically to the total background. The percentages show the total size of the uncertainty relative to the total expected background.

Uncertainty of channel	SRB1	SRB0	TCR	WCR	TVR	WVR
Total background expectation	1.57	5.86	1185.75	2532.98	156.91	745.07
Total statistical ($\sqrt{N_{exp}}$)	± 1.25	± 2.42	± 34.43	± 50.33	± 12.53	± 27.30
Total background systematic	± 0.39 [24.84%]	± 1.74 [29.62%]	± 34.39 [2.90%]	± 50.16 [1.98%]	± 34.07 [21.71%]	± 186.66 [25.05%]
mu_ttbar	± 0.32 [20.5%]	± 0.58 [9.9%]	± 244.53 [20.6%]	± 63.46 [2.5%]	± 29.48 [18.8%]	± 23.86 [3.2%]
alpha_JET_EffectiveNP_Statistical4	± 0.18 [11.8%]	± 0.18 [3.1%]	± 7.61 [0.64%]	± 1.36 [0.05%]	± 12.06 [7.7%]	± 6.47 [0.87%]
gamma_stat_SRB1_cuts_bin_0	± 0.11 [7.1%]	± 0.00 [0.00%]	± 0.00 [0.00%]	± 0.00 [0.00%]	± 0.00 [0.00%]	± 0.00 [0.00%]
alpha_prw	± 0.07 [4.8%]	± 0.12 [2.1%]	± 39.93 [3.4%]	± 65.79 [2.6%]	± 5.00 [3.2%]	± 15.35 [2.1%]
alpha_JET_Flavor_Composition	± 0.07 [4.2%]	± 0.58 [9.9%]	± 29.51 [2.5%]	± 126.22 [5.0%]	± 1.41 [0.90%]	± 39.60 [5.3%]
alpha_JET_JER_EffectiveNP_7	± 0.06 [4.1%]	± 0.16 [2.7%]	± 1.99 [0.17%]	± 7.60 [0.30%]	± 2.00 [1.3%]	± 7.18 [0.96%]

alpha_JET_EffectiveNP_Statistical3	± 0.06 [4.0%]	± 0.16 [2.8%]	± 2.97 [0.25%]	± 30.99 [1.2%]	± 2.84 [1.8%]	± 2.12 [0.28%]
alpha_JET_JER_EffectiveNP_11	± 0.05 [3.2%]	± 0.70 [11.9%]	± 6.04 [0.51%]	± 7.42 [0.29%]	± 0.02 [0.01%]	± 6.58 [0.88%]
alpha_JET_JER_EffectiveNP_2	± 0.04 [2.8%]	± 0.43 [7.4%]	± 14.08 [1.2%]	± 49.20 [1.9%]	± 0.09 [0.06%]	± 9.57 [1.3%]
alpha_JET_JER_EffectiveNP_12restTerm	± 0.04 [2.7%]	± 0.02 [0.36%]	± 2.84 [0.24%]	± 13.77 [0.54%]	± 0.12 [0.08%]	± 3.77 [0.51%]
alpha_JET_EffectiveNP_Statistical1	± 0.03 [2.0%]	± 0.12 [2.1%]	± 6.23 [0.53%]	± 19.72 [0.78%]	± 0.23 [0.15%]	± 0.43 [0.06%]
alpha_JET_JER_EffectiveNP_5	± 0.03 [1.8%]	± 0.13 [2.3%]	± 26.09 [2.2%]	± 30.38 [1.2%]	± 0.43 [0.28%]	± 6.98 [0.94%]
alpha_JET_JER_EffectiveNP_6	± 0.03 [1.7%]	± 0.21 [3.5%]	± 0.63 [0.05%]	± 2.55 [0.10%]	± 0.58 [0.37%]	± 9.74 [1.3%]
alpha_JET_EtaIntercalibration_TotalStat	± 0.03 [1.7%]	± 0.32 [5.5%]	± 0.68 [0.06%]	± 30.31 [1.2%]	± 0.29 [0.18%]	± 6.53 [0.88%]
alpha_JET_Pileup_OffsetNPV	± 0.02 [1.6%]	± 0.34 [5.7%]	± 1.14 [0.10%]	± 52.04 [2.1%]	± 0.35 [0.22%]	± 16.16 [2.2%]
alpha_JET_EffectiveNP_Statistical2	± 0.02 [1.6%]	± 0.13 [2.3%]	± 10.38 [0.88%]	± 4.75 [0.19%]	± 0.65 [0.42%]	± 6.67 [0.89%]
alpha_JET_EffectiveNP_Mixed1	± 0.02 [1.5%]	± 0.61 [10.3%]	± 20.50 [1.7%]	± 79.88 [3.2%]	± 0.71 [0.45%]	± 25.37 [3.4%]
alpha_JET_Pileup_OffsetMu	± 0.02 [1.5%]	± 0.17 [2.9%]	± 0.25 [0.02%]	± 12.28 [0.48%]	± 1.20 [0.76%]	± 9.61 [1.3%]
alpha_JET_JER_EffectiveNP_4	± 0.02 [1.5%]	± 0.59 [10.1%]	± 6.00 [0.51%]	± 18.61 [0.73%]	± 1.99 [1.3%]	± 8.31 [1.1%]
alpha_JET_Flavor_Response	± 0.02 [1.4%]	± 0.11 [1.8%]	± 5.74 [0.48%]	± 51.12 [2.0%]	± 0.51 [0.33%]	± 1.23 [0.17%]
alpha_JET_EffectiveNP_Mixed3	± 0.02 [1.4%]	± 0.32 [5.5%]	± 3.42 [0.29%]	± 12.48 [0.49%]	± 1.02 [0.65%]	± 9.64 [1.3%]
alpha_JET_JER_EffectiveNP_9	± 0.02 [1.4%]	± 0.09 [1.5%]	± 44.70 [3.8%]	± 3.91 [0.15%]	± 1.50 [0.96%]	± 5.30 [0.71%]
alpha_JET_EtaIntercalibration_Modelling	± 0.02 [1.3%]	± 0.49 [8.4%]	± 5.89 [0.50%]	± 52.59 [2.1%]	± 0.19 [0.12%]	± 14.21 [1.9%]
alpha_JET_EffectiveNP_Statistical6	± 0.02 [1.3%]	± 0.60 [10.2%]	± 34.97 [2.9%]	± 12.92 [0.51%]	± 5.67 [3.6%]	± 5.28 [0.71%]
alpha_JET_EffectiveNP_Statistical5	± 0.02 [1.2%]	± 0.04 [0.62%]	± 21.71 [1.8%]	± 0.12 [0.00%]	± 1.13 [0.72%]	± 1.53 [0.21%]
alpha_jvt	± 0.02 [1.2%]	± 0.05 [0.87%]	± 16.19 [1.4%]	± 28.57 [1.1%]	± 1.99 [1.3%]	± 9.09 [1.2%]
alpha_JET_EtaIntercalibration_NonClosure_2018data	± 0.02 [1.2%]	± 0.10 [1.7%]	± 151.23 [12.8%]	± 16.16 [0.64%]	± 3.99 [2.5%]	± 18.71 [2.5%]
alpha_JET_JER_EffectiveNP_3	± 0.02 [1.2%]	± 0.53 [9.1%]	± 15.85 [1.3%]	± 12.60 [0.50%]	± 1.29 [0.82%]	± 8.39 [1.1%]
alpha_JET_Pileup_RhoTopology	± 0.02 [1.2%]	± 0.50 [8.6%]	± 1.87 [0.16%]	± 96.86 [3.8%]	± 0.41 [0.26%]	± 29.19 [3.9%]
alpha_JET_Pileup_PtTerm	± 0.01 [0.76%]	± 0.21 [3.5%]	± 1.20 [0.10%]	± 21.98 [0.87%]	± 0.36 [0.23%]	± 2.55 [0.34%]
alpha_JET_EffectiveNP_Mixed2	± 0.01 [0.76%]	± 0.01 [0.20%]	± 0.64 [0.05%]	± 25.28 [1.00%]	± 1.08 [0.69%]	± 5.02 [0.67%]
alpha_JET_EtaIntercalibration_NonClosure_negEta	± 0.01 [0.71%]	± 0.29 [5.0%]	± 17.83 [1.5%]	± 34.67 [1.4%]	± 1.57 [1.00%]	± 16.92 [2.3%]
alpha_softbtagB	± 0.01 [0.65%]	± 0.16 [2.7%]	± 6.93 [0.58%]	± 0.00 [0.00%]	± 0.86 [0.55%]	± 0.00 [0.00%]
alpha_JET_JER_EffectiveNP_8	± 0.01 [0.61%]	± 0.18 [3.2%]	± 47.55 [4.0%]	± 5.15 [0.20%]	± 0.70 [0.45%]	± 3.43 [0.46%]
alpha_JET_JER_EffectiveNP_10	± 0.01 [0.60%]	± 0.36 [6.2%]	± 7.74 [0.65%]	± 6.22 [0.25%]	± 0.12 [0.08%]	± 0.63 [0.08%]
alpha_elId	± 0.01 [0.55%]	± 0.08 [1.4%]	± 10.76 [0.91%]	± 30.69 [1.2%]	± 1.94 [1.2%]	± 7.31 [0.98%]

alpha__JET__EffectiveNP__Modelling1	± 0.01 [0.52%]	± 0.76 [13.0%]	± 21.02 [1.8%]	± 108.81 [4.3%]	± 0.85 [0.54%]	± 26.48 [3.6%]
alpha__JET__EffectiveNP__Modelling2	± 0.01 [0.50%]	± 0.56 [9.6%]	± 8.71 [0.73%]	± 46.96 [1.9%]	± 0.27 [0.17%]	± 10.65 [1.4%]
alpha__JET__EffectiveNP__Detector2	± 0.01 [0.47%]	± 0.03 [0.58%]	± 4.37 [0.37%]	± 5.03 [0.20%]	± 0.00 [0.00%]	± 2.68 [0.36%]
alpha__MET__SoftTrk__ResoPerp	± 0.01 [0.43%]	± 0.19 [3.2%]	± 0.40 [0.03%]	± 11.39 [0.45%]	± 1.81 [1.2%]	± 16.27 [2.2%]
alpha__muIsoStat	± 0.01 [0.42%]	± 0.01 [0.23%]	± 4.29 [0.36%]	± 9.87 [0.39%]	± 0.62 [0.40%]	± 3.12 [0.42%]
mu__wjets	± 0.01 [0.41%]	± 0.96 [16.4%]	± 35.45 [3.0%]	± 589.76 [23.3%]	± 6.29 [4.0%]	± 166.88 [22.4%]
alpha__muIsoSyst	± 0.01 [0.35%]	± 0.03 [0.47%]	± 5.34 [0.45%]	± 22.25 [0.88%]	± 1.18 [0.75%]	± 4.62 [0.62%]
Lumi	± 0.01 [0.32%]	± 0.01 [0.09%]	± 1.93 [0.16%]	± 4.37 [0.17%]	± 0.35 [0.22%]	± 1.33 [0.18%]
alpha__MUON__SCALE	± 0.00 [0.31%]	± 0.02 [0.39%]	± 1.47 [0.12%]	± 34.32 [1.4%]	± 0.96 [0.61%]	± 6.84 [0.92%]
alpha__EG__RESOLUTION__ALL	± 0.00 [0.28%]	± 0.00 [0.00%]	± 0.26 [0.02%]	± 0.50 [0.02%]	± 0.07 [0.04%]	± 0.60 [0.08%]
alpha__JET__JER__EffectiveNP__1	± 0.00 [0.25%]	± 0.44 [7.6%]	± 4.45 [0.38%]	± 24.29 [0.96%]	± 7.74 [4.9%]	± 23.74 [3.2%]
alpha__JET__EffectiveNP__Detector1	± 0.00 [0.25%]	± 0.08 [1.3%]	± 79.11 [6.7%]	± 18.38 [0.73%]	± 1.94 [1.2%]	± 5.72 [0.77%]
alpha__JET__JER__DataVsMC__MC16	± 0.00 [0.21%]	± 0.09 [1.6%]	± 5.61 [0.47%]	± 24.92 [0.98%]	± 0.74 [0.47%]	± 5.86 [0.79%]
alpha__JET__EffectiveNP__Modelling4	± 0.00 [0.21%]	± 0.57 [9.7%]	± 2.11 [0.18%]	± 1.12 [0.04%]	± 1.63 [1.0%]	± 0.44 [0.06%]
alpha__JET__EffectiveNP__Modelling3	± 0.00 [0.20%]	± 0.29 [4.9%]	± 3.82 [0.32%]	± 6.37 [0.25%]	± 1.89 [1.2%]	± 0.32 [0.04%]
alpha__EG__SCALE__ALL	± 0.00 [0.15%]	± 0.01 [0.14%]	± 1.12 [0.09%]	± 5.01 [0.20%]	± 0.41 [0.26%]	± 2.61 [0.35%]
alpha__MET__SoftTrk__ResoPara	± 0.00 [0.15%]	± 0.16 [2.8%]	± 0.78 [0.07%]	± 11.68 [0.46%]	± 1.56 [1.00%]	± 11.05 [1.5%]
alpha__JET__EtaIntercalibration__NonClosure__posEta	± 0.00 [0.13%]	± 0.30 [5.1%]	± 1.62 [0.14%]	± 12.17 [0.48%]	± 0.43 [0.27%]	± 7.66 [1.0%]
alpha__elReco	± 0.00 [0.12%]	± 0.03 [0.54%]	± 3.12 [0.26%]	± 10.79 [0.43%]	± 0.65 [0.41%]	± 2.30 [0.31%]
alpha__muEffSyst	± 0.00 [0.09%]	± 0.00 [0.04%]	± 0.93 [0.08%]	± 1.49 [0.06%]	± 0.09 [0.06%]	± 0.60 [0.08%]
alpha__MUON__ID	± 0.00 [0.07%]	± 0.01 [0.17%]	± 0.19 [0.02%]	± 8.31 [0.33%]	± 0.44 [0.28%]	± 2.87 [0.38%]
alpha__muEffSystLowPt	± 0.00 [0.06%]	± 0.01 [0.24%]	± 0.99 [0.08%]	± 4.96 [0.20%]	± 0.24 [0.15%]	± 1.01 [0.14%]
alpha__muTtvaStat	± 0.00 [0.06%]	± 0.00 [0.09%]	± 0.79 [0.07%]	± 2.61 [0.10%]	± 0.14 [0.09%]	± 0.58 [0.08%]
alpha__JET__EtaIntercalibration__NonClosure__highE	± 0.00 [0.05%]	± 0.03 [0.47%]	± 1.67 [0.14%]	± 2.19 [0.09%]	± 0.38 [0.25%]	± 2.05 [0.28%]
alpha__JET__PunchThrough__MC16	± 0.00 [0.05%]	± 0.01 [0.09%]	± 0.42 [0.04%]	± 0.33 [0.01%]	± 0.06 [0.04%]	± 0.44 [0.06%]
alpha__MUON__MS	± 0.00 [0.04%]	± 0.00 [0.03%]	± 0.38 [0.03%]	± 0.32 [0.01%]	± 0.11 [0.07%]	± 0.54 [0.07%]
alpha__muEffStat	± 0.00 [0.04%]	± 0.00 [0.01%]	± 0.34 [0.03%]	± 0.73 [0.03%]	± 0.03 [0.02%]	± 0.24 [0.03%]
alpha__elIso	± 0.00 [0.03%]	± 0.02 [0.37%]	± 2.29 [0.19%]	± 12.55 [0.50%]	± 0.81 [0.51%]	± 1.95 [0.26%]
alpha__muTtvaSyst	± 0.00 [0.03%]	± 0.00 [0.01%]	± 0.29 [0.02%]	± 0.86 [0.03%]	± 0.04 [0.03%]	± 0.23 [0.03%]
alpha__muEffStatLowPt	± 0.00 [0.03%]	± 0.00 [0.07%]	± 0.50 [0.04%]	± 2.25 [0.09%]	± 0.12 [0.08%]	± 0.44 [0.06%]

alpha_JET_BJES_Response	± 0.00 [0.02%]	± 0.20 [3.4%]	± 1.69 [0.14%]	± 2.96 [0.12%]	± 0.09 [0.05%]	± 1.14 [0.15%]
alpha_MUON_SAGITTA_RHO	± 0.00 [0.02%]	± 0.20 [3.5%]	± 0.54 [0.05%]	± 43.32 [1.7%]	± 0.00 [0.00%]	± 9.24 [1.2%]
alpha_MUON_SAGITTA_RESBIAS	± 0.00 [0.02%]	± 0.00 [0.04%]	± 0.46 [0.04%]	± 0.41 [0.02%]	± 0.03 [0.02%]	± 0.84 [0.11%]
alpha_EG_SCALE_AF2	± 0.00 [0.02%]	± 0.24 [4.1%]	± 3.67 [0.31%]	± 46.35 [1.8%]	± 1.29 [0.82%]	± 17.71 [2.4%]
alpha_softbtagC	± 0.00 [0.02%]	± 0.02 [0.40%]	± 0.35 [0.03%]	± 0.00 [0.00%]	± 0.07 [0.05%]	± 0.00 [0.00%]
alpha_softbtagFake	± 0.00 [0.00%]	± 0.15 [2.6%]	± 0.67 [0.06%]	± 0.00 [0.00%]	± 0.14 [0.09%]	± 0.00 [0.00%]
alpha_JET_SingleParticle_HighPt	± 0.00 [0.00%]	± 0.24 [4.1%]	± 4.01 [0.34%]	± 46.09 [1.8%]	± 1.30 [0.83%]	± 17.52 [2.4%]
alpha_wjets_resum_sys_TCR	± 0.00 [0.00%]	± 0.00 [0.00%]	± 7.03 [0.59%]	± 0.00 [0.00%]	± 0.00 [0.00%]	± 0.00 [0.00%]
alpha_wjets_fragw_sys_TVR	± 0.00 [0.00%]	± 0.00 [0.00%]	± 0.00 [0.00%]	± 0.00 [0.00%]	± 0.86 [0.55%]	± 0.00 [0.00%]
alpha_ttbar_frag_sys_TCR	± 0.00 [0.00%]	± 0.00 [0.00%]	± 2.30 [0.19%]	± 0.00 [0.00%]	± 0.00 [0.00%]	± 0.00 [0.00%]
alpha_ttbar_add_sys_WVR	± 0.00 [0.00%]	± 0.00 [0.00%]	± 0.00 [0.00%]	± 0.00 [0.00%]	± 0.00 [0.00%]	± 9.21 [1.2%]
alpha_ttbar_add_sys_TVR	± 0.00 [0.00%]	± 0.00 [0.00%]	± 0.00 [0.00%]	± 0.00 [0.00%]	± 12.09 [7.7%]	± 0.00 [0.00%]
alpha_ttbar_hard_sys_WVR	± 0.00 [0.00%]	± 0.00 [0.00%]	± 0.00 [0.00%]	± 0.00 [0.00%]	± 0.00 [0.00%]	± 13.88 [1.9%]
alpha_ttbar_hard_sys_TVR	± 0.00 [0.00%]	± 0.00 [0.00%]	± 0.00 [0.00%]	± 0.00 [0.00%]	± 12.97 [8.3%]	± 0.00 [0.00%]
alpha_wjets_ckkw_sys_WVR	± 0.00 [0.00%]	± 0.00 [0.00%]	± 0.00 [0.00%]	± 0.00 [0.00%]	± 0.00 [0.00%]	± 27.17 [3.6%]
alpha_wjets_gen_sys_TVR	± 0.00 [0.00%]	± 0.00 [0.00%]	± 0.00 [0.00%]	± 0.00 [0.00%]	± 1.72 [1.1%]	± 0.00 [0.00%]
alpha_wjets_renorm_sys_TVR	± 0.00 [0.00%]	± 0.00 [0.00%]	± 0.00 [0.00%]	± 0.00 [0.00%]	± 6.44 [4.1%]	± 0.00 [0.00%]
alpha_ttbar_add_sys_TCR	± 0.00 [0.00%]	± 0.00 [0.00%]	± 84.93 [7.2%]	± 0.00 [0.00%]	± 0.00 [0.00%]	± 0.00 [0.00%]
alpha_wjets_renorm_sys_TCR	± 0.00 [0.00%]	± 0.00 [0.00%]	± 5.58 [0.47%]	± 0.00 [0.00%]	± 0.00 [0.00%]	± 0.00 [0.00%]
alpha_wjets_ckkw_sys_TVR	± 0.00 [0.00%]	± 0.00 [0.00%]	± 0.00 [0.00%]	± 0.00 [0.00%]	± 0.41 [0.26%]	± 0.00 [0.00%]
alpha_wjets_ckkw_sys_WCR	± 0.00 [0.00%]	± 0.00 [0.00%]	± 0.00 [0.00%]	± 31.28 [1.2%]	± 0.00 [0.00%]	± 0.00 [0.00%]
alpha_ttbar_hard_sys_WCR	± 0.00 [0.00%]	± 0.00 [0.00%]	± 0.00 [0.00%]	± 25.89 [1.0%]	± 0.00 [0.00%]	± 0.00 [0.00%]
alpha_ttbar_frag_sys_WCR	± 0.00 [0.00%]	± 0.00 [0.00%]	± 0.00 [0.00%]	± 2.01 [0.08%]	± 0.00 [0.00%]	± 0.00 [0.00%]
alpha_wjets_gen_sys_WCR	± 0.00 [0.00%]	± 0.00 [0.00%]	± 0.00 [0.00%]	± 109.99 [4.3%]	± 0.00 [0.00%]	± 0.00 [0.00%]
alpha_wjets_fragw_sys_WVR	± 0.00 [0.00%]	± 0.00 [0.00%]	± 0.00 [0.00%]	± 0.00 [0.00%]	± 0.00 [0.00%]	± 11.88 [1.6%]
alpha_wjets_renorm_sys_WVR	± 0.00 [0.00%]	± 0.00 [0.00%]	± 0.00 [0.00%]	± 0.00 [0.00%]	± 0.00 [0.00%]	± 11.74 [1.6%]
alpha_ttbar_add_sys_WCR	± 0.00 [0.00%]	± 0.00 [0.00%]	± 0.00 [0.00%]	± 16.40 [0.65%]	± 0.00 [0.00%]	± 0.00 [0.00%]
alpha_wjets_ckkw_sys_TCR	± 0.00 [0.00%]	± 0.00 [0.00%]	± 5.58 [0.47%]	± 0.00 [0.00%]	± 0.00 [0.00%]	± 0.00 [0.00%]
alpha_wjets_gen_sys_WVR	± 0.00 [0.00%]	± 0.00 [0.00%]	± 0.00 [0.00%]	± 0.00 [0.00%]	± 0.00 [0.00%]	± 93.69 [12.6%]
alpha_ttbar_frag_sys_TVR	± 0.00 [0.00%]	± 0.00 [0.00%]	± 0.00 [0.00%]	± 0.00 [0.00%]	± 0.37 [0.24%]	± 0.00 [0.00%]

alpha_ttbar_hard_sys_TCR	± 0.00 [0.00%]	± 0.00 [0.00%]	± 110.70 [9.3%]	± 0.00 [0.00%]	± 0.00 [0.00%]	± 0.00 [0.00%]
alpha_wjets_fragw_sys_WCR	± 0.00 [0.00%]	± 0.00 [0.00%]	± 0.00 [0.00%]	± 66.23 [2.6%]	± 0.00 [0.00%]	± 0.00 [0.00%]
alpha_wjets_gen_sys_TCR	± 0.00 [0.00%]	± 0.00 [0.00%]	± 18.31 [1.5%]	± 0.00 [0.00%]	± 0.00 [0.00%]	± 0.00 [0.00%]
alpha_wjets_resum_sys_WCR	± 0.00 [0.00%]	± 0.00 [0.00%]	± 0.00 [0.00%]	± 48.10 [1.9%]	± 0.00 [0.00%]	± 0.00 [0.00%]
gamma_stat_SRB0_cuts_bin_0	± 0.00 [0.00%]	± 0.98 [16.7%]	± 0.00 [0.00%]	± 0.00 [0.00%]	± 0.00 [0.00%]	± 0.00 [0.00%]
alpha_wjets_fragw_sys_TCR	± 0.00 [0.00%]	± 0.00 [0.00%]	± 2.79 [0.24%]	± 0.00 [0.00%]	± 0.00 [0.00%]	± 0.00 [0.00%]
alpha_wjets_resum_sys_TVR	± 0.00 [0.00%]	± 0.00 [0.00%]	± 0.00 [0.00%]	± 0.00 [0.00%]	± 0.09 [0.05%]	± 0.00 [0.00%]
alpha_ttbar_frag_sys_WVR	± 0.00 [0.00%]	± 0.00 [0.00%]	± 0.00 [0.00%]	± 0.00 [0.00%]	± 0.00 [0.00%]	± 2.40 [0.32%]
alpha_wjets_resum_sys_WVR	± 0.00 [0.00%]	± 0.00 [0.00%]	± 0.00 [0.00%]	± 0.00 [0.00%]	± 0.00 [0.00%]	± 51.16 [6.9%]
alpha_wjets_renorm_sys_WCR	± 0.00 [0.00%]	± 0.00 [0.00%]	± 0.00 [0.00%]	± 485.33 [19.2%]	± 0.00 [0.00%]	± 0.00 [0.00%]

Colophon

This thesis was made in LaTeX 2_ε using the "hepthesis" class [218].

Bibliography

[1] A. D. Martin and F. Halzen, *Quarks and Leptons: An Introductory Course in Modern Particle Physics.* Singapore: Wiley, 1984.

[2] D. Griffiths, *Introduction to Elementary Particles.* Weinheim: Wiley-VCH, 2008.

[3] S. L. Glashow, "Partial Symmetries of Weak Interactions," *Nucl.Phys.*, vol. 22, pp. 579–588, 1961.

[4] S. Weinberg, "A Model of Leptons," *Phys.Rev.Lett.*, vol. 19, pp. 1264–1266, 1967.

[5] A. Salam, "Weak and Electromagnetic Interactions," *Conf.Proc.*, vol. C680519, pp. 367–377, 1968.

[6] P. W. Higgs, "Broken symmetries, massless particles and gauge fields," *Phys. Lett.*, vol. 12, pp. 132–133, 1964.

[7] P. W. Higgs, "Spontaneous Symmetry Breakdown without Massless Bosons," *Phys. Rev.*, vol. 145, pp. 1156–1163, 1966.

[8] C. R. H. G. S. Guralnik and T. Kibble, "Global Conservation Laws and Massless Particles," *Phys.Rev.Lett.*, vol. 13, pp. 585–587, 1964.

[9] T. W. B. Kibble, "Symmetry breaking in non-Abelian gauge theories," *Phys.Rev.*, vol. 155, pp. 1554–1561, 1967.

[10] N. Cabibbo, "Unitary Symmetry and Leptonic Decays," *Phys.Rev.Lett.*, vol. 10, pp. 531–533, 1963.

[11] M. Kobayashi and T. Maskawa, "CP Violation in the Renormalizable Theory of Weak Interaction," *Prog.Theor.Phys.*, vol. 49, pp. 652–657, 1973.

[12] H. Schopper, *Advances of Accelerator Physics and Technologies.* United States of America: World Scientific, 1993.

[13] The ATLAS Collaboration, "The ATLAS experiment at the CERN large hadron collider," *Journal of Instrumentation*, vol. 3, no. 08, p. S08003, 2008.

[14] The CMS Collaboration, "The CMS experiment at the CERN LHC," *JINST*, vol. 3, p. S08004, 2008.

[15] The ATLAS Collaboration, "Observation of a new particle in the search for the Standard Model Higgs boson with the ATLAS detector at the LHC," *Phys.Lett.*, vol. B716, pp. 1–29, 2012, 1207.7214.

[16] The CMS Collaboration, "Observation of a new boson at a mass of 125 GeV with the CMS experiment at the LHC," *Phys.Lett.*, vol. B716, pp. 30–61, 2012, 1207.7235.

[17] NEEDS AN AUTHOR, "Standard model summary plots june 2021." `https://atlas.web.cern.ch/Atlas/GROUPS/PHYSICS/PUBNOTES/ATL-PHYS-PUB-2021-032/`. Accessed: 2021-09-14.

[18] S. Weinberg, "Implications of Dynamical Symmetry Breaking," *Phys. Rev.*, vol. D13, pp. 974–996, 1976.

[19] E. Gildener, "Gauge Symmetry Hierarchies," *Phys. Rev.*, vol. D14, p. 1667, 1976.

[20] S. Weinberg, "Implications of dynamical symmetry breaking: An addendum," *Phys. Rev. D*, vol. 19, pp. 1277–1280, Feb 1979.

[21] L. Susskind, "Dynamics of spontaneous symmetry breaking in the weinberg-salam theory," *Phys. Rev. D*, vol. 20, pp. 2619–2625, Nov 1979.

[22] S. P. Martin, "A Supersymmetry primer," 1997, hep-ph/9709356. [Adv. Ser. Direct. High Energy Phys.18,1(1998)].

[23] B. R. Martin and G. Shaw, *Particle Physics*. Manchester: Wiley, 2008.

[24] M. T. V. Xu and M. Garcia-Sciveres, "ATLAS luminosity measurement using cluster shape recognition as a selection cut in pixel cluster counting," *CERN document saver*, vol. ATL-COM-DAPR-2014-008, 2014.

[25] C. Malone, "Feasibility Study on the use of the ATLAS SCT as a Luminometer," *ATLAS Internal note*, 2015.

[26] C. G. Lester and D. J. Summers, "Measuring masses of semi-invisibly decaying particles pair produced at hadron colliders," *Phys. Lett.*, vol. B463, pp. 99–103,

1999, hep-ph/9906349.

[27] The ATLAS Collaboration, "Search for new phenomena with top quark pairs in final states with one lepton, jets, and missing transverse momentum in pp collisions at s $\sqrt{}$ = 13 tev with the atlas detector," *Journal of High Energy Physics*, vol. 2021, no. 4, pp. 1–66, 2021.

[28] M. Thompson, *Modern Particle Physics*. Cambridge: Cambridge University Press, 2013.

[29] t. P. D. G. e. a. P.A. Zyla, "Review of Particle Physics," *Prog. Theor. Exp. Phys.*, vol. 083C01, pp. 1–2092, 2020.

[30] C. Patrignani and Particle Data Group, "Review of particle physics," *Chinese Physics C*, vol. 40, no. 10, p. 100001, 2016.

[31] P. B. Pal, *An Introductory Course of Particle Physics*. Unites States of America: CRC Press, 2015.

[32] LHCb collaboration, R. Aaij et al., "Test of lepton universality in beauty-quark decays," 2021, 2103.11769.

[33] P. Langacker, *The Standard Model and Beyond (Series in High Energy Physics, Cosmology and Gravitation)*. CRC Press, 2009.

[34] UA1 Collaboration, "Search for centauro like events at the cern proton-antiproton collider," *Physics Letters B*, vol. 122, no. 2, pp. 189 – 196, 1983.

[35] UA1 Collaboration, "Further evidence for charged intermediate vector bosons at the SPS collider," *Physics Letters B*, vol. 129, no. 3, pp. 273 – 282, 1983.

[36] UA2 Collaboration, "Observation of single isolated electrons of high transverse momentum in events with missing transverse energy at the CERN *pp* collider," *Physics Letters B*, vol. 122, no. 5, pp. 476 – 485, 1983.

[37] UA2 Collaboration, "Evidence for $Z^0 \rightarrow e^+ e^-$ at the CERN *pp* collider," *Physics Letters B*, vol. 129, no. 1, pp. 130 – 140, 1983.

[38] UA1 Collaboration, "Experimental observation of lepton pairs of invariant mass around 95 GeV/c^2 at the CERN SPS collider," *Physics Letters B*, vol. 126, no. 5, pp. 398 – 410, 1983.

[39] M. *g*2 Collaboration, "Measurement of the positive muon anomalous magnetic

moment to 0.46 ppm," *Physical Review Letters*, vol. 126, no. 14.

[40] J. Terning, *Modern supersymmetry: Dynamics and duality.* 2006.

[41] M. Ibe, A. Rajaraman and Z. Surujon, "Does Supersymmetry Require Two Higgs Doublets?," 2010, 1012.5099.

[42] E. Witten, "An SU(2) Anomaly," *Phys. Lett.*, vol. B117, pp. 324–328, 1982. [,230(1982)].

[43] The CMS Collaboration, "Searches for heavy Higgs bosons in two-Higgs-doublet models and for $t \to ch$ decay using multilepton and diphoton final states in pp collisions at 8 TeV," *Phys. Rev.*, vol. D90, p. 112013, 2014, 1410.2751.

[44] P. Binetruy, *Supersymmetry: Theory, Experiment, and Cosmology.* Oxford Graduate Texts, OUP Oxford, 2006.

[45] H. Baer and X. Tata, *Weak Scale Supersymmetry: From Superfields to Scattering Events.* Cambridge University Press, 2006.

[46] A. Djouadi et al., "The Minimal supersymmetric standard model: Group summary report," in *GDR (Groupement De Recherche) - Supersymetrie Montpellier, France, April 15-17, 1998*, 1998, hep-ph/9901246.

[47] D. Alves, "Simplified Models for LHC New Physics Searches," *J. Phys.*, vol. G39, p. 105005, 2012, 1105.2838.

[48] J. G. Y. Bai, H. C. Cheng and J. Gu, "Stop the Top Background of the Stop Search," *JHEP*, vol. 07, p. 110, 2012, 1203.4813.

[49] S. Dimopoulos and G. F. Giudice, "Naturalness constraints in supersymmetric theories with nonuniversal soft terms," *Phys. Lett.*, vol. B357, pp. 573–578, 1995, hep-ph/9507282.

[50] D. B. K. A. G. Cohen and A. E. Nelson, "The More minimal supersymmetric standard model," *Phys. Lett.*, vol. B388, pp. 588–598, 1996, hep-ph/9607394.

[51] H. Kleinert and V. Schulte-Frohlinde, *Critical properties of phi**4-theories.* 2001.

[52] The ATLAS Collaboration, "Search for top-squark pair production in final states with one lepton, jets, and missing transverse momentum using 36 ifb of $\sqrt{s} =$13 TeV pp collision data with the ATLAS detector," *JHEP*, vol. 06, p. 108, 2018, 1711.11520.

[53] S. Fichet, "Quantified naturalness from bayesian statistics," *Phys. Rev.*, vol. D86, p. 125029, 2012, 1204.4940.

[54] D. Boerner et al., "Search for top squarks in final states with one isolated lepton, jets, and missing transverse momentum in $\sqrt{s} = 13$ TeV pp collisions using 40 fb^{-1} of ATLAS data," Tech. Rep. ATL-COM-PHYS-2016-1623, CERN, Geneva, Nov 2016.

[55] M. Tanabashi and Particle Data Group, "The review of particle physics," *Phys. Rev. D*, vol. 98, 2018.

[56] J. Ellis and S. Rudaz, "Search for supersymmetry in toponium decays," *Physics Letters B*, vol. 128, no. 3, pp. 248 – 252, 1983.

[57] C. Boehm, A. Djouadi and Y. Mambrini, "Decays of the lightest top squark," *Phys. Rev.*, vol. D61, p. 095006, 2000, hep-ph/9907428.

[58] A. Bartl, H. Eberl, B. Herrmann, K. Hidaka, W. Majerotto, and W. Porod, "Impact of squark generation mixing on the search for squarks decaying into fermions at LHC," *Physics Letters B*, vol. 698, pp. 380–388, Apr. 2011, 1007.5483.

[59] The ATLAS Collaboration, "ATLAS Run 1 searches for direct pair production of third-generation squarks at the Large Hadron Collider," *Eur. Phys. J.*, vol. C75, no. 10, p. 510, 2015, 1506.08616. [Erratum: Eur. Phys. J.C76,no.3,153(2016)].

[60] S. Dimopoulos and H. Georgi, "Softly broken supersymmetry and su(5)," *Nucl. Phys.*, vol. B193, pp. 150–162, 1981.

[61] K. Brading and E. Castellani, *Symmetries in Physics: Philosophical Reflections.* Cambridge University Press, 2010.

[62] I. Aitchison, *Supersymmetry in Particle Physics: An Elementary Introduction.* Cambridge University Press, 2007.

[63] The NA48 Collaboration, "A new measurement of direct CP violation in two pion decays of the neutral kaon," *Phys. Lett.*, vol. B465, pp. 335–348, 1999, hep-ex/9909022.

[64] BaBar Collaboration, "Observation of direct CP violation in $B^0 \rightarrow K^+\pi^-$ decays," *Phys. Rev. Lett.*, vol. 93, p. 131801, 2004, hep-ex/0407057.

[65] J. Krige, *History of CERN, III.* History of CERN, Elsevier Science, 1996.

[66] The LHCb Collaboration, "The LHCb detector at the LHC," *JINST*, vol. 3, p. S08005, 2008.

[67] ALICE Collaboration, "The ALICE experiment at the CERN LHC," *JINST*, vol. 3, p. S08002, 2008.

[68] The ATLAS Collaboration, "Operation and performance of the atlas semiconductor tracker," *JINST*, vol. 9, p. P08009, 2014, 1404.7473.

[69] CERN Bulletin, "ATLAS: Exceeding all expectations. ATLAS: au-delà des esperances," p. 4, Nov 2010.

[70] F. Pastore, "ATLAS Run-2 status and performance," Jul 2015.

[71] J. T. Boyd, "Lhc run-2 and future prospects," 2020, 2001.04370.

[72] The ATLAS Collaboration, "ATLAS inner detector: Technical Design Report, Vol. 1," tech. rep., Geneva, 1997.

[73] The ATLAS Collaboration, "The Silicon microstrip sensors of the ATLAS semiconductor tracker," *Nucl.Instrum.Meth.*, vol. A578, pp. 98–118, 2007.

[74] The ATLAS Collaboration, "ATLAS high-level trigger, data acquisition and controls: Technical design report," tech. rep., 2003.

[75] The ATLAS Collaboration, "ATLAS first level trigger: Technical design report," tech. rep., 1998.

[76] O. Behnke, K. Kröninger, T. Schörner-Sadenius and G. Schott, ed., *Data analysis in high energy physics.* Weinheim, Germany: Wiley-VCH, 2013.

[77] L. Evans and P. Bryant, "LHC machine," *Journal of Instrumentation*, vol. 3, no. 08, p. S08001, 2008.

[78] M. Hostettler, K. Fuchsberger, B. Papotti, T. Pieloni, and Y. Papaphilippou, "Luminosity Scans for Beam Diagnostics," 2018, 1804.10099.

[79] M. Herr, "Concept of Luminosity," *CERN Yellow Report*, 2006.

[80] The ATLAS Collaboration, "Luminosity determination in pp collisions at $\sqrt{s} = 7$ tev using the ATLAS detector at the LHC," *Eur.Phys.J.*, vol. C71, p. 1630, 2011, 1101.2185.

[81] F. L. Manghi, "The LUCID detector ATLAS luminosity monitor and its electronic

system," *Nuclear Instruments and Methods in Physics Research Section A: Accelerators, Spectrometers, Detectors and Associated Equipment*, vol. 824, pp. 311 – 312, 2016. Frontier Detectors for Frontier Physics: Proceedings of the 13th Pisa Meeting on Advanced Detectors.

[82] The ATLAS Collaboration, "The new lucid-2 detector for luminosity measurement and monitoring in atlas," *Journal of Instrumentation*, vol. 13, pp. P07017–P07017, Jul 2018.

[83] The ATLAS Collaboration, "The ATLAS beam conditions monitor," *JINST*, vol. 3, p. P02004, 2008.

[84] The ATLAS Collaboration, "Luminosity determination in pp collisions at $\sqrt{s} = 8$ TeV using the ATLAS detector at the LHC," *Eur. Phys. J.*, vol. C76, no. 12, p. 653, 2016, 1608.03953.

[85] R. Kwee, "Minimum Bias Triggers at ATLAS, LHC," 2008, 0812.0613.

[86] The ATLAS Collaboration, "ATLAS tile calorimeter: Technical design report," 1996.

[87] The ATLAS Collaboration, "Improved luminosity determination in pp collisions at $\sqrt{s} = 7$ TeV using the ATLAS detector at the LHC," *Eur.Phys.J.*, vol. C73, no. 8, p. 2518, 2013, 1302.4393.

[88] H. Pernegger, "The pixel detector of the ATLAS experiment for LHC "run-2"," *Journal of Instrumentation*, vol. 10, no. 06, p. C06012, 2015.

[89] M. S. Alam *et al.*, "The ATLAS silicon pixel sensors," *Nucl. Instrum. Meth.*, vol. A456, pp. 217–232, 2001.

[90] M. Capeans, G. Darbo, K. Einsweiller, N. Elsing et al., "ATLAS Insertable B-Layer Technical Design Report," Tech. Rep. CERN-LHCC-2010-013. ATLAS-TDR-19, Sep 2010.

[91] The ATLAS Collbration, "The barrel modules of the ATLAS semiconductor tracker," *Nucl.Instrum.Meth.*, vol. A568, pp. 642–671, 2006.

[92] The ATLAS Collaboration, "A study of the material in the ATLAS inner detector using secondary hadronic interactions," *JINST*, vol. 7, p. P01013, 2012, 1110.6191.

[93] A. Abdesselam *et al.*, "The ATLAS semiconductor tracker end-cap module,"

Nucl.Instrum.Meth., vol. A575, pp. 353–389, 2007.

[94] T. Vickey, "A read-out driver for silicon detectors in ATLAS," pp. 196–200, 2006.

[95] B. Dolgoshein, "Transition radiation detectors," *Nuclear Instruments and Methods in Physics Research A*, vol. 326, pp. 434–469, Mar 1993.

[96] The ATLAS TRT Collaboration, "The ATLAS transition radiation tracker (TRT) proportional drift tube: design and performance," *Journal of Instrumentation*, vol. 3, no. 02, p. P02013, 2008.

[97] K. A. Olive, "Review of particle physics," *Chin. Phys.*, vol. C38, p. 090001, 2014.

[98] The ATLAS Collaboration, "Construction, assembly and tests of the ATLAS electromagnetic end-cap calorimeters," *Journal of Instrumentation*, vol. 3, no. 06, p. P06002, 2008.

[99] R. Wigmans, *Calorimetry: Energy measurement in particle physics*, vol. 107. 2000.

[100] The ATLAS Collaboration, "Construction, assembly and tests of the ATLAS electromagnetic barrel calorimeter," *Nuclear Instruments and Methods in Physics Research Section A: Accelerators, Spectrometers, Detectors and Associated Equipment*, vol. 558, no. 2, pp. 388 – 418, 2006.

[101] The ATLAS Collaboration, "The ATLAS forward calorimeter," *Journal of Instrumentation*, vol. 3, no. 02, p. P02010, 2008.

[102] The ATLAS Collaboration, *ATLAS muon spectrometer: Technical Design Report*. Technical Design Report ATLAS, Geneva: CERN, 1997.

[103] The ATLAS Collaboration, "The ATLAS central solenoid," *Nuclear Instruments and Methods in Physics Research Section A: Accelerators, Spectrometers, Detectors and Associated Equipment*, vol. 584, no. 1, pp. 53 – 74, 2008.

[104] The ATLAS Collaboration, "Level-1 Technical Design Report," Tech. Rep. ATLAS TDR-12, CERN, Geneva, August 1998.

[105] The ATLAS Collaboration, "The Run-2 ATLAS trigger system," *Journal of Physics: Conference Series*, vol. 762, no. 1, p. 012003, 2016.

[106] G. Duckeck, D. Barberis, R. Hawkings, R. Jones, N. McCubbin et al., "ATLAS computing: Technical design report," 2005.

[107] GEANT4 Collaboration, "Geant4—a simulation toolkit," *Nuclear Instruments and Methods in Physics Research Section A: Accelerators, Spectrometers, Detectors and Associated Equipment*, vol. 506, no. 3, pp. 250–303, 2003.

[108] The ATLAS Collaboration, "The ATLAS simulation infrastructure," *Eur. Phys. J.*, vol. C70, pp. 823–874, 2010, 1005.4568.

[109] The ATLAS Collaboration, "The simulation principle and performance of the ATLAS fast calorimeter simulation FastCaloSim," Tech. Rep. ATL-PHYS-PUB-2010-013, CERN, Geneva, Oct 2010.

[110] The ATLAS Collaboration, "Electron reconstruction and identification in the atlas experiment using the 2015 and 2016 lhc proton–proton collision data at $\sqrt{s} = 13$ tev," *The European Physical Journal C*, vol. 79, Aug 2019.

[111] P. Ferrari, "Tracking and vertexing at ATLAS," *ArXiv e-prints*, Jul 2007, 0707.3071.

[112] N. C. Benekos, R. Clifft, N. Elsing and A. Poppleton, "ATLAS inner detector performance," Tech. Rep. ATL-INDET-2004-002, CERN, Geneva, Dec 2003. revised version number 1 submitted on 2004-01-15 18:11:09.

[113] The ATLAS Collaboration, "Muon reconstruction performance of the ATLAS detector in proton-proton collision data at $\sqrt{s} =$13 TeV," *Eur. Phys. J.*, vol. C76, no. 5, p. 292, 2016, 1603.05598.

[114] K. Yoshihara, M. Queitsch-maitland, T. Yamazaki, D. Handl, J. Wagner-kuhr et al., "Search for new phenomena with top quark pairs in final states with one lepton, jets, and missing transverse momentum using 140 fb^{-1} of $\sqrt{s} = 13$ TeV data with ATLAS," Tech. Rep. ATL-COM-PHYS-2018-1413, CERN, Geneva, Oct 2019.

[115] The ATLAS Collaboration, "Jet energy measurement with the ATLAS detector in proton-proton collisions at $\sqrt{s} =$7 TeV," *Eur. Phys. J.*, vol. C73, no. 3, p. 2304, 2013, 1112.6426.

[116] G. P. S. M. Cacciari and G. Soyez, "The anti-k_t jet clustering algorithm," *JHEP*, vol. 04, p. 063, 2008, 0802.1189.

[117] The ATLAS Collaboration, "Tagging and suppression of pileup jets with the ATLAS detector," Tech. Rep. ATLAS-CONF-2014-018, CERN, Geneva, May 2014.

[118] The ATLAS Collaboration, "ATLAS b-jet identification performance and efficiency measurement with $t\bar{t}$ events in pp collisions at $\sqrt{s} = 13$ TeV," *Eur. Phys. J. C*,

vol. 79, no. 11, p. 970, 2019, 1907.05120.

[119] T. A. Collaboration, "Expected performance of the ATLAS *b*-tagging algorithms in Run-2," Tech. Rep. ATL-PHYS-PUB-2015-022, CERN, Geneva, Jul 2015.

[120] The ATLAS Collaboration, "Performance of *b*-jet identification in the ATLAS experiment," *Journal of Instrumentation*, vol. 11, no. 04, p. P04008, 2016.

[121] The ATLAS Collaboration, "Optimisation of the ATLAS *b*-tagging performance for the 2016 LHC Run," Tech. Rep. ATL-PHYS-PUB-2016-012, CERN, Geneva, Jun 2016.

[122] S. Frixione and B. R. Webber, "The MC and NLO 3.4 Event Generator," 2008, 0812.0770.

[123] G. Corcella, I. G. Knowles, G. Marchesini, S. Moretti, K. Odagiri, P. Richardson, M. H. Seymour and Bryan R. Webber, "Herwig 6: an event generator for hadron emission reactions with interfering gluons (including supersymmetric processes)," *Journal of High Energy Physics*, vol. 2001, no. 01, p. 010, 2001.

[124] The ATLAS Collaboration, "Soft *b*-hadron tagging for compressed SUSY scenarios," Tech. Rep. ATLAS-CONF-2019-027, CERN, Geneva, Jul 2019.

[125] The ATLAS Collaboration, "Performance of vertex reconstruction algorithms for detection of new long-lived particle decays within the ATLAS inner detector," Tech. Rep. ATL-PHYS-PUB-2019-013, CERN, Geneva, Mar 2019.

[126] The ATLAS Collaboration, "Performance of missing transverse momentum reconstruction for the ATLAS detector in the first proton-proton collisions at at $\sqrt{s}=$ 13 TeV," Tech. Rep. ATL-PHYS-PUB-2015-027, CERN, Geneva, Jul 2015.

[127] The ATLAS Collaboration, "Object-based missing transverse momentum significance in the ATLAS detector," Tech. Rep. ATLAS-CONF-2018-038, CERN, Geneva, Jul 2018.

[128] M. Cacciari, G. P. Salam and G. Soyez, "The catchment area of jets," *Journal of High Energy Physics*, vol. 2008, no. 04, p. 005, 2008.

[129] K. Grafström, "Luminosity Determination at Proton Colliders," *Progress in Particle and Nuclear Physics*, vol. 81, pp. 97–148, 2015.

[130] Sir P. Moore, *Astronomy Encylopedia.* London: Philip's, 2002.

[131] L. Bonolis, "Bruno Touschek *vs.* machine builders: AdA, the first matter-antimatter collider," *Rivista del Nuovo Cimento*, vol. 28, no. 11, pp. 1–60, 2005.

[132] M. Bruschi, "The new ATLAS/LUCID detector," in *2015 4th International Conference on Advancements in Nuclear Instrumentation Measurement Methods and their Applications (ANIMMA)*, pp. 1–6, April 2015.

[133] O. Viazlo and the ATLAS LUCID Collaboration, "ATLAS LUCID detector upgrade for LHC Run 2," Tech. Rep. ATL-FWD-PROC-2015-004, CERN, Geneva, Oct 2015.

[134] The ATLAS Collaboration, "Luminosity determination in pp collisions at $\sqrt{s}$ =13 TeV using the ATLAS detector at the LHC," tech. rep., CERN, Geneva, Jun 2019. All figures including auxiliary figures are available at https://atlas.web.cern.ch/Atlas/GROUPS/PHYSICS/CONFNOTES/ATLAS-CONF-2019-021.

[135] The ATLAS Collaboration, "Performance of the ATLAS track reconstruction algorithms in dense environments in LHC Run 2," *The European Physical Journal C*, vol. 77, p. 673, Oct 2017.

[136] The CMS Collaboration, "CMS luminosity based on pixel cluster counting – Summer 2012 update," 2012.

[137] The CMS Collaboration, "CMS luminosity based on pixel cluster counting – Summer 2013 update," 2013.

[138] The ATLAS Collaboration, "Measurement of the Inelastic Proton-Proton Cross Section at $\sqrt{s} = 13$ TeV with the ATLAS Detector at the LHC," tech. rep., CERN, Geneva, Aug 2015. All figures including auxiliary figures are available at https://atlas.web.cern.ch/Atlas/GROUPS/PHYSICS/CONFNOTES/ATLAS-CONF-2015-038.

[139] S. van der Meer, "Calibration of the effective beam height in the ISR," 1968.

[140] H. B. S. White, R. Alemany-Fernandez and M. Lamont, "First Luminosity Scans in the LHC," *Conf.Proc.*, vol. C100523, p. MOPEC014, 2010.

[141] S. Y. Lee, *Accelerator Physics.* Singapore: World Scientific, 2004.

[142] The ATLAS Collaboration, "The performance of the jet trigger for the ATLAS detector during 2011 data taking," *Eur. Phys. J.*, vol. C76, no. 10, p. 526, 2016,

1606.07759.

[143] The ATLAS Collaboration, "Performance of the ATLAS trigger system in 2015," *Eur. Phys. J.*, vol. C77, no. 5, p. 317, 2017, 1611.09661.

[144] The ATLAS Collaboration, "Track Reconstruction Performance of the ATLAS Inner Detector at $\sqrt{s} = 13$ TeV," Tech. Rep. ATL-PHYS-PUB-2015-018, CERN, Geneva, Jul 2015.

[145] J. Cowley, "Personal communication." Personal communication.

[146] A. Barr and C. Gwenlan, "The race for supersymmetry: Using m_{T2} for discovery," *Phys. Rev.*, vol. D80, p. 074007, 2009, 0907.2713.

[147] A. J. Barr, T. J. Khoo, P. Konar, K. Kong, C. G. Lester, K. T. Matchev and M. Park, "Guide to transverse projections and mass-constraining variables," *Phys. Rev.*, vol. D84, p. 095031, 2011, 1105.2977.

[148] C. L. A. Barr and P. Stephens, "A variable for measuring masses at hadron colliders when missing energy is expected; m_{T2} : the truth behind the glamour," *Journal of Physics G: Nuclear and Particle Physics*, vol. 29, no. 10, p. 2343, 2003.

[149] G. Ross and M. Serna, "Mass determination of new states at hadron colliders," *Physics Letters B*, vol. 665, no. 4, pp. 212 – 218, 2008.

[150] W. Cho, K. Choi, Y. G. Kim and C. B. Park, "Transverse mass for pairs of gluinos," *Phys. Rev. Lett.*, vol. 100, p. 171801, Apr 2008.

[151] W. S. Cho, K. Choi, Y. G. Kim and C. B. Park, "Measuring superparticle masses at hadron collider using the transverse mass kink," *Journal of High Energy Physics*, vol. 2008, no. 02, p. 035, 2008.

[152] M. Nojiri, Y. Shimizu, S. Okada and K. Kawagoe, "Inclusive transverse mass analysis for squark and gluino mass determination," *Journal of High Energy Physics*, vol. 2008, no. 06, p. 035, 2008.

[153] W. S. Cho, K. Choi, Y. G. Kim and C. B. Park, "Measuring the top quark mass with the m_{T2} variable," *Phys. Rev. D*, vol. 78, p. 034019, Aug 2008.

[154] S. Hawking, *A brief history of time*. Bantam books, 1998.

[155] The OPAL collaboration, "Search for scalar top and scalar bottom quarks at LEP," *Physics Letters B*, vol. 545, no. 3, pp. 272 – 284, 2002.

[156] V.M. Abazov et al., "Search for pair production of the scalar top quark in the electron+muon final state," *Physics Letters B*, vol. 696, no. 4, pp. 321 – 327, 2011.

[157] The CDF Collaboration, "Search for the supersymmetric partner of the top quark in $p\overline{p}$ collisions at $\sqrt{s}$ =1.96 tev," *Phys. Rev. D*, vol. 82, p. 092001, Nov 2010.

[158] D0 Collaboration, "Search for scalar top quarks in the acoplanar charm jets and missing transverse energy final state in $p\overline{p}$ collisions at $\sqrt{s}$ =1.96 tev," *Physics Letters B*, vol. 665, no. 1, pp. 1 – 8, 2008.

[159] The CDF Collaboration, "Search for pair production of supersymmetric top quarks in dilepton events from $p\overline{p}$ collisions at $\sqrt{s}$ =1.96 tev," *Phys. Rev. Lett.*, vol. 104, p. 251801, Jun 2010.

[160] D0 Collaboration, "Search for admixture of scalar top quarks in the $t\bar{t}$ lepton+jets final state at $\sqrt{s}$= 1.96 TeV," *Phys. Lett.*, vol. B674, pp. 4–10, 2009, 0901.1063.

[161] The CMS Collaboration, "Search for direct stop pair production in the dilepton final state at $\sqrt{s}$ =13 TeV," Tech. Rep. CMS-PAS-SUS-17-001, CERN, Geneva, 2017.

[162] The ATLAS Collaboration, "Search for a scalar partner of the top quark in the jets plus missing transverse momentum final state at $\sqrt{s}$=13 tev with the atlas detector," *Journal of High Energy Physics*, vol. 2017, Dec 2017.

[163] The ATLAS Collaboration, "Search for direct top squark pair production in final states with two leptons in $\sqrt{s}$ = 13 tev pp collisions with the atlas detector," *The European Physical Journal C*, vol. 77, Dec 2017.

[164] The ATLAS Collaboration, "Search for new phenomena with the M_{T2} variable in the all-hadronic final state produced in proton–proton collisions at $\sqrt{s}$ = 13 TeV," *Eur. Phys. J.*, vol. C77, no. 10, p. 710, 2017, 1705.04650.

[165] A. M. Sirunyan, A. Tumasyan et al., "Search for supersymmetry in multijet events with missing transverse momentum in proton-proton collisions at 13 tev," *Physical Review D*, vol. 96, Aug 2017.

[166] The CMS Collaboration, "Search for direct production of supersymmetric partners of the top quark in the all-jets final state in proton-proton collisions at $\sqrt{s}$ =13 tev," *Journal of High Energy Physics*, vol. 2017, Oct 2017.

[167] A. M. Sirunyan, A. Tumasyan et al., "Search for top squark pair production in

pp collisions at $\sqrt{s}$ =13 tev using single lepton events," *Journal of High Energy Physics*, vol. 2017, Oct 2017.

[168] The ATLAS Collaboration, "Search for dark matter and other new phenomena in events with an energetic jet and large missing transverse momentum using the ATLAS detector," *JHEP*, vol. 01, p. 126, 2018, 1711.03301.

[169] T. J. Khoo, *The hunting of the squark.* PhD thesis, University of Cambridge, 2013-01-10.

[170] K. Rosbach, *Search for a supersymmetric partner of the top quark in the one-lepton channel with the ATLAS detector.* PhD thesis, University of Geneva, 2015-05-28.

[171] R. Mahbubani, K. T. Matchev, Konstantin and M. Park, "Re-interpreting the Oxbridge stransverse mass variable MT2 in general cases," *JHEP*, vol. 03, p. 134, 2013, 1212.1720.

[172] The ATLAS Collaboration, "Search for top squark pair production in final states with one isolated lepton, jets, and missing transverse momentum in $\sqrt{s} = 8$ TeV pp collisions with the ATLAS detector," *JHEP*, vol. 11, p. 118, 2014, 1407.0583.

[173] The ATLAS Collaboration, "Search for new phenomena in events with two opposite-charge leptons, jets and missing transverse momentum in pp collisions at $\sqrt{s} = 13$ TeV with the ATLAS detector," *JHEP*, vol. 04, p. 165, 2021, 2102.01444.

[174] The ATLAS Collaboration, "Search for chargino–neutralino pair production in final states with three leptons and missing transverse momentum in $\sqrt{s} = 13$ TeV pp collisions with the ATLAS detector," 6 2021, 2106.01676.

[175] T. A. Collaboration, "Searches for electroweak production of supersymmetric particles with compressed mass spectra in $\sqrt{s} = 13$ tev pp collisions with the atlas detector," *Phys. Rev. D*, vol. 101, no. 5, p. 052005, 2020, 1911.12606.

[176] The ATLAS Collaboration, "Search for top squark pair production in final states with one isolated lepton, jets, and missing transverse momentum in $\sqrt{s} = 8$ TeV pp collisions using 20.3 fb^{-1} of ATLAS data," Tech. Rep. ATL-COM-PHYS-2013-1490, CERN, Geneva, Nov 2013.

[177] The ATLAS Collaboration, "Search for top squarks in final states with one isolated lepton, jets, and missing transverse momentum in $\sqrt{s} = 13$ TeV pp collisions using 10 fb^{-1} of ATLAS data," Tech. Rep. ATL-COM-PHYS-2016-509, CERN, Geneva,

May 2016.

[178] R. Brun and F. Rademakers, "Root user's guide." `https://root.cern.ch/drupal/content/users-guide`, 2015. [Accessed: 2015-06-22].

[179] V. Filippini, "TGenPhaseSpace Class Reference." `https://root.cern.ch/doc/master/classTGenPhaseSpace.html`, Sept 2016. [Accessed: 2016-09-13].

[180] The HERWIG Collaboration, "Herwig++ Physics and Manual," *Eur. Phys. J.*, vol. C58, pp. 639–707, 2008, 0803.0883.

[181] G. Mahlon and S. Parke, "Angular correlations in top quark pair production and decay at hadron colliders," *Phys. Rev. D*, vol. 53, pp. 4886–4896, May 1996.

[182] M. Krämer, A. Kulesza, R. van der Leeuw, M. Mangano, S. Padhi et al., "Supersymmetry production cross sections in pp collisions at sqrts = 7 tev," 2012, 1206.2892.

[183] A. M. Sirunyan, A. Tumasyan et al., "Search for top squarks decaying via four-body or chargino-mediated modes in single-lepton final states in proton-proton collisions at $\sqrt{s}$ =13 tev," *Journal of High Energy Physics*, vol. 2018, Sep 2018.

[184] G. Cowan, K. Cranmer, E. Gross and O. Vitells, "Asymptotic formulae for likelihood-based tests of new physics," *Eur. Phys. J. C*, vol. 71, p. 1554, 2011, 1007.1727. [Erratum: Eur.Phys.J.C 73, 2501 (2013)].

[185] M. Baak, G. J. Besjes, D. Côté, A. Koutsman, J. Lorenz and D. Short, "Histfitter software framework for statistical data analysis," *The European Physical Journal C*, vol. 75, p. 153, Apr 2015.

[186] A. J. Barr and C. G. Lester, "A Review of the Mass Measurement Techniques proposed for the Large Hadron Collider," *J. Phys. G*, vol. 37, p. 123001, 2010, 1004.2732.

[187] R. D. Cousins, J. T. Linnemann and J. Tucker, "Evaluation of three methods for calculating statistical significance when incorporating a systematic uncertainty into a test of the background-only hypothesis for a Poisson process," *Nucl. Instrum. Meth.*, vol. A595, no. 2, pp. 480–501, 2008, physics/0702156.

[188] M. Lorenzo et al., "The RooStats project," *PoS*, vol. ACAT2010, p. 057, Sep 2010. ACAT2010 Conference Proceedings.

[189] The GANGA Collaboration, "GANGA: A tool for computational-task management and easy access to grid resources," *Computer Physics Communications*, vol. 180, no. 11, pp. 2303 – 2316, 2009.

[190] J. Elmsheuser *et al.*, "Distributed analysis in ATLAS using GANGA," *Journal of Physics: Conference Series*, vol. 219, no. 7, p. 072002, 2010.

[191] A. Buckley, J. Butterworth, S. Gieseke, D. Grellscheid, S. Höche, H. Hoeth et al., "General-purpose event generators for lhc physics," *Physics Reports*, vol. 504, no. 5, pp. 145 – 233, 2011.

[192] S. Marzani, G. Soyez and M. Spannowsky, *Looking inside jets: an introduction to jet substructure and boosted-object phenomenology*, vol. 958. Springer, 2019, 1901.10342.

[193] C. Oleari, "The POWHEG-BOX," *Nucl. Phys. Proc. Suppl.*, vol. 205-206, pp. 36–41, 2010, 1007.3893.

[194] The PYTHIA Collabortion, "An introduction to PYTHIA 8.2," *Comput. Phys. Commun.*, vol. 191, pp. 159–177, 2015, 1410.3012.

[195] T. Gleisberg, S. Hoeche, F. Krauss, M. Schonherr, S. Schumann, F. Siegert and J. Winter, "Event generation with SHERPA 1.1," *JHEP*, vol. 02, p. 007, 2009, 0811.4622.

[196] J. Alwall, M. Herquet, F. Maltoni, O. Mattelaer and T. Stelzer, "MadGraph 5 : Going Beyond," *JHEP*, vol. 06, p. 128, 2011, 1106.0522.

[197] The MADGRAPH Collaboration, "The automated computation of tree-level and next-to-leading order differential cross sections, and their matching to parton shower simulations," *JHEP*, vol. 07, p. 079, 2014, 1405.0301.

[198] CDF Collaboration, "Search for Standard Model Higgs Boson Production in Association with a W Boson Using a Matrix Element Technique at CDF in p-barp collisions at sqrts = 1.96 TeV," *Phys. Rev. D*, vol. 85, p. 072001. 29 p, Dec 2011. Comments: Submitted to Physical Review D.

[199] The ATLAS Collaboration, "Measurement of hard double-parton interactions in $W(\to \ell\nu) +$ 2-jet events at $\sqrt{s}$=7 tev with the ATLAS detector," *New Journal of Physics*, vol. 15, no. 3, p. 033038, 2013.

[200] The CMS Collaboration, "Measurement of associated production of vector bosons

and $t\bar{t}$ at $\sqrt{s}$ = 7 TeV," *Phys. Rev. Lett.*, vol. 110, p. 172002. 27 p, Mar 2013. Comments: Replaced with published version. Added journal reference and DOI.

[201] O. B. Bylund, "Modelling Wt and tWZ production at NLO for ATLAS analyses," in *9th International Workshop on Top Quark Physics*, 11 2016, 1612.00440.

[202] A. Buckley, "ATLAS Pythia 8 tunes to 7 TeV data," in *6th International Workshop on Multiple Partonic Interactions at the LHC*, p. 29, 12 2014.

[203] The LHC Collaboration, "Parton distributions for the LHC Run II," *JHEP*, vol. 04, p. 040, 2015, 1410.8849.

[204] R. Kwee, *Development and Deployment of an Inner Detector Minimum Bias Trigger and Analysis of Minimum Bias Data of the ATLAS Experiment at the Large Hadron Collider.* PhD thesis, Humboldt U., Berlin, 9 2011.

[205] The ATLAS Collaboration, "Electron efficiency measurements with the ATLAS detector using the 2015 LHC proton-proton collision data," 2016.

[206] W. Buttinger, "The ATLAS Level-1 Trigger System," tech. rep., CERN, Geneva, Jun 2012.

[207] The ATLAS Collaboration, "Characterisation and mitigation of beam-induced backgrounds observed in the ATLAS detector during the 2011 proton-proton run," *JINST*, vol. 8, p. P07004, 2013, 1303.0223.

[208] The ATLAS Collaboration, "Selection of jets produced in 13TeV proton-proton collisions with the ATLAS detector," Tech. Rep. ATLAS-CONF-2015-029, CERN, Geneva, Jul 2015.

[209] B. Nachman and C. G. Lester, "Significance variables," *Phys. Rev.*, vol. D88, no. 7, p. 075013, 2013, 1303.7009.

[210] The ATLAS Collaboration, "Simulation of top quark production for the ATLAS experiment at $\sqrt{(s)}$ = 13 TeV," Tech. Rep. ATL-PHYS-PUB-2016-004, CERN, Geneva, Jan 2016.

[211] A. Read, "Presentation of search results: The CL(s) technique," *J. Phys. G*, vol. 28, pp. 2693–2704, 2002.

[212] B. Mistlberger and F. Dulat, "Limit setting procedures and theoretical uncertainties in Higgs boson searches," 4 2012, 1204.3851.

[213] I. Shipsey, "Vision and outlook: The future of particle physics," in *Proceedings, 38th International Conference on High Energy Physics (ICHEP 2016): Chicago, IL, USA, August 3-10, 2016*, 2017, 1707.03711.

[214] The Telescope Array Collaboration, "Indications of intermediate-scale anisotropy of cosmic rays with energy greater than 57 eev in the northern sky measured with the surface detector of the telescope array experiment," *The Astrophysical Journal Letters*, vol. 790, no. 2, p. L21, 2014.

[215] D. J. Fixsen, "The temperature of the cosmic microwave background," *The Astrophysical Journal*, vol. 707, no. 2, p. 916, 2009.

[216] The ATLAS Collaboration, "High-luminosity large hadron collider (HL-LHC)," Tech. Rep. CERN-2017-007-M, CERN, Geneva, 2017.

[217] C. Borschensky, M. Krämer, A. Kulesza, M. Mangano, S. Padhi, T. Plehn, and X. Portell, "Squark and gluino production cross sections in pp collisions at $\sqrt{s} = 13, 14, 33$ and 100 TeV," *Eur. Phys. J. C*, vol. 74, no. 12, p. 3174, 2014, 1407.5066.

[218] A. Buckley, "The hepthesis class," 2021.

List of figures

List of tables

List of Acronyms

ALICE A Large Ion Collider Experiment

ASIC Application-Specific integrated Circuits

ATLAS A Toroidal LHC ApparatuS

AdA the Anello Di Accumulazione collider

BCID Bunch-Crossing Identification

BCM Beam Conditions Monitor

BC Bunch-Crossing

BDT Boosted Decision Trees

BSM Beyond Standard Model physics

CERN Conseil Européen pour la Recherche Nucléaire

CKKW Catani-Kuhn-Krauss-Webber

CKM Cabibbo-Kobayashi-Maskawa

CMS Compact Muon Solenoid

CP Charge-Parity

CPU Central Processing Unit

CR Control Region

CDF Collider Detector at Fermilab

DAQ Data AcQuisition system

DGLAP Dokshitzer-Gribov-Lipatov-Altarelli-Parisi

EF Event Filter

ECAL Electromagnetic Calorimeter

EMEC Electromagnetic End-cap calorimeter

EM Electromagnetic

EW Electroweak

FCal Forward Calorimeter

GSW Glashow-Salam-Weiberg

HEC Hadronic End-cap Calorimeter

HERWIG Hadron Emission Reactions With Interfering Gluons

HCAL Hadronic Calorimeter

HF Heavy Flavour

HLT High Level Trigger

IBL Insertable B-Layer

ID Inner Detector

IP Interaction Point

ISR Initial State Radiation

JER Jet Energy Resolution

JES Jet Energy Scale

JVF Jet Vertex Fraction

JVT Jet Vertex Tagger

L1 Level-1 trigger

L2 Level-2 trigger

LB Luminosity Block

LEP Large Electron-Positron Collider

LHCb Large Hadron Collider beauty

LHC Large Hadron Collider

LSP Lightest Supersymmetric Particle

LSR Loose Signal Region

LUCID LUminosity measurement using Cherenkov Integrating Detector

MBTS Minimum Bias Trigger Scintillators

MC Monte Carlo

ME Matrix Element

MET Missing Transverse Energy

MSSM Minimal Supersymmetric Standard Model

MS Muon Spectrometer

NLO Next-to-Leading-Order

NP Nuisance Parameter

OPAL Omni-Purpose Apparatus at LEP

PDF Probability Density Function

PIXEL PIXEL detector

PMT PhotoMultiplier Tube

PMNS Pontecorvo-Maki-Nakagawa-Sakata

PV Primary Vertex

QCD Quantum Chromodynamics

QED Quantum Electrodynamics

QFT Quantum Field Theory

QM Quantum Mechanics

ROD Read-Out Driver

RoI Region of Interest

SCT SemiConductor Tracker

SHERPA Simulation of High-Energy Reactions of PArticles

SMT Soft Muon Trigger

SM Standard Model of particle physics

SRB0 Signal Region with 0 b-tagged jets

SRB1 Signal Region with 1 or more b-tagged jets

SR Signal Region

SUSY supersymmetry

SV Secondary Vertex

SVs Secondary Vertices

TCR Top Control Region

TDAQ Trigger and Data AcQuisition

TF Transfer Factor

TRT Transition Radiation Tracker

TSR Tight Signal Region

TileCal Tile Calorimeter

TVR Top Validation Region

vdM van der Meer

VR Validation Region

WCR W+jets Control Region

WVR W+jets Validation Region